Insertable B-Layer integration in the ATLAS experiment and development of future 3D silicon pixel sensors

Laura Franconi

Thesis submitted for the degree of Philosophiæ Doctor

Abstract

This work has two distinct objectives: the development of software for the integration of the Insertable B-Layer (IBL) in the ATLAS offline software framework and the study of the performance of 3D silicon sensors produced by SINTEF for future silicon pixel detectors. The former task consists in the implementation of the IBL byte stream converter. This offline tool performs the decoding of the binary-formatted data coming from the detector into information (e.g. hit position and Time over Threshold) that is stored in a format used in the reconstruction data flow. It also encodes the information extracted from simulations into a simulated IBL byte stream. The tool has been successfully used since the beginning of the LHC Run II data taking.

The experimental work on SINTEF 3D sensors was performed in the framework of the development of pixel sensors for the next generation of tracking detectors. Preliminary tests on SINTEF 3D sensors showed that the majority of these devices suffers from high leakage currents, low breakdown voltages and short charge carrier lifetimes. These signs of production issues were identified, during the subsequent prototyping run, as random doping deposition caused by a too-thin masking layer. The sensors underwent proton or neutron irradiation (up to $\phi = 9 \cdot 10^{15}$ n_{eq}/cm^2) to allow for fluence-dependent characterisation.

Electrical measurements and charge collection measurements under laser or radioactive source exposure have been carried out. Results of the electrical tests highlight a significant and sensor-dependent spread of these parameters. Common traits can however be identified: the leakage current augments as expected with temperature and with fluence. Radiation does not affect the depletion voltage, which remains at $U_{depl} \leq 20$ V. The breakdown voltage is observed to increase with fluence. Laser-induced charge collection measurements, performed using a TCT setup, show that sensors with diode-like electrical properties collect, even when irradiated at higher fluences, a larger and more uniform charge compared to sensors featuring suboptimal electrical characteristics. Radioactive source tests have been performed using an ALiBaVa read-out system. Results show that the SINTEF 3D sensor proton-irradiated to $\phi = 4.5 \cdot 10^{14}$ n_{eq}/cm^2 maintains a charge collection efficiency of 85% at $U_{bias} = -40$ V.

Experimental results support the findings observed during the latest SINTEF prototype run. Moreover, the three characterisation methods give consistent results. The electrical characterisation is therefore sufficient to identify suboptimally-performing sensors.

Acknowledgement

I would like to take the opportunity to thank all the people who helped me to complete this work and to (almost) sanely go through the Ph.D. years. There are too many names to mention all of them here, so I apologise to anyone not listed, please know I greatly appreciated your support!

First of all, I would like to thank Prof. Alexander Read for his endorsement in the Ph.D. program at the University of Oslo and for the time he has dedicated to proofread my thesis. Thank you also to my second supervisor, Dr. Ole Røhne, for giving me the opportunity of spending time at CERN for my research work.

I would like to thank the Marie Curie TALENT community: it was a unique chance to deepen my knowledge on silicon detectors and to develop skills in fields, such as technology transfer and business modeling, that are usually unexplored during standard Ph.D. experiences. Thanks to this network, I've met excellent colleagues and great friends.

I express my deepest gratitude to Dr. Michael Moll for having welcomed me in the SSD group at CERN. My experimental work would not have been possible without the access to the fully-equipped SSD laboratories. I am really thankful for all the help and fruitful discussions with my SSD colleagues, I really profited from all the knowledge they shared with me and from their precious advice. I am even more grateful for their wonderful friendship and their constant support and encouragement (not to mention the cakes!). A particular mention to my office mates, Sofia and Esteban, for sharing the maddest (and most hilarious) moments. I had such a great time!

Special thanks are dedicated to Fares Djama, Mapo Giordani, Marco Battaglia, Shaun Roe and Didier Ferrere for their support and guidance on the ATLAS-related tasks. I would really like to thank Silvia Miglioranzi for her never-ending patience to reveal to me the mysteries of Athena and for pushing and encouraging me all the time. Steffen, thank you for sharing the craziness of the IBL byte stream converter work. Your competence in C++ was definitely essential!

A sincere thank you to all friends and colleagues (Alessandro, Carlo, Esteban, Federico, Isidre, Michael, Matteo, Sofia, Stefan) who proofread my long thesis: I know I'm not particularly concise :), but I can guarantee that every single comment was highly appreciated. I owe you for all the time you dedicated to me.

Thank you to Sara, Riccardo, Maria Elena, Antonello, Silvia, Luca, Giuz, Jessica, Mauro, Letizia, Eric, Elena, Sandra and Ale for being my Italian friends abroad: having you around always made me feel at home. Daniel, Adrian, Kate, Tamara, you have been great friends since the first summer I spent at CERN. It's always fantastic to see you! Thank you Cecilia, Sara, Robert, Fabi, Greg, Jean, Anders, Kaja, Siri and Dávid for making Norway warmer, even in the coldest winter days.

Grazie di cuore ai miei genitori, a Matteo e ad Anna: avete sempre creduto in me e mi avete sempre fatto nascere un sorriso nei momenti bui. Grazie anche alle mie cugine Giulia, Anna e Stella e agli zii Elena e Michele, un pezzetto di famiglia a Ginevra. Mi avete accolto, nutrito e coccolato. Non so come ringraziarvi!

Thank you to my friends Sara, Maria Grazia, Francesca and Serena, the most brilliant sisters I could ever find.

Last, my deepest and most heartfelt thank you to Carlo. Thank you for everything. You've always been here for me, encouraging and supporting me, even when you didn't know. Grazie!

Laura

Contents

List of Figures

xiii

List of Tables

Acronyms

3DC 3D Consortium

AC Alternating Current

ADC Analog to Digital Conversion (or Converter)

ADC Analog to Digital Counts (unit of charge used in ALiBaVa)

AFP ATLAS Forward Physics

ALiBaVa A Liverpool Barcelona Valencia (Readout System)

ALICE A Large Ion Collider Experiment

AOD Analysis Object Data

ATLAS A Toroidal LHC ApparatuS

BABY 3D SINTEF test structure, with pad-like readout

BCID Bunch Crossing IDentifier

BCM Beam Conditions Monitor

BOC Back Of Crate (card)

BoF Beginning of Fragment

BS ByteStream

BSCnv ByteStream Converter

BT Barrel Toroid

CCE Charge Collection Efficiency

CERN Conseil Européen pour la Recherche Nucléaire, European Organisation for Nuclear Research

CDF Collider Detector at Fermilab

CMS Compact Muon Solenoid

CNM Centro Nacional de Microelectrónica

CP Charge Parity

CSC Cathode Strip Chamber

CV Capacitance-Voltage

CVD Chemical Vapour Deposition

Cz Czochralski

DAQ Data AcQuisition

DB (ALiBaVa) Daughter Board

DBM Diamond Beam Monitor

DC Direct Current

DDTC Double-side Double Type Column

DORIC Digital Opto-Receiver Integrated Circuit

DRIE Deep Reacting Ion Etching

DxAOD Derived AOD

ECT EndCap Toroid

EF Event Filter

EMCal ElectroMagnetic Calorimeter

ENC Equivalent Noise Charge

ESD Event Summary Data

eTCT edge Transient Current Technique

EVNT Event Data

FBK Fondazione Bruno Kessler

FCal Forward Calorimeter

FE-I3 Front-End Integrated (Circuit) 3

FE-I4 Front-End Integrated (Circuit) 4

FEI3 3D SINTEF sensor compatible with FE-I3 geometry

FEI4 3D SINTEF sensor compatible with FE-I4 geometry

FTK Fast Track Trigger

Fz Float Zone

HCal Hadronic Calorimeter

HEC Hadronic Endcap Calorimeter

HEP High Energy Physics

HL-LHC High Luminosity - Large Hadron Collider

HLT High Level Trigger

IBL Insertable B-Layer

ID Inner Detector

IP Interaction Point

IR InfraRed (laser)

IRRAD Irradiation Facility at CERN

ITk Inner Tracker

IV Current-Voltage

GUI Graphical User Interface

JSI Jožef Stefan Institute

L0 Layer 0 (B-Layer)

L1 Layer 1

L1A Level-1 Accept

L1Calo Level-1 Calorimetry (trigger)

L1ID Level 1 IDentifier

L1Muon Level-1 Muon system (trigger)

L2 Layer 2

LAr Lead liquid Argon

LCR Inductance, Capacitance, Resistance (meter)

LEIR Low Energy Ion Ring

LEP Large Electron-Positron (Collider)

LHC Large Hadron Collider

LHCb Large Hadron Collider beauty

LINAC Linear Accelerator

LS1 Long Shutdown 1

LS2 Long Shutdown 2

LSB Least Significant Bit

LVL1 Level-1 (trigger)

LVL2 Level-2 (trigger)

MB (ALiBaVa) Mother Board

MC Monte Carlo

MCC Module Controller Chip

MCz Magnetic Czochralski

MDT Muon Drift Chamber

MEMS Micro-Electro-Mechanical Systems

MIP Minimum Ionising Particle

MPV Most Probable Value

MSB Most Significant Bit

NIEL Non-Ionising Energy Loss

PCB Printed Circuit Board

PKA Primary Knock-on Atom

PS Proton Synchrotron

QCD Quantum Chromo Dynamics

QED Quantum Electro Dynamics

QGP Quark Gluon Plasma

R&D Research and Development

ROB Read-Out Buffer

ROD Read-Out Driver

RoI Region of Interest

ROL Read-Out Link

RPC Resistive Plate Chamber

SM Standard Model

SCT SemiConductor Tracker

SMA SubMiniature version A (connector)

SNF Stanford Nanofabrication Facility

SNR Signal-to-noise ratio

SOI Silicon On Insulator

SPS Super Proton Synchrotron

SQP Service Quarter Panel

SSD Solid State Detector

SUSY SUper SYmmetry

TCal Tile Calorimeter

TCT Transient Current Technique

TDAQ Trigger and Data AcQuisition

TGC Thin Gap Chamber

ToT Time over Threshold

TRT Transition Radiation Tracker

TTC Trigger and Timing Control (system)

VCSEL Vertical Cavity Surface Emitting Laser

VLSI Very Large Scale Integration

Chapter 1

Introduction

High Energy Physics (HEP) aims at identifying the fundamental blocks that compose the entire universe and at understanding the basic principles that rule their interactions. The Standard Model (SM) of particle physics was developed starting from the 1960s. This very successful theory describes, from a quantum physics point of view, the elementary particles and their mutual interactions, namely the electromagnetic, weak and strong forces [1, 2, 3]. All its predictions are presently experimentally confirmed: the discovery of the Higgs boson, the last long-awaited missing particle of the SM, was announced in July 2012. The SM theory, despite being extremely predictive, is not fully comprehensive: among the unaddressed questions, it lacks the inclusion of gravity (this force does not have a description at particle level yet), it only describes $\sim 5\%$ of the matter composing the universe, it does not explain the observed asymmetry between matter and antimatter and it does not describe the neutrino masses.

The Large Hadron Collider (LHC) at CERN is the most powerful instrument we have to progress towards a more complete understanding of the building blocks of nature [4, 5]. This complex machine allows physicists to study, in a laboratory-controlled environment, the frontier of electroweak physics and possibly discover yet-to-be observed particles. It is designed to accelerate and collide high-energy particles (protons and heavy ions) with a frequency of 40 MHz. Many superimposed inelastic collisions take place together with the main event of interest. Overall, about 1000 charged particles arise from the interaction region at each bunch crossing. The experiments around the LHC ring are instrumented with detectors that have been optimised for the measurement and the identification of particles arising from the collisions that may indicate new physics.

The LHC was initially operated at centre-of-mass energy $\sqrt{s} = 7 - 8$ TeV

1

during Run I (2010-2012). Right after the discovery of the Higgs boson, at the end of 2012, a first long shutdown (LS1) has allowed the LHC to increase its capabilities, and during Run II (2015-2018), the machine is expected to reach its nominal values of $\sqrt{s} = 14$ TeV and luminosity $\mathcal{L} = 10^{34}$ cm^{-2}s^{-1}. In the following years, the LHC will be further improved for the future High-Luminosity phase (HL-LHC), where the luminosity will be increased to $\mathcal{L} = 5 \cdot 10^{34}$ cm^{2}s^{-1} [6].

The ATLAS experiment [7] is a hermetic, multipurpose detector system, the largest of the 4 main experiments along the LHC ring. Its Pixel detector, the closest to the interaction point, is a silicon-based detector. It aims at measuring with very high resolution the position of charged particles passing through its volume. It provides the tracking algorithms with information needed to reconstruct particle momenta. This feature is essential in the case of short-lived particles: they are produced at the collision point, but decay shortly after, giving secondary vertices. The identification of such particles is of utmost importance because they often are signature of interesting physics processes. For example, the most frequent decay channel of the Higgs boson is the decay to $H \rightarrow b\bar{b}$. The $b-$quark gives rise to a $B-$meson, a short-lived particle that travels only for a distance of ~ 100 μm before decaying.

During the Run I, the B-Layer (the innermost layer during the first LHC data taking) progressively experienced failures of some components. A badly performing track detector leads to poor particle reconstruction, which, for example, worsen the precision in the measurement of particle properties.

To overcome the degradation of the performance of the Pixel detector, during the LS1 the ATLAS Collaboration installed a new, innermost layer, the Insertable B-Layer (IBL) [8]. This detector restores the inefficiencies of the Run I pixel layer and improves the tracking robustness. Moreover, it provides the ATLAS experiment with higher-resolution measurements of the tracking parameters and is expected to withstand higher radiation damage levels. The new detector, featuring a radius of only 34 mm from the interaction point, is the result of significant Research and Development (R&D) efforts: all components are the state-of-the-art in their sector. The IBL has a smaller pixel size that leads to a better spatial resolution, its sensors are read out with new, faster and radiation-harder read-out chips. Its mechanical support, made out of carbon fiber, is lighter and, in addition to the innovative CO_2 cooling, favours a better thermal conductivity.

The IBL is the first HEP detector to be instrumented with 3D silicon sensors [9], together with the standard planar technology. The 3D layout offers

several advantages: the orientation of the electrodes, etched as columns in the silicon bulk, decouples the amount of collected charge, which has a dependence on the thickness of the sensor, from the distance between electrodes. A shorter inter-electrode distance means shorter collection time and intrinsically better radiation hardness. Moreover, their geometry guarantees smaller clusters for inclined tracks with respect to the planar technology, making them the best choice to instrument the extremities of the IBL detector, in the forward region along the beam direction.

Drawbacks of the 3D technology are the larger capacitance, which increases the noise level, and the more complex production method, which leads to higher production costs and - generally - lower yields. Worldwide, only 4 foundries produce 3D sensors used in HEP experiments: CNM (Spain), FBK (Italy), SINTEF (Norway) and SNF (USA).

In preparation for the HL-LHC phase, the ATLAS experiment will install a new Pixel detector, the Inner Tracker (ITk) [10]. Its design is still under development and 3D sensors are among the possible sensor technologies that could be adopted to instrument it.

The work described in this Ph.D. thesis is twofold: the first part is a software-oriented task consisting of the technical implementation of the byte stream converter for the IBL. The second part is an R&D work on irradiation and measurements of a set of 3D silicon sensors produced by SINTEF [11].

The IBL byte stream converter (BSCnv) is an offline tool that performs the conversion of the binary stream of data coming from the IBL during data taking into information (such as the hit's position and Time over Threshold, a parameter proportional to the collected charge) that is used for the next steps of the data analysis. The BSCnv is also used when carrying out the simulation of the detector: it encodes the simulated data into a stream of bits, providing a tool to verify the simulation accuracy.

The work on silicon sensors produced by SINTEF focused on the characterisation of $p-$bulk 3D sensors from the third SINTEF prototype run. In preliminary tests these sensors showed low yield, with the vast majority of sensors presenting high leakage current, low breakdown voltage and short charge carrier lifetimes. The experimental work focuses on the description of the general characteristics of the sensors and strives to understand the origin of such properties through non-destructive tests. The low yield was suspected to be linked to production issues. This speculation is supported by findings observed during the production of the subsequent SINTEF prototype run: the fabrication

3

procedure was found to create randomly-located doped pits in the silicon. This phenomenon is understood to have happened in the third run as well, and could explain the observed suboptimal performance. Measurement results match the expected behaviour foreseen assuming these findings as the cause of the low-yield of the wafers from the third run.

The tested SINTEF 3D sensors were exposed to proton or neutron irradiation and were measured, before and after irradiation, using three experimental methods, aimed at characterising their electrical properties (IV and CV measurements) as well as their charge collection response under laser (TCT) and radioactive source (ALiBaVa) exposure.

This thesis firstly includes, in Chapter 2, a review of the LHC and of the ATLAS experiment, in the current conditions and the future upgrades. Chapter 3 gives a summary of the silicon sensor technology, with special focus on 3D sensors. The IBL detector is described in detail in Chapter 4. This chapter also reports the original work performed on the byte stream converter. Chapter 5 is dedicated to the description of SINTEF sensors, the irradiation campaigns and the three experimental setups. It also reports the analysis methods developed for the different experimental techniques. Chapter 6 collects the experimental results coming from the measurements of these sensors. Conclusions of the work are drawn in Chapter 7.

Chapter 2

The LHC and the ATLAS Experiment

This chapter is divided in two main parts: the first is dedicated to the presentation of the present status of the LHC as well as its future upgrades. The second part is devoted to the description of one of its experiments, ATLAS.

Section 2.1 briefly describes the structure of the LHC, Section 2.2 discusses the physics motivations for the LHC and for its future upgrade. The LHC schedule, from the first collisions in 2009 to the next 15 years, is illustrated in Section 2.3. Section 2.4 concludes the second chapter with the description of all the subdetectors of the ATLAS experiment.

2.1   The Large Hadron Collider

The Large Hadron Collider, at the European Organisation for Nuclear Research (CERN), is the largest scientific instrument ever built and represents a unique and powerful tool for discovering the fundamental properties of particles and their interactions. Its centre-of-mass energy and luminosity exceed the power of any previous human-built accelerator.

The LHC machine lies around 100 meters underground, in a 27-kilometer tunnel already used for the previous accelerator, the Large Electron-Positron Collider (LEP), which was operated between 1989 and 2000.

The LHC can produce proton-proton, proton-lead ion (Pb) and Pb-Pb collisions from two beams circulating in opposite directions. The maximum centre-of-mass energies are, respectively, $\sqrt{s}_{\text{p-p}} = 14$ TeV, $\sqrt{s}_{\text{p-Pb}} = 8.8$ TeV, and

$\sqrt{s}_{\text{Pb-Pb}} = 2.76$ TeV/nucleon pair. Nominal LHC beams are composed of 2808 bunches (600 bunches for Pb beams), each of which contains $\sim 1.15 \times 10^{11}$ protons ($\sim 7 \times 10^7$ Pb ions) [4, 5].

Luminosity is a fundamental parameter of a particle accelerator that measures its ability to produce particle collisions. It is the coefficient of linear proportionality between the number of events per second, dN_{events}/dt, and the cross section of the event of interest, σ_{event}:

$$\frac{dN_{events}}{dt} = \mathcal{L} \times \sigma_{event}. \tag{2.1}$$

The machine luminosity can be defined as

$$\mathcal{L} = \frac{N_b^2 n_b f_{rev} \gamma_r}{4\pi \epsilon_n \beta^*} F, \tag{2.2}$$

where N_b is the number of particles per bunch, n_b the number of bunches per beam, f_{rev} the revolution frequency, γ_r the relativistic gamma factor. ϵ_n is the normalised beam emittance (the average spread of beam particles in the position-momentum phase space). β^*, the beta function at the collision point, quantifies the strength of final focus: the beta function is defined at each point s, along the accelerator, as $\beta(s) = \sigma^2(s)/\epsilon$, the ratio between the square of the width of the beam, assumed to have a Gaussian shape, and the emittance. Finally, F is the geometric luminosity reduction factor due to the crossing angle at the interaction point (IP) [5].

The design luminosity of the LHC is $\mathcal{L} = 10^{34}$ cm^{-2}s^{-1} for proton-proton collisions and $\mathcal{L} = 10^{27}$ cm^{-2}s^{-1} for Pb-Pb collisions.

The cross section introduced in Equation 2.1 is an important parameter in particle physics. It measures the probability for a reaction to occur: the smaller the cross section, the rarer the interaction.

2.1.1 The LHC accelerator complex

Before entering the LHC ring, particles undergo a series of acceleration steps inside the different machines of CERN's accelerator complex, shown in Figure 2.1 [12]. The proton source is a bottle of hydrogen gas. An electric field is used to strip hydrogen atoms of their electrons to yield protons. The linear accelerator, Linac 2, pushes the protons to an energy of 50 MeV. From there, the particles are injected into the Booster, where they are accelerated to 1.4 GeV.

Protons undergo a further acceleration to 26 GeV inside the Proton Synchrotron (PS). The Super Proton Synchrotron (SPS) is finally used to increase particles' energy to 450 GeV before they are injected to the LHC ring. Here, the bunches are accumulated and accelerated to their peak energy. Once the beams are declared as stable, they are steered to cross at the experimental points and collisions take place.
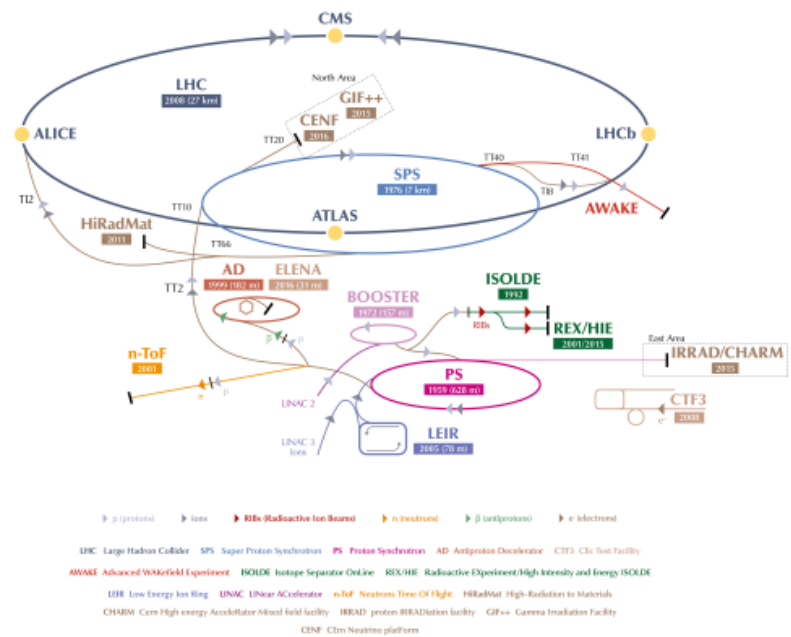
Figure 2.1: CERN's accelerator complex. Image reproduced from [12].

Lead ions are obtained from a source of vaporised lead and enter Linac 3 before being collected and accelerated in the Low Energy Ion Ring (LEIR). Then, they are injected into the PS and follow the same route to their maximum energy as protons.

The accelerated particles collide in four experimental points, in the centres of the four main particle detectors: ALICE[1] [13], ATLAS[2] [7], CMS[3] [14] and

---

[1]ALICE: A Large Ion Collider Experiment.
[2]ATLAS: A Toroidal LHC ApparatuS.
[3]CMS: Compact Muon Solenoid.

LHCb[4] [15]. ATLAS and CMS are general-purpose experiments: they look for any signs of new physics, search for rare processes in the SM, aim at improving the precision of established processes, study B-physics as well as heavy ion physics. ALICE's major aim is the investigation of a fluid form of matter called Quark-Gluon Plasma that is supposed to have existed shortly after the Big Bang, while LHCb is devoted to the understanding of the unbalance between matter and antimatter in the Universe. These aspects will be discussed in Section 2.2.

2.1.2 The LHC structure

The detailed description of the LHC accelerator goes beyond the purposes of this work, but is provided in [4, 5]. Here, only a very broad overview is given.

The LHC ring has eight arcs and straight sections. Four of the eight sections host the HEP experiments, while the others are used for machine utilities: radio frequency, collimation and beam abort.

The LHC is instrumented with more than 7000 superconducting magnets, of different varieties. The two main types are dipoles and quadrupoles. The first bend particle trajectories, forcing them to follow the LHC ring. Dipoles are 15 m long and cover most of the LHC arcs. Every 6 dipoles, there is a main quadrupole and lattice correctors.

Quadrupoles are used for focusing the beams, namely reducing their dispersion in the $x - y$ plane, perpendicular to the beam direction. As one quadrupole can only squeeze the beam in one direction, while defocusing it in the other, pairs of quadrupole magnets, oriented at $90°$, are put close by one another.

In order to ensure their superconductivity, magnets are kept at 1.9 K. This temperature is reached using pressurised superfluid helium. Beams circulate in both directions inside two parallel vacuum pipes, which intersect in the experimental points. The acceleration of the two beams is provided by radiofrequency cavities, operating at 400 MHz.

2.2 The LHC physics programme

The first run at the LHC was marked by a breakthrough for particle physics: on 4 July 2012 the ATLAS and CMS Collaborations announced the discovery, in the search for the Higgs boson, of a new particle carrying a mass of around

---

[4]LHCb: Large Hadron Collider beauty.

126 GeV/c^2 [16, 17]. Its properties were confirmed to be compatible to those predicted for the Higgs boson, the last missing particle of the Standard Model. Following the measurement of the entire Run I dataset, the ATLAS+CMS combined mass of the new particle has been measured to be [18]:

$$m_H = 125.09 \pm 0.21 \text{ (stat.)} \pm 0.11 \text{ (syst.)} \text{ GeV/c}^2.$$

The current and future LHC data taking runs (which will be described in Section 2.3) aim at measuring precisely the properties of this newly-discovered particle, performing other precision measurements in the SM, B-physics and heavy-ion sectors, and searching for small signals, indications of new physics beyond the Standard Model.

2.2.1 The Standard Model of Particle Physics

The Standard Model (SM) is a very successful theory developed starting from the 1960s. Combining special relativity with quantum mechanics, this well-tested theory describes the fundamental particles and their interactions. Figure 2.2 shows all particles comprising the SM and their interactions [19]. After the discovery of the Higgs boson, all the SM elementary particles have been experimentally found and the model is complete.
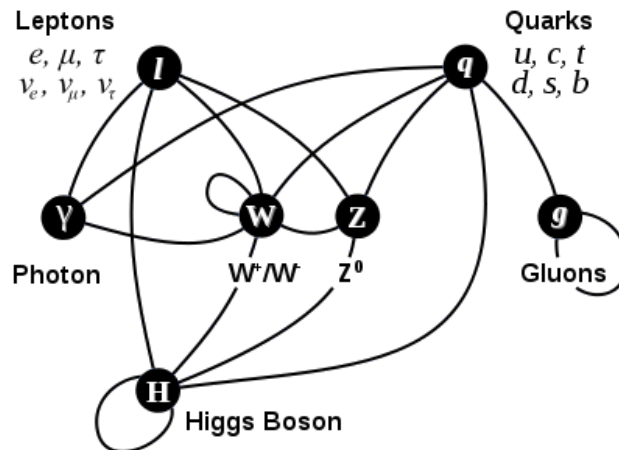
Figure 2.2: Elementary particles of the Standard Model and their interactions. Image reproduced from [19].

The SM classifies all known subatomic particles into fermions, half-integer

9

spin particles that obey the Fermi-Dirac statistics, and bosons, particles of integer spin that follow the Bose-Einstein statistics. There are 24 different types of fermions: 6 quarks and their antiparticles, and 6 leptons and their antiparticles (at the moment it is still possible that neutrinos, unlike charged leptons, may be their own antiparticle). Fermions interact with each other by exchanging a boson. Bosons include the photon γ, responsible for the electromagnetic interaction; the $W^\pm$ and Z bosons, mediators of the charged and neutral weak interactions; 8 gluons g, messengers of the strong force; and the Higgs boson H. The Higgs boson is "visible manifestation" of the Higgs field, a quantum field with non-zero value, that permeates throughout space and is responsible for giving mass to particles interacting with it. The theoretical explanation of the Higgs field was first described by the Physics Nobel winners Peter Higgs and François Englert - and Robert Brout - in 1964 [20, 21].

Leptons are divided in three families, each composed of a weak isospin doublet made of a massive and charged particle (electron, muon, tau) and a massless[5], neutral particle (the corresponding neutrinos). Charged leptons can interact electromagnetically by means of the exchange of a photon. The mathematical description of electromagnetic interactions is given by the Quantum Electro Dynamics (QED). Charged leptons also feel the charged and neutral weak force, mediated by the $W^\pm$ and Z bosons. The weak interaction is the only one neutrinos experience: being neutral and leptons, they interact neither with the photon nor the gluon.

Quarks have fractional charge: u, c and t have charge $+2/3\ e$, while d, s and b have charge $-1/3\ e$. They have never been observed in a free state, but are confined, because of the strong force, in bound states. One important exception is the top quark, which decays prior to hadronisation, thus giving its properties to its decays products. Mesons are formed by a quark and an antiquark $q\bar{q}$, while baryons are comprised of three quarks (or antiquarks) qqq. In 2014, the LHCb Collaboration at CERN announced the discovery, with a significance larger than 9 standard deviations, of pentaquark states in the decay $\Lambda_0^b \to J/\psi K^- p$ [22]. All quarks can interact, besides the already mentioned strong force, with the electromagnetic and weak forces.

All massive particles can exchange Higgs bosons: this implies that all particles

---

[5]Experimental observations of neutrino oscillations discredit the hypothesis of massless neutrinos. Neutrino oscillations can only be explained by invoking a small difference between neutrino flavours' non-zero masses. Given the very small magnitude of their mass, however, in most scenarios (for example, LHC physics) neutrinos can be considered massless.

of the SM, with the exception of neutrinos, can interact with it. Finally, gluons, $W^{\pm}$ and Higgs bosons can also self-interact.

For further details on the SM, see [23, 24, 25, 26].

2.2.2   New physics searches at the LHC

The discovery of the Higgs boson does not exhaust the LHC physics programme or its discovery potential: the future years will be devoted to precision studies and searches for small signals of new physics.

First of all, there is room for improvement in the precision of the measurements of the Higgs boson properties. The SM predicts that at the energy of the Higgs boson mass, $m_H \simeq 125$ GeV, several decay channels are accessible at the LHC luminosity, while others can only being precisely measured at the luminosity foreseen during the High Luminosity (HL) phase.

Secondly, verifying the validity of the SM at energy scales above 1 TeV is essential and can be achieved by probing the variety of production and decay modes of the Higgs boson, precisely measuring the couplings with fermions and bosons as well as determining the self-couplings of the Higgs boson [6, 27].

Operations and upgrades of the LHC will provide the higher integrated luminosity required to perform many precision measurements of rare processes. For example, the $B-$physics programme includes studies on rare interactions such as $B_s \to J/\psi\phi$, $\Lambda_b \to J/\psi\Lambda$, $B_s \to \mu\mu$ and $b \to s\mu\mu$.

The SM, now complete, does not represent an end point: despite successfully describing the building blocks of matter, it leaves unaddressed critical questions. In fact, physicists have not found yet answers to questions such as what is the nature of the dark matter and dark energy, composing 96% of the universe, what is the origin of the asymmetry between matter and antimatter, why is gravity so weak compared to the other forces, and what happened in the very first moments of the universe, during the Big Bang [28].

Theories as extensions to the SM are trying to provide solutions to these problems. These theoretical speculations invoke more symmetries, such as supersymmetry (SUSY), or new forces or constituents, or again, extra dimensions. The evaluation of the Higgs boson mass represents itself a valid hint to the existence of dark matter and of new physics at the TeV scale, which would address open topics such as the hierarchy problem[6].

---

[6]The hierarchy problem is related to the discrepancy between the strength of the weak and the gravitational forces: the Planck Mass, namely the mass of the smallest possible black hole, is ~ 15

11

The study of Quantum Chromo Dynamics (QCD) under extreme conditions of temperature and density will keep being pursued during all the LHC phases, colliding heavy-ion beams at energies more than 30 times higher than that of previous accelerators.

The origin of the imbalance between matter and antimatter could be partially explained by breaking one of the symmetries of the SM: CP symmetry[7] [29, 30]. CP violation was indirectly observed in 1964 in Kaons (mesons composed of a u-quark and a $\bar{s}$−quark) and the LHCb Collaboration, in 2013, reported the observation of direct CP-violation in $B_s^0 \to K^-\pi^+$ decays [31].

Finally, physicists are hoping to discover what could pave the way towards a Grand Unified Theory. This would combine all four forces (electromagnetic, weak, strong and gravity) together.

In order to make new exciting discoveries, HEP experiments must be able to detect and reconstruct with high precision the decay products that give signatures of the presence of theorised particles over a wide range of energies.

2.3   The LHC schedule

The LHC schedule, from its first collision to the next 15 years, is shown in Figure 2.3 [28, 32]. The LHC's first collisions took place in 2009 and, by the end of 2012, the machine delivered 23 fb^{-1} (23 inverse femtobarns[8]) [33]. During this first period, referred to as Run I, the centre-of-mass energy was originally kept to $\sqrt{s} = 7$ TeV in 2011 and increased to $\sqrt{s} = 8$ TeV in 2012.

One of the main features of the operations during Run I was the use of high bunch intensity with 50 ns bunch spacing. As a result, the machine provided good instantaneous luminosity performance, at a cost of a high average number of inelastic collisions superimposed on the event of interest (pile-up) inside the experiments. Figure 2.4 shows, as an example, the pile-up measured inside the ATLAS experiment in 2011 and 2012 [34]. The mean number of collisions

---

orders of magnitude larger than the mass of the W and the Z bosons. The hierarchy problem is related to the Higgs field because its non-zero value is responsible for the weak boson masses.

[7]CP stands for Charge Parity (the CP violation, however, is not sufficient to account for the observed baryon asymmetry of the universe). The CP symmetry, combination of the charge and the parity symmetries, states that laws of physics should hold if a particle is substituted with its antiparticle (C-symmetry) when the spatial coordinates are inverted (P-symmetry).

[8]A barn is a unit of area equal to 10^{-24} cm^2. It indicates the measure of the probability of interaction between particles. The inverse femtobarn, therefore, indicates the number of collision events that take place in a femtobarn.
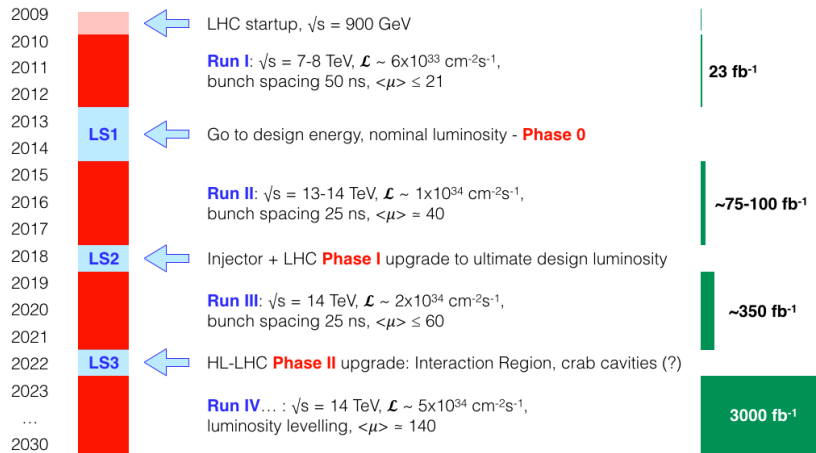
Figure 2.3: LHC road map from first collisions until the end of the HL-LHC run. Image modified from [28, 32].

per bunch crossing inside this experiment doubled between $7\,\text{TeV}$ and $8\,\text{TeV}$, reaching peaks of more than 35 collisions per bunch during the 2012 data collection.
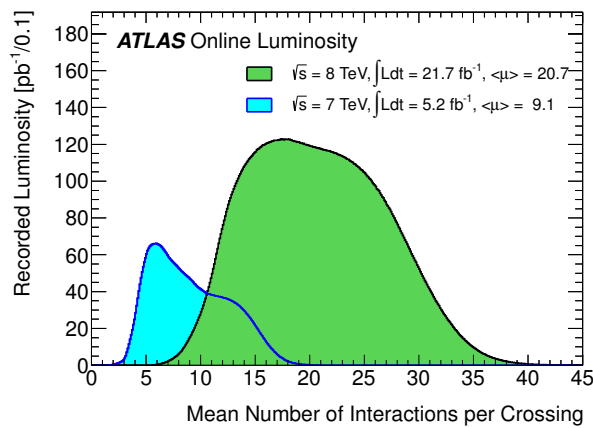
Figure 2.4: Luminosity-weighted distribution of the mean number of interactions per crossing for the 2011 and 2012 p-p collision runs. Image reproduced from [34].

The total proton-proton cross section at $\sqrt{s} = 14\,\text{TeV}$ is expected to be roughly 100 mb; thus, at LHC design luminosity, experiments along the ring will

observe an event rate of approximately 10^9 inelastic events/s. The average pile-up is of the order of 20 and around 1000 charged particles emerge from the interaction region every 25 ns.

In this environment, several experimental challenges arise: firstly, the detectors' trigger systems must be able to select the most interesting processes in order to reduce the huge rate to about 100 events/s and discriminate data with no dead-time; secondly, high-granularity detectors with good time resolution and a large number of synchronized electronic channels are required to operate in a high multiplicity track scenario and to avoid confusion among products of consecutive collisions.

The large flux of particles coming from the interaction area leads also to high radiation levels, requiring radiation-hard detectors, front-end electronics and services.

2.3.1 The first two Long Shutdowns

In 2013 and 2014 the LHC operations were interrupted for a long technical stop, called Long Shutdown 1 (LS1), during which both the LHC and its experiments underwent upgrades and maintenance works. On 3 June 2015, the LHC was switched back on: Run II started. Since then, with the exception of the winter technical stop, the LHC has been accelerating beams with $\sqrt{s} = 13$ TeV and, after a short period at 50 ns, the bunch spacing is now set at its design value of 25 ns.

Various upgrades were performed on the ATLAS experiment: first of all, in the heart of the experiment, a new innermost layer of precision track detector was inserted and the beam pipe replaced (see Chapter 4). A new beam monitor, based on diamond sensors, was installed. There was an improvement of the coverage in the muon system and the renovation of the calorimeter detectors. Also, a general upgrade of the infrastructures and services took place: trigger and acquisition system were improved and a new service quarter panel[9] for the Pixel detector was installed [35, 36, 37].

The next Long Shutdown, called LS2, is already scheduled in 2018. LHC will dedicate this time to overcome beam intensity limitation, for example, collimation, cryogenics, injector upgrade for high intensity, and low emittance bunches. The experiments will also perform many upgrades. ATLAS will

---

[9]The service quarter panel is a device that carries electrical power, cooling and optical data both into and out of the detector. It also hosts the electro-optical converters, which enable bidirectional conversion of electrical and optical signals.

implement the Fast Track Trigger (FTK) [38] and will add a new silicon sensor detector in the forward region (ATLAS Forward Physics, AFP, [39]).

2.3.2   The High Luminosity phase

To extend its discovery potential and precision measurements, the accelerator will need a major upgrade around 2022, during Phase II. Its luminosity will increase by a factor of approximately 10 beyond its original design value, in order to achieve an integrated luminosity of 3000 fb^{-1}, with a peak luminosity of 7×10^{34} cm^{-2}s^{-1} (5×10^{34} cm^{-2}s^{-1} after leveling) and a pile-up of ~ 200 events/bunch crossing [40]. The novel machine configuration, called High Luminosity LHC (HL-LHC), requires around 10 years for its careful study and implementation. It will be based on a number of key innovative technologies, representing exceptional technological challenges, such as cutting-edge 13 T superconducting magnets, very compact and ultra-precise superconducting cavities for beam rotation, new technology for beam collimation and 300-metre-long high-power superconducting links with zero energy dissipation [6]. These upgrades aim at diminishing the total beam current, increasing the luminosity by reducing the beta function and the emittance of the beams, compensating for the geometric reduction factor (which would be reduced as a consequence of the β^* decrease).

The experiments will benefit from the long shutdown to install new strategic upgrades. The ATLAS experiment, for example, will completely upgrade its Inner Detector, inserting the Inner Tracker (ITk), a multilayer detector exclusively made of silicon sensors (for more detail, see Section 2.5). At the same time, ATLAS will also upgrade the muon detector, possibly with the use of micromegas gaseous detectors [41], and implement new muon and electron triggers [42].

2.4   The ATLAS Experiment

ATLAS is the largest experiment along the LHC ring. Shown in Figure 2.5, it has a diameter of 25 m, a length of 46 m and weights roughly 7000 tonnes [43, 44]. Its design aims at providing full hermeticity, namely it covers almost the entire 4π solid angle, so that no particles could, ideally, escape from the detector. Exceptions are represented by neutrinos and yet-to-be-discovered particles, both rarely interacting with matter.
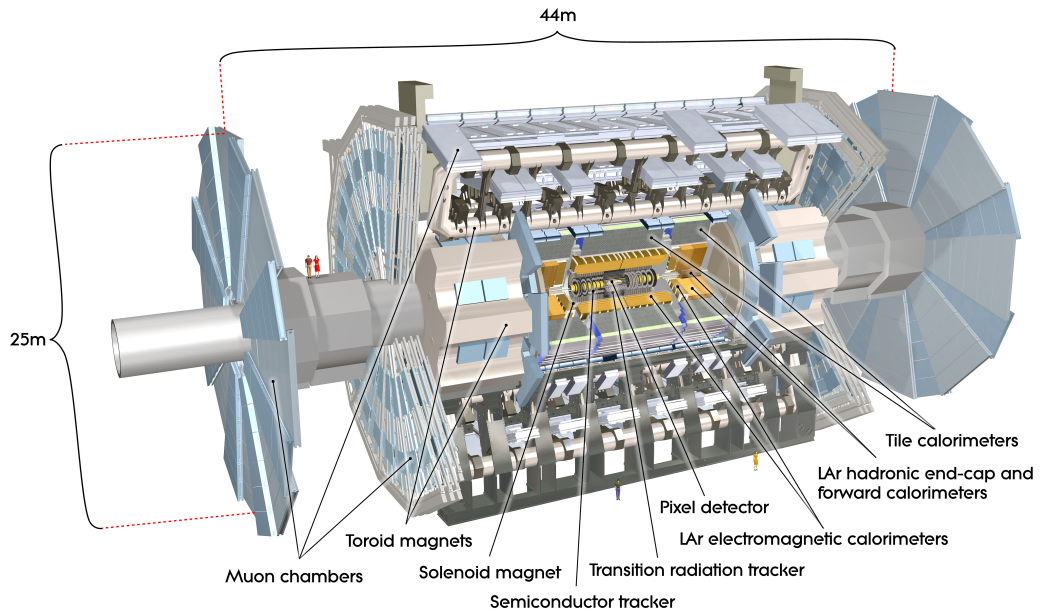
Figure 2.5: The ATLAS detector system. Image reproduced from [43].

The hermeticity is promoted by two design choices: the segmentation of the detector system into a central volume, the barrel, and two endcap regions closing the central part; and the presence of various detectors, organised in concentric layers in the barrel and in planes perpendicular to the beam axis in the endcaps. From the centre of the experiment outwards, ATLAS is composed of the inner detector system, the electromagnetic and the hadronic calorimeters, and the muon system. The inner detector is immersed in a $2\,\mathrm{T}$ solenoidal magnetic field: bending the trajectory of charged particles, it plays a fundamental role in the identification of charge sign and transverse momentum of particles. The large superconducting air-core toroids generate the magnetic field for the muon spectrometer. The peak intensity of their magnetic fields are $3.9\,\mathrm{T}$ and $4.1\,\mathrm{T}$, respectively for the central and the endcap regions.

Each detector layer is specifically designed to provide information, such as energy and position, for a certain type of particle. As will be shortly explained, some detectors are completely "transparent" to certain categories of particles: the particle can cross a layer without depositing any (or very little) energy.

16

The ATLAS coordinate system

The standard ATLAS coordinate system is defined taking the nominal IP as the origin of a right-handed coordinate system [7, 45]. The beam direction defines the $z-$axis, the $x - y$ plane being perpendicular to it. Side A is for $z > 0$, side C is for $z < 0$. The positive $x-$axis points at the centre of the LHC ring, while the $y-$axis points upwards. Cylindrical coordinates r and ϕ are used in the transverse plane: the azimuthal angle ϕ is measured around the beam axis and is defined as $\phi = p_y/p_x$, while the polar angle θ is the angle from the beam axis.

The pseudorapidity η is defined in terms of θ:

$$\eta = -\ln\left(tan\frac{\theta}{2}\right). \tag{2.3}$$

Its range goes between $\eta = 0$ on the $z = 0$ plane, to $\eta \to \pm\infty$ along the beam axis. The choice of using η instead of θ is dictated by the fact that η is invariant under Lorentz boosts[10] along the longitudinal axis: the difference of η between two particles does not depend on γ (the relativistic factor).

The transverse momentum p_T, the transverse energy E_T and the missing transverse energy E_T^{miss} are defined in the $x - y$ plane.

In the barrel region, tracks associated with charged particles are described as helical trajectories, because charged particles are deflected by the magnetic field.

Track parameters are the transverse impact parameter d_0 and the longitudinal impact parameter z_0, the angles of the momentum directions ϕ_0 and θ and the inverse of the particle momentum multiplied by the charge q/p. The transverse impact parameter d_0 is defined as the transverse distance to the beam axis at the point of closest approach to the primary vertex, signed according to the reconstructed angular momentum of the track about the axis [7]. The longitudinal impact parameter z_0 is the z position of the track at the point of closest approach to the primary vertex.

Before describing the ATLAS detectors, it is worth mentioning the mechanisms involved in the interaction of particles with matter.

2.4.1 Interaction of particles with matter

Detectors can reveal the passage of a particle due to interactions with their material. The interaction depends on the detector material and on the nature and

---

[10]Lorentz boost: transformation of the coordinates between two coordinate systems moving at constant velocity relative to each other.

the energy of the particle [46].

Photons interact with matter in three different ways, depending on their energy: at low energies, a photon most probably interacts by means of the photoelectric effect; at medium energies, in the range between 30 keV and 5 MeV, the dominant process is Compton scattering; finally, when the photon energy is large enough to create an electron-positron pair, the main process becomes pair production.

Neutral hadrons, such as neutrons, interact via strong and weak interactions with the constituents of the atoms. More rarely, their magnetic moment can allow them to interact electromagnetically.

Charged particles mostly interact electromagnetically with matter. During the interaction, they experience a loss of energy and deflections of their trajectory. These effects are mainly caused by inelastic scattering with the atomic electrons and elastic scattering with the nuclei, but can also be due to the emission of Čherenkov radiation and nuclear reactions. High-energy electrons mainly lose energy via bremsstrahlung [46].

Inelastic collisions are responsible for the loss of energy and the trajectory deflection of heavy charged particles. Particles are considered "heavy" when heavier than the electron. Examples of heavy particles are muons, protons, pions, other baryons and mesons, and light nuclei.

The average amount of energy lost by the heavy particle per unit path length, $\langle -dE/dx \rangle$, as a function of the momentum transfer (the momentum transferred from the interacting particle on the material) is described by the Bethe-Bloch equation [46]. Its quantum-mechanical expression is:

$$\langle -\frac{dE}{dx} \rangle = -2\pi N_a r_e^2 m_e c^2 \rho \frac{Z}{A} \frac{z^2}{\beta^2} \left[\ln \left(\frac{2m_e \gamma^2 v^2 W_{max}}{I^2} \right) - 2\beta^2 - \delta - 2\frac{C}{Z} \right], \quad (2.4)$$

where the meaning of all symbols are collected in Table 2.1.

The maximum energy transferred in a single collision depends on the mass of the incident particle M and the mass of the scattered atomic electron m_e:

$$W_{max} = \frac{2m_e c^2 \beta^2 \gamma^2}{1 + 2\gamma \frac{m_e}{M} + \left(\frac{m_e}{M} \right)^2}. \quad (2.5)$$

The Bethe-Bloch shape is shown in Figure 2.6 [47]. At non-relativistic energies, $\langle -dE/dx \rangle$ is dominated by the factor $1/\beta^2$ and decreases with increasing velocity until about $v \simeq 0.96 \, c$, where a minimum is reached. As the

Symbol	Meaning
N_a	Avogadro's number ($N_a = 6.022\ 10^{23}\ \mathrm{mol}^{-1}$)
r_e	Classical electron radius
m_e	Electron mass
ρ	Density of the material
Z	Atomic number of the material
A	Atomic mass of the material
z	Charge of the incident particle (in units of e)
β	Relative velocity of the incident particle, $\beta = v/c$
γ	Lorentz factor, $\gamma = 1/\sqrt{1 - \beta^2}$
I	Mean excitation potential
δ	Density correction
C	Shell correction
W_{max}	Maximum energy transferred in a collision

Table 2.1: Meaning of the variables appearing in the Bethe-Bloch equation, found in Equation 2.4 [46].

energy increases beyond, the term $1/\beta^2$ becomes roughly constant and $\langle dE/dx \rangle$ rises again because of the logarithmic dependence [46]. To bring an example, the mean energy loss per unit length at the minimum of the curve in silicon is $\langle dE/dx \rangle = 3.8\ \mathrm{MeV/cm}$. In practical cases, most relativistic particles have an energy in the range of the minimum of the curve and are therefore called minimum ionising particles (MIPs).

In the case of electrons, the treatment of the stopping power differs because other considerations have to be taken into account: among others, the mass of the two interacting particles is the same ($M = m_e$) and more processes may be involved for low energy electrons.

When talking about interactions between particles and matter, important parameters are the radiation length, X_0, and the absorption length, λ. The radiation length, X_0, is defined equivalently as (a) the distance traveled by an electron in a medium before it releases $1/e$ of its energy or (b) 7/9 of the mean free path[11] for pair production by a high-energy photon [47]. The particle energy loss, when expressed in terms of radiation length, is roughly independent of the material. The absorption length, λ, is the distance into a material where the

---

[11]The mean free path is the distance traveled by a particle between successive interactions that modify the trajectory or energy of the particle.
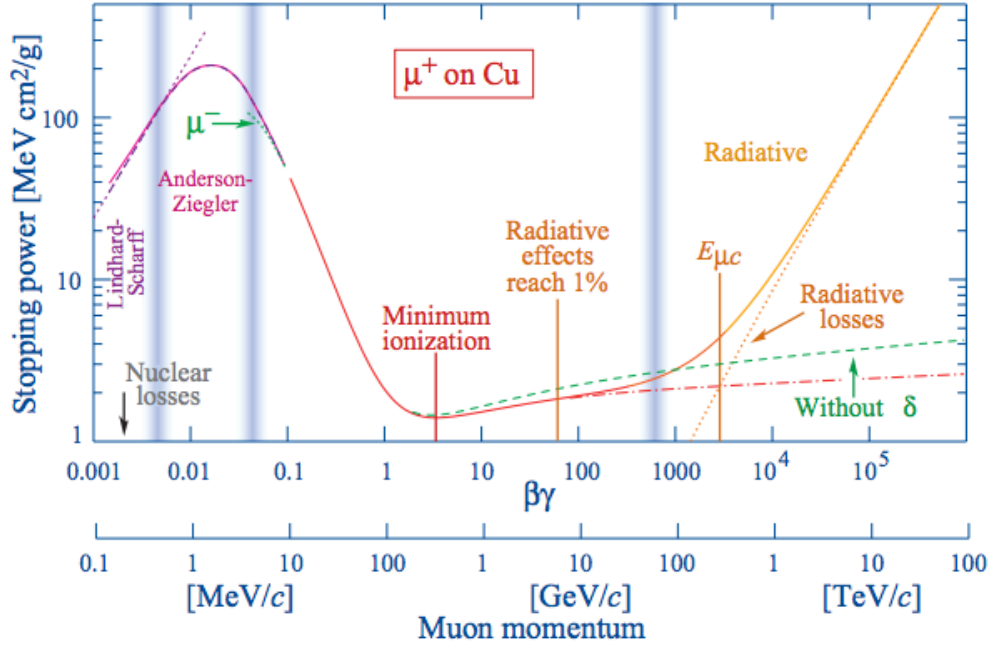
Figure 2.6: Stopping power $\langle -dE/dx \rangle$ for a positive muon in copper as a function of $\beta\gamma = p/Mc$. Image reproduced from [47].

probability, $P(x)$, that a particle has not been absorbed is reduced by a factor $1/e$:

$$P(x) = e^{-x/\lambda}. \tag{2.6}$$

The design of the different types of detector has to take into account X_0 and λ: in tracker detectors it is of utmost importance to minimise the material budget in order to avoid unwanted trajectory deflections of the particles; on the contrary, calorimeters are built to maximise the absorption of the incoming particle energy.

2.4.1.1 Particle detection inside a LHC experiment

Figure 2.7 sketches how different particles interact with the layers of the ATLAS experiment [48]. Large HEP general purpose detector systems at colliders usually have similar structures, like the one of ATLAS. What may vary is the detector technology adopted to instrument the different layers.

Electrons ionise the medium when passing through the tracking detectors and are stopped in the electromagnetic calorimeter. Here, interacting with the

20
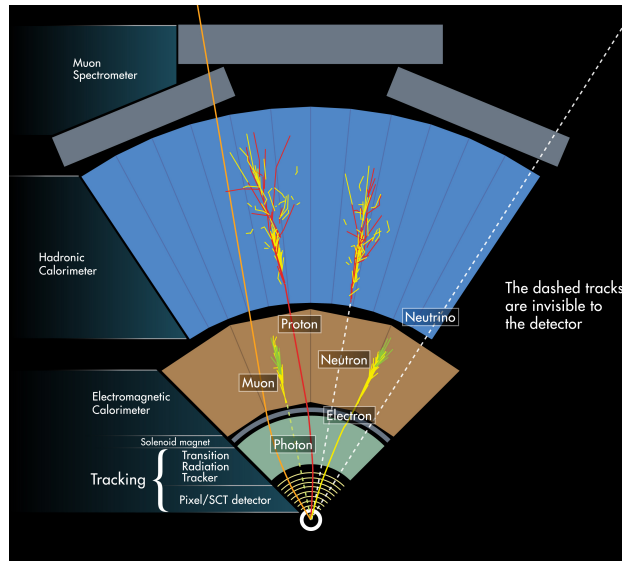
Figure 2.7: Cross sectional sketch of the ATLAS experiment, visualising the layers of the experiment and how particles of different nature interact with the subdetectors. Image reproduced from [48].

detector's medium, they lose all their energy through electromagnetic showers, consisting of the alternation of bremsstrahlung and electron-positron pair creation processes [47].

Photons in the electromagnetic calorimeter leave the same trace as electrons, the only difference being that the first step of the electromagnetic shower is the $e^- - e^+$ pair creation, while electrons' first step is bremsstrahlung. Photons can be distinguished from electrons because they pass through the tracker layers without depositing energy.

Quarks and gluons produced by hard scattering processes inside the detector, after having traveled a very short distance, give rise to jets, narrow cones of particles originating from the hadronisation mechanism. The total energy and direction of a jet is quite similar to the initial energy and direction of its initial quark or gluon [23]. The charged hadrons in the jet interact inside the tracker and the electromagnetic calorimeters, and penetrate to the hadronic calorimeter. Here, they produce hadronic showers. These cascades of secondary particles differ from the electromagnetic showers for the physics interactions involved, the variety of particles produced and the shower dimensions. A hadronic shower is generated by a succession of inelastic hadronic interactions and is characterised

by multiparticle production and particle emission originating from nuclear decays of excited nuclei. Pions are produced in large quantities and in the case a neutral pion, π^0, is created ($1/3$ of the cases), it decays into two photons and gives rise to electromagnetic showers. Usually, hadronic showers spread across a larger volume with respect to the electromagnetic ones, both in the longitudinal and in the transversal widths: the electron/photon showers develop in the transverse direction primarily because of multiple scattering, while hadronic shower spread is caused by large transverse momentum exchanged in nuclear reactions. As a result, hadronic calorimeters are thicker to confine these showers [49].

Neutrons and other neutral hadrons also create hadronic showers and can only be detected in the hadronic calorimeter.

Muons are more penetrating through the experiment: they leave little energy inside all layers. Particles can be tagged as muons if there is an energy release in the muon chambers, in the outer layers of the detectors.

The least interactive fermion of the SM is the neutrino. Its cross section with matter is so tiny that it escapes from the experiment without leaving any charge deposition (neutrinos can, with high probability, cross the entire Earth thickness without having a single interaction). Usually, when computing the conserved total energy of an interaction, the neutrinos' energy is taken into account as missing energy.

2.4.2 Inner detector

The innermost layer of the ATLAS experiment is the Inner Detector (ID).

The Run I layout of the barrel part of the ID is shown in Figure 2.8 [50]. It is composed of the Pixel detector, the SemiConductor Tracker (SCT) and the Transition Radiation Tracker (TRT). During LS1, an additional pixel layer was added as an innermost detector: the Insertable B-Layer is described in detail in Chapter 4.

The ID structure is divided in three regions: the central one is equipped with barrel detectors, whereas in the two high pseudorapidity regions the ID is instrumented with endcap detectors. While modules in the barrel region are arranged in a cylindrical shape, in the endcaps modules consist of discs that are arranged perpendicular to the beam axis.
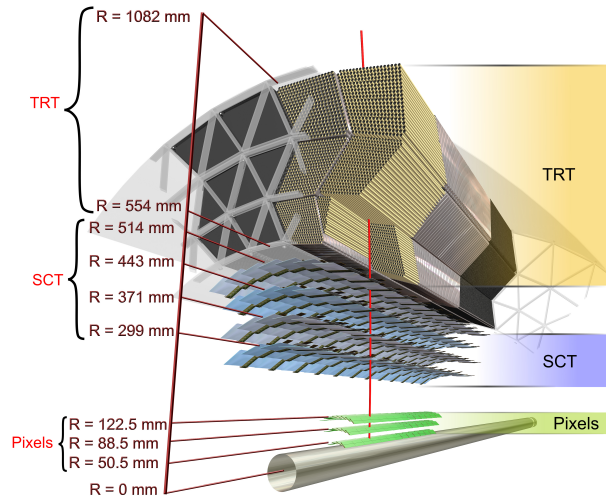
Figure 2.8: The ATLAS Run I Inner Detector. Image reproduced from [50].

2.4.2.1 Role of the ID

Because of its position, the ID plays a fundamental role in the precise measurements of the kinematic parameters of charged particles traveling inside the ATLAS solenoidal magnetic field. Together with the other ATLAS detectors, it is responsible of maximising the pattern recognition, particle identification and triggering. Taking into consideration the LHC environmental conditions and the closeness to the IP, this detector system strictly requires high granularity, to face the high track density, high precision, to maximise measurement resolution, and fast response to sustain the high bunch crossing rate.

The presence of three different types of detectors allows a combination of high-precision "discrete" (few points) hit measurements in the pixel and strip silicon sensors, and low-precision "continuous" (many points) in the TRT. This synergy provides, for the Run I conditions, the best possible track finding and track fitting capabilities, taking into account also the amount of material (silicon is dense, therefore particles traveling across it get deflected) and the material costs.

The Inner Detector is, therefore, responsible for:

1. Covering the pseudorapidity region up to $|\eta| < 2.5$;

2. Obtaining a transverse momentum resolution $p_T \times \sigma(1/p_T)$ better than 30% at $p_T = 500$ GeV/c for $|\eta| < 2$ and $p_T \times \sigma(1/p_T) < 0.5$ for $|\eta| = 2.5$: the p_T is a fundamental property of tracks because it characterises various production processes [51];

3. Identifying isolated and associated tracks with high resolution: the high granularity of the ID detectors allows for the discrimination between close tracks, while the multiple layers provide the track reconstruction with the measurement of the sagitta of charged particles' trajectory, hence their curvature;

4. Identifying electrons and photons: the information recorded by the ID and the electromagnetic calorimeter allows for the discrimination between photons and electrons;

5. Performing high-efficiency $b-$tagging: $b-$tagging is the capability of discriminating high p_T $b-$jets from light-flavour quark- and gluon-jets. $b-$jets are of fundamental importance because they are a signature of many interesting processes (e.g. top physics, Higgs boson searches and studies, new phenomena such as SUSY signals, heavy gauge bosons, etc..). These jets originate from the decay of $B-$mesons. $B-$mesons travel a measurable distance L_{xy} (of the order of $\mathcal{O}(100\ \mu\text{m})$) before creating a jet from a secondary vertex, as shown in Figure 2.9a. A peculiarity of $b-$jets with respect to those produced by the hadronisation of a light quark or a gluon is the magnitude of the impact parameter: as Figure 2.9b shows, the distribution of the signed[12] transverse impact parameter d_0 of $b-$quarks is different than others in the region $d_0 > 0$. In particular, d_0 for light-flavoured quarks can be positive or negative with equal probability and its magnitude depends on the tracking detector resolution and the effects given by multiple scattering; the d_0 distribution for $b-$jets, instead, has a large positive asymmetry as a result of a secondary vertex produced from the $B-$meson decay [52, 53].

   The ID achieves a high transverse momentum resolution, in the plane perpendicular to the beam axis, of $\sigma_{p_T}/p_T = 0.05\%\ p_T\ \text{GeV} \oplus 1\%$ and a high transverse impact parameter resolution, of $10\ \mu$m, for high momentum particles in the central η region [45];

---

[12]The sign of the impact parameter is defined positive (negative) if the point of closest approach of the track to the primary vertex is in front of (behind) the primary vertex with respect to the jet direction.

6. Defining secondary vertices with high precision: this is essential for $b-$tagging;

7. Measuring impact parameters with high precision: the ID detectors are the closest to the IP and their granularity allows for an excellent measurement of the track parameters;

8. Contributing to the Level 2 tracking trigger: the ID provides track seeds and identifies high p_T charged particles.
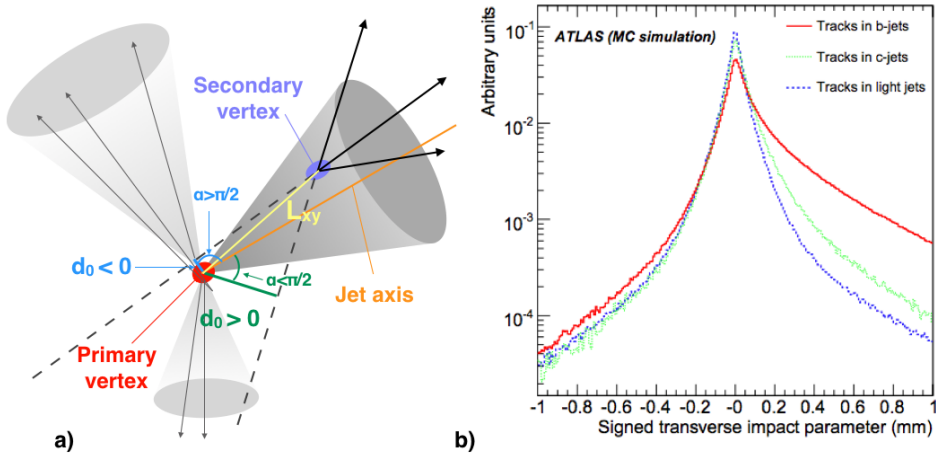
Figure 2.9: (a) Illustration of a 3-jet event with one identified as a $b-$jet because of the presence of a displaced secondary vertex. The sign of the transverse impact parameter d_0 is defined by the value of the angle (α) between the jet axis and the line connecting the primary vertex to the point of closest approach of the track: $d_0 > 0$ if $\alpha < \pi/2$ ($d_0 < 0$ if $\alpha > \pi/2$). Image modified from [52]. (b) Distribution of the transverse impact parameter d_0, signed with respect to the jet axis, for $b-$jets, $c-$jets and light-jets from simulated $t\bar{t}$ events at $\sqrt{s} = 14$ TeV. Image reproduced from [53].

2.4.2.2 The Pixel detector

The Pixel detector of Run I data taking is shown in Figure 2.10a. It is formed by three concentric layers in the barrel region and three discs at both endcaps [54]. It provides 3 precise track points over the full ID acceptance. Most importantly, it collects essential information to determine the impact parameter and to find short-lived particles, such as $b-$quarks.
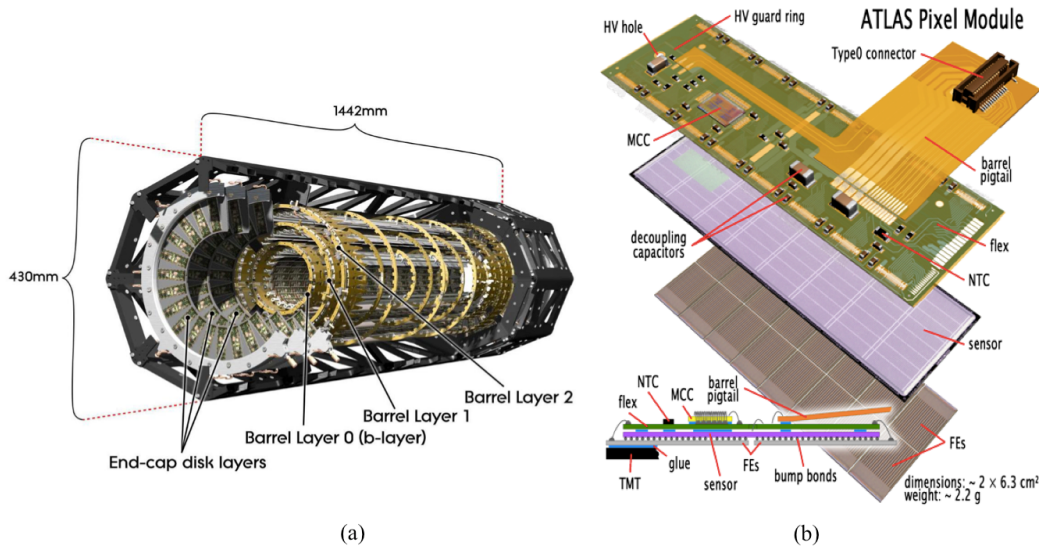
Figure 2.10: (a) The ATLAS Pixel detector features three concentric barrel layers and two endcaps with three discs each. (b) Assembly view and cross section of an ATLAS Pixel detector module. Sixteen front-end chips are bump bonded to the silicon pixel sensor. Interconnections are done on a flexible kapton printed circuit board, which is connected by wire bonds to the electronics chips. Image reproduced from [54].

The barrel layers are named B-Layer (or L0), Layer-1 (L1) and Layer-2 (L2). They are placed at a distance of 50.5, 88.5 and 122.5 mm from the IP (r direction), while the 3 discs are at a distance between 495 and 650 mm from the IP (z direction). The three barrel layers are instrumented with, respectively, 22, 38 and 52 staves, the supporting structures for modules. The entire detector system is, in fact, instrumented with 1744 identical modules, composed of 2×8 planar silicon sensors connected to an equal number of front-end (FE) chips, called FE-I3. The 16 FE-I3 are connected to the Module Controller Chip (MCC), which provides communications between the FE chips and upstream data acquisition system (see Fig 2.10b).

The FE-I3 is an integrated circuit consisting of 2880 individual pixels, arranged in a matrix with 18 columns and 160 rows. It features a typical pixel size of (400×50) μm^2; some pixels (long pixels) have a size of (600×50) μm^2 to bridge the gaps between front-end chips. The small pixel dimensions provide the required high granularity and allow the avoidance of ambiguities associated with the projective geometries. Ambiguities are also solved with the use of advanced

electronic techniques and interconnections for the read-out [7].

The Pixel sensors are n^+-in-n planar silicon sensors, 250-μm-thick, and are segmented accordingly to the matrix of the FE-I3 chip, featuring a pixel size of $(400 \times 50)\,\mu\text{m}^2$.

The Pixel detector was optimised to sustain a high level of radiation, up to $300\,\text{kGy}$ of ionising radiation and over $5 \cdot 10^{14}\,\text{n}_{eq}/\text{cm}^2$ [13] in ten years of operations. As will be shown in Chapter 4, the B-Layer, due to the high radiation levels, will present increasing inefficiencies that could compromise the physics performance of the ATLAS experiment. For this reason, a new pixel layer, the Insertable B-Layer was inserted during LS1 (see Chapter 4).

Other Pixel detector failures appeared during Run I. These failures led to 88 (over 1744) disabled modules by the end of Run I. Figure 2.11a shows the number of disabled Pixel modules at the end of Run I, classified by the failure type [55].
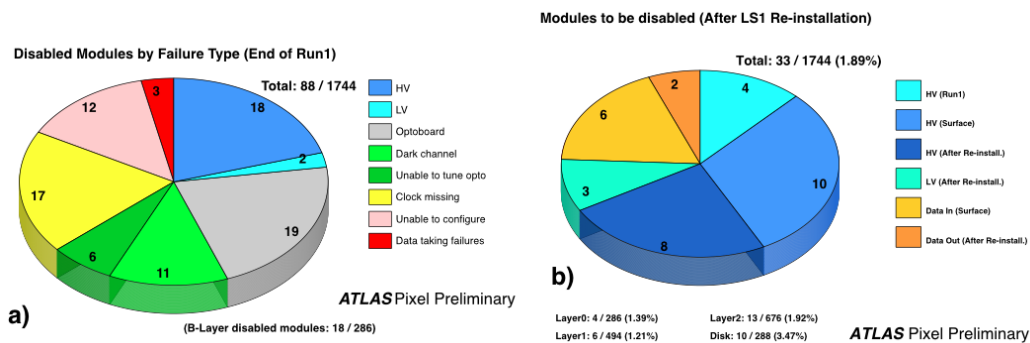
Figure 2.11: (a) Number of disabled modules of the Pixel detector at the end of Run I classified by the type of the failure. (b) Number of modules of the Pixel detector to be disabled after the LS1 refurbishment and re-installation in ATLAS (May 2014), classified by failure mode (High Voltage / Low Voltage / Data In / Data Out) and the phase of causing problems (Run I / Surface / After re-installation). Modules that have issues but remain functional are not included. Image reproduced from [55].

Taking advantage of LS1, the Pixel detector was extracted from the ATLAS experiment and brought to the surface. The detector underwent a series of works aimed at repairing modules, refurbishing it, equipping it with a new service quarter

---

[13]The unit $\text{n}_{eq}/\text{cm}^2$ (1 MeV neutron equivalent per squared centimeter) indicates the amount of displacement damage caused by the irradiating particles that would be produced if a beam of 1 MeV neutrons interacted with the material. More information on radiation damage is given in Section 3.3.

panel (SQP), as well as upgrading the L2 data acquisition (DAQ) hardware by doubling the read-out speed in preparation for the Run II luminosity.

The SQP is a service that contains the electrical services and the cooling pipes and it was placed, during Run I, at a distance up to ~ 1 m from the Pixel modules, in an area that is not accessible without removing the Pixel detector from ATLAS. The SQP also hosts the Optoboards, electro-optical transceivers used for the conversion of the electrical signal coming from the Pixel detector into an optical one, which is then transported via ~ 80 m fibers to the DAQ system (control signals follow the inverse path and are converted from optical into electric signals by the Optoboards).

The replacement of the SQP was motivated by the failure of some lasers in the off-detector system[14]. In the case of failures of the Optoboards, which use the same lasers, the Pixel detector operations would have been compromised. For this reason, it was decided to build new SQPs and place them 6.6 m further from the IP, into a serviceable area [54]. The new SQP also allowed to increase the bandwidth of L1 to be the same as the B-Layer (160 Mbit/s), making it more suitable for the post-LS1 LHC operations.

All Run I disabled modules were extensively investigated, to repair module disconnections wherever possible. After the instrumentation with the new SQPs, the Pixel detector was reassembled and tested.

In December 2013, the Pixel detector was successfully reinstalled inside the ATLAS experiment and in May 2014 all the services were connected and the whole system was re-tested. As displayed in Figure 2.11b, only 33 modules after the reinstallation were still failing, while 98% of the Pixel modules are operable [54].

2.4.2.3   The SemiConductor Tracker

The SemiConductor Tracker (SCT) provides the track reconstruction with nominally 4 hit points and contributes to the measurement of momentum, impact parameter and vertex position [7]. It consists of eight layers that cover 61 m^2. The layers are paired two-by-two to provide precise measurements in the $r - \phi$ and z coordinates (to get the z coordinate, strips of the pair are disaligned by a 40 mrad angle stereo). In the barrel region, the layers are concentrically located at radii of

---

[14]The off-detector system is composed of elements of the DAQ system such as the Back-of-Card, the Read-Out Driver and the Read-Out Buffer [56].

30, 37, 44 and 51 cm from the beam axis. Each endcap is equipped with 8 discs, placed at a distance of $810 < |z| < 2797$ mm from the IP.

The SCT detector is instrumented with microstrip sensors that have an area of 6.36×6.40 cm^2 and are (285 ± 15) μm thick [57]. The pitch, namely the distance two neighbour AC read-out channels, was determined by a compromise between precision, granularity, occupancy and noise performance. After combining these inputs, a pitch of 80 μm was chosen: the corresponding accuracy of the position measurement, in the direction perpendicular to the strip, is 17 μm [57].

Each module consists of four single-sided p^+-in-n silicon detectors: on each side of the module, two detectors are wire-bonded together, creating 12.8 cm-long strips. Such pairs are glued together back-to-back with an angle of 40 mrad, separated by the heat transport plate. The electronics are mounted on the sensors.

Endcap modules have a similar structure, but are aligned radially and the sensors have a trapezoidal shape. To ensure an optimal η coverage in the endcap sectors, endcap strips are longer (~ 12 cm in the outer radii and ~ 6 cm in the innermost radius).

2.4.2.4 Transition Radiation Tracker

The Transition Radiation Tracker (TRT) provides a large number of hits, typically from 30 to 36 hits per track. Covering up to $|\eta| < 2.0$ and radial distance from 563 to 1066 mm, this detector is composed of straw tubes that provide information only in the $r - \phi$ plane with an intrinsic accuracy of 130 μm per straw. The straws are parallel to the beam axis in the barrel region, while they are arranged radially in the endcaps [53].

Each straw has a diameter of 4 mm and is equipped with a 30 μm gold-plated tungsten-rhenium wire that provides fast response and good mechanical and electrical properties. The straws are filled with a non-flammable gas mixture of 70% Xenon, 20% CO_2 and 10% CF_4. The small diameter and the wire isolation inside the gas volume promote the TRT operation at very high rates. Electron identification is enhanced by exploiting the transition-radiation photons created in a radiator, made of polypropylene, between the straws. This technique is intrisically radiation hard.

Each of the 420k channels provides a drift-time measurement and is characterised by two independent thresholds that allow the detector to differentiate between tracking hits and transition-radiation hits: the former are generated by the deposition of energy due to the ionisation of the gas and pass the lower

threshold; the latter, produced by the high-energy transition-radiation photons, pass the higher threshold [7].

2.4.2.5 The Beam Conditions Monitor and Diamond Beam Monitor

In the unlikely event that the beams circulating inside the LHC ring lose their trajectory and hit the collimators protecting the detectors, this high instantaneous dose could severely damage the detectors. The Beam Conditions Monitor (BCM) is devoted to detect such accidents and trigger a beam abort before major problems arise. It reveals also the presence of beam-gas interactions, which are due to leakage of the beam pipe and represent both a source of background for the LHC experiments and a threat to the LHC operations [58].

The BCM has 4 modules for each station, each module being composed of two $1\,\mathrm{cm}^2$ radiation-hard diamond sensors mounted back-to-back. Its radiation-tolerant electronics has a rise time of $1\,\mathrm{ns}$, suitable to discriminate between normal collision products and the background events mentioned before. Beam-gas interactions and beam loss, in fact, can also originate in regions far from the IP, upstream (or downstream) with respect to it: their products reach the two stations of the BCM with a time difference of $\Delta t = 2z/c \approx 12.5\,\mathrm{ns}$. On the contrary, particles coming from the collisions reach the two stations roughly at the same time, in accordance with the bunch crossing ($\Delta t = 0, 25, 50$ ns) [57].

During LS1, the BCM was backed up with a new beam conditions monitor, the ATLAS Diamond Beam Monitor (DBM). This new detector consists of 4 three-module telescopes placed around the beam pipe on both sides. The DBM is instrumented with the same technologies adopted by the IBL detector in terms of front-end chips and services, but its sensors are 75% diamond and 25% silicon [59].

With respect to the BCM, the DBM has a larger acceptance, acts as a bunch-by-bunch beam spot monitor and allows for a distinction between hits and beam halo tracks.

2.4.3 Magnets

The ATLAS magnet system consists of a superconducting solenoid, surrounding the Inner Detector and providing it with a 2 T magnetic field, and three large air-core toroids generating magnetic field for the muon spectrometer [57].

The design of the central solenoid was carefully optimised to provide the required magnetic field without compromising the performance of the calorimeter,

hence keeping the magnet material budget as low as possible: this results in an assembly of ~ 0.66 radiation lengths at normal incidence [57]. The flux is returned by the steel of the hadronic calorimeter and its girder structure.

Each of the three toroids, placed in the barrel and the two endcaps, consists of eight coils arranged radially and symmetrically around the beam axis. One toroid is located in the barrel of the ATLAS experiment (Barrel Toroid, BT), and the other two are placed in the endcap regions (ECTs), rotated $22.5°$ with respect to the BT coil, to implement overlap and to optimise the bending power between coil systems [7].

2.4.4 Calorimeters

The ATLAS electromagnetic (EMCal) and hadronic (HCal) calorimeters are placed, the second external to the first, outside the central solenoidal magnet. They are hermetic in the angle ϕ that cover the pseudorapidity region up to $|\eta| < 4.9$.

These detectors are required to completely contain, respectively, the electromagnetic and hadronic showers and, at the same time, must limit the punch-through into the muon system. These strong requirements on particles' containment have implications for the minimum thickness of these detectors: the depth of the EMCal exceeds 22 radiation lengths in the barrel and $24\ X_0$ in the endcaps; the HCal thickness is $11\ \lambda$ at $|\eta| = 0$ [57].

The EMCal ensures, with its high granularity, a precise measurement of the positions and directions of the electromagnetic showers, in order to maximise the sensitivity to physics channels such as $H \rightarrow \gamma\gamma$. The coarser granularity of the other calorimeter detectors is sufficient for its physics needs of jet reconstruction and E_T^{miss} measurements.

2.4.4.1 Electromagnetic calorimeters

The EMCal is divided in three parts, the central barrel (up to $|\eta| < 1.475$) and the two endcaps ($1.375 < |\eta| < 3.2$), each contained inside a cryostat. This high-granularity device is a lead-Liquid Argon (LAr) sampling calorimeter with accordion-shape lead absorber plates and kapton electrodes: the lead layers promote the production of secondary particles, to which liquid argon layers are sensitive [57].

Three layers comprise the high-granularity central region ($|\eta| < 2.5$) and two layers in the more forward η region and in the overlaps between barrel and

endcaps. The first layer, acting like a "preshower" detector, is highly segmented in η. It measures with high-precision the position of the crossing particle and plays a fundamental role in the particle identification. The second layer collects most of the electromagnetic shower. The third layer collects the shower tails and is therefore less segmented.

The lead absorber plates are coated with stainless-steel foils, glued using a resin-impregnated glass-fibre fabric for providing mechanical strength. The more forward η, the thinner the lead absorber: this choice is oriented at limiting the decrease of the sampling fraction as η increases.

The read-out electrodes are placed in the gaps between the absorbers: the three conductive copper layers separated by kapton sheets provide the high-voltage potential and read out the AC coupled signal.

In the central region ($|\eta| < 1.7$) a presampler, instrumented liquid argon layer, measures the energy lost in front of the EMCal. A Liquid Argon Forward Calorimeter (FCal) is placed in the high-η region, for $3.1 < |\eta| < 4.9$, fulfilling the required pseudorapidity coverage. It acts both as an electromagnetic and as a hadronic shower container.

2.4.4.2 Hadronic calorimeter

The outer part of the ATLAS calorimetry system is instrumented with the hadronic calorimeters. Three detector technologies are exploited: the Tile Calorimeter (TCal), the Liquid-Argon hadronic endcap calorimeter (HEC), and the previously mentioned FCal.

2.4.4.2.1 Tile calorimeter The Tile Calorimeter (TCal) is built with scintillator tiles as active medium and steel plates as absorbers. While maximising the efficiency for the particle containment, this design minimises the costs. The TCal covers the range $|\eta| < 1.7$ and consists of one barrel and two extended barrel regions. Radially, the tile calorimeter extends from an inner radius of 2.28 m to an outer radius of 4.25 m. It is segmented in three layers of attenuation lengths equal to 1.5, 4.1 and 1.8 respectively.

The scintillating tiles are read out by wavelength shifting fibers into separate photomultipliers at both ends. Photomultipliers are low-noise devices characterised by a fast signal, of the order of few nanoseconds.

2.4.4.2.2 LAr Hadronic endcap calorimeter In the endcap regions, the Hadronic Endcap calorimeter (HEC) is composed of two independent wheels per endcap that share the electromagnetic LAr cryostats. The detector is a succession of layers of copper and 8.5 mm LAr gaps. Its cells are fully projective in ϕ, but only "pseudo-projective" in η. For simplicity, the layout of the detector is cylindrical. The HEC extends to $|\eta| < 3.2$ and overlaps with the FCal.

2.4.4.2.3 LAr forward calorimeter The Forward Calorimeter (FCal) is located in the high η region. For this reason, it has to cope with a high level of radiation. It is fully integrated into the endcap cryostats, allowing for a better uniformity of the calorimetric coverage and, at the same time, reducing the radiation background in the muon system. For reducing the neutron albedo[15] in the inner detector, the FCal was placed 1.2 m further from the IP. This recession leads to a limit in the thickness of the detector, reduced to $10\ \lambda$, and to the requirement of a high-density device [57].

The design consists of three modules in each endcap: the first is made of copper and is best suited for electromagnetic measurements, while the other two, made of tungsten, measure the hadronic shower energy.

2.4.5 Muon spectrometer

Immersed in the magnetic field produced by the toroidal magnets, the muon system tracks the bent trajectories of muons crossing the detector. The barrel toroid covers up to $|\eta| < 1.4$, from $1.6 < |\eta| < 2.7$ the magnetic field is generated by the endcap toroids. In the region $1.4 < |\eta| < 1.6$ the field is given by the overlap of these two magnets: the resulting magnetic field is oriented perpendicular to the muon tracks and minimises multiple scattering.

The design of the muon spectrometer is determined by the requirements to sustain the high flux of particles. These demands are reflected in performance parameters such as rate capability, ageing and granularity. Its structure respects the shape of the ATLAS experiment and follows the layout of the toroidal magnets: it is divided in three cylindrical layers in the barrel and three planes perpendicular to the beam axis in the endcaps; in each part, it is divided in 8 sections, interleaved with the toroid structure.

---

[15]The neutron albedo is the fraction of neutrons that, when hitting a material surface, is reflected back [60].

Four detector technologies instrument the muon system: two (the Monitored Drift Tubes and the Cathode Strip Chambers) are devoted to the precise measurement of the track coordinates in the principal bending direction of the magnetic field; the other two, namely the Resistive Plate Chambers and the Thin Gap Chambers, provide both the trigger on muon tracks and the second, perpendicular track coordinate, parallel to the beam axis.

The purpose of the tracking detectors of the muon spectrometer is to provide the measurement of a stand-alone transverse momentum resolution of 10% for $1\,\mathrm{TeV}$: this corresponds to a sagitta along z of about $500\,\mu$m, to be measured with a resolution of $\leq 50\,\mu$m [57]. For such a measurement, it is fundamental to know the locations of the detectors with high precision, better than $30\,\mu$m: an optical alignment system has been implemented to monitor the position and internal deformation of the tracking chambers.

Muons with a momentum as small as $\sim 3\,\mathrm{GeV}$ can be measured by the spectrometer alone. At the other end of the energy scale, the spectrometer alone is capable of correctly identifying the charge and momentum of muons with an energy of $\sim 3\,\mathrm{TeV}$.

The trigger detectors aim at:

- Discriminating muon transverse momentum;

- Identifying bunch-crossing;

- Retrieving fast and coarse tracking information, used in the high-level trigger stages;

- Measuring the second coordinate in the non-bending ϕ projection to complement the MDT measurement;

- Providing robustness against random hits due to n or γ background in the experiment hall.

The trigger is provided by the coincidence condition in both the η and ϕ directions: this choice suppresses spurious triggers caused by the conversion of photons.

2.4.5.1 Monitored Drift Tubes

Monitored Drift Tubes (MDTs) instrument the outer shell of the ATLAS experiment in the region $|\eta| < 2.7$ (with the exception of the innermost endcap layer, limited to $|\eta| < 2.0$). Their basic unit is a drift tube, operated at 3 bar with

a gas mixture of Ar/CO_2 ($93\%/7\%$), known for its good ageing properties. The central wire, in tungsten-rhenium, collects the ionised electrons with a potential of 3080 V. Each drift tube has an intrinsic resolution of 80 μm, that sums up to 35 μm when taking into consideration the three to eight layers of these tubes composing the MDTs.

The tube structure intrinsically provides good robustness of the detector as well as high operation reliability, as each tube is operated almost independently. The cylindrical shape renders the measurement accuracy weakly dependent on the track angle of incidence because the coordinate is determined by the radius of the circle around the wire to which the track is tangential.

MDT chambers are rectangular in the barrel and trapezoidal in the endcaps: their shape maximises the solid angle coverage despite the constraints imposed by the neighbouring materials (magnet coils, supports and services). Most of the chambers have two groups of tube layers, called multi-layers, separated by a mechanical spacer. Chambers have four tube layers in the innermost region and three layers in the outer one.

2.4.5.2 Cathode Strip Chambers

The flux of particles and the muon track density are highest in the forward direction, for $2 < |\eta| < 2.7$. Cathode Strip Chambers (CSCs) were chosen to instrument this region because of their good properties related to radiation hardness, insensitivity to neutrons, high granularity and capability to measure both track coordinates simultaneously.

CSCs are multiwire proportional chambers filled with an Ar/CO_2 mixture and located at $|z| = 7$ m. Each chamber has four cathode planes segmented into strips in orthogonal directions. Perpendicularity between strips allows both to measure two track coordinates and to resolve multitrack ambiguities, by correlating the magnitude of the collected charge in the two planes. The spatial resolution is 40 μm along the bending plane and 5 mm along the non-bending (ϕ) plane.

2.4.5.3 Resistive Plate Chambers

The precision tracking chambers are complemented by a system of trigger chambers that output a signal within a few tens of nanoseconds after the particle's passage (the time spread is $\sim 15 - 25$ ns, hence the beam crossing can be tagged). The Resistive Plate Chambers (RPCs) were chosen as triggering detectors in the

barrel region because of their good spatial and time resolution, sufficient rate capability and layout simplicity.

There are three RPC layers in the barrel, which alternate with layers of MDT chambers. The large lever arm between the inner and the outer layers allows the selection of high-momentum tracks, while the lever arm between the innermost and the second innermost one permits the measurement of low-p_T tracks.

RPCs are gaseous detectors. Their layout consists of two electrode plates kept parallel to each other at a distance of 2 mm by insulating spacers. The electric field between the electrodes is ~ 4.9 kV/mm and accelerates electrons to produce avalanches that are then collected by the anode. They are filled with $C_2H_2F_4$/Iso-C_4H_{10}/SF_6 (94.7%/5%/0.3%), a gas mixture that ensures low operative voltage, non-flammability, low cost and good avalanche properties.

2.4.5.4 Thin Gap Chambers

Thin Gap Chambers (TGCs) instrument the endcap region together with the CSC and are used as trigger detectors for their good time resolution and high rate capability. A time resolution better than 3.7 ns has been achieved for a single layer, showing no deterioration under background rates as high as 170 kHz/cm^2 [61].

Based on the same operation principle as multi-wire proportional chambers, TGCs provide the track's azimuthal coordinate thanks to their good spatial resolution, given by the adjustable read-out channel granularity (their wires are assembled in groups of different sizes). The good time resolution is essential to correctly tag the bunch-crossing with an efficiency higher than 99%, while the fine granularity is needed to provide a sufficiently sharp cut-off in the triggering muon's momentum.

A TGC device is a gaseous detector that differs from the standard multi-wire proportional chambers for the distance between the anode wire and the cathode plane being smaller than the wires inter-distance (1.4 mm vs 1.8 mm). This configuration, used in combination with a highly-quenching gas mixture (CO_2 and n-C_5H_{12}), allows its operation in quasi-saturated mode, with relatively low gain. The high-quenching properties of the gas mixture avoid the creation of streamers. The very short distance between electrodes allows good time resolution. By construction, all particles originating in the IP cross the TGC detectors at an angle larger than $10°$, thus avoiding the low field region created perpendicularly to the planes midway between two wires.

Mounted on concentric rings, the big wheel is instrumented with seven TGCs,

arranged in two doublets and one triplet, the latter being used for detecting false coincidence from background hits, which are more common in the endcap region than in the barrel. TGCs cover $1.05 \leq |\eta| \leq 1.92$ in the outer ring and $1.92 \leq |\eta| \leq 2.4$ in the forward ring.

2.4.6 Trigger and Data Acquisition

The LHC machine delivers collisions with up to a frequency of 40 MHz inside the ATLAS experiment. This corresponds to roughly $10^7 - 10^9$ proton-proton interactions each second. The equivalent amount of data collected by the detectors at each second is way beyond the available transmission and storage capabilities. Moreover, physics requirements demand the selection of very rare events out of the extremely high backgrounds present in the LHC environment. The total p-p collision rate is too large, therefore only a small fraction can be stored.

To identify the most interesting events, a highly selective and efficient trigger system is needed to couple with the DAQ system. The ATLAS Trigger, shown in Figure 2.12 [7], is a three-level system for online event selections, able to reduce the physics rate to $\sim 100 - 300$ Hz, with a total event size of ~ 1.3 MB [62, 63]. Each trigger stage is responsible for refining the decisions made by the previous level and for selecting the most interesting events according to a set of more and more stringent selection criteria.

The first level, the Level-1 (LVL1) trigger, which reduces the rate to 75 kHz, is a hardware-based triggering system that makes an initial selection using reduced-granularity information coming from a subset of detectors, in the calorimetry (L1Calo) and muon (L1Muon) detector systems. The LVL1 trigger adopts, for each data taking period, a LVL1 "trigger menu", a collection of up to 256 combinations, expressed in terms of coincidences or vetoes, of trigger items upon which to select events of interest. The LVL1 trigger menu includes configurable algorithms to trigger on object candidates such as high-p_T muons, identified in the RPC and TGC muon detectors, and high-p_T electrons and photons, jets, hadronically-decaying τ leptons, muons and large E_T^{miss} and E_T in the calorimeters. These physics triggers can be subjected to energy isolation cuts, dead times and prescaling.

The LVL1 trigger must be able to correctly identify the bunch crossing containing the event of interest. This strong constraint corresponds to the double requirement to have pipelines in the detector front-end electronics and a very short latency. The ATLAS LVL1 trigger has a latency, from the bunch crossing to the
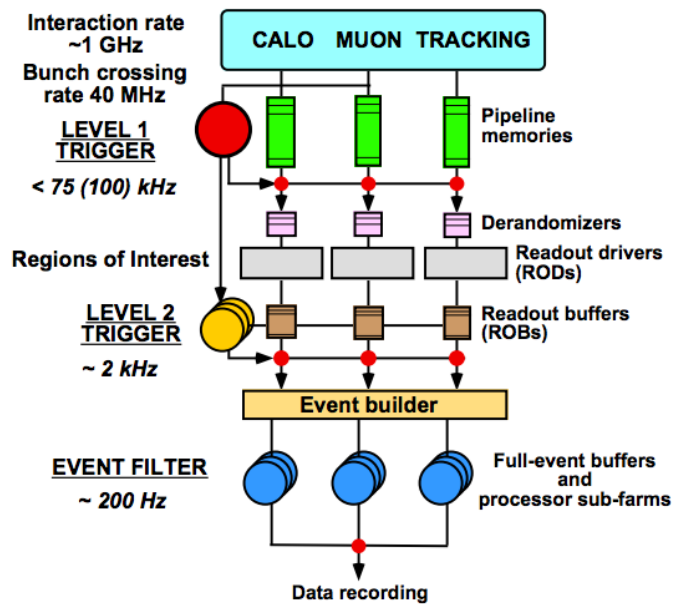
Figure 2.12: The ATLAS trigger system. The Level-1 trigger uses information from the calorimeter and the muon detectors to decide whether to keep the event, while information from all detectors is stored in pipelines. It also identifies the Regions of Interest, which are then analysed by the Level-2 for a second skim. The Event Filter trigger, in the end, reconstructs the event to base its final decision on the complete event information. Only accepted events are stored. Image reproduced from [7].

delivery of the output to the detector's front-ends, of $2.0~\mu$s [7].

The output of the LVL1 is a single-bit "Level-1 Accept" (L1A), which indicates to the detector front-end read-out systems, via a Trigger Timing and Control system (TTC), whether to read out the event buffered in the pipelines of the front-end electronics.

The LVL1 trigger also identifies the so-called Regions of Interest (RoIs), regions in the detector that show interesting features. This information is passed to the software-based Level-2 (LVL2) trigger, the first step of the High Level Trigger (HLT) [62].

The LVL2 trigger uses the RoIs as seeds to selectively access the Read-Out Buffers (ROBs), where data from the detectors are temporarily stored, to gain the full-precision and full-granularity information to make the LVL2 decision. It performs a fast reconstruction on data coming from modules within RoIs and

combines data from different RoIs.

The LVL2 rejection power on the different objects comes from the sharpening of p_T thresholds, as in the case of muon objects, and from the use of full calorimeter granularity, adopted for a better identification of electrons and photons. The LVL2 trigger has a latency of $1 - 10$ ms and reduces the event rate to ~ 1 kHz. Being a software-based trigger, the limit on the rate reduction only depends on the optimisation of the selection algorithms.

The last trigger stage, the Event Filter (EF), the second level belonging to the HLT, performs the final selection exploiting offline physics and event reconstruction algorithms adapted to the online environment, calibration and alignment information as well as the map of the magnetic field. As mentioned before, it has a final output rate of $\sim 100 - 300$ Hz, with an output data rate of ~ 100 MB/s. This tremendous data rate corresponds to around 3 PB/year.

Three features determine the EF rejection power: first, it accesses the entire event data, hence making available all information relevant to the selection criteria. Second, it adopts, when necessary, tighter p_T thresholds with respect to the LVL2 requirements. Third, it uses more sophisticated algorithms that implement complex calculations, such as the vertex and track fitting using bremsstrahlung recovery for electrons, that are too lengthy for the LVL2 time constraints [7].

Data passing all three levels of the triggering system is sent to mass storage, where it can be accessed to be reconstructed using offline algorithms and can be further used for analyses.

2.5   The Pixel upgrade project for the HL-LHC

After the Phase II upgrade, the levelled luminosity of the LHC will be pushed to $5 \cdot 10^{34}$ cm^{-2}s^{-1} and the pile-up will increase to ~ 200 events/bunch crossing, corresponding to ~ 1000 tracks per unit of pseudorapidity. A simulation of a $t\bar{t}$ event in the HL-LHC conditions is shown in Figure 2.13 [64]. The fluence in the central region of ATLAS will reach $2 \cdot 10^{16}$ 1 MeV n$_{\text{eq}}$/cm^2, according to the simulations reported in Figure 2.14 [65]. The current ATLAS tracker was not conceived to withstand these conditions and will be replaced by a new tracking system, the Inner Tracker (ITk) [66].
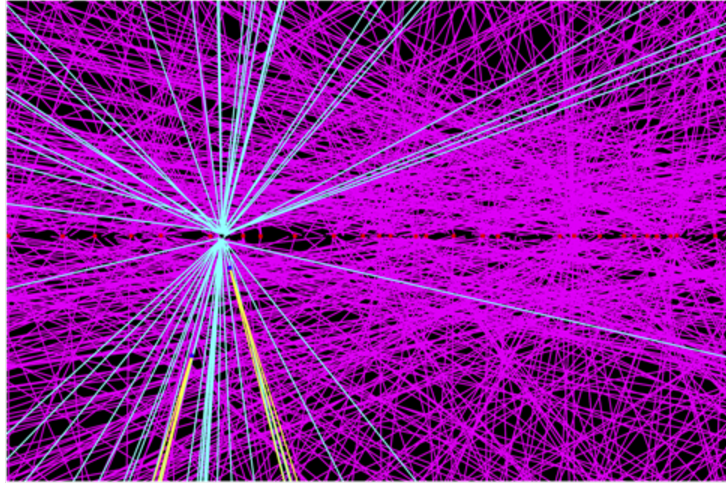
Figure 2.13: Simulation, in the $r - z$ view, of a $t\bar{t}$ event (coloured in cyan) at average pile-up of $\mu = 200$ collisions per bunch crossing. Vertical scale is 2.5 cm and the horizontal one is 12 cm. All reconstructed tracks have $p_T > 1$ GeV. Image reproduced from [64].
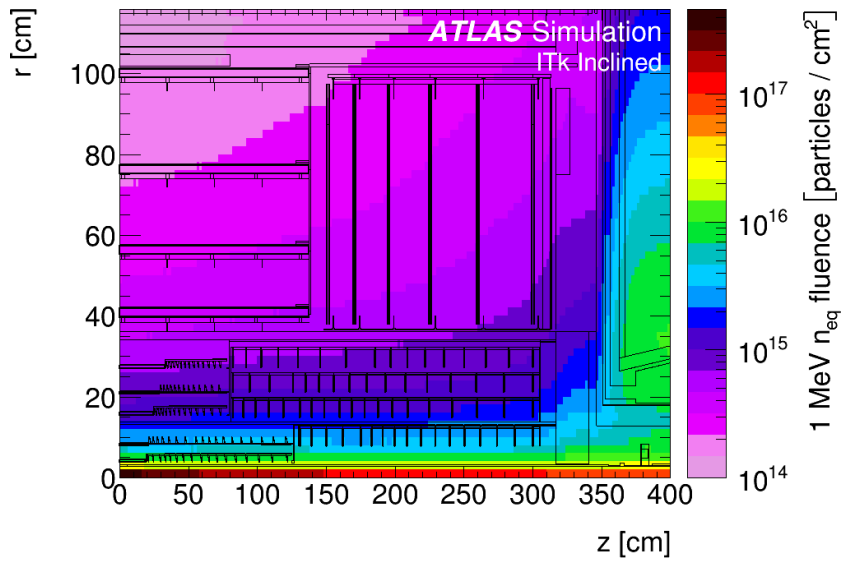
Figure 2.14: Fluence in the ITk region from a FLUKA [67] simulation of one of the possible ITk layouts. The fluence is normalised to 3000 fb^{-1} of p-p collisions at 14 TeV. No safety factors are included. Image reproduced from [65].

2.5.1 Motivations and requirements

The current ATLAS inner detector presents three main limitations to its use in the HL-LHC environment: (i) it was optimised for lower levels of radiation damage, surviving an integrated luminosity $\mathcal{L} \leq 400 \text{ fb}^{-1}$ ($\mathcal{L} \leq 850 \text{ fb}^{-1}$ for the IBL) and a fluence of $\phi \sim 5 \cdot 10^{14} \text{ n}_{\text{eq}}/\text{cm}^2$ ($\phi \sim 2 \cdot 10^{14} \text{ n}_{\text{eq}}/\text{cm}^2$ in the case of the SCT); (ii) its bandwidth is insufficient to handle the foreseen pile-up: there would be limitations, and therefore inefficiencies, both in the buffering and in the links between the on-module electronics and the read-out driver cards; (iii) the large amount of tracks per unit of η would compromise the capability of resolution of close-by tracks and the outer layers would become inefficient because of the large occupancy [66].

The ITk concept is guided by several physics requirements: it should track particles in conditions of high pile-up, measure the p_T and the direction of isolated particles, in particular $e^{\pm}$ and $\mu^{\pm}$, reconstruct the vertices of the pile-up events and identify those of hard scattering events. The ITk should also identify secondary vertices coming from $b-$jets with high efficiency and purity, have good resolution of tracks in dense-jet regions and identify τ decays as well as tracks originating from converted photons [66].

Alongside the physics requirements, the ITk should also meet space constraints, as it will be inserted in the same space now occupied by the ID, ranging from the beam pipe (larger than the current one, $R = 29$ mm), to $R \sim 1033$ mm. Moreover, engineering considerations may influence the layout: the possibility to assemble and commission the entire tracker on the surface before installation, the clam-shell structure of its internal layers to allow for an easy removal while maintaining the beam pipe in place, and the retractability of the endcaps to give access to the barrel region [40].

2.5.2 The ITk layout

The ITk detector is designed to extend up to $|\eta| < 4$. Various layouts are being proposed and their performance are under study. The baseline layout consists of 4 layers of barrel pixels + 3 short-strip and 2 long-strip layers, arranged in a cylindrical shape, and 6 pixel + 7 strip endcaps. Given that each strip layer provides 2 hits/track, this design ensures at least 11 hits per track, essential to minimise the number of fake tracks[16] at high pile up.

---

[16]Fake tracks are tracks reconstructed with hits that were not generated by the passage of a single particle.

The extended layout has a structure similar to the current inner layers, with staves and modules arranged parallel to the beam pipe and tilted for overlap and hermeticity in the $r - \phi$ plane.

In the inclined layout, the pixel modules are supported by special staves, called "alpine", that allow the pixels to always face perpendicularly to the incoming tracks. This pixel geometry leads to a reduction of the cluster size, lowering the occupancy of the detector, and limits the material crossed by the particles.

The conical layout smoothens the transition between barrel and endcap with a cone-shaped structure at the end of the barrel.

Other layouts foresee, if performance would considerably improve, the addition of one pixel layer within the same space. In all layouts, the pixel endcap modules are arranged in rings of different radii placed at different z, to limit the material budget while maintaining the performance.

2.5.3   Sensor technology options for the ITk pixel layers

The pixel sensors instrumenting the ITk inner layers will need to guarantee a survival up to fluences of $\phi = 2 \cdot 10^{16}$ 1MeV n_{eq}/cm^2 and contribute to the material budget $X_0 < 1.5\%$ in the inner layer and $X_0 < 2\%$ in the outer layer [68]. They will cover a total area of about 10 m^2.

Ongoing R&D studies aim at improving the current sensor technologies and at developing new ones, with the goal of identifying the best option to instrument the new layers. The final choice will be largely driven by the radiation tolerance requirements and the need for a finer granularity, higher bandwidth and reduced material. In particular, material budget requirements translate into thinner sensors, with a thickness of $w < 150$ μm. Costs will determine the outer radius of the pixel detector, while the endcap radii will be optimised for performance.

At the moment four categories of technologies fall within the possible short-list:

Planar sensors: standard planar sensors are a well-known technology. The use of slim/active edge thin n^+-in-p sensors is the baseline for the outer layers. The experience gained with the IBL shows adequate levels of radiation hardness, compatible with the expected fluence at the outer radii and they have limited costs;

3D sensors: they instrument the IBL detector and have shown to be radiation tolerant and overdeplete at low voltages even after irradiation. They look

promising for the instrumentation of the inner layers;

Diamonds: they show the advantages of having very low noise, good radiation tolerance and no cooling requirements, but have high costs;

CMOS: the great interest in this technology is motivated by the low power requirements, the possibility to implement chip logic at the sensor level (passing from hybrid to monolithic concepts) and, above all, their industrial production, which leads to low costs. Their radiation hardness and readout speed are still to be demonstrated and R&D activities are ongoing [66, 68].

R&D studies also focus on the determination of which front-end electronics technologies could be coupled to the ITk pixel sensors. The outer layers could be instrumented with a newer version of the front-end chip used in the IBL, which features a pixel size of (250×50) μm^2, sufficient to keep occupancy low. The inner layers, instead, require a higher pixel granularity. This choice will increase the resolution on the track impact parameter, hence improving the two-track resolution and reducing the occupancy.

Modules will be of three types: 2-chip modules (with two chips coupled to a single sensor) will be used in the inner layers, quad-modules (2×2 chips/sensor) will be used in the outer layers, quad- and hex-modules (3×2 chips/sensor) in the endcaps [66]. The presence of larger modules goes in the direction of a reduction of the costs, since the cost of module bump bonding scales with number of chips, not with surface area.

Chapter 3

Silicon detectors

Silicon sensors instrument the innermost layers of many large HEP detector systems, such as the ATLAS experiment.

In this chapter, special attention is dedicated to solid state detector technologies. First, a general description of their working principle and physical properties is provided in Section 3.1. Next, in Section 3.2, an overview of the geometries, from the simple pad to the more complex strip and pixel detectors is given. Emphasis is put on the description of the 3D geometry (Section 3.2.3). The last Section, 3.3, reports the effects of radiation on the sensors.

3.1   General description of a silicon sensor

Silicon sensors belong to the family of solid state sensors based on semiconductor crystals. They are widely exploited in the field of HEP: their fast response, good time resolution and high spatial resolution performance provide high precision tracking information.

Their principle of operation is based on the ionisation of the atoms composing the crystal lattice: the passage of a charged particle creates electron-hole ($e^- - h$) pairs that can be collected by means of an applied electric field [46].

Besides their great performance, the exceptional interest in using solid state sensors is motivated by the fact that, with respect to other ionisation-based sensors (e.g. gas detectors), the average energy required to create $e^- - h$ pairs in a silicon sensor is much lower ($E^{Si}_{e-h} = 3.6$ eV, while for gas detectors it is $E^{Ar}_{e-h} = 15$ eV) [69]. To say it in other words, the same crossing particle produces a larger amount

of ionisation, which leads to a better signal-to-noise ratio, hence reducing the rate of fake hits.

Drawbacks of silicon sensors are their high stopping power and their sensitivity to radiation damage. To address the first issue, research on silicon sensors is going in the direction of thinning the sensors, at the cost of a reduction of the magnitude of the signal and of a more complex production and handling. The impact of radiation on silicon sensors is described in Section 3.3.

3.1.1 Properties of semiconductors

In solid state materials, energy levels available for electrons are distributed in a band structure. This is the direct consequence of Pauli's exclusion principle, which states that fermions cannot occupy the same quantum state simultaneously [25]. At the atomic level, this implies that electrons in an atom cannot occupy the same quantum state in the same instant.

Let's take into consideration two atoms of silicon. Belonging to the IV group of the periodic table, they have 4 electrons in the last atomic shell. When they are far apart, their electrons are arranged in the orbitals of an isolated atom (see Figure 3.1). When the two atoms get closer, their external orbitals deform to create a covalent bond. If Pauli's principle did not hold, the electrons of the two atoms would end up being in the same quantum state, but, instead, the energy levels of the electrons slightly shift into separate levels. This phenomenon is called splitting.
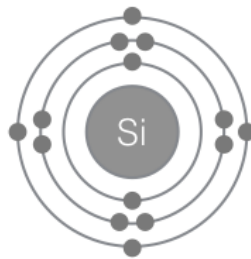
Figure 3.1: Electronic structure of an isolated atom of silicon. The atomic number for Si is 14, therefore there are 14 electrons distributed over the $1s\,2s\,2p\,3s\,3p$ orbitals. In the outer orbital, 4 states are empty and available for bonding.

In a lattice structure, the presence of many atoms causes the formation of band structures, as the splitting of many discrete and closely-spaced energy levels can

be considered as a continuum band of values. The band structure is illustrated in Figure 3.2. Two electrons with opposite spin can reside in the same level, therefore a band is formed by as many energy levels as the number of electron pairs in the lattice [46, 70].
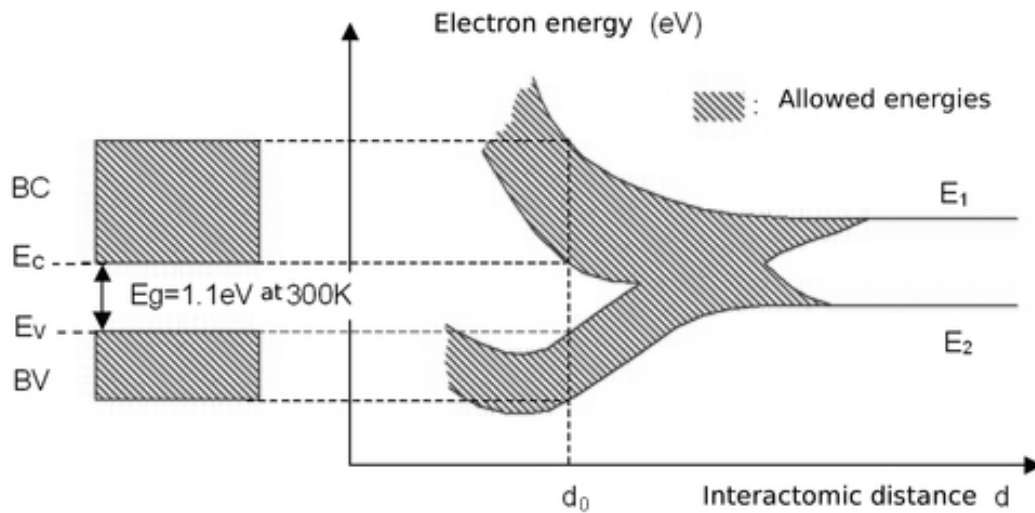
Figure 3.2: Splitting of the energy levels of two atoms of silicon when they get closer and closer. At far distance, the energy levels are discrete, but as atoms get nearer, splitting takes place. The silicon lattice is stable when its atoms have an interatomic distance of $d_0 = 5.43$ Å. Image reproduced from [70].

Two bands can completely overlap (degenerate bands), have a partial overlap or be completely separated. Between two separate bands, there is the so-called band gap, where there is no energy level available for the electrons.

The highest energy band is the conduction band: here, electrons are disentangled from their original atom and are free to move across the crystal; the lower energy band is the valence band, where electrons are still bonded to their individual atom.

The band gap is an intrinsic property of the material; it depends on temperature and pressure and is responsible for the electrical properties of materials. As shown in Figure 3.3 [71], solid materials can be classified, depending on their band gap width, into:

Metal: there is no band gap, the valence and conduction bands are partially overlapped or the conduction band is partially filled. As a result, if an electric field is applied, current can easily flow;

47
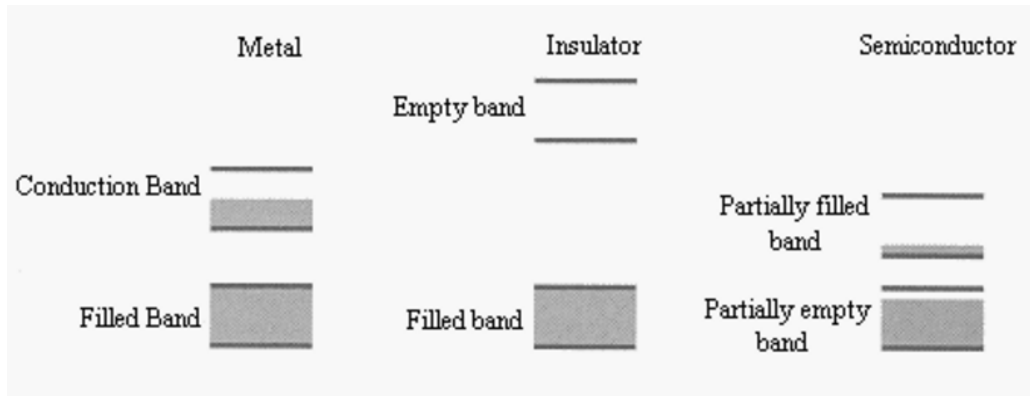
Figure 3.3: Energy band levels for (a) metal, (b) insulator, and (c) semiconductor. Image reproduced from [71].

Insulator: the valence band is completely filled with electrons. The band gap is large, therefore at normal temperature there are no electrons in the conduction band;

Semiconductor: the band gap is present, but very small; at room temperature, electrons in the valence band can acquire enough thermal energy to "jump" into the conduction band. When applying an electric field, a small current can be measured. Typical semiconductors are the elements silicon and germanium, and the compound gallium arsenide. Their respective energy gap widths are 1.12, 0.67 and 1.42 eV.

The band gap in semiconductors can be direct or indirect. In the first case, illustrated in Figure 3.4a, the electron can be promoted to the conduction band with no change in crystal momentum. In the case of an indirect band gap (Figure 3.4b), the transition of an electron between the valence and the conduction band is assisted by a phonon, the collective excitation of the crystal lattice [72]. Typical semiconductors with indirect gaps are silicon and germanium, while gallium arsenide has a direct gap.

The energy required to created an $e - h$ pair ($E_{e-h}^{Si} = 3.6$ eV) is usually larger than the energy gap width ($E_g^{Si} = 1.12$ eV). The energy difference is partially absorbed by the lattice and re-emitted as phonons, and partially lost during elastic collisions of the electrons with the lattice [73].
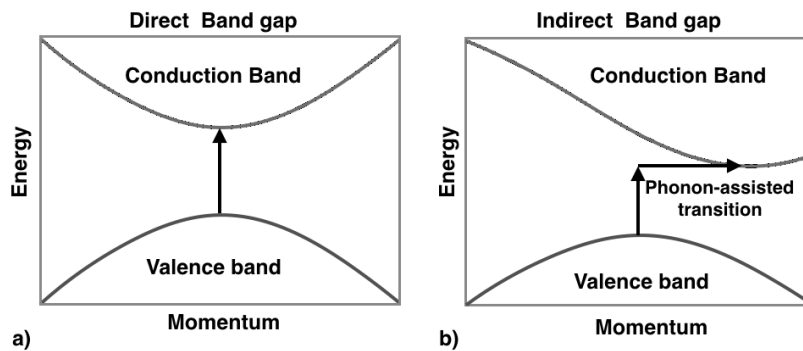
Figure 3.4: Energy vs. crystal momentum in the case of (a) direct and (b) indirect band gaps. Image modified from [72].

3.1.1.1 Charge Carriers in a pure semiconductor

Whenever an electron is promoted to the conduction band, it releases a free space in the valence band: a hole is created. The schematic representation of the silicon structure, with a free electron and a free hole, is depicted in Figure 3.5 [69].
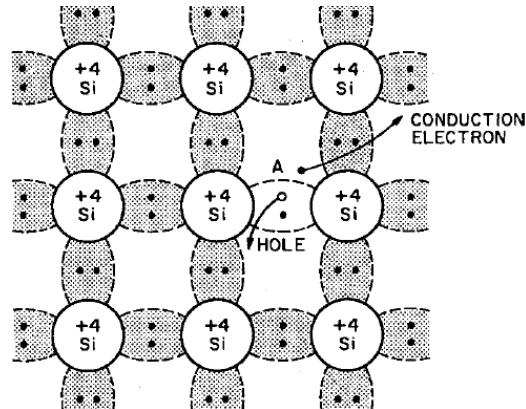
Figure 3.5: Schematic of the bond representation of the crystal structure of silicon, with one broken bond, which lets free an electron and a hole. Image reproduced from [69].

Both the electron and the hole are available for conduction: the electron is free to move around the lattice on the conduction band, while the hole movement can be visualised as a neighbouring valence electron that "jumps" into the vacant position (the hole moves in the opposite direction) [69]. Overall, the hole can

be considered a positively charged virtual carrier. The current measured in a semiconductor is due to the motion of both electrons and holes, unlike conductors, in which the current is only generated by electrons' movement.

Electrons and holes occupy the energy levels E following the Fermi-Dirac distribution:

$$f(E) = \frac{1}{1 + e^{\frac{E - E_F}{k_B T}}},\tag{3.1}$$

where k_B is the Boltzmann constant, while E_F is the Fermi energy (for intrinsic semiconductors[1] is also indicated as E_I). E_F is the maximum electron energy at a temperature $T = 0$ K: all energy levels with energy $E < E_F$ are completely filled ($f(E < E_F) = 1$), while energy levels above E_F are empty ($f(E > E_F) = 0$).

Inside a semiconductor, new $e^- - h$ pairs are continuously created and, at the same time, other pairs can be recombined. The concentration of carriers in equilibrium conditions in a pure semiconductor is defined as:

$$n_i = \sqrt{N_C N_V} e^{-\frac{E_g}{2k_B T}},\tag{3.2}$$

where n_i is the intrinsic carriers' concentration, N_C and N_V are, respectively, the densities of levels in the conduction and valence bands, and E_g is the band gap energy. It is possible to demonstrate that N_C and N_V are proportional to $T^{\frac{3}{2}}$. Equation 3.2 becomes:

$$n_i = A T^{\frac{3}{2}} e^{-\frac{E_g}{2k_B T}}.\tag{3.3}$$

Pure semiconductors have an equal density of electrons (n) and holes (p):

$$n = N_C e^{-\frac{E_g}{2k_B T}}\tag{3.4}$$

$$p = N_V e^{-\frac{E_g}{2k_B T}}\tag{3.5}$$

At room temperature, $n_i^{Si} = 1.5 \cdot 10^{10}$ cm^{-3}. The atom density in a pure silicon crystal is $\approx 10^{22}$ cm^{-3}, therefore only 1 every 10^{12} atoms is ionised.

An important parameter to describe the physics of silicon crystals is the mobility, namely the variable that parameterizes the mathematical relation

---

[1]A semiconductor crystal is defined as pure or intrinsic when it has no spurious atoms.

between the speed of electrons and holes and the applied electric field:

$$\vec{v_e} = \mu_e \vec{E}, \tag{3.6}$$

$$\vec{v_h} = \mu_h \vec{E}. \tag{3.7}$$

For fields $|\vec{E}| < 10^3$ V/cm and for set temperature and doping concentrations, the mobilities μ_e and μ_h are approximately constant.

3.1.1.2   Extrinsic semiconductors

Silicon crystals are rarely used for detection purposes in their intrinsic form. In practice, they are always doped, both unintentionally, because it is extremely difficult to obtain a pure silicon crystal, and on purpose, by adding impurity atoms during the crystal growth or the following processes.

Typical doping concentration is $\sim 10^8 - 10^{12}$ cm^{-3}. Despite being a very small fraction with respect to the density of the silicon atoms, the introduction of these dopants changes the sensor's properties [74]. Doping atoms, in fact, modify the ratio between electrons and holes and can slightly distort the periodical structure of the crystal.

Dopants can be classified as:

Donors: atoms from the V family, e.g. Arsenic (As) or Phosphorous (P). They have 5 valence electrons, while only 4 are requested to bond to the neighbouring silicon atoms: the fifth electron is not bound to any specific atom and is free to move across the lattice (see Figure 3.6a). The silicon is $n-$type doped and electrons are called majority carriers.

Acceptors: atoms from the III group, typically Boron (B). The spurious atom lacks an electron to form the covalent bond with the neighbouring silicon atoms (Figure 3.6b). A hole is formed and is available for conduction, through the mechanism described in 3.1.1.1. The silicon is $p-$type doped and the majority carriers are holes.

It is important to remark that the overall charge balance is not compromised and the silicon wafer is neutral. Indeed, the excess of free carriers is balanced by the different atomic number of the dopant atoms [69, 75].

From the point of view of the energy band model, the introduction of impurities in the crystal leads to the generation of localised energy levels, with the consequent change of electrical properties of the bulk. If new energy levels from
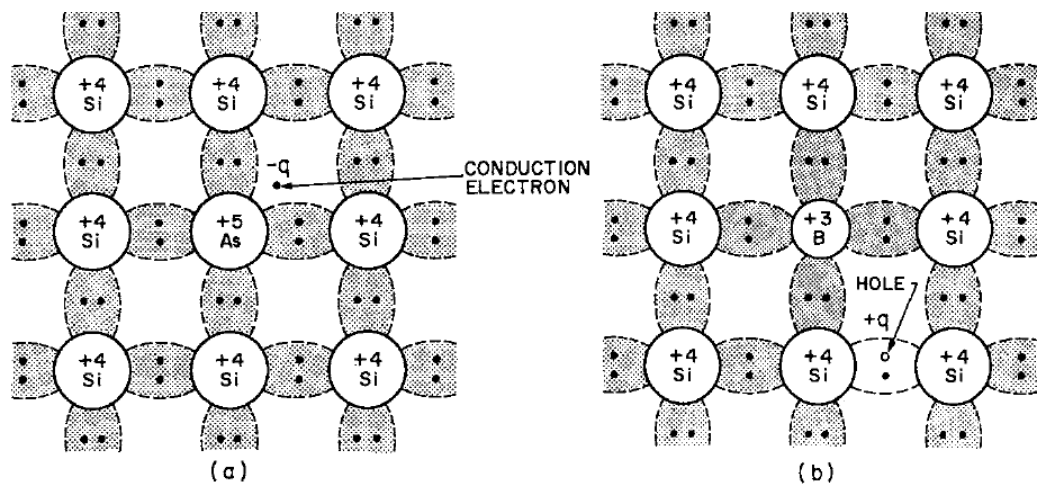
Figure 3.6: Schematic of the bond representation of a doped crystal structure: (a) the dopant atom belongs to the V family. The extra electron is available for conduction. (b) The dopant atom belongs to the III group: the lack of a bonding electrons releases a hole, available for conduction. Image reproduced from [69].

donors E_D are available close to the conduction band ($E_C - E_D = 0.045$ eV for P atoms and 0.054 eV for As atoms), these states are all ionised at room temperature and its electrons are promoted to the conduction band. In the case of $p-$type doped sensors, new energy levels E_A close to the valence band ($E_A - E_V = 0.045$ eV for B atoms) allow electrons from the valence band to jump to these higher energy levels, creating new holes in the valence band.

3.1.2 The p-n junction

The reversely biased p-n junction is the basic building block of silicon sensors. This junction is obtained by contacting, at microscopic levels, an $n-$type and a $p-$type silicon structure.

Figure 3.7 shows the charge configuration before the two sides of the junction are put in contact (a) and after having been brought together (b), in conditions of thermal equilibrium and no external fields. Before the contact, free carriers (electrons and holes) are uniformly distributed in their respective volume. After the contact, electrons diffuse in the $p-$type side and recombine with the holes diffused from the $n-$type region. The recombination causes two effects: firstly, an excess of positive charge is formed in the $n-$type region and a surplus of

negative charge is created in the $p-$type volume. This is originated by the no-longer balanced charge of the dopant atoms. The second effect is the generation of an electric field that counteracts, and eventually stops, the diffusion across the junction. The lack of free carriers in the junction region is a space-charge volume [69].
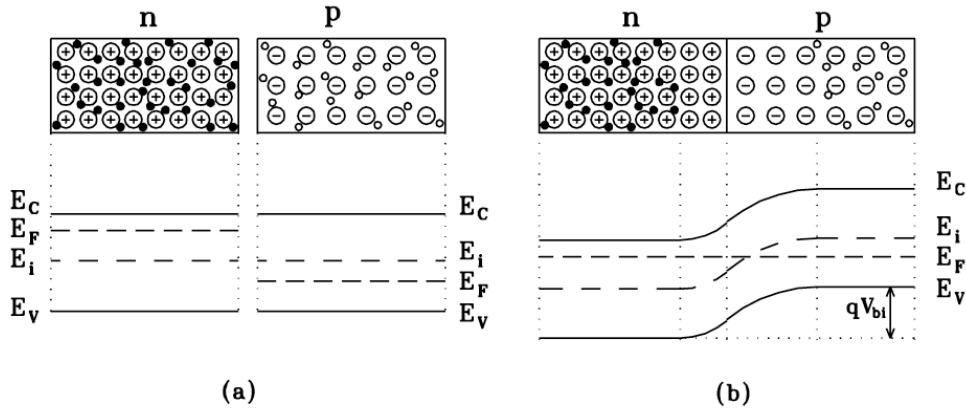
Figure 3.7: Formation of a p-n junction in conditions of thermal equilibrium and no external electric field. (a) $p-$ and $n-$ types are separated; (b) the two sides of the junction are brought together. Image reproduced from [69].

Considering the band model, the self-created electric field corresponds to a difference of potential called built-in voltage U_{bi}, generated by the requirement that the Fermi energy levels of the two sides of the junction must align at thermal equilibrium [69].

If an external electric field, $\vec{E}$, is applied, the width of the depleted volume varies. If the polarity of $\vec{E}$ is opposite to the internal electric field (it is called forward biasing), the depletion region shrinks, free carriers are able to cross the junction and the current increases very rapidly with the applied voltage.

More interesting is the case of the reverse biasing (e.g. negative potential on the $p-$side, $n-$side at ground potential). This voltage attracts holes in the $p-$type region towards the p contact and attracts electrons in the $n-$type volume towards the n contact: in this case the depleted volume increases. Moreover, the higher the voltage, the larger the depleted region. This region grows symmetrically only if the doping concentration on both sides is the same; most of the times, however, the two values differ and the depleted volume expands more in the less doped side.

The width of the depleted region $w(U)$ can be mathematically expressed as

a function of the built-in voltage U_{bi}, the externally applied voltage U_{ext}, the absolute permittivity for vacuum ε_0 and the relative permittivity for silicon ε_{Si}:

$$w(U) = \sqrt{\frac{2\varepsilon_0\varepsilon_{Si}\left(U_{ext} + U_{bi}\right)}{e|N_{eff}|}}. \tag{3.8}$$

The variable N_{eff} is the effective doping concentration, given by the difference between the number of donors N_D and the number of acceptors N_A:

$$N_{eff} = N_D - N_A. \tag{3.9}$$

The depleted region can grow until it reaches the entire thickness of the detector $w(U_{dep}) = d$. In this configuration, the sensor is completely depleted. If the potential is increased even further, then the sensor is overdepleted.

Silicon sensors should always be operated when fully depleted: this condition ensures that all the charge generated by the incoming particle is collected and, at the same time, the electric field suppresses the leakage current.

3.1.2.1 The leakage current

The leakage current is generated by thermally-created $e - h$ pairs that do not recombine and by the motion of free electrons promoted to the conduction band as a result of the extra energy levels of impurity atoms. It has an important dependence on the temperature:

$$I \propto T^2 e^{-E_g/(2k_B T)}. \tag{3.10}$$

A temperature variation leads to a change in the leakage current [76]:

$$I(T_2) = I(T_1) \cdot R(T_1, T_2) = I(T_1) \cdot \left(\frac{T_2}{T_1}\right)^2 exp\left[-\frac{E_g}{2k_B}\left(\frac{1}{T_2} - \frac{1}{T_1}\right)\right]. \tag{3.11}$$

From this equation, the effective gap energy E_g^{eff} can be estimated as:

$$E_g^{eff} = -\ln\left[\frac{I(T_2)}{I(T_1)} \cdot \left(\frac{T_1}{T_2}\right)^2\right]\frac{2k_B(T_1 T_2)}{T_1 - T_2}. \tag{3.12}$$

This parameter describes the effective energy required by the carriers to cross the energy gap in the semiconductor structure. Unlike the gap energy E_g, the value of E_g^{eff} is independent of the temperature.

3.1.2.2 The capacitance

A planar sensor behaves as a planar capacitor (other geometries will be discussed in Section 3.2.2). Its capacitance C, as a function of the applied voltage U, can be computed as:

$$C(U) = \varepsilon_0 \varepsilon_{Si} \frac{A}{w(U)},$$

(3.13)

where A is the area of the electrodes.

By measuring the capacitance of the depleted sensor, it is possible to calculate N_{eff}:

$$N_{eff} = \frac{C^2}{A^2} \frac{2\left(U_{bi} + U_{ext}\right)}{e\varepsilon_0 \varepsilon_{Si}}.$$

(3.14)

3.1.3   Silicon crystal growth techniques

Despite being the second most abundant element in the Earth's crust, silicon is very rarely found in elemental form; it virtually only exists in compounds. In HEP applications, which require uniformity of the signal across the entire volume, the silicon wafer must be grown as a monocrystal. The contamination of the crystal lattice with undesired atom species must be minimised to avoid the presence of extra energy levels in the energy gap, which in turn would cause extra leakage current. Silicon wafers are requested to have a resistivity higher than $1\ \mathrm{k\Omega cm}$ to guarantee full depletion at a reasonable applied voltage (for a $\sim 300\text{-}\mu\mathrm{m}$-thick sensor, $U_{dep} \leq 300$ V).

There are various methods for growing the detector substrates. Here, only the Float Zone, the Magnetic Czochralski and the Epitaxial methods are presented in the following, keeping in mind that they do not complete the list.

3.1.3.1   The Float Zone wafer growth

The Float Zone (FZ) is the method adopted for the production of all silicon sensors used in the LHC experiments. The growth takes place under vacuum or in an inert gaseous atmosphere. It requires a high-purity polycrystalline rod and a monocrystalline crystal. The latter is used as seed for the growth, because it gives the base orientation of the resulting crystal. After putting the seed and the rod in contact, the polycrystal material is melted using a radio-frequency heating coil and, when cooling down, it orientates according to the crystal structure of the seed. The doping is provided by flushing doping gases such as phosphine (PH_3) or diborane (B_2H_6) to obtain respectively $n-$ and $p-$doped silicon wafers [77].

3.1.3.2 The Magnetic Czochralski wafer growth

The Czochralski method (invented in 1916) is named after its inventor, the chemist Jan Czochralski. It is widely used in the integrated-circuit industry [75].

The standard Czochralski process consists of melting, on a rotating quartz support, a highly pure polycrystal of SiO_2 with additional required dopants. A monocrystal seed is dropped in the melted volume and slowly raised. The melted silicon in contact with the seed cools down when getting far from the melted volume, and orientates its atoms following the monocrystal structure. The quartz support partially melts with the polysilicon, making the Cz material rich in oxygen. The oxygen presence has double impact: on one hand, in fact, it introduces unwanted electrically active defects in the forbidden energy gap; on the other hand, however, the gaseous element acts as a gettering agent for metal impurities in the lattice and can pin dislocations, making the crystal stronger, particularly during thermal cycles [77].

Magnetic Czochralski uses a magnetic field to control the temperature and density gradients. The outcoming ingots are more uniform and can be less rich in oxygen with respect to FZ products.

3.1.3.3 The Epitaxial wafer growth

The method used to produce Epitaxial silicon wafers is based on the deposition of a mono-crystal on a seed crystal substrate [78]. The material is deposited via a method called Chemical Vapour Deposition (CVD) on a low-resistivity wafer (typically Czochralski silicon). The same lattice structure is maintained between the two crystals. The oxygen concentration in the Epi-layer is inhomogeneous because of the out-diffusion from the oxygen-rich substrate. The concentration of oxygen presents a gradient across the thickness of the Epitaxial silicon, the higher concentration being located close to the interface between the two wafers.

The advantage of this method is the possibility of growing high-purity substrates with very thin active regions, resulting in detectors with high fields even at low bias voltage.

3.1.4 Alternatives to silicon

Other materials could be used as semiconductor sensors. However, an accurate comparison among different materials has demonstrated that silicon is still the most suitable material for tracking purposes. The reasons for this choice

are its abundance, its well understood production processes and its moderate manufacturing costs, lowered by its massive industrial use [77].

Alternative to silicon are elements such as germanium and diamond (carbon crystal), and compounds such Gallium Arsenide (GaAs). Their properties are summarised in Table 3.1 and a brief overview of these materials is presented in the following.

Property	Si	Ge	GaAs	Diamond
Atomic number (Z)	14	32	31/33	6
Atomic weight (A)	28.1	72.6	144.6	12.0
Density [g/cm^3]	2.33	5.32	5.32	3.51
Atoms [10^{22} cm^{-3}]	4.96	4.41	4.43	17.7
Crystal structure	diamond	diamond	zincblende	diamond
Lattice constant [Å]	5.43	5.64	5.63	3.57
Thermal conductivity [W/(cm·K)]	1.5	1.05	0.45	10-20
Dielectric constant (ε)	11.9	16.0	13.1	5.7
Band gap [eV]	1.12	0.66	1.42	5.47
	indirect	indirect	direct	indirect
Energy to create $e-h$ pair [eV]	3.6	2.9	4.3	13
Radiation length [cm]	9.4	2.3	2.3	18.8
Average dE/dx [MeV/(g·cm^2)]	1.66	1.37	1.45	1.75
Average signal [$e-h$ pair/μm]	80	260	130	36
Electron mobility [cm^2/(V·s)]	1450	3900	8500	1800
Hole mobility [cm^2/(V·s)]	450	1900	400	1200
Intrinsic carrier density (n_i) [cm^{-3}]	$1.1 \cdot 10^{10}$	$2.4 \cdot 10^{13}$	$1.8 \cdot 10^6$	$< 10^3$
Intrinsic resistivity [Ω cm]	$3.1 \cdot 10^5$	47	10^8	$> 10^{11}$
Saturation field [V/cm]	$2 \cdot 10^4$	$8 \cdot 10^3$	$3 \cdot 10^3$	$2 \cdot 10^4$
Saturation velocity (e) [10^6cm/s]	10.5	5.5	8.0	22

Table 3.1: Properties of silicon, germanium, gallium arsenide and diamond at room temperature [77].

Germanium

Like silicon, Germanium (Ge) is a semiconductor material that belongs to the IV family of the periodic table. Having a very small energy gap width ($E_g = 0.67$ eV), this semiconductor requires cryogenic temperatures to be operated as tracking detector (usually it is cooled down to 77 K using liquid nitrogen). For this reason, it is little exploited in High Energy Physics, but finds applications in gamma spectroscopy, where the small energy gap shows the advantage of allowing very precise energy measurements.

Diamond

Diamond is actually an insulator, as its energy gap is of the order of 5.5 eV [79]. It is produced in its polycrystalline form via a CVD process.

Diamond presents various appealing properties: it shows high resistivity (10^{11} Ωcm) and does not require a reversed biasing for operation; the large energy gap makes the material very poor in free carriers, therefore the noise level is very small and so is the leakage current. Its thermal conductivity is more than 10 times higher than in silicon. This makes the diamond less prone to thermal runaway (see Section 3.3.1) and reduces its cooling requirements. Furthermore, a metal layer is sufficient to create contact and a simple structure of the detector is thus possible. Most importantly, this material presents an excellent radiation hardness, showing little signal degradation even after heavy irradiation [80].

Diamond, however, also shows some disadvantages: the manufacturing process of CVD diamond wafers is quite expensive and complex; the signal height is small because of the high ionisation energy, ~ 13 eV; also, its polycrystalline structure is a limiting factor for the propagation and the homogeneity of the signal across the entire volume of the sensor.

Nevertheless, diamond sensors have been employed in various experiments operating in the past, such as BaBar and CDF[2], and are now instrumenting the Diamond Beam Monitor of the ATLAS and CMS experiments (see Section 2.4.2.5) [7, 14, 81, 82].

Gallium Arsenide

This compound can be easily operated at room temperature, as its band gap is 1.42 eV. This rather large band gap determines low levels of noise, high resistivity and a good radiation hardness [69, 83]. With its direct band gap, GaAs has good

---

[2]CDF: Collider Detector at Fermilab

capability for light absorption and emission, therefore it finds applications in the photonics sector.

One of the advantages of GaAs over Si is the higher carrier mobility, so signal can be collected much faster. If the crystal is grown with an excess of argon, defects may be introduced (e.g. an Ar atom can take the lattice site of a gallium). These defects, concentrated in the central region of the band gap, influence the electrical properties, allowing the charge collection to saturate at moderate voltages even after irradiation. Its radiation hardness, however, is not as good as in the case of silicon: it has been estimated that its charge collection efficiency, inside the ATLAS experiment, would have been reduced to only 25% after 10 years of operation [84].

3.2 Silicon detectors used in High Energy Physics

This section is dedicated to the description of silicon detectors used in High Energy Physics applications.

This type of sensor, as seen in the previous section, show major advantages with respect to detectors based on ionisation of gas: the small band gap allows the generation of a large amount of $e - h$ pairs per unit path length; their higher density promotes a big signal even in a thin detector (this, however, has the disadvantage of influencing more the trajectory of the particle inside detector systems such as the ATLAS experiment). Moreover, carriers have high mobility inside the medium: this corresponds to a fast signal, of the order of ~ 10 ns, which in turn permits their use in high rate environments, like the ones at particle colliders. Finally, both the sensor and the electronics are usually made of silicon, therefore it is possible to integrate the sensor and (part of) the electronics in a single device [69].

3.2.1 Signal formation

The passage of a particle ionises the silicon medium creating $e - h$ pairs. The carriers drift following the reverse biasing electric field, towards the electrodes of the opposite polarity. A MIP creates about $80 \ (e - h)_{pair}/\mu$m: for a standard sensor thickness of $300 \ \mu$m, this sums up to $\simeq 24000 \ e^-$ (equivalent to $\simeq 4$ fC).

The signal is not generated by the actual collection of the charges on the electrodes, but it is created by the time-varying change of the potential on the electrodes induced by the movement of the drifting carriers. This induced current

is collected and converted into a voltage pulse by means of a charge sensitive amplifier. Ideally, the output signal height is proportional to the deposited energy.

The current induced by a single carrier on the electrode is modelled by the Shockley-Ramo theorem [85]: it states that the charge Q and current i, induced on an electrode by a moving point charge q, are given by:

$$Q = -q\varphi_0(\vec{x}) \tag{3.15}$$

$$i = q\vec{v} \cdot \vec{E}_0(\vec{x}) \tag{3.16}$$

where $\vec{v}$ is the instantaneous velocity of the charge q, φ_0 and $\vec{E}_0$ are respectively the weighting potential and the weighting field. φ_0 is the electric potential that would exist at q's instantaneous position if a few conditions were satisfied: first, the selected electrode is at unit potential; second, all other electrodes are at ground; third, all charges are removed. $\vec{E}_0$ is the corresponding field. These last two parameters only depend on the device topology and on the charge movement.

3.2.2 Silicon detector geometries

The design of silicon sensors has evolved, following the more and more pressing requirement of a high spatial resolution, from the simple pad sensor to strip, to planar and 3D pixel detectors. Using more complex electrical structures leads, in fact, to a higher granularity, which results in an improvement in tracking precision as well as hit discrimination, the discrimination between the position of two close particles releasing energy in the silicon sensor.

3.2.2.1 Pad sensors

The simplest structure of a silicon sensors used in High Energy Physics experiments is a diode operated under reverse biasing with its depleted region acting as a solid state ionisation chamber. Figure 3.8 shows the sketch of the cross sectional view of a pad silicon detector.

One of the two sides of the junction has a higher doping concentration than the other: the junction profile results are asymmetric with respect to half the thickness of the sensor. In Figure 3.8, the highly-doped p^+ implant is narrower and more doped than the n side. This allows to make the collection faster, because the read-out electrode can be placed closer to the region where the depletion starts its

growth (in Figure 3.8, the depletion starts at the top of the sensor, close to the p^+ implant).
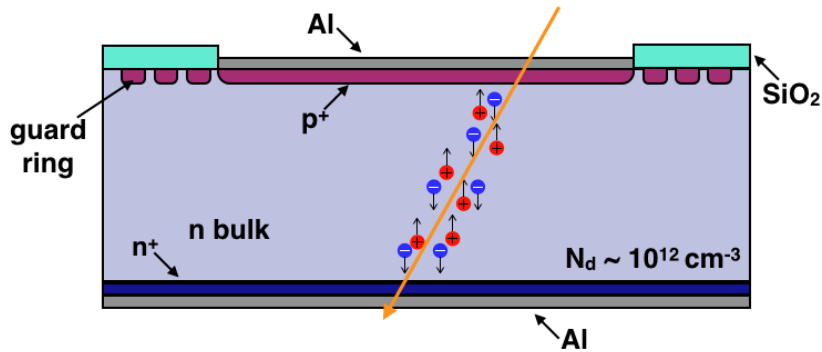
Figure 3.8: Cross sectional view of a pad silicon detector.

The surface is never left bare: after cutting and polishing the sensor, the silicon atoms at the surface present many open (dangling) bonds that, if not properly closed, rearrange deforming the crystalline structure or including spurious atoms caught from the atmosphere. To avoid this effect, an insulating layer is on the surface. Typically, silicon sensors are insulated with SiO_2. The oxide provides good insulation and, at the same time, can be used as part of the electronics (see Section 3.2.2.2.2).

The top and bottom layers of the silicon sensors are covered by metallic (conductive) structures, aimed at a better distribution of the biasing voltage as well as a more efficient signal collection. To improve the ohmic contact, an additional highly doped layer is added between the doped bulk and the metal. In Figure 3.8, the bulk is n doped and the bottom layer is doped n^+.

Finally, one or more guard rings are placed close to the physical edge of the sensor. These structure are extremely important for the containment of the electric field lines, defining the end of the depletion region at the physical edge of the sensor. The guard rings are put at decreasing voltages going towards these edges, thereby avoiding the risk of breakdowns. They also prevent the dispersion of the charge carriers along the edges, favouring a complete charge collection.

3.2.2.2 Strip detectors

The demand for improved position measurements was addressed by the development of micro strip detectors. These devices are composed of parallel

61

read-out strips arranged at an inter-distance of the order of tens of micrometers.

One strip detector provides only one coordinate. The second coordinate can be obtained by the overlap of a second detector with the strips oriented with a different angle: if an angle of $90°$ is chosen, the same resolution is obtained for both coordinates; if the angle differs, then one coordinate has a higher resolution, at the expense of the second one.

Biasing and read-out connections are placed at one of the extremities of the strip electrodes. The connection to the electronics is normally obtained by means of wire bonds. These metal wires, thin as a fraction of a human hair, are applied using the wire bonding technique, described in [86] as "a solid phase welding process that uses thin wire and a combination of heat, pressure and/or ultrasonic energy".

3.2.2.2.1 Hit measurement and charge sharing The position measurement is provided by the strip that collects the signal. In the case the charge is shared among multiple strips, this measurement can be estimated by using a charge-weighted centre-of-mass algorithm. In this way, an improvement of the spatial resolution, up to a factor ten, can be achieved.

Charge sharing is affected by the depth of the depleted volume, the Lorentz angle (see Section 3.3.6), the uniformity in the charge collection and the particle's angle of incidence.

3.2.2.2.2 AC and DC coupling Metal electrodes can be in direct contact with the highly doped implant (Figure 3.9a) or can be separated by a SiO_2 interface (Figure 3.9b). The oxide interface is fundamental not only to avoid dangling bonds and protect the bare silicon wafer, as mentioned before, but it also defines the electrical connection of the sensor to the electronics [87].

The oxide layer separating the highly doped silicon from the metallic connection acts like a capacitor, decoupling the input bias, which provides the reverse bias to deplete the silicon bulk, from the output signal.

The case of a DC coupled sensor (see Figure 3.9a) is different. Here, there is direct contact between the p^+ implant and the aluminium and the reverse bias current needs to be handled by the external read-out electronics, for example using a Bias Tee to decouple the high voltage from signal.
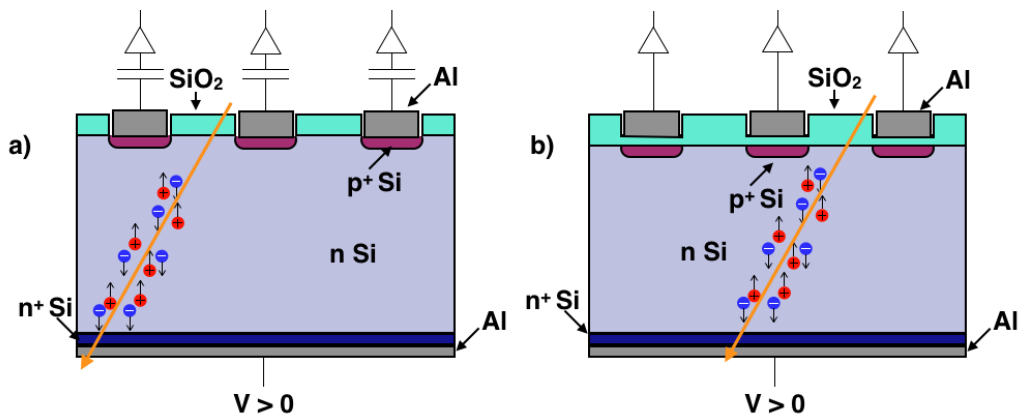
Figure 3.9: Microstrip detectors with (a) DC and (b) AC coupling. Image reproduced from [87].

3.2.2.3 Pixel silicon sensors

A further, transversal segmentation of the strip electrodes is the basic idea behind pixel sensors. The resulting pixel cells have typical dimensions of the order of few tens to few hundreds of micrometers. This value is expected to decrease in the future: a smaller pixel size leads to a better spatial resolution.

Figure 3.10 presents the side view of a hybrid pixel silicon detector. The term hybrid indicates that electronics and sensor are produced separately and then connected [88]. The one-to-one connection between the unit cell and the corresponding element of the front-end chip is achieved by means of a bump-bonding technique, whereby small balls of soldering material make the contacts between the sensor pixels and the read-out pixels (illustrated in Figure 3.10). Obviously, the density of the front-end elements must equal that of the sensor cells [89].

The front-end chip provides several functions for each individual pixel cell. Examples are:

- Amplification of the signal charge;

- Filtering of the noise;

- Temporary storage of the signal for a later read-out;

- Application of a signal threshold;
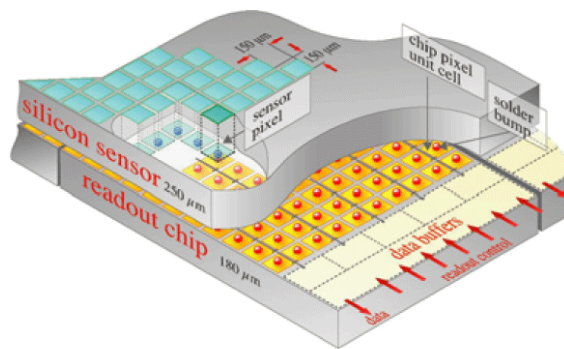
Figure 3.10: Cross sectional view of a pixel silicon detector and its front-end chip. Image reproduced from [88].

- Set of a marker for the read-out cycle;

- Restoration of the pixel electronics after the read-out (or a certain delay, if read-out is not requested) [69].

All these functions have to be implemented in an area smaller than the sensor pixel, because some services, such as read-out control and transfer buses, are present at the cell level [69]. Extra space, typically on one side of the chip, is required to connect the front-end to the read-out chain used during data acquisition.

The pixel technology provides the most performant sensors, in terms of position and time resolution, but their production is expensive. Costs are mostly driven by the moderate yield of the bump-bonding step. For this reason, research is recently devoted to the development of new technologies that implement the electronics into the silicon wafer. These devices, called monolithic, can be realised because a common substrate, silicon, is used for both the chip and the sensor. New monolithic technologies include MAPs, CMOS, HVCMOS and SOI devices [90, 91, 92, 93]. Their description goes beyond the aim of this work.

3.2.3 3D pixel silicon sensors

A novel architecture for pixel silicon sensors was proposed by S. I. Parker in 1997 [9]. This approach foresees a different orientation of the electrodes: rather than being implanted on the surfaces of the silicon substrate, as in the case of

planar sensors, the electrodes are etched through the whole or part of the thickness of the wafer.

A three-dimensional view of a 3D silicon sensor is presented in Figure 3.11 on the left-hand side. On the right-hand side, the top view of a pixel cell is depicted. Electrodes of the opposite doping are staggered to form a matrix. Usually, 3D sensors are n-in-p, meaning that the bulk is $p-$type, to avoid type inversion at high fluences (see Section 3.3.3.2), and the collecting electrode is n^+ doped. Considering the higher mobility of electrons over holes in silicon, the use of the n^+ electrode as collecting electrode makes the signal collection faster.
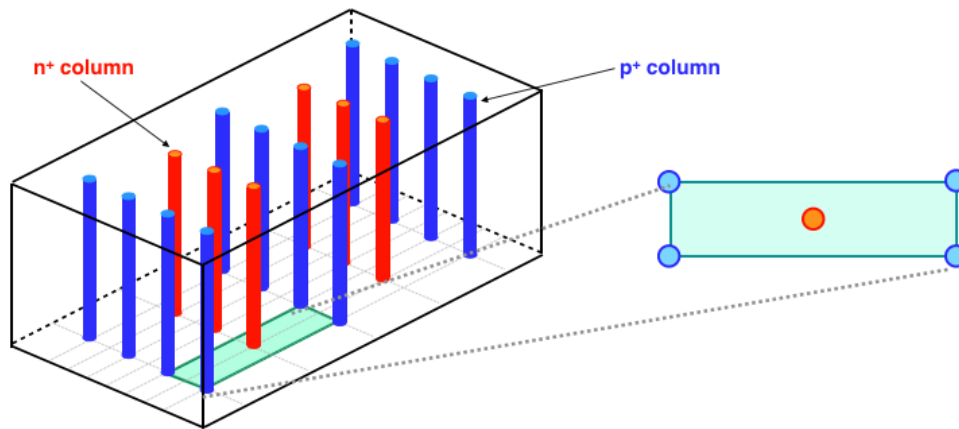
Figure 3.11: Left: Three-dimensional view of a 3D pixel silicon sensor. Right: zoomed top view of a 3D pixel cell.

Figure 3.12 compares the planar and 3D technologies. 3D silicon sensors offer a variety of advantages over the standard architecture [94, 95]. The inter distance between the cylindrical electrodes can be chosen "ad hoc" and is no longer dependent on the thickness of the sensor. Typical distances between n^+ and p^+ electrodes of the order of $50\ \mu$m can be obtained, making the drifting path of the charges much shorter than in planar sensors. This feature has important implications: first of all, the 3D technology is intrinsically radiation harder, as the probability of the charges to get trapped during their drift is significantly reduced. Secondly, the charge collection is faster, hence 3D sensors can be used for fast-tracking algorithms. Thirdly, the signal height is comparable to the one of planar sensors, as, for the same thickness, the average number of generated $e - h$ pair is identical. Closer electrodes, however, also leads to a higher capacitance, which

causes a higher level of noise [87]. Moreover, the more complex production process is more expensive and generally determines a lower yield.
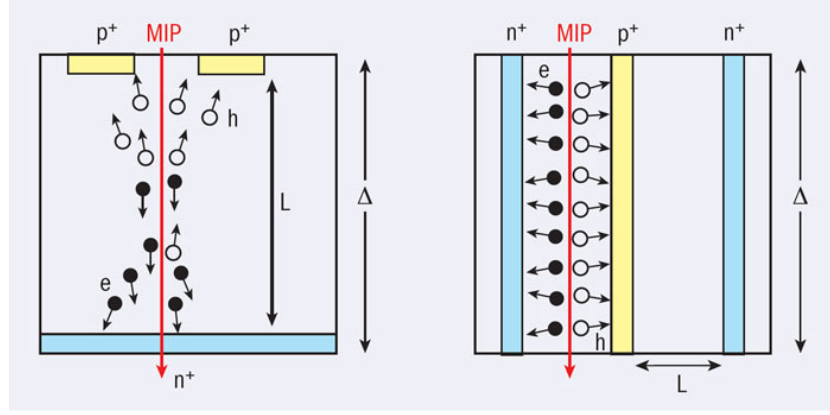
Figure 3.12: Side views of planar (left) and 3D (right) technologies. Image reproduced from [95].

Due to the different spatial orientation of the electrodes, the capacitance cannot be computed using Equation 3.13, but the cylinder capacitor formula should be adopted [76]:

$$C_{3D} = 2\pi\varepsilon_0\varepsilon_{Si}\frac{W}{\ln\frac{d}{r_{col}}} \tag{3.17}$$

where W and d are, respectively, the overlapping depth and the inter-electrode distance; r_{col} is the radius of the columnar electrodes.

Assuming the same approximation, the depletion voltage can be computed for 3D sensors as [96]:

$$U_{depl,\ 3D} = \frac{qN_d}{2\varepsilon_0\varepsilon_{Si}}\left(r_d^2\left[\ln\left(\frac{r_d}{r_{col}}\right) - 0.5\right] + 0.5\ r_{col}^2\right), \tag{3.18}$$

where r_d is the radius of the depleted region. The equation indicates that, in 3D sensors, the full depletion voltage is roughly proportional to the square of the electrode spacing.

The simulation of the electric field configuration is reported in Figure 3.13 [96]. In the overdepleted sensor, the field reaches its maximum in the vicinity of both column types, where its direction is radial because of the column shape. The corners not occupied by the electrodes, corresponding to the midpoints between collecting electrodes, experience a very low field originated

66

by the sensor symmetry. This geometry has two effects: on the one hand, the charge deposited in these regions will be collected more slowly; on the other, the charge sharing between pixels is reduced because the electric field line bend the drifting of the electrodes away from the pixel borders [96].
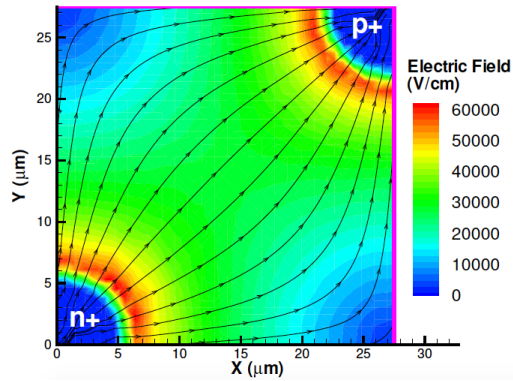
Figure 3.13: TCAD simulation of the electric field between a p^+ and a n^+ electrode of a 3D sensor. The full-3D detector is biased at $U = 100$ V. The electric field line indicate the direction of $\vec{E}$, but their spacing is not proportional to the field strength. Image reproduced from [96].

The vicinity of electrodes, of the order of $50 - 100$ μm, determines the formation of strong electric fields when applying moderate voltages. Full depletion, in fact, can be obtained at $U \sim 10$ V. A reduced power consumption is hence possible and the cooling requirements are more relaxed.

The decoupling of the orientation electric field from the direction of flight of the incident particle has a double effect: first, it reduces the time arrival spread of all charges, because charges are produced roughly at the same distance to the collecting electrode. Second, it makes 3D sensors very little influenced by the presence of an external magnetic field (see 3.3.6).

3.2.3.1 Pixel cell configuration in 3D sensors

Keeping the same size for the pixel cell, various electrode configurations are possible. Figure 3.14 shows the configurations, from the simplest one, 1E, in which there is a single collecting electrode, to the most complex 5E, in which the pixel cell includes 5 collecting electrodes. As the number of collecting electrodes increases, the inter distance between a p^+ and a n^+ electrode decreases, hence the same electric field can be achieved with a smaller potential difference. At the

same time, however, a larger number of electrodes reduces the pixel efficiency, because the fraction of inactive volume, represented by the electrodes themselves, is larger.
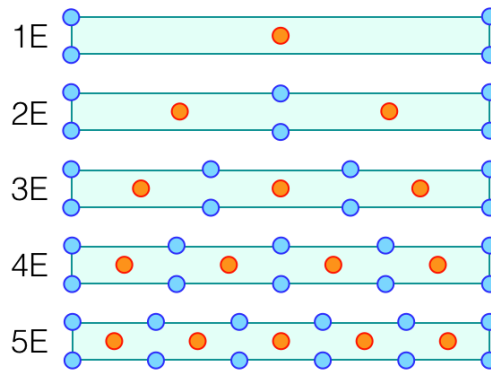
Figure 3.14: Pixel cell configurations, from 1E to 5E.

3.2.3.2 Production process of 3D sensors

Presently, 3D silicon sensors are produced on standard Float zone 4 or 6-inch $p-$doped silicon wafers, using a combination of two technologies: Micro-Electro-Mechanical Systems (MEMS) and Very Large Scale Integration (VLSI). Despite the use of these well-established technologies, the production of 3D silicon sensors is still a very delicate, complex and expensive process.

The Deep Reacting Ion Etching process (DRIE) [97], developed for MEMS, is the key technology used to produce 3D silicon sensors. It is used to create very deep and narrow holes in the silicon, with an aspect ratio (width/depth) up to $\sim 1 : 50$. The holes are then doped, by a diffusion process, to form the p^+ and n^+ electrodes [98]. The narrower the electrode, the more efficient the charge collection, because it reduces the probability that a particle with incident angle perpendicular to the surface of the sensor (and hence parallel to the electrodes) passes through the non-sensitive electrode volume. Moreover, the uniformity of the electrodes is of primary importance to ensure a uniform response across the sensor, as the electric field is the same across the thickness of the sensor.

There are two main methods for the production of 3D silicon sensors:

Full-through The first method (Fig 3.15 left) was firstly developed at SNF[3]

---

[3]SNF: Stanford Nanofabrication Facility

(Stanford, USA), and adopted also by SINTEF (Oslo, Norway). It foresees the electrodes to be etched through the entire thickness of the sensor (full-through 3D sensor). Both electrode types are etched from the same side (single-side process) and are entirely filled with polysilicon. At the same time, active ohmic trenches are implemented at the edges, making the edge active and therefore extending the electric field to the physical edge of the sensor. The bottom side of the wafer is oxide-bonded to a support wafer, for stiffness constraints.

DDTC Independently developed by CNM[4] (Barcelona, Spain) and FKB[5] (Trento, Italy), Double-side Double Type Column (DDTC) sensors are produced by etching the junction electrodes from the front side and the ohmic electrodes from the back. No support wafer is needed. In DDTC sensors, columns can be etched through the entire thickness of the sensor (full-through sensors, see Figure 3.15 right), or they can stop few microns before reaching the opposite wafer-side (partially-through sensors, illustrated in Figure 3.15 centre). The partially-through sensors present a low electric field region in proximity of the non-overlapping volume. Therefore, they reach full sensitivity only when operated at a higher bias voltage with respect to full-through sensors [99].
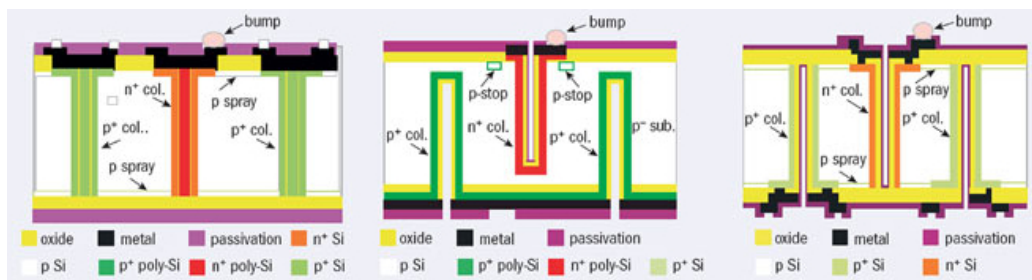
Figure 3.15: Different 3D designs. Left: Full-through design with active edges. Centre: DDTC partially-through design, with columns not passing through the entire thickness of the silicon wafer. Right: Double-side design with full-through columns. Image reproduced from [95].

---

[4]CNM: Centro Nacional de Microelectrónica
[5]FBK: Fondazione Bruno Kessler

69

3.3 Radiation damage in silicon sensors

Instrumenting the innermost layers of High Energy Physics experiments, silicon sensors are exposed to the highest fluence of particles coming from the interaction point. A simulation of the condition of radiation fluence in the ATLAS experiment is shown in Figure 3.16a (normalised to an integrated luminosity of $550\,\mathrm{fb}^{-1}$ and a peak luminosity of $3\cdot 10^{34}\,\mathrm{cm}^2\mathrm{s}^{-1}$, obtained using the PHOJET pp event generator [100] and FLUKA particle transport code [67]). Figure 3.16b includes a simple parameterization of the data for the case $z = 0$, obtained from a fit to the data for $2 < r < 20$ cm. The dependence on z is small, meaning that the parameterization for $z = 0$ can provide fluence estimates over the whole Pixel region [8].
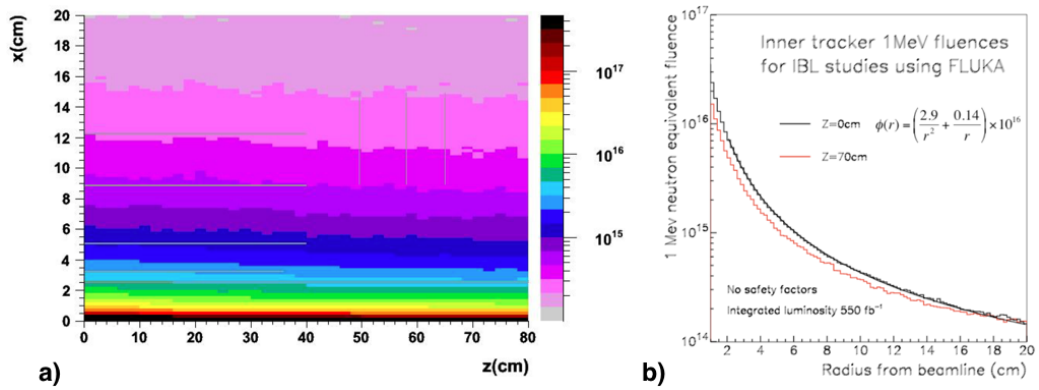
Figure 3.16: (a) 1 MeV neutron equivalent silicon damage fluences normalised to an integrated luminosity of $550\,\mathrm{fb}^{-1}$ as a function of the (x, z)-position with respect to the collision point. (b) Corresponding 1 MeV neutron fluences versus radius from beam line, for cases $z = 0$ and $z = 70$ cm. Image reproduced from [8].

This tremendous amount of particles induces microscopic damage in the silicon lattice, which, in return, has macroscopic effects: an increase in the leakage current proportional to the fluence, a substantial change of the depletion voltage and a decrease of the charge collection efficiency [77]. Particle detectors are required to keep a good signal over noise ratio and a low power consumption during their operational lifetime.

70

3.3.1 Thermal runaway

Radiation-damaged silicon sensors present an increase in the leakage current linearly dependent on the accumulated radiation dose [101]. As the leakage current increases, the silicon sensor heats up with an ohmic heat generation: as seen in Section 3.1.2.1, there is a strong dependence of the leakage current on the temperature. An increase in leakage current, therefore, causes an increase in leakage power, which consequently augments the temperature. As a higher temperature facilitates the $e - h$ pair production, more free carriers are generated and take part in the leakage current. This vicious cycle, if not interrupted by providing an efficient cooling, leads to thermal runaway. In this condition the sensor cannot be operated.

3.3.2 Surface and bulk damage

Radiation can affect silicon sensors both on the surface and in the bulk. The surface damage is mainly caused when a particle ionises the passivating SiO_2 layer: the released electron is free to move, while the remaining ion is bound to the structure. A concentration of positive charge on the surface is generated and, correspondingly, in the volume below the passivation layer, an accumulation of electrons occurs. Two effects arise: the development of a conductive layer between the read-out electrodes, which in turns reduces the inter electrode distance, and the formation of a local high field region that can induce local breakdowns, with a consequent increase in the noise levels.

The bulk damage is caused by the non-ionising interactions of a crossing particle with a silicon atom bound to the lattice. The displacement of one (or more) atom(s) of the crystal can happen if the transferred energy is sufficient to remove the atom from its periodical position. This atom, called Primary Knock-on Atom (PKA), leaves a vacancy behind. The so-called silicon interstitial and the vacancy form a Frenkel pair [75, 102]. At room temperature, Frenkel pairs have very high mobility, therefore they annihilate (in 60% of the cases) or can get closer to each other or to a doping atom, changing the electrical characteristics of the sensor.

The energy transferred by an incident particle of mass m_p and energy E_p to a silicon atom of mass M_{Si}, in the non-relativistic case, is:

$$\Delta E = 4 \frac{m_p M_{si}}{(m_p + M_{si})^2} sin^2 \left(\frac{\theta}{2} \right) E_p, \tag{3.19}$$

where θ is the incident angle [103].

The minimum energy for displacing the atom, to overcome the binding energy, is ~ 25 eV. Obviously, the transferred energy may be much higher. In the case the PKA's kinetic energy is small, the recoiling atom creates a singular interstitial, generating a point defect. Point defects are usually high energy states that create energy levels in the forbidden energy gap. These new levels can capture and release electrons. On the contrary, when the transferred energy is large, the PKA gains a lot of kinetic energy. The energy is released while the particle slows down: at the beginning, collisions are mainly electromagnetic and are completely recoverable. As the the kinetic energy decreases, however, nuclear interactions prevail and the recoil atom can generate clusters of displacement damage along its path.

Although different defects affect the silicon's properties in distinct ways, the ROSE Collaboration [104] at CERN has developed a good base model for quantifying, with some limitations, the amount of radiation-induced damage in a silicon sensor. The basic assumption of the so-called Non-Ionising Energy Loss (NIEL) scaling hypothesis [105] is that the radiation damage, as well as the corresponding signal loss, scales linearly with the non-ionising energy released during the collision, and it does not depend either on the spatial structure of the displacement, or on the following annealing.

Depending on the nature of the particle, different processes occur: neutrons release the maximum NIEL, as they only interact via inelastic scattering. Slow charged hadrons also interact electromagnetically, such that little of the energy loss contributes to the creation of PKA-clusters, resulting in a small cluster size. The number of clusters created by fast hadrons, is, however, substantially larger. A simulation of the effect of the irradiation of particles of different nature and energy is shown in Figure 3.17 [106].

The mathematical formulation of the NIEL hypothesis describes the dislocation damage cross section:

$$D(E) = \sum_{\nu} \sigma_{\nu} \int_0^{E_R^{max}} f_{\nu}(E, E_R) \, P(E_R) \, dE_R, \qquad (3.20)$$

where σ_{ν} is the cross section of each of all possible interactions with silicon of a particle of energy E; $f_{\nu}(E, E_R)$ is the probability to produce a PKA with energy E_R and $P(E_R)$ is the Lindhard partition function, which describes the fraction of the recoil energy deposited in displacements [77, 107].

72
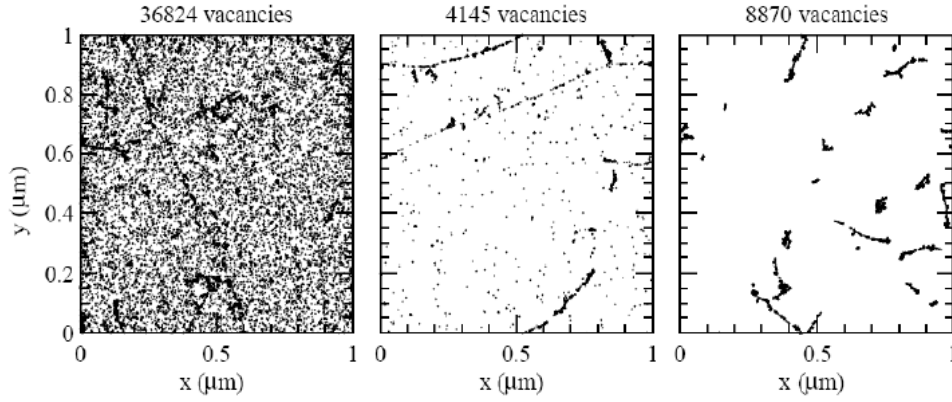
Figure 3.17: Simulation of defect formation caused by the passage of different types of irradiating particles. Left: 10 MeV protons. Centre: 24 GeV/c protons. Right: 1 MeV neutrons. Image reproduced from [106].

The displacement damage caused by NIEL can be rescaled to a reference value, namely the amount of energy lost by a 1 MeV neutron. The scaling factor is called hardness factor κ and is defined as

$$\kappa := \frac{\int D(E)\,\phi(E)\,dE}{D(E_n = 1 MeV) \int \phi(E)\,d(E)},\tag{3.21}$$

where $\phi(E)$ is the fluence of a specific particle having energy E, expressed in particles/cm^2.

Using the hardness factor, it is possible to scale the fluence of the specific particle to an equivalent fluence given by 1 MeV neutrons:

$$\phi_{eq} = \kappa\,\phi = \kappa \int \phi(E)dE.\tag{3.22}$$

Fluences of different radiation types at different irradiation facilities can be therefore directly compared by using κ.

3.3.3 Macroscopic effects of radiation damage

The microscopic nature of radiation damage is reflected in the change of macroscopic parameters.

3.3.3.1 Radiation effects on the leakage current

At room temperature, the presence of new energy levels in the forbidden energy gap allow some electrons to have enough energy to jump to the conduction band (and, similarly, to create some holes in the valence band). This causes the presence of free carriers in the depleted region, which leads to an increase of current

$$\Delta I_{leak}(\phi) = I_{leak}^{post\ irrad}(\phi) - I_{leak}^{pre\ irrad} = \alpha\ \phi\ Vol, \qquad (3.23)$$

where I_{leak} is the leakage current, ϕ is the fluence, Vol is the depleted volume and α is the damage constant [77]. The latter parameter depends on the temperature and on the annealing (see Section 3.3.4), while it is independent of how the silicon wafer was produced. It is usually quoted after 4 minutes at $80\,°\mathrm{C}$ to be $4 \cdot 10^{-17}$ A/cm for high resistivity ($\sim 2 - 8$ kΩcm) silicon wafers.

3.3.3.2 Radiation effects on the depletion voltage

Acting on the effective charge concentration N_{eff}, radiation affects also the depletion voltage. Various processes are responsible for these doping changes, i.e. radiation may cause a doping atom to be captured into a new defect complex, which may have a different charge state. In particular:

- Donors and acceptors can be removed due to the formation of defect complexes containing donors/acceptors (vacancy-phosphorous and vacancy-boron complexes);

- Defect complexes can be created and can absorb positive/negative charge states in the space charge region (effective donors/acceptors).

Figure 3.18 shows the type inversion, happening when a $n-$type silicon is irradiated at fluences above $\phi \sim 2 \cdot 10^{12}$ $\mathrm{n_{eq}/cm^2}$ [75]. As the fluence increases, the effective doping concentration diminishes until the number of donors balances the number of acceptors and the sensor is intrinsic. The fluence at which $N_{eff} = 0$ depends on the initial doping concentration. Further irradiating the crystal, the doping effectively becomes $p-$type and its concentration rises linearly with the fluence.

It has experimentally been measured [108] that heavily irradiated sensors develop a so-called double junction. The mechanism of its creation is presented in Figure 3.19. The holes are uniformly produced across the junction and flow, following the reverse biasing, towards the p^+ electrode, causing the hole
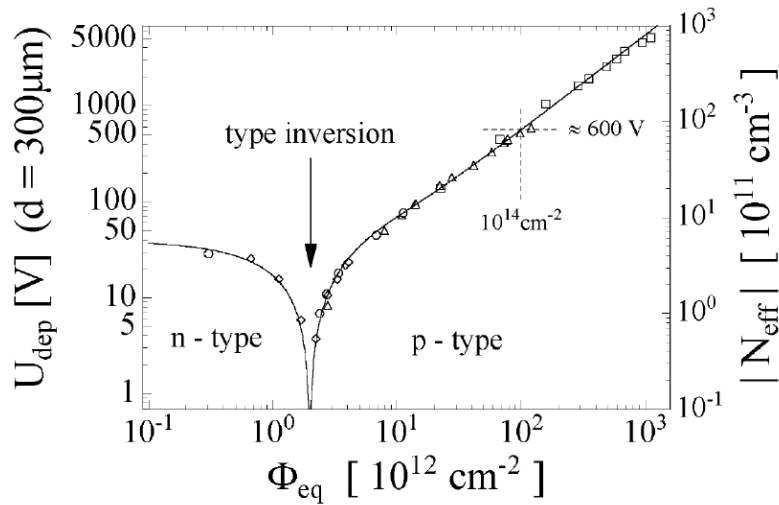
Figure 3.18: Fluence dependence of the effective doping of an initially $n-$type silicon sensor. The sensor was irradiated with 1 MeV equivalent neutrons. Image reproduced from [77].

current J_h to linearly increase towards the p^+ electrode (p^+ doping has a higher concentration with respect to p doping). At the same time, uniformly generated electrons flow towards the n^+ electrode, forming an electron current J_e that steadily increases as z decreases (Figure 3.19a). Although the actual carrier densities depend upon the mobilities and the properties of the field, they vary monotonically across the thickness (Figure 3.19b). The trapping of mobile carriers causes a net positive charge density near the p^+ electrode and a net negative charge close to the n^+ electrode. Because the positive space charge is associated with n^+ doped silicon bulk, while the negative space charge is associated with p^+ doped silicon volume, the creation of these net charge densities is explained as the generation of two p-n junctions (Figure 3.19c). The corresponding electric field (Figure 3.19d) has two maxima at the n^+ and p^+ electrodes and presents a minimum when the effective carrier density ρ_{eff} is 0 [108].

3.3.4 Annealing

The performance of silicon sensors after irradiation strongly depends on time and temperature. Radiation damage varies with time: this phenomenon is called annealing.
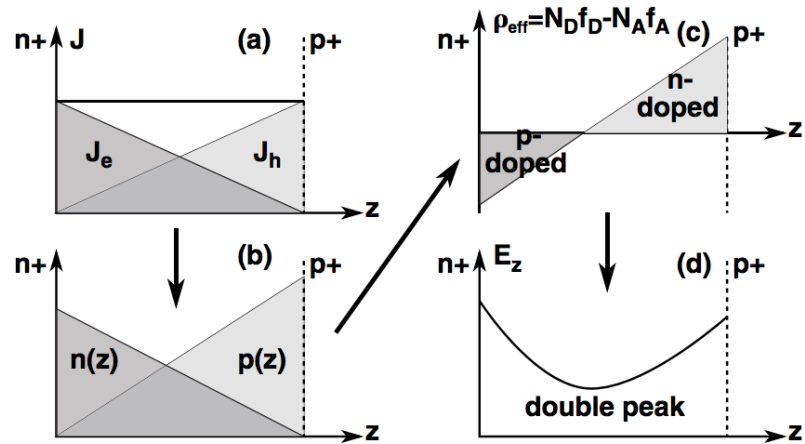
Figure 3.19: Sketch of the formation of the double junction in irradiated sensors. (a) Holes and electrons' currents; (b) Carrier densities; (c) Net charge densities; d) Electric field across the sensors, exhibiting the double peak. Image reproduced from [108].

There are two main mechanisms of annealing: migration and complex formation, and dissociation.

Migration and complex formation: thermal excitation allows the defect to move across the lattice, until it recombines (interstitial + vacancy → Si) or it associates with another defect creating a new defect complex.

Dissociation: thermal energy may also cause the inverse process, allowing a complex to split into its constituents and giving to at least one of them enough energy to migrate.

The leakage current is positively affected by the annealing: on a long timescale, in fact, the reversed bias current decreases exponentially with time and stabilises after several months [77, 75, 109].

The effect of annealing on the effective doping concentration N_{eff}, and therefore on the depletion voltage, is more complex. The Hamburg group has extensively studied this effect and suggests that N_{eff} varies with time following

$$\Delta N_{eff}\big(\phi_{eq}, t(T_a)\big) = N_{eff,0} - N_{eff}\big(\phi_{eq}, t(T_a)\big)$$
$$= N_A\big(\phi_{eq}, t(T_a)\big) + N_Y\big(\phi_{eq}, t(T_a)\big) + N_C\big(\phi_{eq}\big) \quad (3.24)$$

76

where $N_{eff,0}$ is the effective doping concentration before irradiation, ϕ_{eq} is the 1 MeV neutron equivalent fluence, $t(T_a)$ is the annealing time at a fixed temperature T_a.

Three components characterise the annealing: the short annealing, N_A, the long-term annealing, N_Y, and the stable damage, N_C. The short annealing is an initial annealing step. It is called beneficial annealing because, for type-inverted sensors, the depletion voltage decreases with time. During this phase, defects that were activated during the irradiation stage return to their neutral inactivated status. The effective doping concentration rises: in type-inverted detectors, N_{eff}, being negative, becomes less negative and for not type-inverted substrates the positive N_{eff} becomes more positive.

The de-activation of all defects follows an exponential decay

$$N_A(t, T_A) = \phi_{eq} \sum_i \Big(g_{A,i} e^{(-t/\tau_{A,i})} \Big), \tag{3.25}$$

where $g_{A,i}$ is the defect introduction rate for the ith reaction and $\tau_{A,i}$ is the decay time constant, which depends on the annealing temperature. Equation 3.25 can be approximated with a single, average exponential

$$N_A(t, T_A) = \phi_{eq} \Big(g_A e^{-t/\tau_A} \Big). \tag{3.26}$$

The parameter g_A is independent from the substrate and the doping and it has been experimentally measured [77] to be:

$$g_A = (1.81 \pm 0.14) \cdot 10^{-2} \text{ cm}^{-1}. \tag{3.27}$$

The second term, N_Y, refers to the reverse annealing. This phase has a different effect on the evolution of the depletion voltage, as U_{dep} decreases for non-inverted $n-$type sensors and has a steady increase in inverted sensors. An empirical parameterization of N_Y is

$$N_Y(t, T_A) = N_{Y,\infty} \left(1 - \frac{1}{1 + \frac{t}{\tau_Y}} \right). \tag{3.28}$$

The reverse annealing has value 0 after irradiation, and saturates to the fluence-dependent value of $N_{Y,\infty}$, during the long period.

Similarly to the short annealing, $N_{Y,\infty}$ is proportional to the fluence by a parameter g_Y, which does not show dependencies on radiation type, fluence or

material:

$$g_Y = (5.16 \pm 0.09) \cdot 10^{-2} \text{ cm}^{-1}. \tag{3.29}$$

The reverse annealing has a higher impact on the depletion voltage and it is the reason why, during operations, silicon sensors are kept at temperatures below $0°C$ and, more generally, room temperature should be avoided for irradiated sensors.

Finally, N_C represents the stable damage. While the beneficial annealing can be completed in slightly more than 2 days and the reverse annealing is blocked when keeping the sensors at low temperature, the contribution from the stable damage is the most relevant in the long term operation, because it does not depend on annealing temperature or time. Literature [77] reports that oxygen-richer substrates are less prone to stable damage.

3.3.5 Trapping

Impurities as well as radiation damage can create energy levels in the centre of the forbidden energy gap. In the case a free carrier gets captured in one of these levels, it is re-emitted after a long time, of the order of milliseconds. Since typical signals in silicon are of the order of nanoseconds long, the trapped carrier does not contribute to the signal. As a result, the signal itself is degraded and the charge collection efficiency is lowered, because the ratio signal/noise is reduced.

3.3.6 Influence of the Magnetic field

If silicon sensors are operated inside a magnetic field, their charge carriers feel the effect of the Lorentz force F_L. This force is defined as the sum of forces exerted by the biasing electric field and the external magnetic field:

$$\vec{F_L} = q\vec{E} + q\vec{v} \times \vec{B}. \tag{3.30}$$

While the electric force is parallel to the electric field, the magnetic component of the force has a direction depending on the $\vec{v} \times \vec{B}$ product. Consequently, charge carriers drift along a direction at an angle, called Lorentz angle θ_L, with respect to the electric field lines [110]. Depending on the angle of incidence, the effect is a spread of the charge over a larger surface, as shown at the top of Figure 3.20. The charge spread is minimum when the incident particle crosses the sensor at the Lorentz angle (see bottom of Fig 3.20).

In 3D sensors the effect of the Lorentz angle is sensibly reduced: the value of the angle is close to 0, because the electric and the magnetic fields are coplanar [111].

Knowing the magnitude of the Lorentz angle is of fundamental importance to optimize the spatial resolution of segmented silicon detectors. This optimisation can be achieved by tuning the angular orientation of the detectors. An example is presented in Section 4.3.
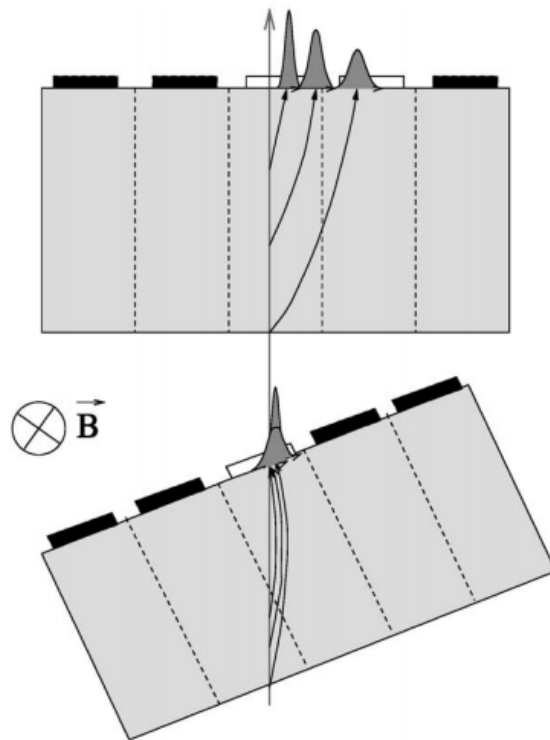
Figure 3.20: Charge carriers drifting under the influence of a magnetic field. Top: the incident particle is perpendicular to the surface of the sensor. Signal is widely spread. Bottom: the particle's incident angle is equal to the Lorentz angle: the magnetic field effect is compensated. Image reproduced from [110].

Chapter 4

The ATLAS Pixel Insertable B-Layer

This chapter describes the Insertable B-Layer (IBL) detector. After a brief introduction (Section 4.1), the motivations for its insertion are listed in Section 4.2. Sections 4.3 and 4.4 describe the new layer's layout and its expected performance, respectively. Section 4.5 is dedicated to the description of the ATLAS data flow and offline framework, preliminary information needed to discuss the byte stream converter, the tool specifically implemented to decode the information collected by the detector. This last section also describes the preliminary validation of the byte stream converter code.

4.1 The IBL

On May 2014, during the LS1, the first HEP detector instrumented with 3D sensors was inserted inside a particle physics experiment at the LHC. The Insertable B-Layer (IBL) is the new innermost layer of the ATLAS experiment. It is contributing to ensure the excellent vertexing and $b-$tagging performance of the Pixel detector during the data taking of the ATLAS experiment until the HL-LHC era.

Its construction has represented a big technological challenge. First, the IBL is only 34 mm away from the interaction point: this small radius required the development, for both the sensors and the front-end electronics, of new technologies with a radiation hardness level higher than those guaranteed by the previous generation of detectors.

Second, the space constraints of the Run I configuration did not leave enough space for the IBL insertion between the B-Layer and the Run I beam pipe (inner radius of 29 mm). For this reason, the old beam pipe was replaced with a new one characterised by a smaller diameter of 25 mm. The new clearance of 12.5 mm was enough for the IBL installation. Still, the mechanical constraints are quite tight and the IBL layout is strongly based on the available space.

Third, the IBL requirements on the material budget were very stringent: the design had to be optimised for tracking and vertexing performance, therefore its impact on the radiation length must be as small as possible. Indeed, the IBL radiation length is only 1.5% of X_0 at $z = 0$ and represents only 60% of the material budget of the B-Layer [8].

The IBL includes state-of-art technologies in all its parts: besides the front-end chips and the sensors, the light support structures are made of low density carbon foams, the cooling is provided by evaporating CO_2 cooling technology, conductors for the services are made of aluminium to limit the material budget.

Last, the mechanical design of this detector implements the possibility of an "in situ" extraction of the beam pipe: in case of a vacuum failure, in fact, the old beam pipe could not be effortlessly removed as it was installed together with the 3-layer Run I Pixel detector.

4.2 Motivation for the IBL insertion

The addition of the IBL is motivated by several strong physics and performance requirements [8]:

Tracking robustness: The performance of the Run I Pixel detector is degrading with time because of the radiation damage induced by the high sustained fluence. While the performance of the larger outer layers, L1 and L2, can be partially restored in the offline reconstruction of the data, radiation damage of the B-Layer significantly affects the resolution of the impact parameter.

The IBL provides more robust tracking capabilities, completely restoring and improving vertexing and $b-$tagging performance, even in the case of a complete failure of the B-Layer. It is designed to survive radiation damage up to $5 \cdot 10^{15} \mathrm{n_{eq}}/\mathrm{cm}^2$ NIEL and a total ionising dose of 250 Mrad.

Luminosity effects: The Run I Pixel detector was designed to cope with a peak luminosity up to $1 \cdot 10^{34}$ cm^{-2}s^{-1}, whilst, before the end of 2020, the

luminosity is foreseen to reach twice as high. This corresponds to an increase in pile-up, which determines a substantial rise in the occupancy. A high occupancy in the B-Layer leads to read-out inefficiencies, which, in turn, degrade the $b-$tagging performance.

The redundancy offered by the IBL detector, together with its low occupancy, promotes a reduction of the fake rate given by random combinations of clusters in events with high pile-up background and contributes to a good tracking performance of the ATLAS experiment despite luminosity effects.

Tracking precision: The short distance of the IBL detector to the interaction point allows for a better capability of resolving close by tracks and leads to an improvement of the impact parameter resolution, significantly contributing to the enhancement of the sensitivity in the physics channels involving the b quark, e.g. $WH \rightarrow l\nu b\bar{b}$. The impact parameter resolution is foreseen to be reduced from 100 μm to 60 μm in the z direction, and from 10 μm to 7 μm in the $r\phi$ plane. Light jet rejection, defined as the inverse of the fraction of true light-jets that are tagged as $b - jets$, is expected to improve by a factor 2 [112].

4.3 The IBL layout

A photograph of the IBL detector during the delicate phase of installation inside the ATLAS experiment is shown in Figure 4.1 [113].

In the following paragraphs, the structure of the IBL detector is described in more detail.

4.3.1 Staves and cooling

The IBL is a barrel detector formed by 14 supporting structures called staves, extending to $|\eta| < 3.0$. Full hermetic coverage in ϕ is provided by the small overlap between staves. The tilt angle of $14°$ in ϕ, almost fixed by the space constraints, was chosen to compensate for the Lorentz angle. The full coverage in the longitudinal direction is not possible, unlike the case of the Pixel detector where the modules are tilted and partially overlapping in the z direction, because the space constraints do not allow for overlap of the IBL modules in this direction.
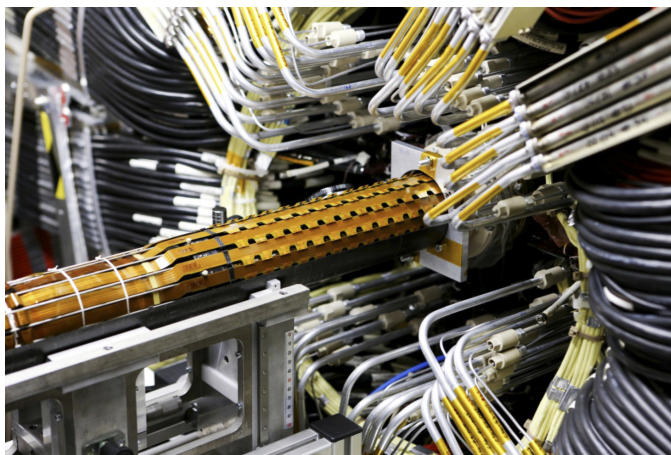
Figure 4.1: The IBL detector during the installation inside the ATLAS experiment. Image reproduced from [113].

However, the use of slim edge in the sensor technologies adopted by the IBL reduces the dead region between sensors.

Figure 4.2 shows the IBL cross sectional view and a zoom of one instrumented stave [114]. The staves are made of carbon foam, material with great heat conduction properties, and host the titanium cooling pipe in their centre, for optimising the heat removal.

The cooling is based on the evaporative CO_2 technology, studied to be more efficient in terms of mass flow and pipe size. Its design meets three goals: the minimisation of the material budget, a good pressure resistance and a good matching of the thermal expansion with the surrounding materials [115].

4.3.2 Modules, electronics and sensors

The basic unit of the IBL detector is a hybrid module, composed of a silicon sensor and a FE-I4 front-end chip. Sensor and chip are DC-coupled via bump-bonds.

Modules are mounted on the stave following the arrangement shown in Figure 4.3 [54]. The central region of the stave is instrumented with planar sensors, while both ends are equipped with 3D sensors. Two reasons motivate the choice of instrumenting the high-η regions with 3D sensors: first, the 3D technology shows a better resolution in z even after irradiation, due to the orientation of its electrodes. Second, at high-η tracks arrive at a more shallow angle (with respect to the surface of the sensor) and the inefficiencies of $90°$ tracks
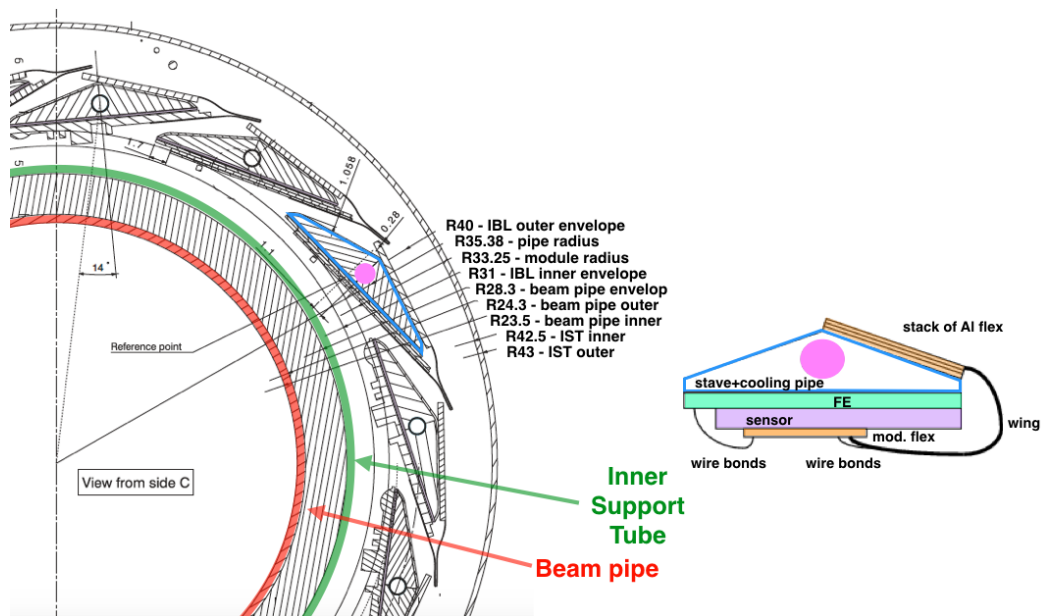
Figure 4.2: Layout of the IBL in $r\phi$ view. Left: an IBL quadrant, viewed from the ATLAS C-side. Right: Zoom of the layout of one module. Image modified from [114].

passing through the electrodes are avoided.

The two types of sensors have different areas: while the 3D sensor dimensions roughly equal the ones of a single front-end chip, planar sensors are twice as large (dimensions are reported in Figure 4.3). Planar technology has become a standard for the manufacturing of silicon sensors and can be easily produced over large surfaces with good yield; the production of 3D sensors is instead more complex and reaching good and uniform performance over large surfaces is more critical.

The front-end, after being thinned to a thickness of 150 nm, is flip-chipped to the sensors using SnAg solder bumps. Then, a double copper layer flex circuitry (module-flex) is glued onto the sensors and wire bonds are used for electrical connections between the front-end and the module flex (as shown in Figure 4.3) [54].

4.3.2.1 The FE-I4 chip

The FE-I4B (from now on called only "FE-I4", for simplicity) is the improved version of the FE-I4A, a front-end chip specifically developed as radiation-hard

85
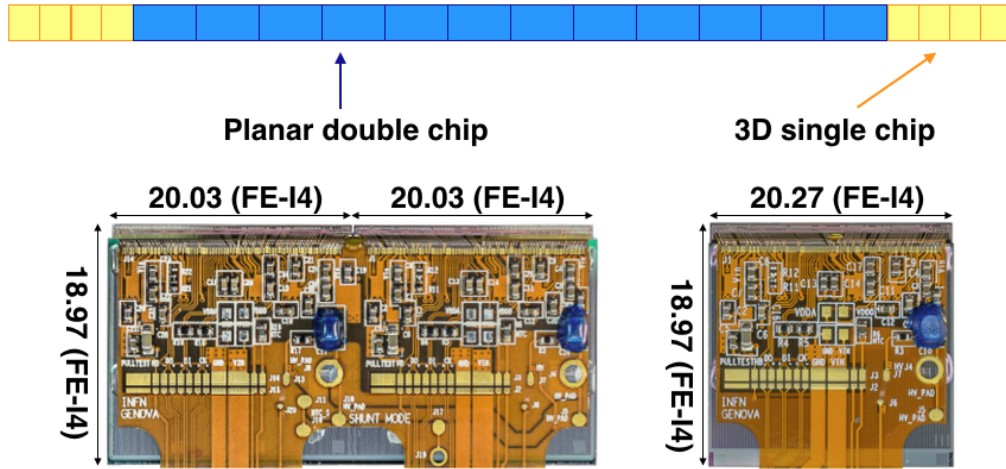
Figure 4.3: Top: Stave layout. Each stave is instrumented with double chip planar sensors in the centre and 3D single chip sensors at high η. Bottom: photos of dressed IBL two-chip (left) and single-chip (right) modules. Image reproduced from [54].

read-out chip for the ATLAS Pixel Upgrade.

The FE-I4 chip is an integrated circuit consisting of 26800 individual pixels, arranged in a matrix with 80 columns and 336 rows [116]. It features a pixel size of $250 \times 50 \, \mu\text{m}^2$. Covering a total area of $(20.03 \times 18.97) \, \text{mm}^2$, the FE-I4 chip is to date the largest chip used in High Energy Physics and is roughly four times larger than the front-end FE-I3, used in the Run I ATLAS Pixel detector [98, 117].

The chip is designed in a 130 nm IBM CMOS technology. Each individual pixel has an independent amplification stage with adjustable shaping, followed by a discriminator with independently adjustable threshold. The chip records the firing time and the Time over Threshold (ToT) with 4-bit resolution, in counts of an external clock at 40 MHz. The ToT is the period of time during which the signal is above a preset threshold level. The ToT value is proportional to the signal amplitude (the higher the signal is, the longer it stays above threshold), and it is therefore proportional to the charge collected by the pixel. The charge can be retrieved from ToT measurements using a calibration factor. The collected information can be retrieved when a trigger is provided. The data output is serial over a current-balanced pair, primary 8b/10b encoded with a rate of 160 Mb/s (the corresponding rate of the Pixel detector is 160 Mb/s using double links for the B-Layer, 80 Mb/s for Layer-1 and 40 Mb/s for Layer-2 [118]). Details of the FE-I4

architecture and functioning are reported in [116].

4.3.2.2 IBL n$^+$-in-n planar sensors

Planar sensors are built on a high-resistivity $n-$type bulk and n^+-doped read-out electrodes. The entire production of IBL double-chip planar sensors was made by CiS (Germany) on 200-μm-thick FZ wafers.

The planar technology is reliable and conservative in terms of manufacturing costs and was already adopted for the instrumentation of the Run I Pixel detector. Nevertheless, IBL planar sensors present the innovative feature of the slim edge, which reduces the inactive region from 1100 μm to only 200 μm (see Figure 4.4). This is possible thanks to the partial overlap of the 13 guard rings with the implants of the edge pixels [119].

Planar sensors have two pixel sizes: normal and long. The long pixels are implanted at the sensor' edges and in correspondence of the gap between front-end chips, to reduce inactive areas. Normal pixels populate the rest of the surface.
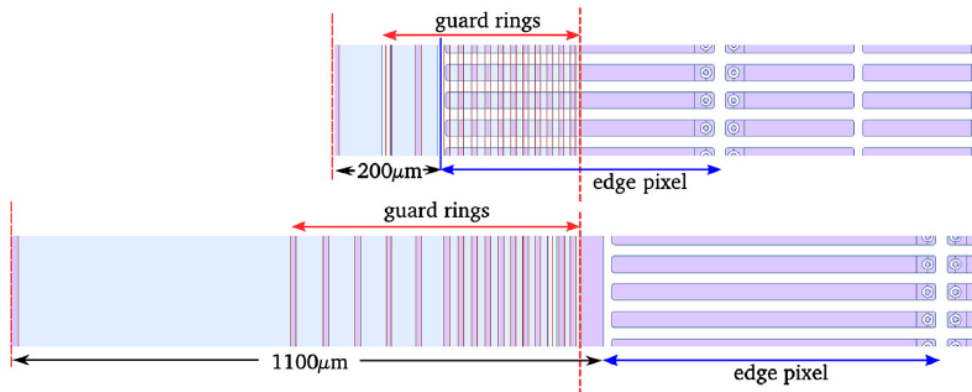
Figure 4.4: Comparison between the new IBL slim edge (top) and the Run I Pixel edge (bottom). The partial overlap between the edge pixel and the guard rings determines a reduction of the inactive area to 200 μm. Image reproduced from [119].

4.3.2.3 IBL n$^+$-in-p 3D sensors

IBL 3D sensors were developed and produced by CNM (Spain) and FBK (Italy). Their technology exploits the DDTC method. Sensors are fabricated on 230-μm-thick high-resistivity $p-$doped FZ wafers. The choice of $p-$doped

silicon material is motivated in Sections 3.2.3 and 5.1.2. The IBL 3D sensors have electrode configuration is 2E, which means that the distance between opposite sign columns, in the $250 \times 50 \ \mu m^2$ pixel cell, is $\sim 67 \ \mu m$, a good compromise between signal efficiency and capacitive noise.

The CNM design is based on a partially-through design, where columns are not etched through the entire thickness of the wafer. This structure implies that there is no need to use the isolant $p-$spray on the back-side to avoid shortcuts on the surface between the two column types. Electrodes are filled with polysilicon. Edge effects are avoided by using a n^+ doped 3D guard ring at ground potential surrounded by a fence of ohmic columns at bias voltage [119].

FBK 3D sensors have full-through electrodes and the $p-$spray is used to provide isolation on both sides. Edge effects are shielded by multiple ohmic columns, creating a guard fence.

4.4   IBL simulated performance

The IBL impact on physics has been extensively studied [8, 120, 121] by fully integrating the new detector into the ATLAS Inner Detector simulation software. Results of these simulations are presented here.

Figure 4.5 shows the expected resolution of the transversal and longitudinal track parameters as a function of $|\eta|$, for single muons at $1, 5$ and 100 GeV in the case of zero pile-up [8]. Blue and red curves show, respectively, Monte Carlo (MC) simulations run using the Run I and Run II detector layouts (without and with the IBL detector). The IBL strongly contributes to the precision of the measurement of the impact parameters, both in the transverse and longitudinal directions. The enhancement is more pronounced in the case of low energy muons. These improvements are due to the IBL reduced radius and the smaller pixel size in z (250 rather than $400 \ \mu m$).

Light jet and $c-$jet rejections as functions of the $b-$tagging efficiency are shown in Figure 4.6. Results have been obtained using multivariate algorithms (MV1c and MV2c20) that are a mixture of different $b-$tagging methods. MV1c was developed during Run I and includes the ATLAS Run I geometry (without the IBL) and reconstruction software, while MV2c20 is the new, Run II algorithm. For details on the algorithms, see [120]. To compare the Run I and Run II MC data on an equal basis, Run II distributions were re-weighted to Run I beam conditions.

The improvements included in the MV2c20 algorithm, when compared to the
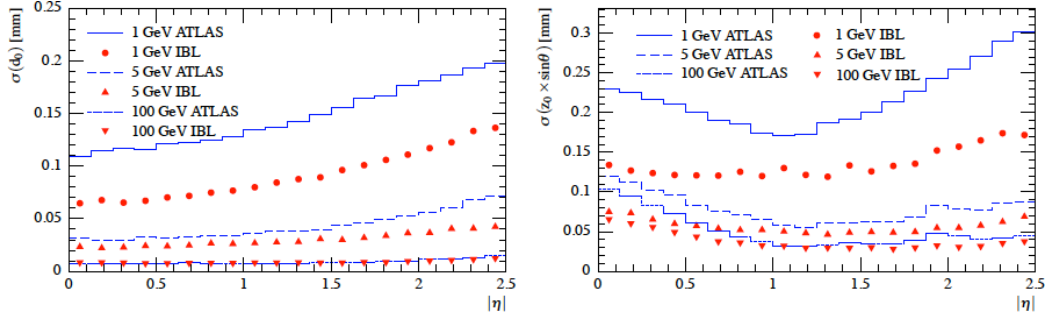
Figure 4.5: Simulation, in conditions of no pile-up, of the track parameter resolutions, for single muons at different energies, as a function of $|\eta|$. Blue curves show MC simulations in the configuration of ATLAS during Run I, without the IBL; red curves refer to the Run II detector, after the insertion of the IBL. Left: transverse impact parameter d_0. Right: longitudinal impact parameter $z_0 \sin \theta$. Image reproduced from [8].
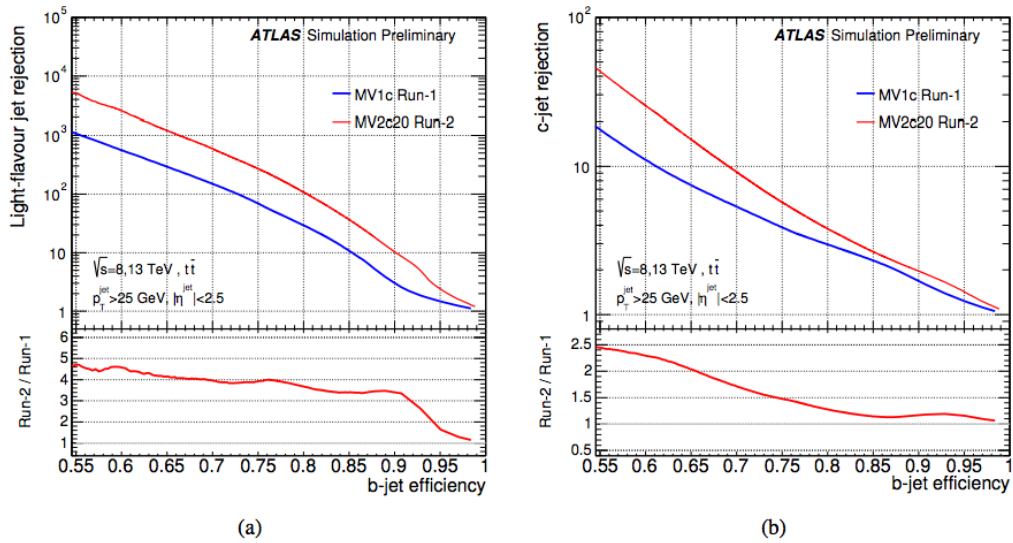
Figure 4.6: Light jet (a) and $c-$jet (b) rejection as a function of the $b-$tagging efficiency. Compared are the results between the Run I and Run II ATLAS setups. Results are obtained using $t\bar{t}$ simulated events, re-weightening the energies and the pile-up conditions to allow a direct comparison between the two Runs, and applying a combination of $b-$tagging methods. Image reproduced from [120].

previous MV1c algorithm, lead to an enhancement of the light-flavour jet rejection by a factor ~ 4 and of the $c-$jet rejection by a factor larger than 1.5 for a 70%

$b-$jet efficiency.

Figure 4.7 reports the light-jet rejection performance for a fixed 60% $b-$tagging efficiency as a function of the average number of pile-up interactions. All results are obtained by applying, on simulated $t\bar{t}$ events, a combination of two default ATLAS $b-$tagging algorithms (included in the previously-mentioned methods): the IP3D algorithm, which uses information on the impact parameter, and the SV1 algorithm, based on secondary vertex measurement.

In Figure 4.7a, the comparison is focused on different track selections depending on the pile-up conditions [121]. The performance with the IBL at an istantaneous luminosity of $2 \cdot 10^{34}$ cm^{-2}s^{-1} is better than the performance of the Run I in case of no pile-up [121].

The impact of the IBL in case of failure of the B-Layer was studied. Figure 4.7b shows the case of $b-$tagging efficiency with fully efficient or 10% failing B-Layer. As shown, the IBL not only recovers the failures, but exceeds the performance of the current detector without such failures.
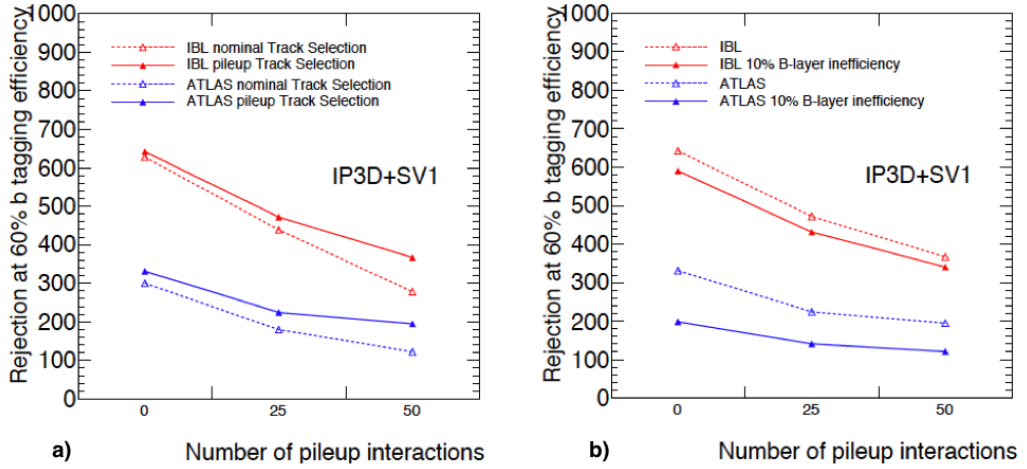
Figure 4.7: Light-jet rejection performance for a fixed 60% $b-$tagging efficiency as a function of the average number of pile-up interactions. Results are obtained by the combination of two standard $b-$tagging algorithms applied on simulated $t\bar{t}$ events. Comparisons with and without the IBL are made: (a) for different track selections; (b) in the case of a fully working or 10% inefficient B-Layer. Image reproduced from [121].

Figure 4.8 shows the light-flavour jet rejection performance as a function of p_T and $|\eta|$. A comparison between two $b-$tagging algorithms, respectively

defined using the Run I detector and reconstruction software (blue) and the Run II $b-$tagging algorithm (red), is illustrated [120]. The presence of the IBL induces a large improvement on the resolution of the impact parameter for low p_T ($5 - 10$ GeV), whilst at high jet p_T the enhancement of the light jet rejection is due to the new algorithms.

a)   **b)**
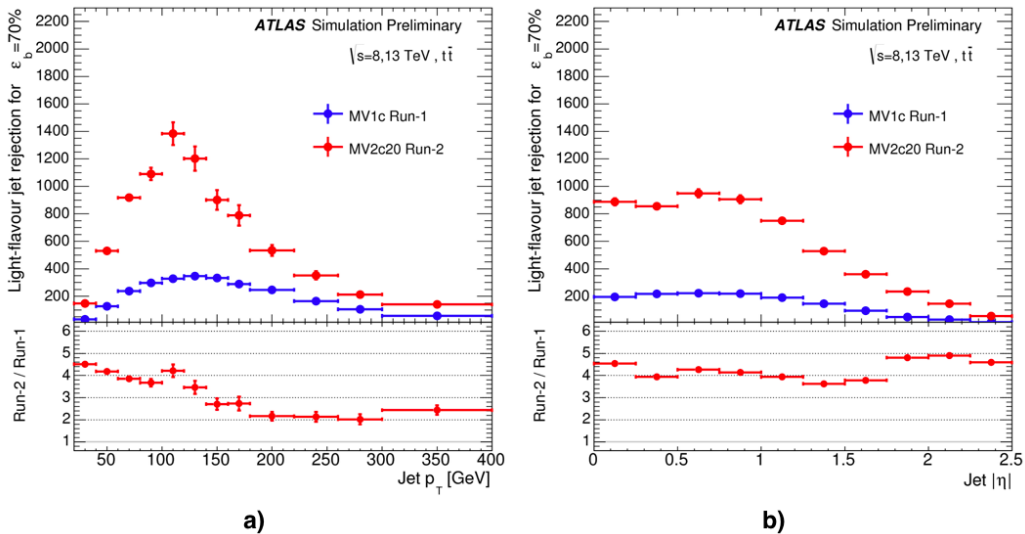
Figure 4.8: Light jet rejection performance for a fixed 70% $b-$tagging efficiency as a function of (a) the jet pT and (b) $|\eta|$. Compared are two $b-$tagging algorithms: MV1c is defined using the Run I detector and reconstruction software (blue), MV2c20 is currently used during Run II (red). Image reproduced from [120].

The IBL, featuring low mass, reduced radius and smaller pixel size, significantly improves the performance of the ATLAS Inner Detector system. This is especially true in conditions of high pile-up.

4.5   The IBL byte stream converter

The integration of the IBL inside the ATLAS experiment represented a big challenge not only from the hardware point of view, but it also required an adaptation of the software devoted to the extraction of the data from the detector and to the translation of this data into a format that is usable by the reconstruction and, later, by the analyses.

91

The IBL front-end chips collect the information on the ToT and the position of the firing pixel and, if the event has been accepted by the HLT, send this binary-formatted data to the successive steps of the ATLAS data flow (described in Section 4.5.2). The information needs to be converted into a format that reconstruction algorithms can handle to identify the cluster charge deposition and the hitting position of the crossing particle. The conversion is performed by an offline software tool, the IBL byte stream converter (BSCnv). Implemented in the ATLAS offline framework (see Section 4.5.3), the BSCnv also performs the complementary conversion, encoding the information generated in simulations of the detector into a byte stream format.

The code is also used to read out data from the DBM detector: being instrumented with the same read-out chips, the IBL and the DBM adopt the same data format.

4.5.1 Why a new converter for IBL

Several motivations drove the need to implement a new byte stream code for the IBL:

- Different pixel matrix: the Pixel detector is instrumented with FE-I3 chips featuring a pixel matrix of 160 rows $\times 18$ columns, while the IBL exploits the 336 rows $\times 80$ columns FE-I4 chip.

- New concept of modularity: in the IBL, the offline module[1] corresponds to 1 or 2 front-end chips, while in the Pixel, the "unit" is represented by the MCC, which connects 2×8 FE-I3 chips.

- Different connections between front-end chips and Read-Out Driver (ROD): as explained in Section 4.5.2, one ROD reads out all FE-I4 chips of one stave. In the Pixel detector the correspondence between ROD and MCC is 1:1.

- Different data format: the data formats of the two detectors present several dissimilarities (see Section 4.5.4.1). One of the most noticeable new features is the introduction of "condensed hit words".

---

[1]The definition of "module" depends on the functionality. From the offline point of view, a "module" is defined by the physical piece of silicon, therefore it corresponds to one FE-I4 chip for IBL 3D sensors and two FE-I4 chips for planar sensors. This choice is motivated by the fact that, in the offline reconstruction, misalignment may happen between different silicon sensors, but within the single piece of silicon, all pixels are always in the same relative position.

The new IBL byte stream converter code was implemented inside Athena, the
ATLAS Offline framework (see Section 4.5.3). It was chosen to integrate the
new code as part of the already-existing Pixel converter tool with the intent of
considering the IBL as the fourth layer of the Run II ATLAS Pixel detector.

4.5.2 The ATLAS data flow

The ATLAS Data flow is responsible for receiving the detector data, serving a
subset of data to the HLT, and transporting the selected data to the mass storage.

Data collected by the ATLAS subdetectors are, in first place, temporarily
buffered inside the front-end pipeline memories of each subdetector. When the
front-ends receive a L1A (see Section 2.4.6), they transmit the data through the
Back-of-Card (BOC) to the RODs. RODs sort data associated with a bunch
crossing in formatted event fragments before sending it, via the Read-Out Links
(ROLs), to the Read-Out Buffers (ROBs). The ROD also transmits control
commands, such as level1-reset and the charge calibrations, to the front-ends.
From the ROBs, a subset of data is sent to the HLT/DAQ system for the second
selection stage. If the event passes the HLT criteria, the data is transferred to mass
storage and offline reconstruction is performed on it.

RODs, coupled to the BOC cards, represent the first off-detector components
of the Data flow chain. ROLs are responsible for transmitting error-free data.
They are based on the S-Link protocol, which has been accepted as the ATLAS
standard for communication between RODs and ROBs. ROBs are grouped in 4-
6 units into a ROBIN and a Read-Out System (ROS) contains multiple ROBIN
cards.

As described in Section 2.4.2.2, the Pixel detector's front-end chips are
connected, in group of 16, to an MCC and each MCC is connected, through an
Optoboard, to one ROD/BOC. In the case of the IBL, instead, the front-ends are
directly linked to the Optoboards.

The IBL data flow is sketched in Figure 4.9. Red arrows indicate the direction
of data, while blue ones refer to the route of commands. All 32 FE-I4 chips
of one stave are read out by one ROD, via 2 Optoboards. Each Optoboard has
two VCSEL[2] transmitters and one DORIC[3] receiver. Each VCSEL receives data
from 8 FE-I4 chips and forwards it to the ROD-BOC, while the DORIC transmits

---

[2]VCSEL = Vertical Cavity Surface Emitting Laser.
[3]DORIC = Digital Opto-Receiver Integrated Circuit.

commands to 8 pairs of front-ends (one pair of FE-I4 chips is one DAQ module[4]). The BOC hosts 4 receivers (Rx) and 2 transmitters (Tx). The BOC sends back the elaborated data to the ROD that redirects it, via the ROL, to the ROB [122]. The choice of instrumenting the BOC, rather than the ROD, with the S-Link is motivated by the higher BOC data transfer speed.
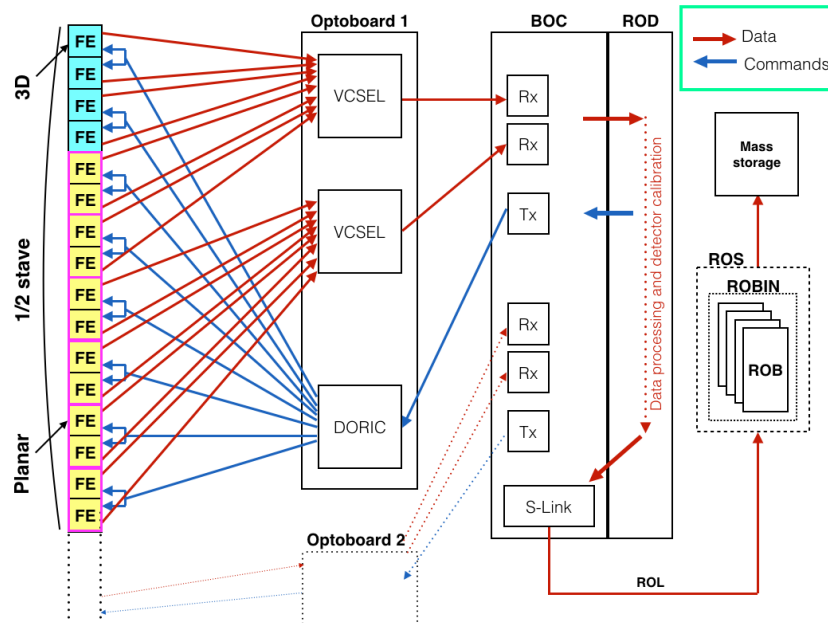
Figure 4.9: The IBL data flow. Data pass from the front-end chips to the optoboards to the ROD-BOC and eventually to the mass storage. Commands instead are transmitted from the ROD to the front-end chips.

4.5.3 The Athena framework

Athena is the offline control framework used by the ATLAS Collaboration. It is a concrete implementation of an underlying architecture, GAUDI, originally developed by LHCb. Nowadays, GAUDI represents the kernel of software common to both experiments and co-developed, while Athena, based on this kernel, adds ATLAS-specific features [123].

Athena provides flexible and easy-to-use software for implementing event simulation, reconstruction and visualisation, as well as tools for easing the writing

---

[4]From the DAQ point of view, a "module" is the hybrid structure formed by the sensor and the front-end chip.

of analysis programs. Its underlying structure serves to isolate the final users from irrelevant technicalities such as, for example, the software libraries used for data input/output. Athena includes specifications of a number of components and their mutual interactions: a component is a block of software that has defined interface and functionality (the interface is a collection of methods and the description of their purposes, also called functionalities). The Athena framework is developed by adding new functionalities while leaving the interface unchanged.

4.5.4 The byte stream format

Event fragments coming from the different ATLAS detectors must have the same structure: information read out from the detector (after the trigger) is enclosed by headers and trailers in raw data event format. These are sent as a single stream of bytes, called byte stream (BS).

The structure of a full event fragment, shown in Figure 4.10, has a "multi-shell" shape: each event fragment contains multiple sub-detector fragments, each of which collects various ROS fragments. Each ROS fragment collects many ROB fragments, each of which contains only one ROD fragment (according to the correspondence 1:1 between ROD and ROB). Each ROD contains several module fragments. The header of each part of the chain contains information for event formatting and clarifies which part of the acquisition chain sent the fragment.
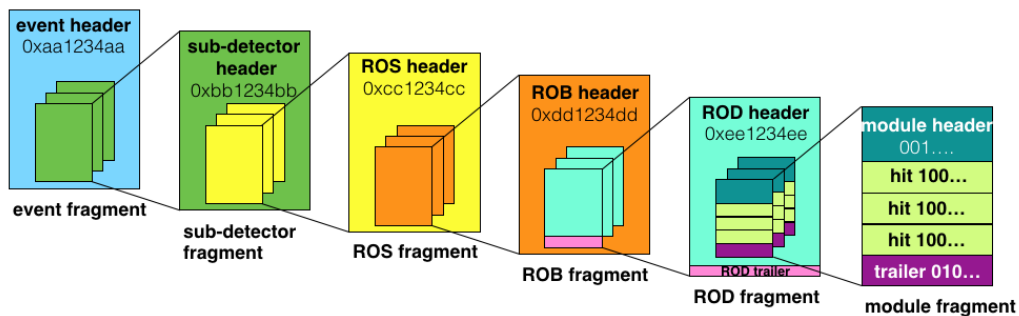
Figure 4.10: The ATLAS Raw data and byte stream. Image modified from [124].

In the following, a more detailed description of the ROD and module sections of the byte stream for the Pixel detector is presented, as they are the most relevant parts of the data format for the purpose of the performed task.

The byte stream is a sequence of 32-bit words. The ROD byte stream data format is presented in Table 4.1. The ROD byte stream is enclosed by the

'Beginning of Fragment' (BoF) and the 'End of Fragment' words, respectively at the beginning and at the end of the fragment, which are composed of a fixed marker header in the 16 MSBs[5] and of a S-Link status word in the LSBs[6], defined by the S-Link communication towards the ROB.

'Beginning of Fragment' marker	'0xB0F0' + S-Link flags
Start of ROD header	'0xEE1234EE'
Header size	'0x9'
Format version number	0x03010000'
Source identifier	'0xrrssRRRS'
Run number	'0' + 31-bin run number
Extended LVL1 ID	24-bit TTCrx LVL1ID + 8-bit ROD ECRID
Bunch crossing ID (BCID)	12-bit TTCrx BCID
ATLAS LVL1 trigger type	8-bit CTP(LTP) L1TT
Detector event type (ROD/TIM)	DET
Module data	(...)
Status 1: bit errors	error flags
Status 2: count of words with errors	error count, ROL status
Number of status words	'0x2'
Number of data words	nData
Status block pos.: '0' before/'1' after data	'0x1'
'End Of Fragment' marker	'0xE0F0' + S-Link flags

Table 4.1: Structure of the ROD byte stream [124]. The columns indicate the bit composition (right) and their meaning (left). Symbols of the Source ID correspond to: 'r' = reserved, 's' = sub-detector ID (0x11 for L1 and L2, 0x12 for discs, 0x13 for B-Layer, 0x14 for IBL, 0x15 for DBM), 'R' = ROD Identifier, 'S' = S-Link Identifier (0x0 to 0x3).

After the BoF, the ROD fragment contains the header marker and collects a few words required to identify the ROD (the source Identifier, called sourceID) and tag the triggered event (run number, extended L1ID, Bunch-crossing ID and LVL1 trigger type and detector event type).

The ROD header is followed by fragments of all modules connected to the particular ROD. In the IBL case, there are 8 module fragments, sent by each of the 8 FE-I4 chips connected to the same ROD-BOC Rx.

---

[5]MSB = Most Significant Bit.
[6]LSB = Least Significant Bit.

The ROD fragment ends with the ROD trailer, which consists of a sequence of words to transmit the errors and other information of summary. When the ROB receives the ROD byte stream, it cuts out the ROL markers, but keeps the information of the status flags of the ROD trailer.

4.5.4.1 The Pixel and IBL byte stream formats

A module byte stream consists of a header word that identifies which module is sending the fragment, the hit words, an error flag word (if any) and the module trailer word.

The byte stream formats for the Pixel and the IBL detectors are shown in Table 4.2 and the meaning of each bit is listed in Table 4.3. In both byte stream formats, the first 3 MSBs identify and distinguish the different module byte stream words (underlined in Table 4.2). Header, hit, error flag and trailer words start respectively with `001`, `100`, `000` and `010`.

The IBL byte stream format is illustrated in the following. As the Pixel byte stream format is described in detail in [124], only major differences with respect to the IBL byte stream will be highlighted.

The IBL needs 5 bits (the `n` bits in the byte stream format of Table 4.2, named "link number") to uniquely identify the module: the 2 MSBs refer to the ROD-BOC Rx number (with range from 0 to 3, on a single stave), while the 3 LSBs, running from 0x0 to 0x7, identify the "FE index", the FE-I4 chip connected to the ROD-BOC Rx (1 out of 8 FE-I4 chips). The ROD-BOC Rx number bits are redundant with respect to the ROD header (the 2 LSBs of the sourceID, see Table 4.1). Moreover, the 5 link number bits are redundant within the IBL byte stream over the header, hit, flag and trailer words.

The IBL header contains information on the link number, Bunch Crossing Identifier (BCID), the LVL1 Accept Identifier (L1ID). The BCID is a number that defines the bunch crossing at which an event occurred; valid BCID numbers are 0 to 3563 per LHC orbit. The L1ID, together with the BCID information, uniquely identifies an event within a small time frame (~ 1 s) [125, 126].

Hit words include the information on the coordinates (column/row) of the pixel that has fired and on the charge the pixel has collected, expressed in terms of Time over Threshold (ToT).

Pixel and IBL hit words show several differences:

- Pixel hit words also need to specify which of the 16 FE-I3s over the MCC is transmitting the hit, while the connection between ROD-BOC Rx and IBL

97

	Pixel	IBL
Header	`001PtlbxxnnnnnnnnvvvvLLLLBBBBBBBB`	`001nnnnnfLLLLLLLLLLLLLLBBBBBBBBBB`
Hit	`100xFFFFTTTTTTTTxxxCCCCCRRRRRRRR`	`100nnnnn(TTTT)`$_a$`(TTTT)`$_b$`CCCCCCCRRRRRRRRR`
Condensed Hits		`101RRRRR(TTTT)`$_{1a}$`(TTTT)`$_{1b}$`CCCCCCCRRRRRRRRR`
		`1CCCRRRRRRRRR(TTTT)`$_{2a}$`(TTTT)`$_{2b}$`CCCCCCCRRRR`
		`1(TTT)`$_{4b}$`CCCCCCCRRRRRRRRR(TTTT)`$_{3a}$`(TTTT)`$_{3b}$`CCCC`
		`111(TTTT)`$_{5a}$`(TTTT)`$_{5b}$`CCCCCCCRRRRRRRRR(TTTT)`$_{4a}$`(T)`
FE Flag Error	`0001FFFFxxx11111eeeeeeeeEEEEEEEE`	`000nnnnnxssssssxxxxxxxSSSSSSSSSS`
Raw Data	`011DDDDDDDDDDDDDDDDDDDDDDDDDDDDD`	`011DDDDDDDDDDDDDDDDDDDDDDDDDDDDD`
Trailer	`010ZHVxxxxxxxxxxxxxxxxxxxxxxxxx`	`010nnnnntCKPleeeerrrrrrrrrxxxxx`

Table 4.2: Byte stream formats for the Pixel and the IBL detectors. The code convention is listed in Table 4.3.

	Pixel				IBL		
P	Preamble Error	t	Time out error	n	link number	f	IBL FE-I4 flag bit skip
l/b	L1ID/BCID error	n	link number	L	L1ID	B	BCID
v	L1ID skip	L	L1ID	T	Time over Threshold	C	Pixel Column
B	BCID	F	FE Number	R	Pixel row	s	Service code
T	Time over Threshold	C	Pixel Column	S	Service code counter	D	raw data
R	Pixel Row	e	MCC Error Code	t	Time out error	C	condensed mode
E	FE Error Code	D	Raw Data	K	Link masked	P	Preamble error
Z	trailer bit error	H	Header Trailer Limit Error	l	L1ID skip	e	Trailer errors
V	Data Overflow Error	x	unused bit (set to 0)	r	Skipped triggers	x	unused bit (set to 0)

Table 4.3: Alphanumeric code convention of the variables of Table 4.2.

modules is 1:1.

- Column and row numbers differ for the two detectors: in the FE-I4 chip, unlike the Pixel front-end, the numbering of rows and columns starts at 1 and not zero.

- The number of bits dedicated to the ToT in each hit word: Pixel modules send a 8-bit ToT information, while the ToT resolution for IBL only relies on 4 bits. One IBL hit word, nevertheless, accomodates 8 bits for the ToT information, because it collects the information on ToTs of two neighbouring pixels (pixels that belong to the same column and have consecutive row numbers): the 4 MSBs refer to the hit sent by the pixel with local coordinates (column, row), the 4 LSBs are the ToT collected by the pixel with coordinates (column, row+1). This mechanism is called "dynamic phi-pairing". In the case the second pixel has no hit, a default "no-hit" value is hosted in the 4 bits.

- The presence of the so-called "condensed" hit words is exclusive of the IBL byte stream format. This new format optimises the bit transfer: if 5 (or more) pixels have fired from one FE-I4 chip, the chip itself compacts the 5 hit information into 4 words. Therefore, if taking into account the dynamic phi-pairing mechanism, 4 IBL condensed hit words can overall stream hit information on up to 10 pixels.

The front-end flag word includes service code bits and their counter. The meaning of each bit is specified in [116].

The trailer lists some flag bits that can be raised both because of an error, such as the time-out error (indicating that a link has not received data within an adjustable time-out period), or because, for example, of the presence of condensed hit words in the stream.

4.5.5   The byte stream converter

The stream of bytes coming from the IBL must be converted into a format that can be used by the offline data analysis to identify space points by ToT calibration and hit clustering. This task is performed by the byte stream converter (BSCnv), a collection of Athena packages that decodes the uncalibrated detector raw data from ROD fragments into transient Raw Data Objects (RDOs), the C++ object representation of the byte stream information [127].

RDOs are defined by an Athena class in the `InnerDetector/InDet-RawEvent/InDetRawData` package. They contain information, for each hit, on the pixel identifier (pixelID), a 32-bit object that uniquely identifies the pixel (by containing all position information concerning the pixel, from the barrel/end-cap position to the η- and ϕ-indexes of the pixel with respect to the offline module). RDOs also include another 32-bit word that accomodates information on the ToT, the BCID, the L1ID and the L1A.

The `InnerDetector/InDetEventCnv/PixelRawDataByteStreamCnv` is the package responsible for the conversion of the Pixel and IBL byte streams. It is implemented as an Athena Tool package and is automatically called when an algorithm asks for the data of the particular Pixel detector element. This package includes both the decoder (`PixelRodDecoder` class) and the encoder (`PixelRodEncoder` class): the first one performs the conversion between raw detector data into RDOs, while the latter takes care of converting (simulated) RDOs into raw byte stream.

The `PixelRawDataByteStreamCnv` package makes use of many service functions contained in another Athena package, the `InnerDetector/InDet-DetDescr/PixelCabling`.

4.5.5.1 The IBL bytestream decoder

Three classes of the `PixelRawDataByteStreamCnv` package are involved in the decoding process: `PixelRawDataProvider`, `PixelRawDataProviderTool` and `PixelRodDecoder`. The first class creates the output container (`PixelRDO_Container`), gets the list of ROBs from the `PixelCabling`, and retrieves input data (in form of ROB fragments) from the ROBDataProvider. It calls the function `PixelRawDataProviderTool::convert()`. This function loops over the ROB fragments and, at each cycle, calls `PixelRodDecoder::fillCollection()`.

The `PixelRodDecoder::fillCollection()` function, while looping over the 32-bit data words, unpacks the information contained in the words according to the byte stream format previously described.

Information is extracted from each word by masking and shifting the bits of the word. As an example, to extract the information on the L1ID in the header, one has to apply the following "formula" (using hexadecimal and binary notations):

```
Header word:    001nnnnnfLLLLLLLLLLLLLBBBBBBBBBB
L1ID = (Header word >> 10) & 0x1FFF
```

meaning that the header bits are shifted towards right by 10 bits (effectively removing the 10 LSBs) and then a mask of 13 1s (0x1FFF) is applied to isolate the L bits (effectively removing the 9 MSBs).

First of all, when receiving a new word, the decoder controls if the order of the words is respected: within an event fragment, the header has always to be the first word, the trailer is the last one and hit words may be present between header and trailer. If the order is not respected, a warning is sent to the Athena message service.

Processing the header word, the decoder identifies the event number (unpacking L1ID and BCID) and the specific front-end chip that is transmitting the module fragment. The link number bits (the 5 n bits in the data format) are cross-checked all across the module fragment, for consistency. If these bits vary within one module fragment, a warning message is sent. Then the decoder proceeds to convert the hit word(s), first unpacking condensed hit words (if present) and then the non-condensed ones.

Condensed words are unpacked as shown in Figure 4.11:

a. They are saved into an array of `uint32_t` called `condensedWords[4]`. The five hit information (ToT, column and row of the hit) are encapsulated into these `condensedWords`, (in Figure 4.11a each hit information is written in a different colour). As an example, the second hit, in blue, is retrieved by doing:

```
hitwords[1] = ((condensedWords[0] >> 24) & 0x1F) +
                 ((condensedWords[1] & 0x7FFFF) << 5),
```

meaning that `condensedWords[0]` is shifted right by 24 bits and only 5 bits are taken (thus isolating the RRRRR bits) and from the `condensedWords[1]` the 19 LSBs are extracted and shifted to the left by 5 (to accommodate the RRRRR bits as LSBs).

b. The bits used to identify the words (101, 1, 1, 111, respectively identifying the first to fourth condensed hit words) are removed from the `condensedWords` and these words are divided into an array of `hitwords[5]`, each element containing information about one hit.

101

c. Each `hitwords[i]` is decoded to extract the ToT (8 bits), the column and row; the 8-bit ToT is decoded to identify potential double hits in row-neighbouring pixels, according to the dynamic phi-pairing (see 4.5.4.1).

d. The RDO collection is filled with all the hits extracted from the condensed words.

FE flag words are decoded according to the format specified in Table 4.2. The trailer word concludes the module fragment, each bit reporting the presence of an error (if the bit is set to 1) to the message service.


```
a)  condensedWords[0] = 101RRRRRTTTTTTTTCCCCCCCRRRRRRRRR
    condensedWords[1] = 1CCCRRRRRRRRRTTTTTTTTCCCCCCCRRRR
    condensedWords[2] = 1TTTCCCCCCCRRRRRRRRRTTTTTTTTCCCC
    condensedWords[3] = 111TTTTTTTTCCCCCCCRRRRRRRRRTTTTT

b)  hitwords[0] = TTTTTTTTCCCCCCCRRRRRRRRR
    hitwords[1] = TTTTTTTTCCCCCCCRRRRRRRRR
    hitwords[2] = TTTTTTTTCCCCCCCRRRRRRRRR
    hitwords[3] = TTTTTTTTCCCCCCCRRRRRRRRR
    hitwords[4] = TTTTTTTTCCCCCCCRRRRRRRRR
```

$$
\text{c)} \quad \text{hitwords[i]} = \begin{cases} \text{tot[i]} = \text{TTTTTTTT} = (\text{TTTT})_1(\text{TTTT})_2 \\ \text{col[i]} = \text{CCCCCCC} \\ \text{row[i]} = \text{RRRRRRRRR} \end{cases}
$$

```
d)  hit[i,1] = ((TTTT)₁, col[i], row[i])
    hit[i,2] = ((TTTT)₂, col[i], row[i]+1)
```

Figure 4.11: Treatment of the IBL condensed hit words in the `PixelRod-Decoder`. For further explanation, see text.

4.5.5.2 The IBL byte stream encoder

While the decoder extracts the event information from the byte stream, the `PixelRodEncoder` performs the conversion of ATLAS-formatted data (RDOs) into simulated byte stream.

The encoding part of the `PixelRawDataByteStreamCnv` package is composed by three classes: the `PixelRawContByteStreamCnv`, `Pixel-RawDataByteStreamCnvTool` and `PixelRodEncoder`. The first class

accesses the `PixelRDO_Container` and calls the `convert()` function of the `PixelRawDataByteStreamCnvTool` class. This function creates an instance of `PixelRodEncoder` class for each ROD-BOC Rx and calls the `PixelRodEncoder`'s main function, `PixelRodEncoder::fillRod()`.

The implementation of the `PixelRodEncoder` was performed keeping separated the Pixel and the IBL conversion. The information required to compose the words is extracted from the RDOs, by exploiting several `PixelCabling` functions. Then, words are built following the detector-specific data format. In the IBL case, the construction of the condensed words occurs after the identification and the ordering, within a single event, of all the RDOs from the same front-end.

4.5.5.3   The `PixelCabling` package

The `PixelCabling` package contains several service functions used by the converter package and is responsible for the mapping of the physical position of each module inside ATLAS to values related to the read-out of each module. An offline identifier (offlineID) can be created from the physical position, while an online identifier (onlineID) is built from the read-out related values. These two identifiers are unique for each offline module.

The offlineID is used, in the decoder, to index a new RDO collection and to retrieve the pixelID, by combining the offlineID with the FE number[7] and the pixel row/column coordinates. In this way, the hit position included in the RDOs refers to the unique coordinates of the pixel within the whole ATLAS experiment.

When initialised, the `PixelCabling` package fills, from a text configuration file, several C++ std::maps that associate, for example, module onlineID to module offlineID, ROBID to RODID, offlineID to ROBID, etc. These associations are extracted from static connectivity maps, included in the package, or from the data acquisition connectivity database. The static connectivity maps are text files that define, for each offline module, the association between the module identifier and its physical location. These files are structured as a table, filled with information described in Table 4.4.

---

[7]The "FE number" is the front-end number within the offline module. In IBL, FE = {0,1} for planar sensors and FE = 0 for 3D sensors. In the Pixel detector, it is in the range {0, 15}.

Variable	Meaning	IBL	Pixel	DBM
Position parameters				
Barrel_EC	barrel or endcap layer	0	0 for barrel, ±2 for discs	±4
Layer_disc	layer/disc number	0 (Run II cfg.)	1 to 3 (used to be 0 to 2 in Run I cfg.)	0 to 2
Phi_module	module number in ϕ direction	0 to 13	0 to 51	0 to 3
Eta_module	module number in η direction	-10 to 9	-6 to 6	0
ROBID	ROB identifier	ROBID = 0xDDRRRL (DD = 0x14, RRR = FE index, L = BOC-ROD Rx)	ROBID = 0xDDRRRR (DD = 0x11 to 0x13, RRRR = MCC identifier)	like IBL
RODID	ROD identifier	RODID = 0xDDRRR0 (DD = 0x14, RRR = FE index)	RODID = ROBID	like IBL
Link and formatter (FMT)				

40Link/80Link and 40FMT/80FMT	• For the IBL and the DBM, the 40/80Link column values reflect the number of the front-end chip with respect to the single ROD-BOC Rx:
	  – module = 3D sensor: 40Link = $[0, 7]$ and 80Link = 0xF (null value);
	  – module = planar sensor: both 40Link and 80Link have value $[0, 7]$ (increasing along η).
	 40/80FMT = 0;
	 • For Pixels, the n bits of the module header are related to the Link and FMT values: FMT $<<$ 4
		Link. The read-out speed stored in the conditions database is used to decide whether to use the 40MBit or the 80MBit columns.			

Geographical ID	string containing the module name			

Table 4.4: Information contained in the connectivity map files.

4.5.6 Code validation

The IBL byte stream converter was implemented during the physical construction of the IBL detector. For this reason, preliminary validation tests were performed using Monte Carlo (MC) simulated data (RDOs) or byte stream data produced by single front-ends or single staves during tests performed over a subpart of the detector. Real data coming from the entire detector were only available after the installation of the new detector inside the ATLAS experiment, when the commissioning of the IBL started.

4.5.6.1 Preliminary validation

Results shown in this paragraph were obtained during the course of the code validation process, and have to be considered as preliminary. Output text messages were temporarily added to the code (both in the `PixelRodDecoder` and in the `PixelRodEncoder` classes) in order to simply extract and analyse the relevant information, such as coordinates and ToT for each hit.

The validation process consisted of taking simulated RDOs, transforming them into simulated byte stream running the encoder, running the decoder to re-obtain the RDOs (closing a cycle) and, in the end, comparing the hit information used as input of the encoder with the hit information returned by the decoder.

Figures 4.12a and 4.12b are 2D maps showing the distribution, for respectively the encoder's input and the decoder's output, of the ToT-weighted hits across the IBL modules, adopting the phi- eta-index coordinate system of a module, hence "overlapping" all the IBL modules (single- and double chips). The left side of the top maps is more populated than the right side simply because more modules are overlapped: planar sensors cover the area of 2 FE-I4 chips, their eta-index extends to 160, while 3D sensors are single chip (thus eta-index ≤ 80).

The difference between the two maps is shown in Figure 4.12c. A value equal to 0 over the entire map would mean that the encoder input equals the decoder output, namely input RDOs equal output RDOs.

The preliminary result of Figure 4.12c indicates a small ToT unbalance was found in 2 pixels, as more visibly shown in Figure 4.12d. Although this difference is indication of a small bug in the code, it should be stressed that these results are not definitive and were obtained at the end of 2014. My involvement in the task was considered complete and further validation steps and developments were handed over to other members of the ATLAS Pixel Offline group. Moreover, it is no longer possible to perform such simple analysis with the new data and the new

byte stream converter code because the output messages from which information was extracted have been removed for cleaning the code (and more sophisticated validation tools should be used).
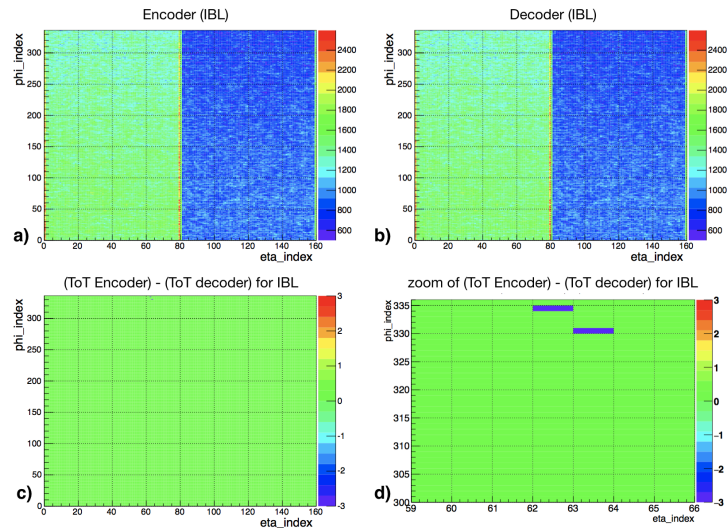

Figure 4.12: Preliminary validation of byte stream converter of the IBL detector. (a) Map filled with IBL ToT-weighted hits extracted from the input of the encoder; (b) Map filled with IBL ToT-weighted hits extracted from the output of the decoder; (c) Difference between the entries in the encoder and the decoder maps; (d) Zoom of (c), to better visualise the two pixels presenting unbalanced ToTs.

For reference, the same maps were produced for Pixel hits: Figures 4.13a and 4.13b show the distribution of the ToT-weighted hit simulated in Pixel modules (MCC), while 4.13c shows the difference between the ToT hits of corresponding pixels. The absence of entries in the latter image is representative of the fact that between the input of the encoder and the output of the decoder there is no discrepancy.

Figure 4.14 shows the distribution of the number of hits in the Run II Pixel detector, obtained from simulated data following the prescriptions of the ATLAS Trigger group. The code runs the encoder, followed by the trigger code, during which the decoder gets called. As expected, the mean value of the distribution is 4, corresponding to the number of layers of the Run II Pixel detector (IBL + 3 Pixel layers).
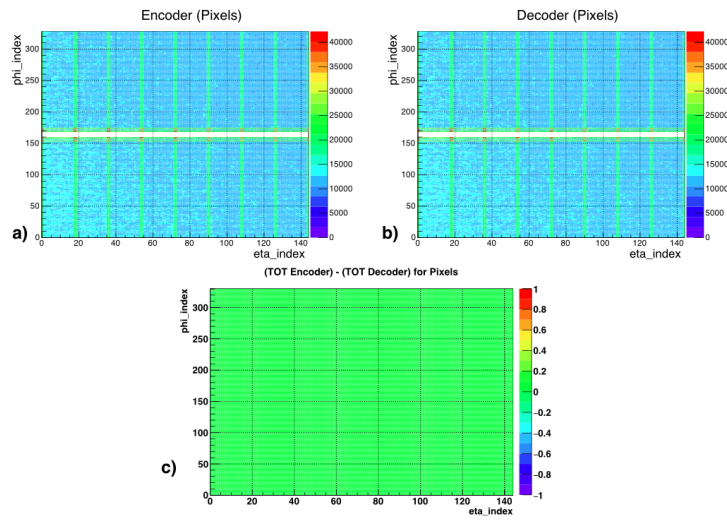
Figure 4.13: Reference BSCnv validation for the Pixel detector. (a) Map filled with Pixel ToT-weighted hits extracted from the input of the encoder; (b) Map filled with Pixel ToT-weighted hits extracted from the output of the decoder; (c) Difference between the encoder and the decoder maps. The absence of entries shows that there is no discrepancy between the encoder input and the decoder output for Pixels.

Figure 4.14: Distribution of the number of hits in the Run II Pixel detector, obtained by simulating single track particles in conditions of no pile-up. The mean value is 4, corresponding to the 4 layers of IBL + Pixel barrel.

4.5.6.2 The first cosmic data with IBL

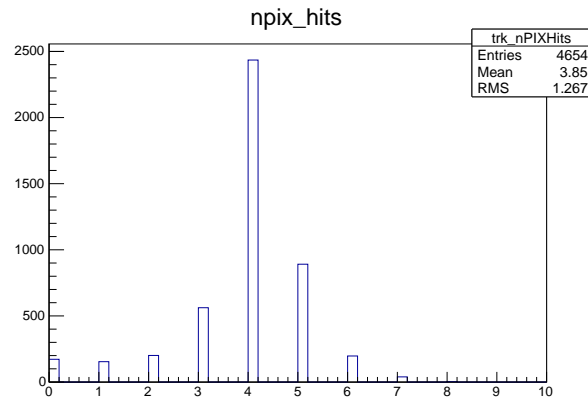The first event display showing the hits coming from the IBL detector and reconstructed as a muon cosmic ray is shown in Figure 4.15 [128]. It was collected on 26 November 2014, during one of the milestone runs aimed at the re-commissioning of the ATLAS experiment in preparation for Run II.

This image is meaningful for several reasons: it shows that the IBL is up and running, and it is able to collect data within the whole ATLAS data acquisition system; the detector is well-aligned; the track-finding and reconstruction algorithms correctly integrate the new detector. The hit points used by the offline reconstructions were extracted from the IBL byte stream using the decoder code: this event display, therefore, is an indication of the correct implementation of this new software tool.
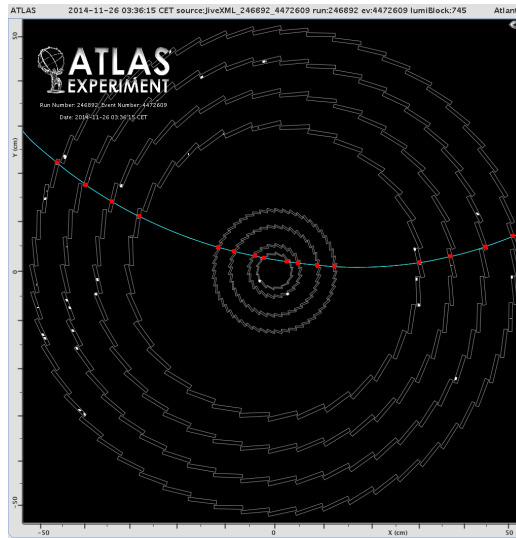
Figure 4.15: Event display of a muon cosmic ray crossing the ATLAS Pixel detector, recorded on 26 November 2014. From the innermost layer to the outermost, the IBL, the three Pixel layers and the four double-SCT layers are represented in white. The crossing muon's reconstructed track is drawn in green. White dots represents all hits recorded in each layer, while red dots are the hits used for reconstructing the muon track. Image reproduced from [128].

The IBL proved to be ready for Run II data taking: Figure 4.16 shows a reconstructed event display of a proton-proton collision recorded by ATLAS on 3 June 2015, when the LHC first declared stable beam at $\sqrt{s} = 13$ TeV. The left view is the cross sectional view and the bottom-right view is the longitudinal

zoomed view. Light blue lines represent reconstructed particle tracks, while coloured filled circles are the hits recorded by the silicon tracking layers. In this event, 17 collision vertices have been reconstructed [129].
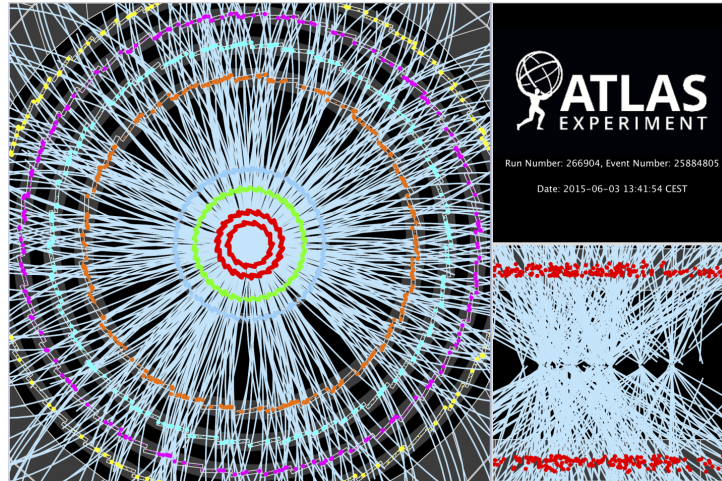
Figure 4.16: Event display of a proton-proton collision recorded by ATLAS on 3 June 2015, when the LHC first declared stable beam at $\sqrt{s} = 13$ TeV. Reconstructed tracks are light blue lines, and hits in the silicon tracking layers are shown as coloured filled circles. In the view in the bottom right, it is shown that the event is characterised by multiple pp collisions, with 17 (not all visible in the picture) collision vertices. Image reproduced from [129].

Chapter 5

Experimental methods

The work described in this thesis focused on the characterisation of 3D silicon sensors produced at SINTEF for the ATLAS upgrade for the HL-LHC phase (see Section 2.3.2). The tested sensors were fabricated during the third prototype run, which presented a low yield at wafer level: most of the samples showed, in preliminary measurements, high values of leakage current and low breakdown voltages. These characteristics point to production issues, which were not known when the measurement campaign described in this thesis took place. The objectives of the measurements presented here, therefore, are the identification of the origin of such problems and the evaluation of the key properties of these sensors.

Electrical, laser and radioactive source characterisations are three experimental techniques employed to measure properties such as depletion and breakdown voltages, junction capacitance and charge collection. These properties were assessed also as a function of the radiation fluence: sensors were irradiated to several fluences up to values similar to the one expected for the innermost layers of the LHC experiments after 10 years of operations at the HL-LHC.

In the laboratories of the CERN Solid State Detectors (SSD) group[1], three experimental setups allow for these types of measurements. In particular, preliminary characterisation of the electrical properties of the sensors can be performed with the IVCV setup, the laser characterisation is done using the TCT+ setup, and the charge collection can be measured employing the ALiBaVa read-out system.

---

[1]The SSD group belongs to the Experimental Physics - Detector Technologies - Detector Development (EP-DT-DD in short) section of the CERN organisation.

This chapter is divided into two parts: the first (Sections 5.1 and 5.2) is dedicated to the presentation of the SINTEF 3D sensors, whose experimental results are reported in Chapter 6, and the irradiation campaigns they underwent. The second part (Sections 5.3 to 5.5) describes the three experimental setups.

5.1 SINTEF 3D silicon sensors

The 3D technology was originally proposed by S. I. Parker and was successfully fabricated for the first time in 1997 [9]. His idea was developed by C. J. Kenney [130], who introduced the concept of active edge to reduce the dead material close to the edges. Full-3D silicon sensors (see Section 3.2.3.2) have been fabricated at Stanford Nanofabrication Facility (SNF) since 2001. In 2006 the 3D Consortium (3DC) was formed among the University of Manchester, the University of Hawaii, the University of Oslo and SINTEF, with the aim of transferring the technology to an industrial setting for a large-scale, automatised production [131]. The collaboration later widened to include the SNF, the University of Prague and the University of Purdue. A new collaboration was established, in view of the ATLAS IBL upgrade, among the four foundries SINTEF (Norway), Stanford (US), CNM (Spain) and FBK (Italy).

The SINTEF MiNaLab laboratory [11] started its production of 3D silicon sensors in 2007. Its role in the collaboration is to adapt the original process developed at SNF to satisfy the requirements for a serialised production [132]. Challenges in the small-to-medium scale production are represented by the three-dimensional processing, the wafer bonding and the thick polysilicon deposition: the laboratory is equipped with several state-of-the-art tools that make the facility suitable for such production.

Three runs of 3D detectors have been completed, to date, by SINTEF MiNaLab and a fourth one is ongoing. The first series produced some usable detectors. Devices of the second run have been coupled to read-out electronics and successfully measured in beam tests. The third generation of SINTEF 3D sensors has been characterised in the framework of this work.

5.1.1 Sensor production method

SINTEF 3D silicon sensors are produced on 4-inch and 6-inch float zone wafers, double-sided polished, with a resistivity in the range of $2 - 30$ kΩcm. The device wafer, $230 - 250$-μm-thick, is oxide-to-oxide bonded to a 300-μm-thick support

wafer. The thickness of the wafers depends on the runs and may slightly vary from wafer to wafer within the same production batch. The support wafer is essential for the fabrication of the active edge, relieving mechanical stress and providing support.

The production method is illustrated in Figure 5.1. The device and support wafer are initially prepared for the DRIE process: they are protected by a 1.5-μm-thick silicon dioxide on both sides and then oxide-to-oxide bonded. Layers of nitride and aluminium are applied on both exposed surfaces.

The DRIE process is performed twice, once for each doping type (the n^+-doped columns are produced first). The procedure includes several steps: first, the etching of the aluminium layer is performed using a photolithographic process. The device wafer is etched using the DRIE process to obtain columns with a diameter of $d \sim 14\,\mu$m. When the procedure is repeated for the p^+-type doping, ~ 5-μm-thick trenches are etched around the sensor to produce active-edge sensors. Then, the aluminium layers are removed and the electrode holes (and the trench) are filled with doped polysilicon, which is then diffused during an annealing phase. New oxide and nitride layers are deposited over the holes and a new aluminium layer is laid to cover the exposed surfaces.

The production process is finalised by etching the oxide away from the column openings, metallising the top of the electrodes and applying a passivation layer between aluminium contacts to ensure isolation [133]. The top metallisation allows for electrical tests.

5.1.2   Four SINTEF prototype runs

By the end of 2012, SINTEF produced three prototype runs of 3D silicon sensors and it is now processing a fourth run.

Run-A   The first run was fabricated in 2007. The production of 25 $n-$type $\langle 100 \rangle$ wafers with a resistivity of $2\,k\Omega$cm was aimed at demonstrating the achievability of the production of 3D sensors with active edge on large surfaces [134, 135].

First tests showed a large bowing of the wafers (of the order of $150\,\mu$m) induced by the high mechanical stress during fabrication and caused by the asymmetry in the thickness of the oxide layers in the front and back of the wafer. Overall, four wafers survived the process and one showed good electrical properties. After few hours of operation, however, all its sensors suffered from irreversible breakdown. Preliminary measurements suggested that this
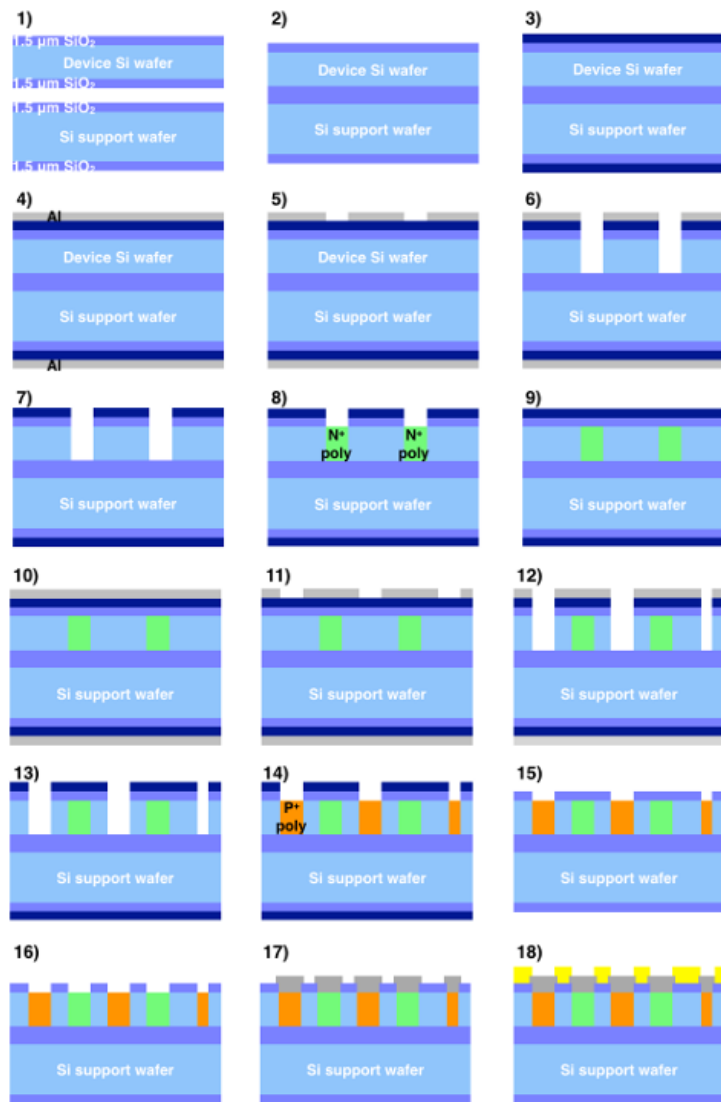
Figure 5.1: Steps for the production of 3D silicon wafers at SINTEF MiNaLab. Steps 1-2: device and support wafers are covered by SiO_2 on both sides and oxide-to-oxide bonded to each other. Steps 3-4: layers of nitride and aluminium are applied. Steps 5-7: electrodes are obtained by etching the aluminium and device wafer exploiting, respectively, a photolithographic process and the DRIE technique. Holes are then filled with n^+-doped polysilicon and dopants diffuse during an annealing phase. Steps 9-14: steps 3-8 are repeated for the p^+-doped electrodes. A trench is also etched around the sensor to obtain active-edge sensors. Step 15: The nitride layer is removed from the surfaces. Steps 16-17: the oxide is etched away in correspondence of the n^+ column openings and metallisation is applied to provide good ohmic contact. Step 18: a passivation layer is added between the aluminium contacts to ensure isolation. Image modified from [133].

configuration is not optimal for n^+-read-out devices with $p-$type active edge: the edge acts as a part of the p-n junction rather than terminating the electric field lines. The following runs used $p-$type wafers, with n^+ junction electrodes.

Run-B Wafers adopted during Run B were $p-$type doped: among the advantages, the choice of this type of bulk allows for active-edge trenches of the same type as the bulk. Several process modifications were applied including oxide thicknesses and wafer bonding. Changes allowed for higher robustness in the mechanical stability and resulted in higher yield.

Run-C The third run used 230-μm-thick active wafers, with a resistivity of $10 - 30$ kΩcm. Sensors columns have a diameter of $13 - 15$ μm. The surface of the wafers was designed to maximise the number of IBL-like sensors: the $4-$inch wafers contain 8 sensors that are compatible with the FE-I4 read-out chip.

During this run, the yield of the wafers was observed to be very low: only 2 over 25 wafers have good sensors. Overall, 34% of the FEI3 sensors and 9% of the FEI4 devices showed a breakdown voltage $U_{bd} > 40$V [136]. Sensors in the large majority of wafers (23 over 25) failed the leakage current criteria and are characterised by short carrier lifetime. In these wafers, the production temporary metal layer was substituted with a diagnostic metal layer, which offers extra features that allow for more in-depth measurements. The diagnostic metal layer is segmented in strips, to localise and isolate the problematic parts of the sensors, and to allow for strip measurements. This thesis' experimental work was performed on sensors from this batch.

Run-D The ongoing prototype run, started in 2014, uses $6-$inch Silicon-on-Insulator (SOI) wafers with an active thickness of either 50 μm or 100 μm. Two types of n^+ columns have been implemented: both full-through and partially-through. The column diameter is reduced to $3 - 4$ μm for 100-μm-thick columns: the DRIE process was modified to achieve such high aspect ratio. In view of the upgrade of the ATLAS pixel detector for the HL-LHC phase, sensors on the wafers have a pixel size of either 50×50 μm^2 or 100×25 μm^2.

During the adaptation of the DRIE process to the smaller column diameter, it was observed that the procedure created defects in the mask: these flaws caused a random formation of pits in the silicon. The same problem was found to have happened also during Run-C (this issue will be described in more detail

in Section 6.1.1). For this new prototyping run, the DRIE process was therefore made more robust and future measurements will assess the quality of this batch.

5.1.3 SINTEF 3D wafer layout

For this work, sensors from six wafers from Run-C were used. As the main goal for the prototyping run was the verification of the performance of IBL-like sensors, wafers were drawn to maximise the number of these $\sim 2 \times 2\,\mathrm{cm}^2$ sensors. Large sensors were placed in the central area of the wafer, to strive for a good yield.

The layout of Run-C wafers is shown in Figure 5.2. These wafers contain 8 FE-I4 sized, 9 FE-I3 sized, 3 CMS-pixel sized sensors and more than 200 test structures.
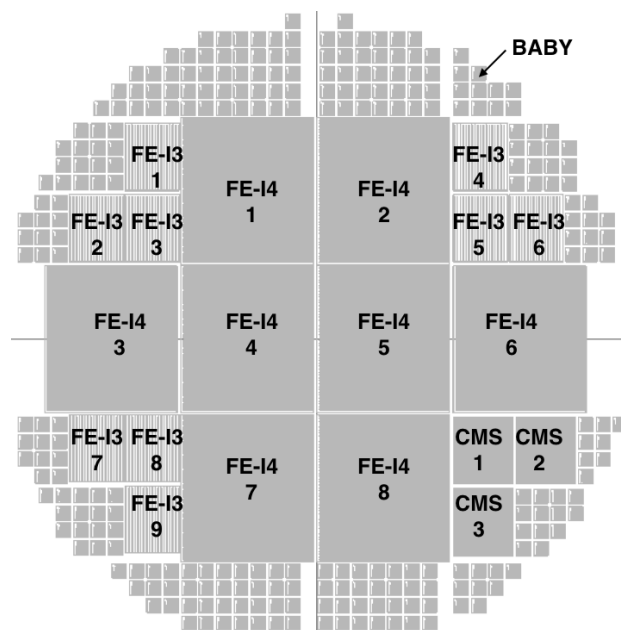

Figure 5.2: Layout of the SINTEF silicon wafer. The $4-$inch wafer is divided in 8 FE-I4-like, 9 FE-I3-like, 3 CMS-like sensors and more than 200 test structures (named BABY sensors).

The characteristics of the SINTEF sensors produced in Run-C are listed in Table 5.1. The electrode configurations (1E to 5E) are drawn in Figure 3.14. The outermost strips of the FE-I3-like and FE-I4-like sensors (respectively strips 1, 18 for FE-I3-like sensors and strips 1, 80 for FE-I4-compatible sensors)

116

Sensor type	Sensor dimensions [mm²]	Pixel size [μm²]	Electrode config.	Interel. distance [μm]	No. of strips
FEI4	20.2×18.5	250×50	2E	~ 67	80
FEI3	7.5×9.5	400×50	3E	~ 71	18
CMS	8.4×9.5	100×75	1E	~ 63	81
BABY 1E	2×2	400×50	1E	~ 202	
BABY 2E	2×2	400×50	2E	~ 103	
BABY 3E	2×2	400×50	3E	~ 71	
BABY 4E	2×2	400×50	4E	~ 56	
BABY 5E	2×2	400×50	5E	~ 47	

Table 5.1: Geometrical properties of the SINTEF 3D silicon sensors of Run-C wafers.

are connected to a larger pixel area, corresponding to a different electrode configuration: four read-out electrodes per pixel (4E) for FE-I3-like sensors and three read-out electrodes per pixel (3E) for FE-I4-compatible sensor. The inter-electrode distance is maintained constant also for the outermost pixels. These pixels extend to the active edge, therefore maximising the active area coverage to the edges.

To ease the reading, henceforth when talking about SINTEF sensors, "FEI4" will refer to the sensor that has the geometry compatible with the FE-I4 chip[2], "FEI3" will indicate the sensor FE-I3 chip-compatible and "BABY sensors" will denote the small test structures. The CMS-type sensors were not characterised.

The diagnostic layer was applied on the wafers to connect all the read-out electrodes of the pixel sensor in patterns: in all sensors the metal connects, for each device, all p^+ electrodes together to provide bias to the entire sensor; the n^+ electrodes are shorted in strips in the case of large sensors (FEI3, FEI4 and CMS) and are all connected together in the case of BABY sensors. The temporary metal layer is equipped with pads for wire bonding and IVCV measurements: for BABY sensors, the multiple n^+ pads are electrically shorted. The layouts of the temporary metal layer for a BABY sensor, a part of a FEI3 and a part of a FEI4 sensors are shown in Figure 5.3.

---

[2]Note the slightly different notation: FEIx, with no hyphen between FE and Ix, was chosen to identify the SINTEF sensor whose geometry correspond to that of the FE-Ix front-end chip.
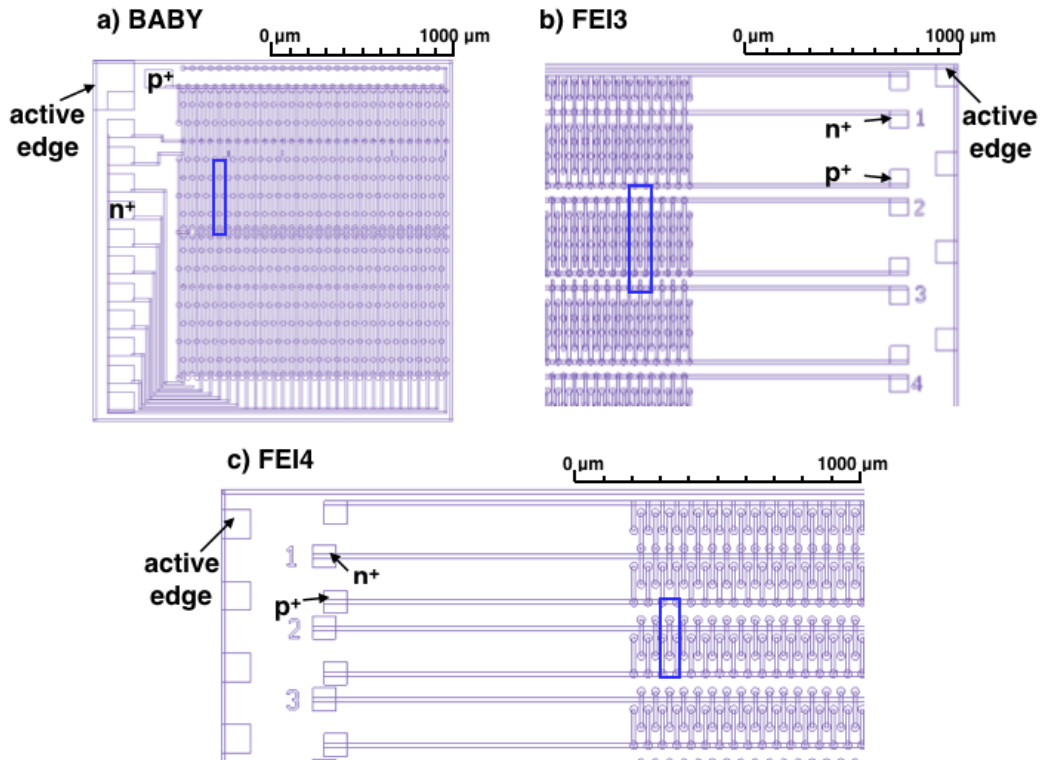
Figure 5.3: Layouts of the temporary metal layer for (a) an entire BABY sensor, (b) a part of a FEI3 and (c) a part of a FEI4 sensors. The p^+ and n^+ electrodes as well as the active-edge metal pads are indicated. Each pixel, whose dimensions are illustrated by the blue rectangle, has a bump-pad that is used to connect the pixel to the read-out electronics. In BABY sensors, all p^+ electrodes are connected together to the top-left pad and all n^+ electrodes are grouped into the n^+ pads, which are all electrically ganged. In FEI3 and FEI4 sensors the p^+ columns are all connected together, while the n^+ ones are stripped: all in-line columns belong to one independent strip.

5.1.4 Measurement campaign on SINTEF 3D sensors

The third prototype run of 3D silicon sensors at SINTEF showed an overall low wafer-level yield: out of 25 produced, only wafers C2 and C25 contained sensors with good electrical properties, in terms of breakdown voltage and leakage current after full depletion. On these two wafers, the temporary metal layer was replaced with a final metal layer with a pixel layout. Their FEI4 sensors were diced out, bump-bonded and measured in beam tests. The outcomes of beam tests are beyond

the scope of this thesis and are collected in [137].

Studies reported in this thesis were performed on some BABY sensors from wafer C25 and on sensors, of diverse geometries, from other wafers of Run-C. The objective of this project was the identification of the origins of the observed issues on Run-C sensors and the general characterisation of their properties. At the time the tests were conducted, the findings from the Run-D prototyping (see Section 6.1.1) were not known.

Overall, sensors from 6 wafers were tested. Sensors from wafers C16 and C17 were characterised at wafer-level, wafers C21 and C26 were diced at SINTEF, whilst sensors from wafer C23 and the shards from wafer C25 were sent to CiS [138] for dicing. The BABY sensors were diced in matrices of 2×2 sensors, to be able to handle them: each physical piece of silicon hosts, therefore, up to 4 BABY sensors, typically with two different pixel cell configurations (e.g. 2 sensors with 2E configuration and 2 sensors with 3E configuration are present on the silicon die).

Performed on FEI4 sensors of wafers C16 and C17, this first set of current-voltage (IV) measurements was repeated on the same sensors before and after the wafers underwent various treatments: baking, plasma cleaning and a second baking. These treatments were aimed at improving the electrical behaviour of a sensor: exposing it to a high temperature may remove some defects in the silicon lattice and release possible mechanical strains from the polysilicon structure; the plasma cleaning may remove possible unwanted chemicals from the wafer's surface. A significant improvement of the electrical properties after these treatments is thus expected in the case of doping or surface issues originating during the production phase.

At CERN, the electrical characterisation was performed over a large number of FEI3, FEI4 and BABY sensors. A selection of sensors was then sent for proton or neutron irradiation campaigns, which are described in Section 5.2.

The measurement campaign included tests of both unirradiated and irradiated sensors. Priority was given to proton-irradiated devices, as in the HL-LHC conditions the radiation damage at the inner radii will mainly be caused by charged hadrons [139]. A large quantity of FEI3, FEI4 and BABY devices were electrically characterised after irradiation. Laser-induced charge measurements (see Section 5.4), despite being feasible on both strips and BABY sensors, were only performed on the latter structure. Radioactive source characterisations were done on a few FEI3 and FEI4 sensors. Planar devices and 3D sensors produced by CNM were characterised to provide a comparison to the SINTEF sensors.

5.2   Irradiations

To study the evolution of the performance of SINTEF sensors as a function of the fluence and of the type of irradiating particle, a selection of samples was irradiated at different fluences at the PS-IRRAD CERN facility [140] with 24 GeV/c protons, while a second selected group was irradiated at the JSI-TRIGA neutron irradiation facility in Ljubljana, Slovenia [141]. Both irradiation campaigns fell under the AIDA-2020 project, funded from the European Union's Horizon 2020 Research and Innovation programme under Grant Agreement No. 654168 [142].

The selection of the sensors was performed based on the following criteria:

- At least one sensor of each type (dimension and pixel configuration) had to be irradiated at each fluence;

- Sensors were requested to show good electrical performance (good IV and CV curves, see Section 5.3) before irradiation;

- For BABY sensors, as the silicon die consists of 2×2 sensors, it was required that at least one sensor of the silicon unit showed good IV-CV curves.

BABY sensors, FEI3 and FEI4 sensors were irradiated at either of the two irradiation facilities at a fluence between $5 \cdot 10^{13}$ and $1 \cdot 10^{16}$ particles/cm^2. Due to time constraints, a single sensor was sent only once to the irradiation facility and was therefore irradiated to one specific fluence.

After irradiation, all sensors were kept at low temperature, to avoid further annealing. Two power cuts, however, caused the freezer in which the samples were stored to stop working for some time over the Christmas break and over a weekend, therefore some unexpected and uncontrolled annealing took place. The total annealing time has been estimated to be 9 days at room temperature[3].

To allow direct comparison between fluences of the two irradiation facilities, the hardness factor, κ, should be used. Table 5.2 summarises the κ values of the PS and JSI irradiation centres [141, 143].

---

[3]The estimated value was calculated by Esteban Currás Rivera.

Source Name	Particle Type	Hardness Factor κ
CERN PS	Monochromatic protons, 24 GeV/c	0.56
Ljubljana Triga nuclear reactor	Neutron fission spectrum	0.9

Table 5.2: Hardness factors of the irradiation facilities exploited during this work. The hardness factor is used for a direct comparison of the fluences. Values collected from [141, 143].

5.2.1 IRRAD irradiation facility at PS-CERN

IRRAD is the new CERN irradiation facility, located in the PS East Hall area. Operating in the beam line T8, it delivers particle bursts, made of 24 GeV/c protons, coming from the PS accelerator in spills of ~ 400 ms. The delivered beam is gaussian and has a dimension of (12×12) mm^2 at full width half maximum and a particle fluence of about $1 \cdot 10^{16}$ p/cm^2 is reached in 5 days. Irradiation is performed at room temperature ($t = 21$ °C), so uncontrolled annealing may take place during the irradiation.

Table 5.3 summarises the set and measured fluences for the PS irradiation. The hardness factor κ used for the conversion is listed in Table 5.2. The fluence is measured using the aluminium foil activation method, described in [144]. Other techniques for this type of measurement are described in [145].

5.2.2 TRIGA-Mark-II reactor at JSI

Neutron irradiation was performed in the TRIGA Mark II research reactor hosted at the Jožef Stefan Institute (JSI) in Ljubljana (SI). The reactor produces nuclear fission neutrons with a continuous energy spectrum. The total flux is $4 \cdot 10^{12}$ cm^{-2}s^{-1}. This high flux implies very short irradiation time, which in turn allows uncontrolled annealing during irradiation to be limited.

Table 5.4 provides the set and measured fluences for the neutron irradiation. The hardness factor κ used for the conversion is listed in Table 5.2.

Expected Fluence	Measured PS Fluence	
ϕ_{set} [p/cm^2]	ϕ_{meas} [p/cm^2]	$\phi_{eq} = \kappa \cdot \phi_{meas}$ [n$_{eq}$/cm^2]
$5 \cdot 10^{13}$	$(5.82 \pm 0.90) \cdot 10^{13}$	$(3.32 \pm 0.51) \cdot 10^{13}$
$1 \cdot 10^{14}$	$(1.83 \pm 0.27) \cdot 10^{14}$	$(1.04 \pm 0.15) \cdot 10^{14}$
$5 \cdot 10^{14}$	$(4.40 \pm 0.55) \cdot 10^{14}$	$(2.51 \pm 0.32) \cdot 10^{14}$
$1 \cdot 10^{15}$	$(7.92 \pm 1.02) \cdot 10^{14}$	$(4.51 \pm 0.58) \cdot 10^{14}$
$5 \cdot 10^{15}$	$(3.81 \pm 0.48) \cdot 10^{15}$	$(2.17 \pm 0.27) \cdot 10^{15}$
$1 \cdot 10^{16}$	$(8.75 \pm 1.08) \cdot 10^{15}$	$(4.99 \pm 0.62) \cdot 10^{15}$

Table 5.3: Expected and measured fluences at which sensors have been exposed at the PS irradiation facility at CERN. Fluences are expressed in particles/cm^2 (p/cm^2), and in 1 MeV neutron equivalent (n$_{eq}$/cm^2).

Expected Fluence	Measured JSI Fluence	
ϕ_{set} [p/cm^2]	ϕ_{meas} [p/cm^2]	$\phi_{eq} = \kappa \cdot \phi_{meas}$ [n$_{eq}$/cm^2]
$5.00 \cdot 10^{13}$	$5.00 \cdot 10^{13}$	$4.50 \cdot 10^{13}$
$1.00 \cdot 10^{14}$	$1.00 \cdot 10^{14}$	$9.00 \cdot 10^{13}$
$5.00 \cdot 10^{14}$	$5.00 \cdot 10^{14}$	$4.50 \cdot 10^{14}$
$1.00 \cdot 10^{15}$	$1.00 \cdot 10^{15}$	$9.00 \cdot 10^{14}$
$5.00 \cdot 10^{15}$	$5.00 \cdot 10^{15}$	$4.50 \cdot 10^{15}$
$1.00 \cdot 10^{16}$	$1.00 \cdot 10^{16}$	$9.00 \cdot 10^{15}$

Table 5.4: Expected and measured fluences at which sensors have been exposed at the TRIGA reactor at JSI. Fluences are expressed in particles/cm^2 (p/cm^2), and in 1 MeV neutron equivalent (n$_{eq}$/cm^2).

5.3 Electrical characterisation

The electrical characterisation of the sensors is of fundamental importance for evaluating the overall quality of the sensors. Measuring the variation of the leakage current and of the capacitive impedance of the sensors as a function of the bias potential (in short: IV and CV characteristics, respectively) allows for assessment of the parameters that characterise the silicon sensor.

In particular, the IV curve is related to both the depletion and the breakdown voltages. The value of the leakage current after depletion is indication of the

amount of lattice imperfections that create discrete energy levels in the band gap. These defects can be caused by production issues or due to the radiation damage. The CV curve gives information on the full depletion voltage and allows for the calculation of the effective doping concentration. It should be noticed that, for the peculiar geometry of the 3D sensors, the concept of "full depletion voltage" is complex, in the sense that at first the depletion region expands cylindrically around the junction electrode, until the depleted regions of two long-side neighbouring pixels connect. Then, the depletion region expands with an elliptical shape toward the undepleted region. This process can be observed as a double knee at voltages lower than the plateau region. Further "knees" at higher voltages can appear in measurements over a single strip when the neighbouring strips are not put to ground: once the volume between two electrodes is depleted, the depletion grows outside this volume's boundaries and expands towards the neighbouring strips.

5.3.1 IV characterisation

The SSD IV setup is sketched in Figure 5.4. The sensor is placed on a thermally-controlled chuck. Two micromanipulators ending up with a needle with a tip size of 20 μm provide the contacts to bias the sensor. In the case the sensor can be biased from the back plane, the chuck provides the bias and the two needles are used to contact the top electrode and the guard ring; in the case both p^+ and n^+ electrode pads are on the top of the sensor, as it is the case of SINTEF 3D sensors, then the needles are put in contact with the two electrode types. A vacuum pump ensures sensor and micromanipulators stay still, to avoid unwanted scratches and to improve the temperature conduction between the chuck and the sensor. Mounted on a 2-axis stage, the chuck is a commercial device[4], whose temperature is stabilised by thermoelectric elements cooled through a liquid ethanol circuit connected to a chiller unit[5]. To avoid condensation, dry air with a dew point below $-100\,°\text{C}$ is flushed inside a sealable box that contains chuck, micromanipulators and sensor. High voltage is provided by a Keithley 2410 power supply (max voltage up to ±1100 V); the leakage current is read out by a Keithley 6487 picoAmpere-meter with an internal resistance smaller than 1 Ω.

The IV and CV measurements measure the value of leakage current or capacitance, among other parameters, as a function of the changing bias voltage. They end when the maximum set voltage is reached or when the leakage current

---

[4]The chuck is fabricated by ATT Systems.
[5]The chiller is produced by Huber.

reaches compliance. The compliance current is a parameter, set before the beginning of the scan, that identifies the maximum current that the sensor is allowed to draw. It is meant to protect the sensor from a too high leakage current that could break it.

A Labview interface, developed by the SSD team, controls the whole setup: voltage, temperature and data acquisition.
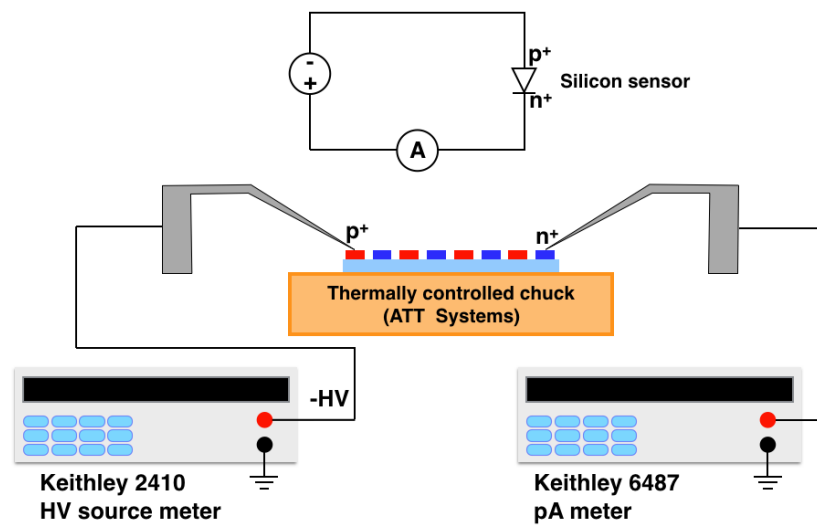

Figure 5.4: Sketch of the electrical connections of the IV setup. Image adapted from [75].

An example of IV curve of an unirradiated BABY sensor is shown in Figure 5.5. The curve can be divided in three regions: at low voltage, the leakage current has a rapid increase, until it reaches the depletion voltage, identified by the sharp change of slope of the curve. Equation 3.18 indicates the depletion voltage for 3D sensors in the cylindrical approximation. The plateau region extends over the voltage range of operability of the sensor. The further change of slope is marked by the breakdown voltage: the generated intense electric field accelerates the charge carriers to the point they have enough energy to ionise the material, creating an avalanche. As a result, the sensor responds no longer to external radiation and should not, therefore, be operated at such (or higher) voltages.
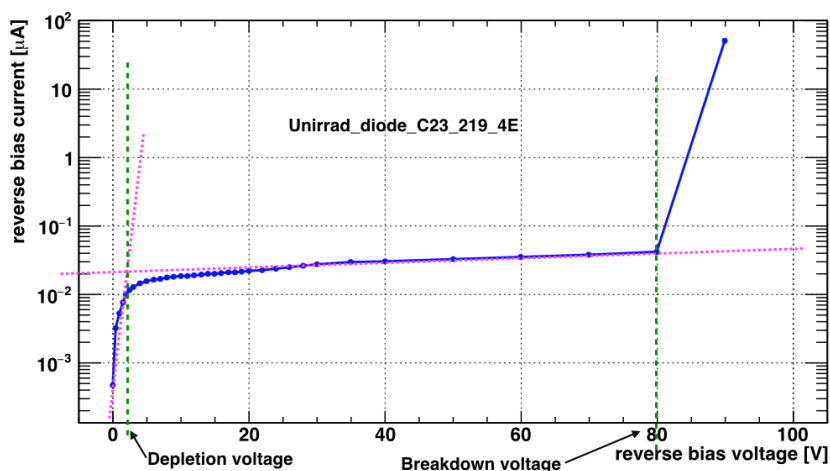
124

Figure 5.5: Example of IV measurement on an unirradiated SINTEF 3D BABY sensor. The depletion and breakdown voltages are indicated.

5.3.2 CV characterisation

The measurement of the capacitance, a macroscopic quantity, gives information about the depth of the depletion region, as Equations 3.13 and 3.17 suggest for, respectively, planar and 3D geometries. Equation 3.14, valid only for planar sensors, also indicates that measuring the capacitance allows the effective concentration of dopants to be evaluated.

The experimental setup used to measure the CV curve is shown in Figure 5.6. While the configuration inside the sealable box is the same as for IV measurements, different devices are used to measure the capacitance.

CV measurements are based on the simultaneous use of two voltage sources: an applied AC voltage signal and a DC voltage that is swept in time [146]. In the SSD CV setup, the capacitance is measured by a LCR meter connected between the two electrodes. This device, able to measure the capacitance with 1 pF accurracy, generates a sinusoidally oscillating voltage, tunable in amplitude and period. The identification of the correct test frequency has an important role: as shown in Figure 5.7, the impedance of a capacitor has a significant dependence on the frequency [147].

The sensor returning current signal has a phase and an amplitude shift that correspond to the real and the imaginary parts of the impedance. Providing the LCR meter with a circuit model that best approaches the circuit under test, the device outputs a pair of corresponding real measurable quantities. For
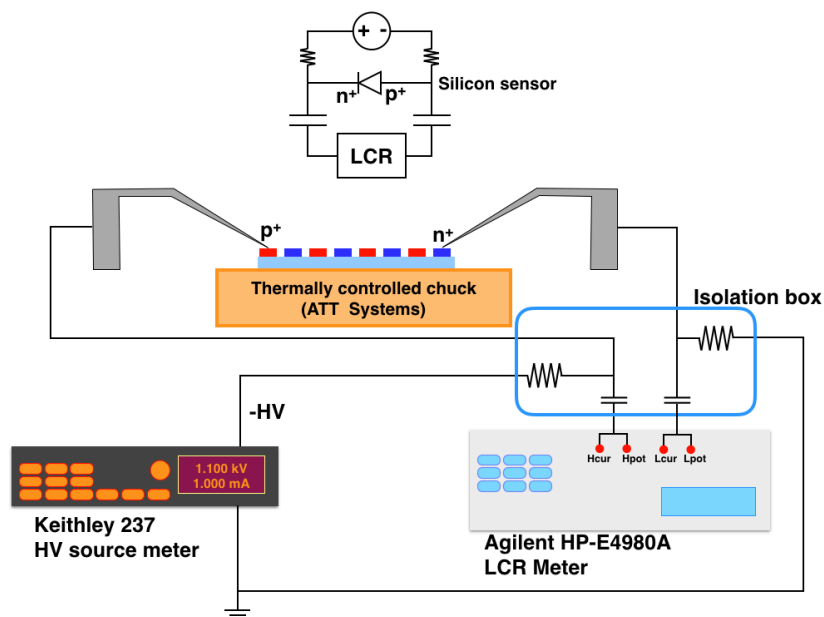
Figure 5.6: Sketch of the electrical connections of the CV setup. Image adapted from [75].

silicon sensors, the best model is the Capacitance-Conductance parallel model ($C_P - G_p$): the simplest realistic way of depicting a silicon sensor is a capacitor in parallel with a resistor.

To disentangle the high voltage required to bias the sensor and the AC voltage necessary for the capacitance measurement, a decoupling circuit (the isolation box in Figure 5.6) is added to the circuit between the LCR meter and the sensor. The box, acting as a high-pass filter, presents a low impedance to the signal generated by the LCR meter and, at the same time, blocks the DC component. In order to measure uniquely the capacitance of the sensor under test, each CV measurement is preceded by a "open correction" measurement, during which the sensor is disconnected from the rest of the setup and the LCR meter measures capacitance and conductance of the setup itself. These values are then taken into account, in the Labview interface, when performing the actual CV measurement.

The bias voltage is sourced by a Keithley 237 SMU. Differently from the Keithley device used in the IV setup, this voltage regulator is analog, non-switching and does not try to compensate for the voltage oscillations produced by the LCR meter, which would affect the returning signal to the LCR device.

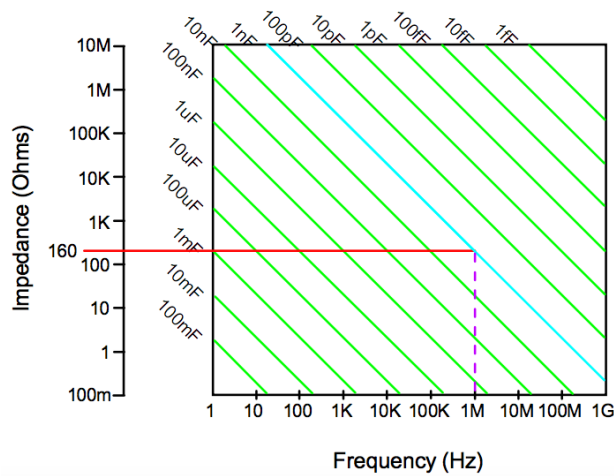Figure 5.8 presents a CV curve for the strip of an irradiated FEI3 sensor, shown

Figure 5.7: The impedance of various perfect capacitors versus frequency. Depending on the frequency, the capacitor shows a different impedance: for example, a 1 nF capacitor presents an impedance of $160\,\Omega$ at $\nu = 1\,\mathrm{MHz}$, and $160\,\mathrm{k}\Omega$ at $\nu = 1\,\mathrm{kHz}$. The choice of the correct range of frequencies is therefore mandatory for a meaningful measure of the capacitance. Image reproduced from [147].

as $1/C^2$ vs. voltage. As expected, the capacitance decreases ($1/C^2$ increases) as the depletion region expands (Equations 3.8, 3.13 and 3.17). The end capacitance is defined when the capacitance reaches a plateau: the sensor is fully depleted.

5.3.3 IV and CV data analysis

Data analysis performed on IV and CV data aims at identifying the electrical properties of SINTEF sensors, such as the depletion and breakdown voltages, the leakage current in the plateau region and the end capacitance, and describing these characteristics as a function of the fluence.

The Labview data acquisition program writes the collected data into a text file. This information, retrieved by a dedicated script developed by the SSD group, is converted into a ROOT [148] TTree. My IVCV analysis takes as input the TTree and performs the analysis in two steps: first, for each IV or CV curve it extracts the parameters and their associated errors; next, it uses these values to build graphs showing the dependence of the parameter on fluence.
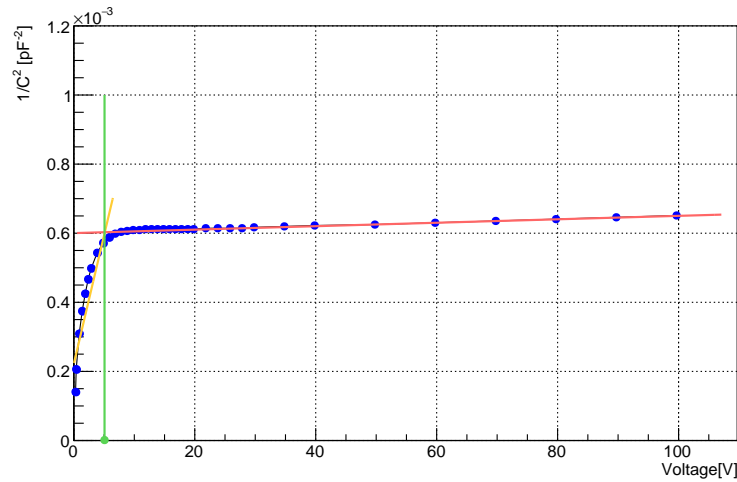
Figure 5.8: Example of CV measurement (on a strip of a SINTEF 3D FEI3 sensor irradiated to $\phi = 2.5 \cdot 10^{14}$ n$_{\text{eq}}$/cm^2), shown as $1/C^2$ vs. U. The yellow line is the fit to the data points that describe the initial decrease of the capacitance as a function of the applied voltage, during the sensor's progressive depletion. The capacitance becomes constant (orange fit) when the sensor is fully depleted. The depletion voltage is indicated by the green line.

5.3.3.1 Extraction of the electrical properties for each measurement dataset

Figures 5.5 and 5.8 qualitatively show the methods for extracting the electrical parameters from, respectively, IV and CV curves.

Taking into consideration the different shapes of the two curve types, two different approaches are adopted as fitting procedure.

5.3.3.1.1 IV curve fitting

For fitting the IV curve, it is first necessary to isolate the data points belonging to the three regions defined in Figure 5.5. For simplicity, the values of the leakage current and of the voltage are multiplied by the sign of the polarity applied to the sensor, so that these values should lie only in the first quadrant of the Cartesian plane.

IV curves of SINTEF 3D sensors may be rejected before being analysed if any of the following conditions is true:

1. the curve presents too few points (less than 15),

2. all data points have a current smaller than 100 pA,

3. the value of the current at the highest voltage is not above 10 nA.

The first requirement ensures that the compliance current was not reached at very low voltages (e.g. $U < 12$ V); the second makes sure that the sensing needles were correctly connected to the sensor. The third rule reinforces the quality of the measurement, because usually the good IV curves either show a breakdown, reaching a compliance current of the order of $50 - 100$ μA (depending on the dimensions of the sensor), or their plateau current is larger than 10 nA (in the irradiated sensor's case). Whenever the fitting procedure fails, the output parameter is given the default value of -999 and, in the next step of the analysis, it is ignored.

Good curves are then analysed: the first step is the identification of the plateau region, which determines, by exclusion, the ranges of the first increase and the breakdown regions. The plateau is identified following two assumptions:

- The IV curve should be a monotonically increasing function;

- On a IV curve, most of the data points should lie on the plateau region.

The first assumption ensures that all data points showing a leakage current smaller than the leakage current at $U = 0$ V are excluded from any fit. Based on the second assumption, a histogram filled with the quantity $\log_{10}(I_{leak})/U_{bias}$ (I_{leak} is the leakage current and U_{bias} is the applied voltage for a set point of the IV curve) is built applying the cuts

$$(U_{bias} \geq 3 \text{ V}) \text{ \&\& } (I_{leak} > 0 \text{ A}) \text{ \&\& } (I_{leak} < 10 \text{ } \mu\text{A}). \qquad (5.1)$$

The mean and RMS values of the distribution are extracted from this histogram and are used to perform a more stringent selection to the data, adding a further cut

$$\left| \frac{\log_{10}(I_{leak})}{U_{bias}} - mean \right| < RMS. \qquad (5.2)$$

The mean ($mean_1$) and RMS (RMS_1) values of this second histogram are computed. Data points (U_i, I_i) are accepted as plateau points if they satisfy the condition:

$$\left| \frac{\log_{10}(I_i)}{U_i} - mean_1 \right| < f \cdot RMS_1, \qquad (5.3)$$

129

where $f = 1$ for unirradiated sensors and $f = 5$ for irradiated ones. This less strict requirement on irradiated sensors is motivated by the fact that the plateau of irradiated sensor's IV has a higher slope than that of unirradiated curves.

The data points associated with the plateau region are fitted with a linear function $fitPl$, defined in the range $[U_{Plat}^{min}, U_{Plat}^{max}]$, respectively the minimum and maximum voltages of the plateau region. The fit $fitPl$ is drawn in Figure 5.9 with a magenta-coloured line.

The first region, where the leakage current grows from 0 to the plateau value, is defined by that data points that satisfy

$$\left(I_{leak}(U_i) \geq I(U = 0 \text{ V}) \right) \ \&\& \ \left(U_i < U_{Plat}^{min} \right). \tag{5.4}$$

A second linear fit, $fitFirst$, is computed in this range. In Figure 5.9 it is drawn in light green. Linear fits appear curved because of the logarithmic scale applied on the $y-$axis.

The breakdown region is defined in the range $[U_{Plat}^{max}, U_N]$, where U_N is last point of the IV curve that satisfies two conditions:

$$(a) \quad I(U_N) > 10 \ \mu\text{A} \tag{5.5}$$

$$(b) \quad \left((I(U_N) - I(U_{N-1})) > 10 \text{ nA} \right). \tag{5.6}$$

The first constraint checks that the curve actually shows a breakdown voltage. The second requirement is recursively applied to remove the last, N^{th} point if its leakage current differs too little from the one of the previous point. This aims at avoiding a mis-fitting of the breakdown region because of the presence of multiple points close to the compliance current limit that would wrongly flatten the fit. The threshold value is tuned on the set of measurements on SINTEF sensors.

Once the endpoints of the breakdown region are defined, a third linear fit, $fitBD$, is performed. In Figure 5.9 it is drawn with a dark green line.

If the fits correctly follow the data points in the three region, the analysis extracts the depletion and the breakdown voltages. The first is calculated as the intersection of $fitPl$ with $fitFirst$: assuming that $fitPl$ and $fitFirst$ have respectively equations

$$I = p_0^a + p_1^a \cdot U \tag{5.7}$$
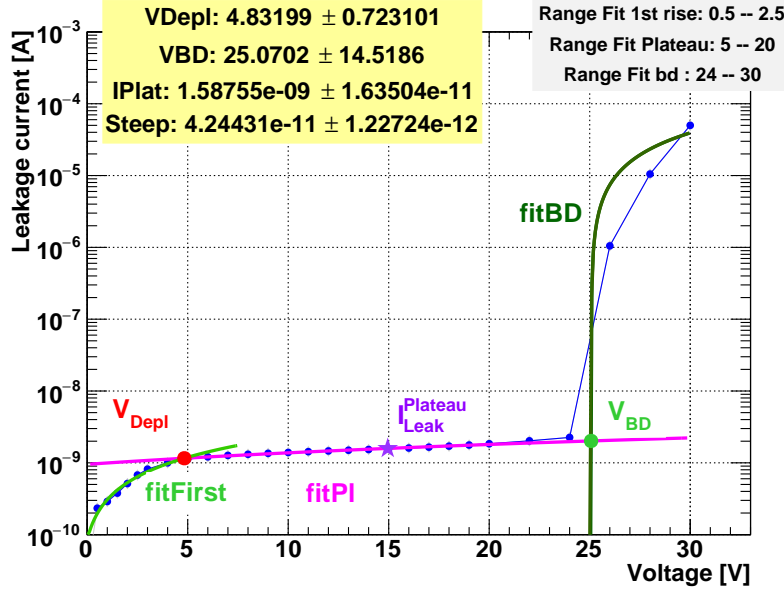
$$I = p_0^b + p_1^b \cdot U, \tag{5.8}$$

Figure 5.9: Example of an IV curve (unirradiated BABY sensor 1E, No. 085 from wafer C23) fitted using the IVCV data analysis. Data points are in blue. The magenta line is the fit over the plateau region ($fitPl$), the light and dark green lines are, respectively, the first ($fitFirst$) and the breakdown ($fitBD$) fits. All fits are linear functions (the $y-$axis is in logarithmic scale). The red filled circle marks the depletion voltage, the violet star corresponds to the value of the middle-plateau current and the green marker identifies the breakdown voltage.

the depletion voltage and its error are computed as

$$
U_{Depl} = \frac{p_0^b - p_0^a}{p_1^a - p_1^b}, \quad \Delta U_{Depl} = \sqrt{\sum_{i=1}^{2} \sum_{j=a,b} \left(\frac{\partial U_{Depl}}{\partial p_i^j} \Delta p_i^j \right)^2} \tag{5.9}
$$

where p_i^j are the parameters of the two fits.

The breakdown voltage is similarly computed as the intersection of $fitPl$ with $fitBD$. The errors associated with the breakdown voltage are sometimes very high: this is an effect of the low number of data points (typically of the order of 2 to 4) used to perform the $fitBD$.

The leakage current in the plateau region I_{Plat} is calculated using the fitting parameter computed as the current value in the middle point of the plateau range:

$$I_{Plat} = p_0^a + p_1^a \cdot \left(\frac{U_{Plat}^{min} + U_{Plat}^{max}}{2} \right) = p_0^a + p_1^a \cdot U_{Plat}. \qquad (5.10)$$

The error on the leakage current, ΔI_{Plat}, is calculated from the errors on the fitting parameters:

$$\Delta I = \sqrt{(\Delta p_0^a)^2 + (\Delta p_1^a \cdot U_{Plat})^2}. \qquad (5.11)$$

The analysis, in some cases, does not recognise the correct range on which the fits should be applied. When this happens, the user manually enters the range extremes into a text file that is read out at the beginning of the analysis. The fits are then forced to be performed in the specified intervals.

5.3.3.1.2 CV curve fitting

The depletion voltage and the end capacitance can be extracted from CV measurements when the curve is drawn in terms of $1/C^2$ vs. voltage. This way, the relation between these two quantities can be approximated to an increasing linear function at low voltages, when the capacitance diminishes as a result of the expansion of the depletion region inside the silicon volume, followed by a plateau region when the sensor reaches full depletion. The analysis does not take into account the possibility of a double knee in the shape of the CV curve. This approximation does not affect to a great extent the outcomes and helps keep the analysis simple.

As in the case of the IV data, the bias voltage is first corrected by the sign of the polarity, in order to deal with positive numbers.

The identification of the plateau region is implemented in the data analysis in two ways: the first adopts an approach similar to the one used in the IV analysis. First, it fills a histogram with C/U values (C is the capacitance and U the bias voltage) of the data points that satisfy the condition

$$(U > 3 \text{ V}) \ \&\& \ (C > 5 \text{ pF}), \qquad (5.12)$$

and computes the mean and RMS values. These parameters are used to make a stronger cut adding the condition

$$\left| \frac{C}{U} - mean \right| < RMS. \qquad (5.13)$$

After recomputing the new mean and RMS values ($mean_1$ and RMS_1), the

analysis chooses the data points that fall within the range $mean_1 \pm RMS_1$. These data points, as in the case of the IV plateau, are fitted with a linear function, $fitTop$. In Figure 5.10, the $fitTop$ is drawn in light blue.
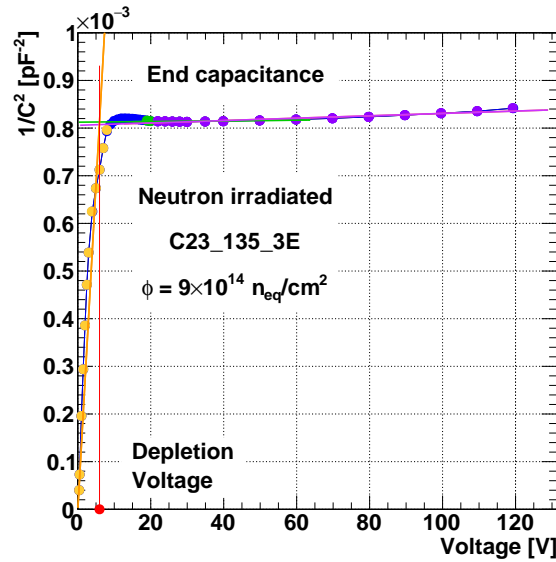

Figure 5.10: Example of a CV curve, represented as $1/C^2$ vs. voltage, fitted using the IVCV data analysis. The light blue line is the fit $fitTop$, $fitSkim$ is the violet line. The orange line draws $fitVert$ and fits the orange data points. The depletion voltage (red line and marker) is extracted calculating the intersection of the plateau fit with $fitVert$.

The second approach, instead, selects as plateau points the data points that comply with the rule

$$(C > 5 \text{ pF}) \;\&\&\; (U > 15 \text{ V}) \;\&\&\; \Big(\frac{C_{i+1} - C_i}{U_{i+1} - U_i} < 0.1\Big), \tag{5.14}$$

where i is the index of the ith data point. This set of conditions gives constraints on the minimum value of both the capacitance and the voltage, and imposes the slope of the CV curve "plateau" to be smaller than 0.1.

The first points belonging to the plateau, those that fulfil the requirement $U_i < U_0 + 5$ V (where U_i is the voltage of the ith point and U_0 is the lowest voltage of the plateau series, when it is firstly defined), are removed from the series. This precaution is taken to avoid an influence over the fit of the points close to the

133

$1/C^2 - U$ knee. In the presence of a double knee, it is even more important to avoid the knee areas.

The remaining data points selected using the second approach are fitted with a linear function, $fitSkim$ (drawn in violet in Figure 5.10).

Ideally, the capacitance after depletion should have a constant value. Therefore, the fit that shows the lowest slope (in absolute value) is chosen between the two fits resulting from the methods. If the slope of the chosen fit ($bestFit$) exceeds

$$p_1^{Plat} > 5 \cdot 10^{-6} \text{ pF}^{-2} \text{ V}^{-1}, \tag{5.15}$$

the measurement is considered bad and no further analysis is performed. Otherwise, once the plateau fit is identified, the data points that satisfy the condition

$$U_i < U_0 - 10 \text{ V} \tag{5.16}$$

(where U_0 is the lower boundary of the $bestFit$ range) are included in the collection of data that describes the initial decrease of the capacitance. The condition excludes the points corresponding to the knee of the CV curve. The selected points are fitted with linear fit $fitVert$ (drawn in orange in Figure 5.10).

The analysis on the measurement is abandoned if

$$p_1^{vert} < 5 \cdot 10^{-6} \text{ pF}^{-2} \text{ V}^{-1}, \tag{5.17}$$

namely if $fitVert$ is too flat or its slope is negative.

The depletion voltage and its error are calculated following Equation 5.9. The capacitance is computed as

$$C = \sqrt{\frac{1}{|p_0^{Plat}|}}, \tag{5.18}$$

while its error is calculated, following the error propagation rules, as

$$|\Delta C| = \frac{1}{2} \cdot (|p_0^{Plat}|)^{-\frac{3}{2}} \Delta p_0^{Plat}. \tag{5.19}$$

5.3.3.2 Construction of the fluence graphs

The fitting procedure is used to extract the depletion and breakdown voltages, the plateau leakage current and their errors from the IV curves, and the depletion voltage and end capacitance, together with their errors, from the CV characteristics.

134

To identify the dependence of the extracted parameters on the fluence, two methods were devised, the second being formulated after observing some problems related to the first.

5.3.3.2.1 The first approach The first idea was to fill, for each sensor geometry, a 2-dimensional histogram containing the parameter value, measured after irradiation, for each sensor (for BABY sensors) or each sensor's strip (for FEI3 and FEI4 sensors). As an example, Figure 5.11 shows, on the left-hand side, a 2D histogram filled for the breakdown voltage values of FEI4 sensors as a function of the fluence. Each 2D bin indicates the number of strips of the irradiated FEI4 sensor that share similar values of the breakdown voltage. From each 2D distribution, a TProfile histogram is extracted. This ROOT class provides a simpler way, with respect to 2D histograms, to visualise the same information, displaying the mean value of y and its error on the mean, σ_y, for each bin in x [149]. The right-hand side of Figure 5.11 presents the TProfile of the distribution of the breakdown voltage of FEI4 sensors. In this figure, the dark green line is the mean value of the breakdown voltage for non-irradiated FEI4 sensors (the averaged value of the parameter extracted for each strip of each FEI4 is considered). The horizontal solid and dashed green lines define the mean value and its uncertainty for the unirradiated sensors.

5.3.3.2.2 Problems concerning the first approach This first approach suffers from various problems related to the nature of the analysed data. First, it is meaningful only if the number of entries for a defined fluence is sufficient. This may be the case of FEI3 and FEI4 sensors, because for each sensor 17-18 strips were measured. Out of this amount, a good number of entries per fluence can be obtained. In the case of BABY sensors, however, the statistics on each type of configuration and each fluence is significantly reduced: only up to 4 BABY sensors were irradiated and available for measurements for each fluence and pixel geometry.

Second, sensors within the same category (namely sensors with same dimensions, electrode geometry and fluence) show quite different IV and CV curves. As a direct consequence, the extracted parameters for each curve have significantly different values and the overall error on the mean value becomes large. This is observed in particular for unirradiated sensors. The reason behind it may be the higher temperature at which unirradiated sensors were measured (the temperature was set to $t_{unirr} = +20\,°\mathrm{C}$, for unirradiated sensors against

135

$t_{irr} = -20\,°C$ for irradiated devices) that gives rise to a larger noise, which affects the measurements.

Third, regardless of the significant number of available sensors within a group, the statistics may be limited, in some cases, because many IV curves do not show a real plateau and have to be rejected (or, similarly, the CV curve cannot be correctly fitted). This is an effect of the highly-doped p-spray used to isolate the electrodes on the surface and it mostly affects the large sensors (FEI3 and FEI4).

Last, the errors associated to the parameters may be large because of the reduced number of data points used for the fit. For example, in the case of the breakdown voltage, the fit on the IV curve relies on few data points (2 to 4) and this leads to large errors associated to the breakdown voltage.

5.3.3.2.3 The second approach Because of these issues, a second approach was defined and adopted. An example of its outcome is shown in Figure 5.12, where the same data sample presented in Figure 5.11 is used.

In this method, only the strip (for large sensors) or sensor (for BABY sensors) that presents good parameter values for both the unirradiated and the irradiated measurements is taken into consideration. "Good value" means that the fitting procedure was successful and the extracted measure differs from -999, the value attributed when the fitting fails.

The unirradiated and the irradiated parameter values are drawn on two pads of the same canvas (the unirradiated value on the left pad, the irradiated measure on the right pad, as shown in Figure 5.12). In the irradiated case, the value is plotted as a function of the measured fluence.

This method makes the variation of the parameter with the fluence of the single sensor/strip clearer because no mean value is computed: it is thus possible to appreciate the value spread among sensors/strips at each fluence and to directly compare the variation of the parameter before/after irradiation of a single sensor/strip. In Figure 5.12, a colour/marker pair indicates the same strip of a sensor (or the same BABY sensor), measured before and after irradiation.

5.4   Laser characterisation

Laser characterisation can be performed using the Transient Current Technique (TCT). This method consists in the measurement of the time-resolved instantaneously-induced current of carriers that allows for extraction of information on the
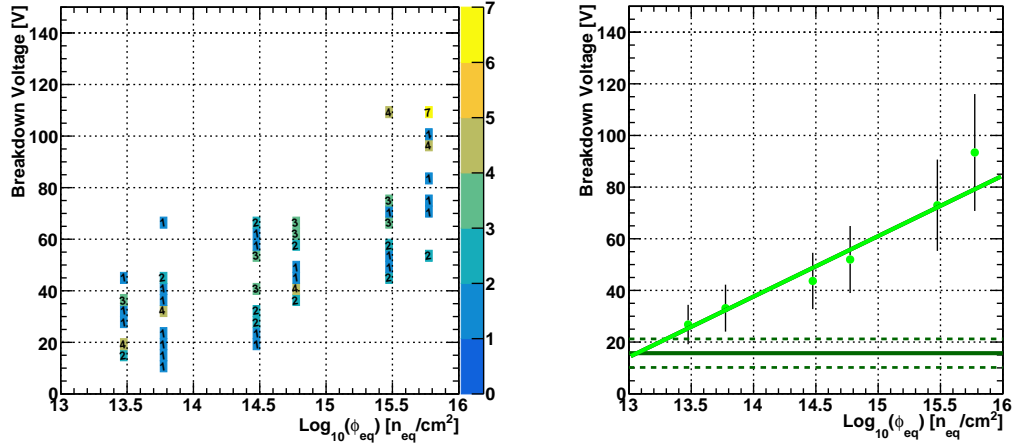
Figure 5.11: First analysis approach. Left: example of a 2D histogram filled with the values of the breakdown voltage for FEI4 sensors as a function of the logarithm of the fluence. Right: profile extracted from the 2D histogram on the left. The data points are the mean values of the histograms for each fluence value; the error is standard error on the mean. The light green line is the linear fit to the data points, while the horizontal solid and dashed dark green lines respectively represent the mean breakdown voltage and its uncertainty for the unirradiated sensors.

drift velocity profile and thus on the electric field configuration. Charge collection efficiency measurements as well as surface uniformity scans can be performed using this technique.

The signal is induced by a short laser pulse, of $\mathcal{O}(100\,\mathrm{ps})$. This fast pulse ensures that all charges are produced in an amount of time smaller than the typical charge collection time: the width and shape of the typical $\mathcal{O}(10\,\mathrm{ns})$ signal depends on the type of charges transporting the signal and their collection time [150].

TCT setups use red ($\lambda_R = 660$ nm) or infrared ($\lambda_{IR} = 1064$ nm) lasers, which can be shone from top or bottom of the sensor. The IR laser can also be used to scan the sensor across its thickness, illuminating it from the side, and in this case the technique is called edge-TCT (eTCT).

The two wavelengths have a different penetration depth: the IR laser acts like a MIP because its energy is lower than the silicon band gap. IR light entirely crosses the silicon sensor thickness (at $t = -20\,^\circ C$ the absorption length is > 1 mm) and creates $e - h$ pairs through the full thickness [150]. The red laser, on the contrary, releases all its energy within the first 10 μm from the surface: the laser intensity

137
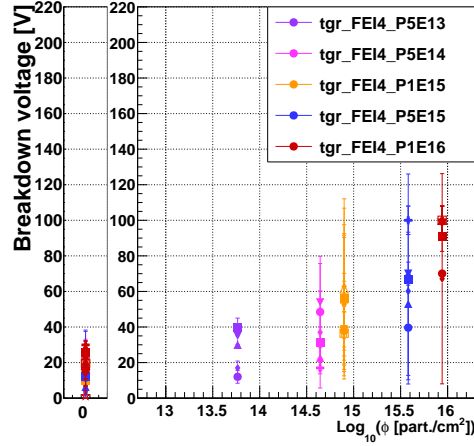
Figure 5.12: Example of an output canvas using the second analysis approach. The canvas has two pads: the left one contains the values of the parameter for each sensor before irradiation; the right pad, instead, shows the value of the parameter after irradiation. Only data of sensors that are measured both before and after irradiation are reported: each sensor or strip, irradiated at a single given fluence, is defined by a marker colour - common to the same fluence - and an individual marker style.

follows a steep exponential decrease with depth inside the silicon and is reduced to $1/e$ of the initial value at only $\sim 3\ \mu$m.

In a planar sensor, using a red laser gives the advantage of having the possibility to measure separately the current component given by the electrons from the one given by the holes. The pulse shape is, in fact, related to the field configuration encountered, at each instant, by the drifting charges, as described by Ramo's theorem (see Section 3.2.1).

Taking as example an n-in-p planar sensor, when illuminating its n^+-doped side (Figure 5.13a), the $e - h$ pair cloud is produced in the proximity of the electrode surface. Electrons are immediately collected by the n^+ electrode giving a high, short pulse. The measured signal is therefore mainly given by the drift of holes across the full sensor thickness towards the p^+. As the electric field decreases towards the $p-$side, the induced signal is lower and lower.

On the contrary, when shining with red laser from the bottom (Figure 5.13b), the holes are immediately collected giving a high and short signal, while electrons drift towards the increasing electric field and induce a higher and higher signal on

138

the junction electrode.

Given its large penetration depth, the IR laser ionises the silicon atoms along the entire sensor's thickness. Its output signal is given by the contribution of both electrons and holes (Figure 5.13c) [151]. Acting like a MIP, the IR laser is used to measure the charge collection of a sensor.
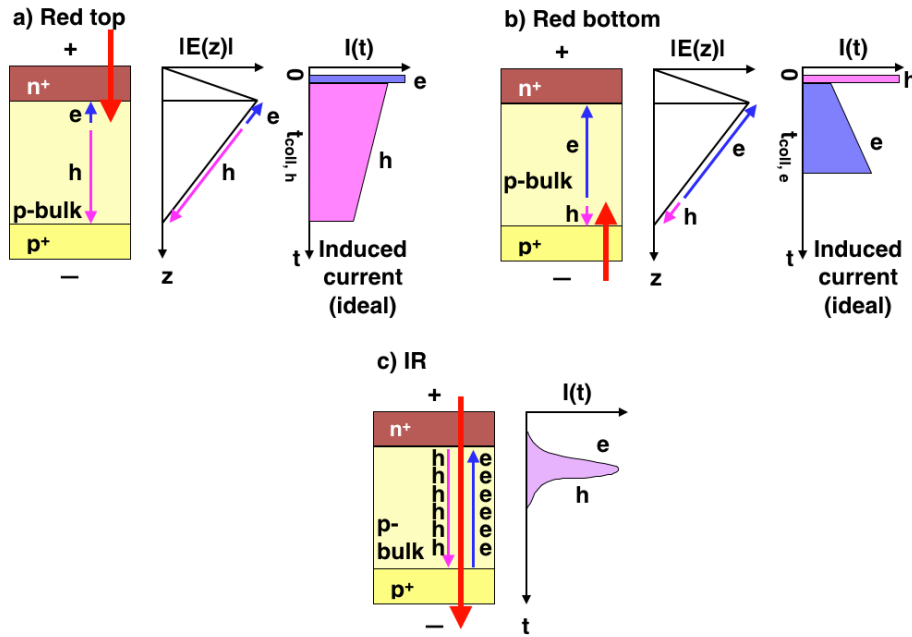
Figure 5.13: Sketches showing the charge drifting of holes and electrons in a TCT measurement, in the case of (a) red laser from the top, (b) red laser from the bottom, (c) IR laser. Image adapted from [151].

Signal height changes if lasers hit metal surfaces, because the light gets reflected. In the case the laser is reflected outside the sensor, there is no charge collection. Vice versa, if the IR light is reflected inside the silicon, photons cross twice the sensor and the net effect is a higher collected charge.

The eTCT technique consists in illuminating the sensor from the side, performing a scan across the thickness of the sensor. With this method it is possible, for example, to infer the shape of the electric field between the two electrodes of planar sensors and measure the depletion depth. In a fully depleted planar sensor, all the generated charge is collected at all z positions: what varies is the shape of the signals, shorter in time and higher in amplitude for z closer to the junction electrode, longer and lower in z positions closer to the other electrode.

In the case of underdepleted sensors, however, an eTCT measurement senses the boundary of the depleted region: outside of the depleted volume, charges do not drift and their movement is only caused by thermal diffusion.

5.4.1 The TCT+ setup

The TCT+ setup is one of the laser setups available in the CERN SSD labs. Both eTCT and normal TCT measurements can be performed. The sensor under test can therefore be illuminated from the frontside and from the backside with red and IR lights, and from the side with IR light.

The system is sketched in Figure 5.14. Figure 5.15 shows a photo of the interior of the cooling box and the laser part.
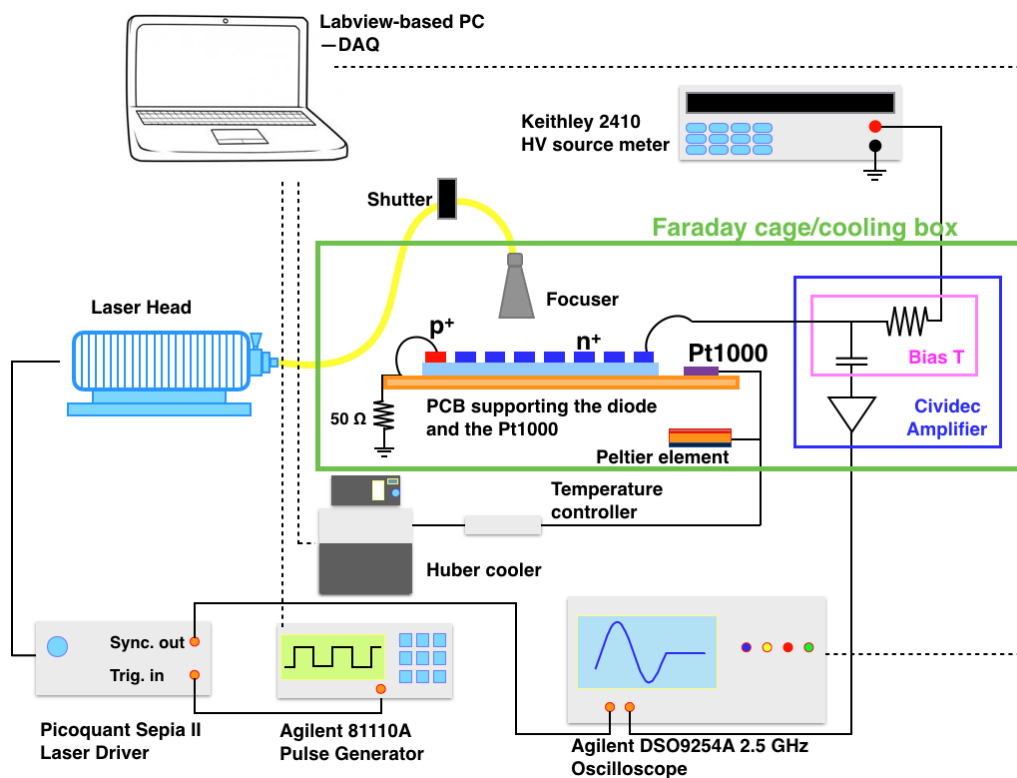
Figure 5.14: Sketch of the TCT+ setup. Image adapted from [75].
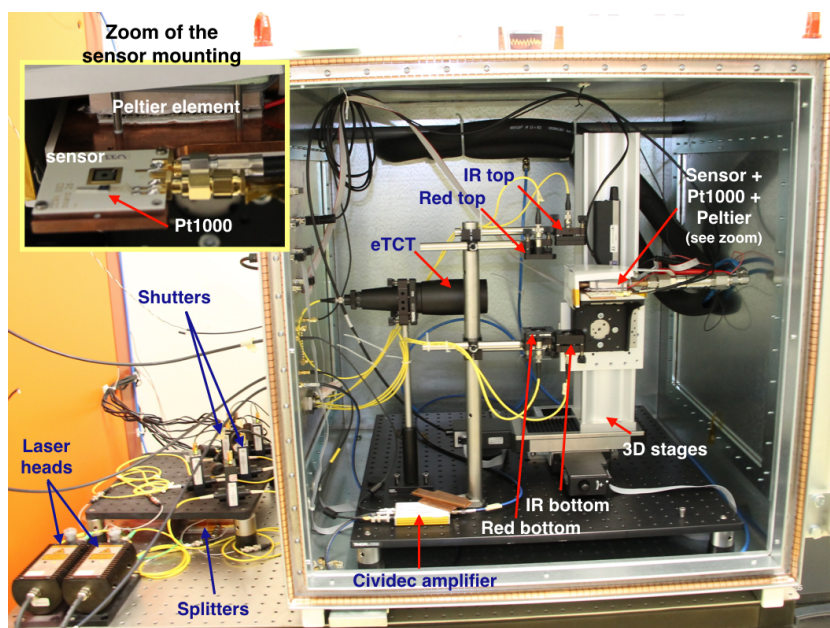
Figure 5.15: Photo of the TCT+ setup: the interior of the box and the laser system are visible. A zoom of the sensor mounting is shown.

5.4.1.1 Electrical connections

In this setup, the sensor is glued to a custom-made PCB in correspondence of a small hole that allows bottom lasers to reach the sensor. Wire bonds connect the electrodes to two SMA connectors: in the case of a n-in-p sensor, the p^+ is grounded via a $50\,\Omega$ resistance, while the n^+ electrode is connected, via a bias-Tee and an amplifier, to a fast, $2.5\,$GHz-bandwidth amplifier, followed by a Keithley 2410 power supply. The bias-Tee has the function of splitting the AC output current that corresponds to the signal from the DC current used to deplete the sensor. If this precaution was not adopted, the high bias voltage would enter into the oscilloscope, damaging it. Using a current Cividec amplifier [152], the bias-Tee is already integrated into the amplifier device. The Cividec amplifier is biased at $12\,$V. The outcoming signal is sent to the oscilloscope, which collects and digitises 256 signals and saves their average shape.

5.4.1.2 Laser chain

The lasers are driven by a pulse generator at a nominal frequency of $200\,$Hz. This device can activate either the red or the IR laser heads. The laser intensity

provided by the laser driver can be modified according to needs: standard settings for the laser intensities are 40% for red and 60% for IR lights. Fine-tuning of the intensity of the lasers can be set on the laser heads by manually changing the aperture through which the laser passes. Depending on the aperture, the amount of energy deposited in the sensor can be varied. Figure 5.16 shows, for red and IR lights, the amount of energy deposited in the sensors in units of MIPs [153]. These heads are connected to a series or splitters that distribute the two lights to the laser optics. Their schematics is shown in Figure 5.17. Both lights are initially split in 90%-10%. The larger fraction of the red laser is equally split in two, reaching either the red top or red bottom optics. The 90% of IR laser is divided as well into two equal parts, one directly reaching the eTCT optics and the other being split again in two before reaching either the IR top or IR bottom optics. The remaining 10% from each laser is sent to a corresponding reference, biased photodiode. Data from these reference diodes are recorded during the data taking and are used to normalise different measurements to the same initial conditions by dividing them by the laser power. The laser power is computed following:

$$P = \frac{U_{signal}[V]}{R} \cdot \frac{1}{\mathcal{R}}, \tag{5.20}$$

where U_{signal} is the peak signal measured by the reference diode, R is the impedance ($R = 50\ \Omega$) and $\mathcal{R}$ is the responsivity of the photodiode. The latter parameter is provided by the constructor of the photodiode and measures the electrical output per optical input. It is expressed in W/A and depends on the wavelength of the laser.

In order to determine which optical path receives light, laser optics are preceded by electrically-controlled shutters, set by a TTL signal sent by an Agilent 34980A switch. Laser beams are focused, using lens, to a diameter of $\sim 10\ \mu$m.

5.4.1.3   Environmental control

The PCB supporting the sensor is screwed onto an aluminium interface board, which is mounted onto a 3-axis stage system. The stages are remotely controlled by a Newport Motion controller ESP301.

The PCB also hosts a Pt1000 thermistor that is used for measuring the temperature of the sensor under test. The second component of the cooling system is the Peltier element: glued to the aluminium interface board with a thermal glue, it takes care of reaching and stabilising the desired temperature of the sample.
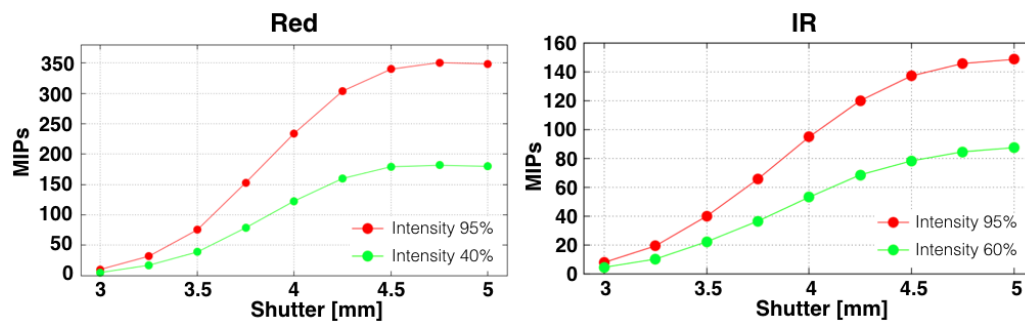
Figure 5.16: Number of MIPs as a function of the laser head aperture, for red (left) and IR (right) lights. The green curves are the standard settings for the laser intensities, the red curves refer to 95% of the maximum intensity. Image reproduced from [153].
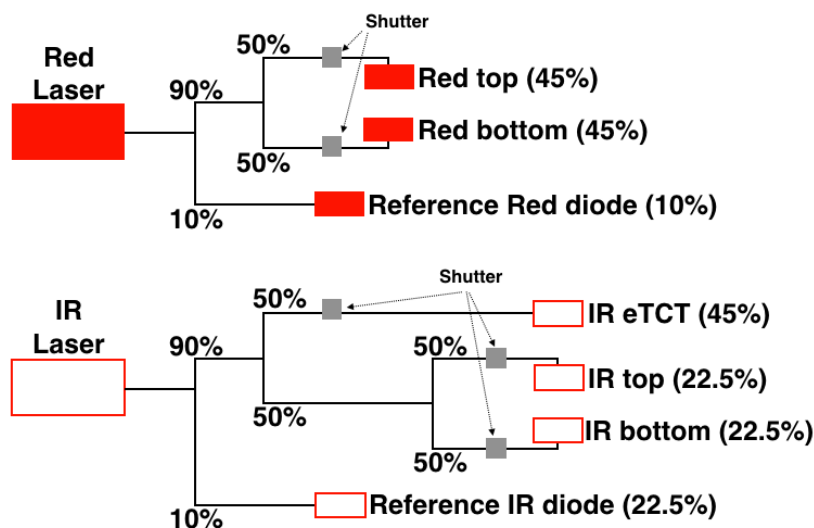

Figure 5.17: Laser splittings for the red and IR laser paths. Percentages indicate the fraction of the light that goes into each direction in the particular splitter node. In the end, red top and red bottom lasers receive 45% of the initial intensity, IR eTCT gets 45% of the IR light and the IR top and bottom get 22.5% of the initial light. The remaining 10% of intensity of both red and IR lasers is sent to the reference diodes. Each laser optics is preceded by a shutter.

This device exploits the Peltier effect: applying a voltage difference between the two faces of the device, depending on the polarity, one surface becomes warmer, while the other cools down. The heat is removed from the warm face by a closed

liquid circuit controlled by the chiller. The Peltier element is controlled by the Laird PR-59 temperature controller.

The sensor, the interface board with the Peltier element, the laser optics and the stages are located inside a box[6], which acts as electromagnetic shield and thermal insulator. Dry air is circulated inside the box to avoid condensation.

5.4.1.4 Data acquisition system

A Labview interface, implemented by the SSD group, controls all the aspects of the TCT+ setup: the cooling system, the stage motion, the high and low voltage supplies, the lasers and the data acquisition system. The older version of the Labview program was able to perform 1 measurement step in ~ 5 s, while now, after a time-optimisation, it collects data at a speed of 1 step every 1 s. Scans in the three directions as well as loops over temperature and voltage ranges can be performed.

5.4.2 Analysis on the laser-induced charge

The TCT+ data acquisition system outputs a text file containing all information concerning the performed run, such as all the waveforms collected by both the sensor and the reference photodiode, the temperature recorded at each event, the type or run, the coordinate scanned during the measurement, etc.

The output file can be analysed using the analysis code developed by members of the SSD team. This analysis produces a complete set of plots and histograms that illustrate the basic outcomes of the single run, some of which will be shown in Section 6.3.

A further step in the analysis, developed during this thesis work, can be done towards the comparison among sensors. TCT+ measurements were performed only on SINTEF 3D BABY sensors, which were exposed to different fluences or have different pixel cell configurations. A study can be carried out to understand the variation of the collected charge against either of these two parameters (e.g. evolution of the charge as a function of the fluence for a given pixel configuration and dependence on the charge on the pixel configuration for a given fluence).

The analysis described in the following aims at extracting a mean value of the collected charge from the xy scans performed at different voltages, which can be the input for the mentioned plots. From surface scans the collected charge as

---

[6]The box is produced by ETS-Lindgren.

a function of the position (charge map) is measured. The evaluation of a single charge value out of 2D charge maps is not straightforward because of the peculiar geometry of 3D sensors that features a large fraction of the surface being covered by the temporary metal layer (Table A1 shows the fractions of metal-free surface for the different pixel configurations as well as the percentage of the volume occupied by the electrodes).

Different approaches were therefore studied to identify a charge value representative of each xy measurement: options included the identification of the maximum value across the charge map, or the computation of the mean or the mode values over all the points of the map. All these procedures suffer from limitations: the maximum value, for example, is biased by the possible presence of hot spots, the mean value obtained averaging all points across the xy scan underestimates, in top-light measurements, the mean charge because of the low collected charge in correspondence of metal strips and columns.

The chosen approach is based on the idea presented in [154]: the output value is the average of the charges collected only in the high-charge regions, assuming that the low-charge regions are areas where the laser hits the metallic strips (shown in Figure 5.3a) and is reflected away from the sensor. This assumption is known to lead to an overestimation of the mean value of the charges collected in the metal-free areas, because it excludes from the averaging the uncovered regions characterised by a low electric field, where the charge collection efficiency is reduced.

The method, applied to measurements where the laser is applied from the top of the sensor, consists in computing the average value of the charge across the charge map (e.g. the map in Figure 5.18a) after applying a flexible cut. The cut is calculated as follows: first, the map is sliced in vertical projections along the $y-$axis for each $x-$bin (roughly perpendicular to the strips). The $x-$bin whose integral over the $y-$bins is the highest is chosen for the following step. The adoption of the $y-$projection with the highest charge, shown in Figure 5.18b, implies that the electrodes are avoided and the minima in the projection correspond to the case where the laser hits the metal strips.

The analysis identifies the threshold as

$$Q_{thr} = \begin{cases} (Q_{max} - Q_{min}) \cdot f + Q_{min}, & \text{if } f \geq 0 \\ 0, & \text{if } f = -1 \end{cases} \quad (5.21)$$

where Q_{max} and Q_{min} are respectively the maximum and minimum values of the

145

chosen $y-$projection of the charge map and f is a fixed fraction of this sum. For example, if $f = 0.5$, then the threshold charge will be the mean value between the maximum and the minimum. The only exception is represented when setting $f = -1$: in this case, the threshold charge is set to 0 and all the map points are taken into consideration.

This threshold Q_{thr} is adopted to discard, in the 2D map, the bins corresponding to the metal strips and the electrodes: the charge above threshold of the 2D map feeds a 1D histogram of the charge distribution from which the mean and the standard deviation are extracted.

These two values are normalised by the laser power measured at each scan (using Equation 5.20) and then used as a value and associated error to be plotted against fluence. Typical values of the power intensity are $P_{red} \sim 70~\mu$W for the red laser and $P_{IR} \sim 80~\mu$W for IR light.

The analysis does not consider scans performed using IR bottom illumination: as it will be discussed in Section 6.3, charge maps obtained from such measurements are more difficult to interpret (because of the internal reflection of the laser on the surface metal) and do not provide more information than the one obtained by analysing IR top scans.

(a) Charge map.
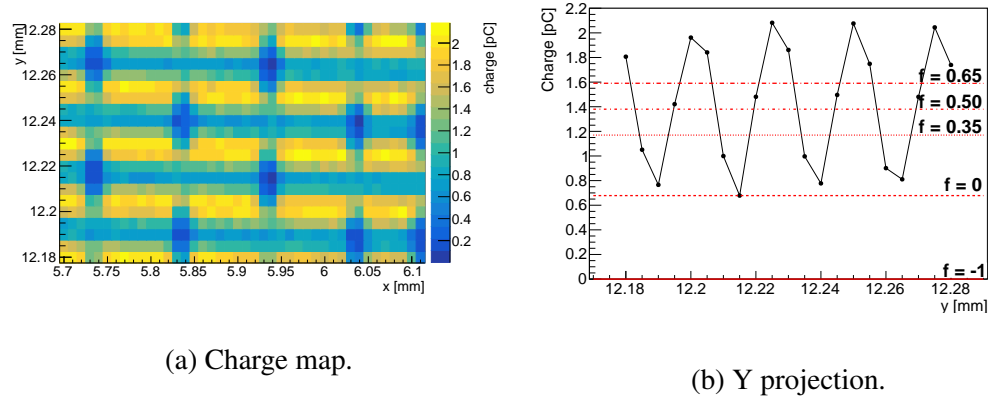
(b) Y projection.

Figure 5.18: Left: Charge map from an IR top xy scan of the unirradiated sensor 222 (2E) from wafer C23. Right: $y-$projection of the charge distribution of the $x-$bin with the highest total charge integrated over y ($x = 5.97$ mm). Minima represent the charge collected when the laser light is mostly blocked by the metal strips, while maxima are the charge collected in the metal-free areas.

146

5.5 Radioactive source characterisation

Radioactive source measurements are used to evaluate the performance of the sensor in the most realistic conditions. Properties such as charge collection and signal strength (the ratio between the collected signal and the noise of the sensor) can be assessed also as a function of the radiation damage.

5.5.1 The ALiBaVa system

The commercially-available Analogue Liverpool Barcelona Valencia (ALiBaVa) [155] read-out system was used to read out the signal produced by the sensor when crossed by a β particle from a ^{90}Sr source.

Figure 5.19 shows the setup [156]. The ALiBaVa system is mainly composed by two devices: the Mother Board (MB) and the Daughter Board (DB), connected via a flat cable.
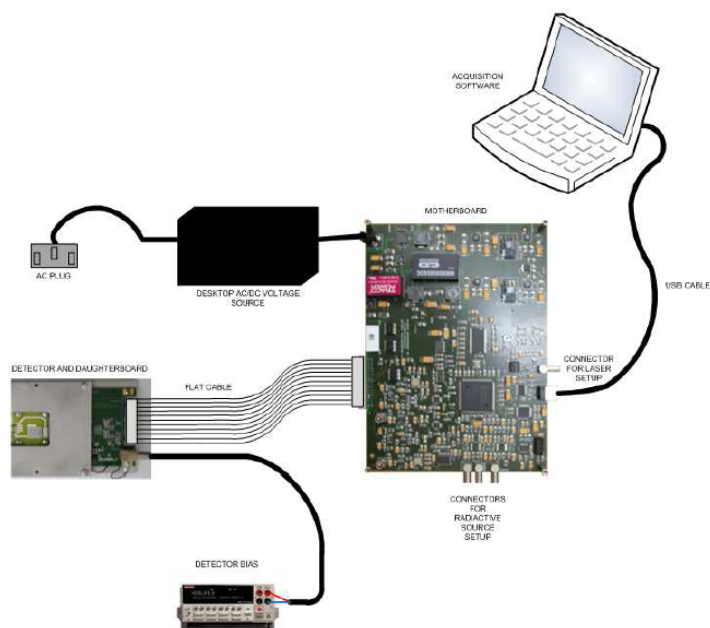
Figure 5.19: Sketch of the ALiBaVa setup. Image reproduced from [156].

The DB is equipped with two independent Beetle ASICs [157, 158], read-out chips developed by the LHCb Collaboration for its strip detector. The Beetle chip has 128 input channels with independent amplifiers and pulse shapers. Each chip

has 4 output driver ports, each connected to 32 channels. The output signal of the shaper rises in around 25 ns from 10% to 90% of the peak.

The MB receives the signals from the DB and, when an external trigger is used, from the triggering system. The data acquisition software, part of the ALiBaVa package, and the MB are connected by an USB cable.

The ALiBaVa setup can run in five modes: the pedestal, calibration, laser synchronisation, laser and radioactive source runs. In the pedestal run, the MB generates an internal trigger for the data acquisition of random events whose data are used to compute the pedestal and the raw noise. From the calibration run, the conversion between the ADC[7] data and the charge is extracted: the Beetle chip injects calibration pulses to all channels and reads back the ADC counts. Since the ALiBaVa setup is capable of reading both positive and negative signals, both polarities of the injected charge are scanned during calibration. The laser synchronisation and laser runs were not used for this work. The first is used to define the delay between the input trigger, fed to the laser generator to produce the laser pulse, and the output signal. Defining the correct delay is essential to collect the data at the maximum of the signal. The laser run performs the data acquisition when a laser source is used. Last, the radioactive source run consists in the measurement of the charge collected in the sensor when exposed to a radioactive source. The trigger is externally provided by a scintillator.

A detailed description of the ALiBaVa read-out system is provided in [159].

5.5.2   The SSD ALiBaVa setup

In the SSD lab, the ALiBaVa system is hosted inside a climate chamber. The Binder MKT115 climate chamber can operate in the temperature range $[-70, +180]$ $°C$ and is provided with a flux of dry air.

A custom-made interface board, able to accommodate the sensor board and the DB, is mounted onto a remotely-controlled $xy-$stage. The radioactive source flux can be regulated by using different collimators, 1-cm$-$thick brass cylinders with a central hole of $1, 2$ and 3 mm in diameter. In all measurements, the 2 mm$-$diameter collimator was used. In the vertical axis three pieces of equipment must be aligned: the radioactive source, the sensor and a ~ 160 mm^2 plastic scintillator, coupled to a photomultiplier. The ^{90}Sr radioactive source available in the SSD lab has an activity of 26.68 MBq.

---

[7]ADC = Analog to Digital Conversion.

Figure 5.20 shows the ALiBaVa system mounted inside the climate chamber. An aluminium interface was designed to host the ALiBaVa daughter board and a custom-made PCB onto which the fan-in(s) and the sensor(s) are glued (see Figure 5.21). The electrical connection between the daughter board, its fan-in, the sensor's fan-in and the sensor itself is provided by wire bonds.
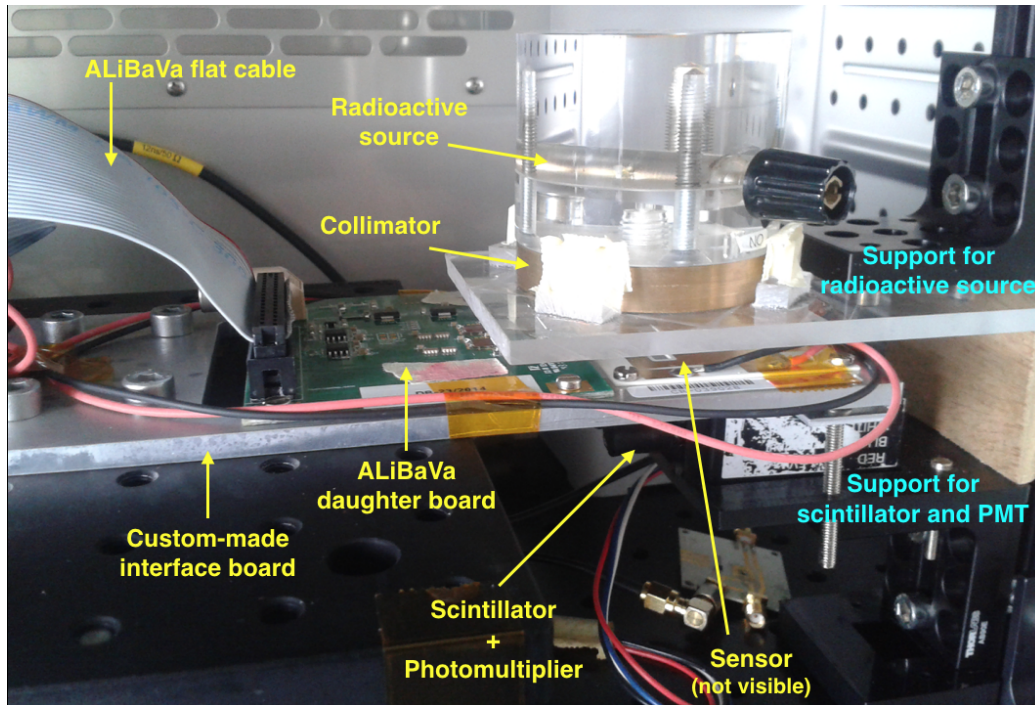

Figure 5.20: Photo of the ALiBaVa experimental setup inside the climate chamber.

As the output signal must be decoupled from the DC current biasing the detector, AC coupled fan-ins must be used for DC coupled sensors and, vice versa, DC coupled fan-ins can be used for AC coupled devices. The ALiBaVa fan-ins have a pitch of $80\ \mu$m. The SINTEF 3D FEI3 and FEI4, however, have a different pitch and a smaller number of strips with respect to the 128 Beetle chip channels. As a consequence, to maintain the wire bonds as short as possible, not all Beetle chip channels are connected. Figure 5.22 shows the wire bond connection for the FEI3 and FEI4 sensors. Moreover, because of the larger dimension with respect to the fan-in width, only half of each FEI4 sensor was wire bonded.

The scintillator+photomultiplier system provides the trigger signal that starts the data acquisition at the MB level. The trigger is propagated via the flat cable to the DB. The DB samples the signal synchronously to an internal clock running at
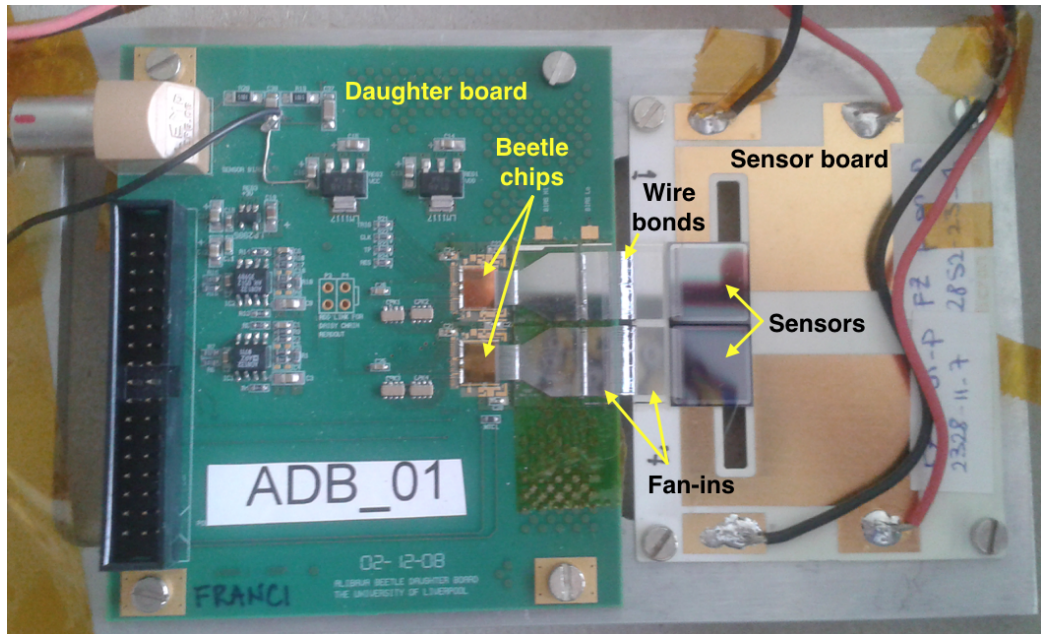
Figure 5.21: Photo of the custom-made interface board, populated with the ALiBaVa daughter board, the custom-made sensor board onto which two planar sensors have been wire bonded, through the fan-ins, to the Beetle chips.
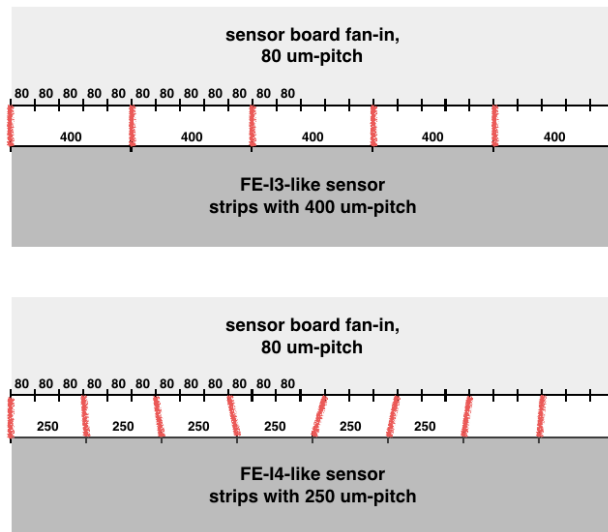
Figure 5.22: Wire bond connections between the ALiBaVa AC-coupled fan-in and the SINTEF 3D FEI3 and FEI4 sensors.

40 MHz, while a time delay counter provides the timing information between the trigger signal and the 4 closest samples: the signal measured by both the Beetle chips is acquired during a 100 ns time window.

From a timing point of view, the β particle passes through the sensor and the scintillator at about the same time: the two signals are generated simultaneously. The signal from the sensor is temporarily stored in the DB, while the photo emission of the scintillator is converted into an electrical signal in the photomultiplier and it is then propagated to the MB. From here, the trigger is issued to the DB via the flat cable and sensor's data is read out and stored, as raw ADC counts, in a binary file by the data acquisition system. The propagation of the trigger signal determines a delay between when the trigger is issued and when data are read out from the DB. This latency, which depends on the physical length of the cables, is compensated by reading the DB "in the past" (by a certain amount of internal clocks). The default value of the latency is 128 (in units of 25 ns). The standard value must be kept when performing the calibration run, but has to be set according to the setup when taking a Radioactive Source run.

The data acquisition program is provided by ALiBaVa and features a GUI[8] where settings, such as the number of events to collect, the trigger levels and the parameters of the Beetle chip, can be specified. It also includes a variety of online plots, suitable for monitoring the progress of the run.

5.5.3   The ALiBaVa data analysis

The output file saved by the acquisition system has a binary format. It is divided into two parts: a header, where the information about the run (type of the run, start time of the run etc.) is saved, and the data block, where the ADC counts are saved for each Beetle chip channel at each event. The data format is described in the ALiBaVa manual [160]. Analysing the data, it was discovered that the header data format, as described in the manual, does not take into account the possible different computer architectures and defines the time of start of the run as a 32 bit variable. However, in the case the DAQ computer has a 64-bit architecture, this variable is saved in 64 bits. If it was not corrected, this discrepancy would have led to a wrong decoding of the input datafile.

Data collected by the ALiBaVa read-out system are analysed by custom-made ROOT macros, implemented for this thesis work. The binary file is first decoded,

---

[8]GUI = Graphical User Interface.

according to the ALiBaVa data format for the different run types, and information is stored into a ROOT TTree.

5.5.3.1 Pedestal and raw noise

The pedestal and raw noise for each channel are computed analysing data from the pedestal run. The pedestal is the measured ADC value when no particle crosses the sensor. It has a channel-to-channel electronic variations. The raw noise is the width of the pedestal distribution for a single channel and represents the noise generated by the sensor, the front-end electronics and the external environment [161]. The pedestal is computed for each channel as the mean value of the distribution across all events:

$$Ped_{str} = \frac{1}{N_{\text{events}}} \sum_{ev=1}^{N_{\text{events}}} (ADC_{str,ev}^{Ped}) \tag{5.22}$$

where N_{events} is the total number of events, $ADC_{str,ev}^{Ped}$ is the raw ADC value collected during the pedestal run for each strip str at each event ev.

The raw noise is the standard deviation of the pedestal distribution for each strip. Channels close to the edge of the read-out chip are masked by default, and so are those that have a too-large raw noise. Masked channels are no longer processed in the rest of the analysis. Because of the different pitch of the SINTEF sensors causing some ALiBaVa channels to be disconnected from the sensor, the masking procedure is approached by reading a file with the list of the connected strips, masking by default all non-connected strips, and evaluating only the raw noise of the connected ones.

5.5.3.2 Common mode

The common mode shift is the random variation of the channel input enhanced by environmental origins, like pick-up effects of the sensor and the instability of the reference grounds induced by the power supply. It affects in the same way all the channels connected to a single Beetle port and changes on an event basis. It is computed from the radioactive source run.

For calculating its value, a histogram, built for each event and each port, is filled with the values of the pedestal-corrected raw ADC ($ADC^{PedCorr}$):

$$ADC_{str,ev}^{PedCorr} = ADC_{str,ev}^{Sr90} - Ped_{str}, \tag{5.23}$$

namely subtracting the mean pedestal previously computed, Ped_{str}, to the raw ADC counts of the radioactive source run ADC^{Sr90}. The mean and RMS of the $PedCorrADC$ distribution represent the first, raw, common mode $cmmd1$ and its RMS σ_{cmmd1}.

The final common mode is given by the mean value of a second distribution filled with $ADC_{str,ev}^{PedCorr}$ that satisfy the condition

$$|ADC_{str,ev}^{PedCorr} - cmmd1| < \sigma_{cmmd1}. \tag{5.24}$$

5.5.3.3 Signal and noise

The signal is the charge produced by the interaction of a particle with the sensor. It can be calculated subtracting from the raw ADC of the radioactive source run the pedestal and common mode previously calculated:

$$signal_{str,ev} = ADC_{str,ev}^{Sr90} - Ped_{str} - cmmd_{port,ev}. \tag{5.25}$$

The noise, defined as the random fluctuation in an electrical signal, is calculated as the RMS of the signal distribution. It can be expressed in terms of equivalent noise charge (ENC).

5.5.3.4 Charge collection

The knowledge of the signal and the noise for each event is used to compute the signal-to-noise ratio (SNR), which gives an indication of the strength of the signal. This parameter is used in the clustering algorithm to determine the collected charge. The cluster seed strip is identified by requiring

$$SNR_{seed} > 5. \tag{5.26}$$

The cluster expands over the neighbouring (connected) strips as long as the condition

$$SNR_{neighbour} > 3 \tag{5.27}$$

is true. If the neighbouring strip is masked, then the cluster extreme is found and no more strips in that direction are checked. In the case the analysis runs over data from SINTEF sensors, the clustering process continues even if a masked strip is found: this expedient is used because of the special strip pitch of the sensors and their non-uniform connection to the Beetle chip channels.

The total cluster charge distribution is then plotted. The cluster selection is refined by applying a cut: the final cluster charge distribution is fed only by the charge collected in a 10 ns window centered around the maximum of the Beetle chip shaper output signal. The obtained charge distribution is fitted with a Landau-Gaussian convolution function. The most probable value (MPV) of the convolution is the reference value for the collected charge, expressed in ADC counts or in electrons depending on whether the calibration factor has been applied. This factor is extracted from the calibration curves, measured during a calibration run. Such curves, measured for each channel, describe the variation of the ADC counts as a function of the injected charge. In the range of interest ($Q < 1 \cdot 10^5$ e$^-$), they have a linear proportionality. The calibration factor is the coefficient of proportionality.

The conversion between ADC counts and electrons is therefore:

$$Q[\text{e}^-] = \frac{Q[\text{ADC}]}{cal}, \tag{5.28}$$

where cal is the calibration factor.

Chapter 6

Experimental results

The experimental results from the measurements on the SINTEF 3D silicon sensors performed by exploiting the techniques (and experimental setups) described in Chapter 5 are reported in this chapter.

The chapter is organised in four sections: the properties of the sensors used for the purpose of this work are summarised in the first section, while the experimental results from the IVCV, the TCT and the ALiBaVa measurements are described in the following three sections.

6.1 The measured sensors

These measurements described in this chapter are the first laboratory characterisation of the third prototype run of SINTEF 3D sensors. Three types of sensors were measured: BABY, FEI3 and FEI4 sensors. The BABY sensors are small structures in which all junction electrodes are shorted together and so are all ohmic columns. The FEI3 and the FEI4 sensors have a metal layer that connects all p^+ columns in a single matrix, while the junction electrodes are connected in strips (there are 18 strips in a FEI3 sensor and 80 in a FEI4 sensor). More details on the geometrical properties of the sensors are indicated in Table 5.1. A summary of the sensors (types and wafers of origin) from SINTEF Run-C that were tested using the three experimental methods is reported in Table 6.1. Among the 6 measured wafers, only wafer C25 is a "good" wafer, whose sensors presented good electrical properties in preliminary measurements and were the only FEI4 sensors coupled to FE-I4 read-out chips via bump bondings and measured in beam tests.

To compare the performance of SINTEF 3D sensors to other devices, sensors with planar geometry and 3D sensors produced by other institutes (CNM, Barcelona) were tested. Two planar devices were measured: a $n-$bulk pad and a $p-$bulk strip sensor. They have a thickness of 300 μm and an active area of, respectively, $\sim 5 \times 5$ mm^2 and $\sim 1 \times 1$ cm^2. The strip sensor has a strip pitch of 80 μm and a total capacitance of ~ 40 pF. The CNM 3D sensor is a double-sided 3D detector in which a matrix of 90×90 electrodes is implanted in a 300-μm$-$thick $n-$doped silicon wafer for a depth of 250 μm (columns are not fully through), with a pitch of 55 μm. Its electrical configuration is similar to that of BABY sensors, with all same-type electrodes connected together.

Wafer Name	Measured sensors	Measurement methods
C16	FEI4	IV[1]
C17	FEI4	IV
C21	FEI3	IV, CV[2], RS[3]
	FEI4	IV, CV, RS
C23	BABY	IV, CV, Laser[4]
	FEI3	IV, CV, RS
	FEI4	IV, CV, RS
C25[*]	BABY	IV, CV, Laser
C26	FEI3	IV, CV, RS
	FEI4	IV, CV, RS

Table 6.1: List of the wafers from Run-C whose sensors were measured with the three experimental methods. [1] IV is the measurement of the current vs. voltage; [2] CV indicates capacitance vs. voltage scans; [3] RS stands for radioactive source measurements; [4] Laser refers to laser measurements.
[*] Wafer C25 is the only Run-C wafer whose sensors showed good electrical properties in preliminary tests.

6.1.1 Origin of the problems of the Run-C SINTEF sensors

The measured sensors belong to a prototype run that overall showed high leakage current and low breakdown voltage. At the time the measurements on sensors from this batch were taken, there was no clue of the production issues causing these behaviours. The turning point occurred during the currently-undergoing production of Run-D (see Section 5.1.2), when SINTEF discovered that the

possible origin of these issues lies in a few steps of the production method. In particular, problems happen during the metal sputtering, the process aimed at uniformly distributing the metal on the wafer surface (steps 3-4 and 9-10 of Figure 5.1): rather than obtaining a thick and uniform coverage, the process may have resulted into an irregular and thin layer. As a result, the consecutive etching and polysilicon filling steps may have created some pin-holes, effectively generating extra randomly-distributed "electrodes". These structures do not show the same hole profile as the normal electrodes do, as they do not penetrate through the entire wafer thickness. Nevertheless, they alter the electric field on the surface and in the bulk of the sensor and lead to an increase in the leakage current, given by the shorter-than-foreseen inter-electrode distance.

6.2   Electrical characterisation results

Preliminary measurements on a large number of SINTEF 3D sensors were performed using the IVCV setup. These tests aimed at understanding the behaviour of the sensors from the purely electrical point of view (e.g. excluding interactions with particles) before and after irradiation. In particular, it was of interest to evaluate the magnitude of electrical properties (depletion and breakdown voltage, leakage current, full depletion capacitance) as a function of the fluence.

Initial tests were performed to assess the possibility to improve the IV and CV curves' shape by exposing the sensors to different treatments (Section 6.2.1). Measurements were repeated before and after the wafer dicing (see Section 6.2.2), at different temperatures and LCR frequencies (Sections 6.2.3 and 6.2.4). Section 6.2.5 reports the observed stability of the IV curves, for some sensors, when the same measurement was repeated several times. The dependency of the electrical properties on the pixel geometry and on the pixel cell dimensions was studied (Sections 6.2.6 and 6.2.7). The dependence of the electrical properties after irradiation are discussed in Section 6.2.8. Finally, Section 6.2.9 lists the most recurring unexpected behaviours observed during the IVCV measurement campaign.

6.2.1 Baking and plasma cleaning effects on the leakage current

The electrical characterisation was performed in different stages and after the sensors were exposed to different treatments. The first electrical characterisation (IV measurements) of SINTEF 3D sensors took place in the clean room of the MiNaLab laboratories in Oslo on single strips of FEI4 sensors from wafers C16 and C17. In order to probe a large amount of sensors while limiting the testing time, as measurements were performed manually, only every fifth strip was measured. This choice ensures a sampling of the electrical performance across the entire surface of the sensor, but it is not effective to identify local breakdowns, if the corresponding strip is not measured.

Both C16 and C17 wafers were undiced. Measurements were taken at room temperature, with no control on the stability of the temperature at the wafer level. Measurements on the same strips were repeated after the two wafers underwent various treatments: in sequence, baking, plasma cleaning and a second baking. The exposure to a high temperature may remove some defects in the silicon lattice and release mechanical strains; plasma cleaning may remove undesired chemicals from the surface.

Figure 6.1 reports the IV measurements, before and after each treatment, of some strips of the FEI4 No. 4 sensor from wafer C17. This sensor is located in the centre of the wafer, therefore it should have a reduced risk of presenting production issues typical of the regions closer to the wafer's edges, where the control over the thickness of the different layers is less effective, especially in case of a large magnitude of the wafer's bowing.

The exposure of the wafers to the series of treatments determined no systematic effects across the measured strips. Many strips showed a reduction of the breakdown voltage after the wafer was treated, while substantially leaving unchanged the leakage current in the plateau region. This trend is better illustrated in Figures 6.2a and 6.2b, where the effect after each treatment is shown for one single strip. With respect to the untreated curve (blue circles), the first baking decreased the breakdown voltage, the plasma clean did not induce any considerable effect on the IV characteristics and the second baking had a nondeterministic effect: data shows that it could either improve the IV curve, with respect to two previous treatments (generally without restoring the initial performance) or worsen it.

A counter-example of these trends is shown in the example of Figure 6.2c,
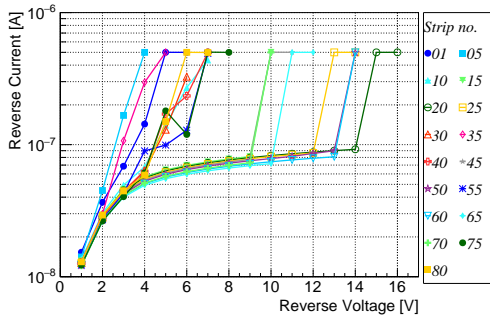
(a) Before treatment.
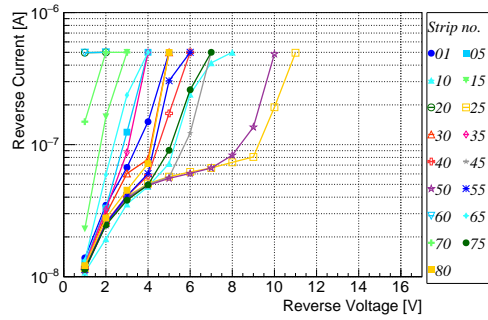
(b) After the first baking.
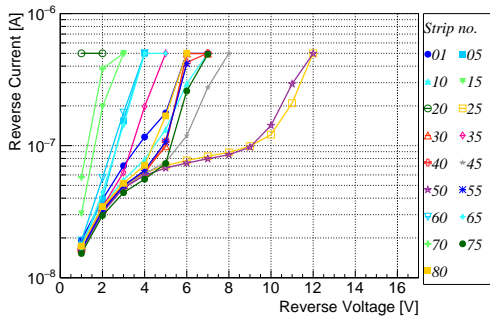
(c) After the baking and the plasma cleaning.
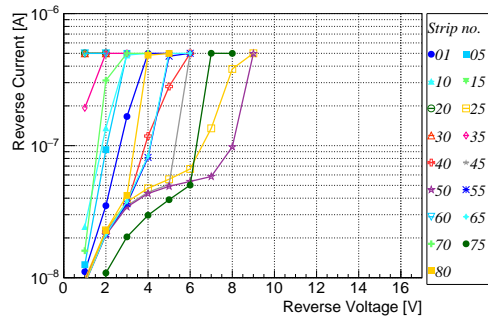
(d) After first baking, plasma cleaning and second baking.

Figure 6.1: IV curves of some strips of a FEI4 sensor from wafer C17 before and after different treatments.

where the effect of each treatment does not follow the previous observations: the untreated strip reached immediately the compliance current, the first baking improved the electrical characteristics, which were degraded after the plasma cleaning and improved again by the second baking.

This outcome, not proving an enhancement of the electrical properties after any treatment, indicates that the origin of the low yield of the Run-C SINTEF sensors cannot be associated to any uniformly-distributed doping or surface effects. Instead, these measurements support the findings of SINTEF during the Run-D production batch (see Section 6.1.1), which relate to the random generation, during Run-C production, of extra pin-holes.
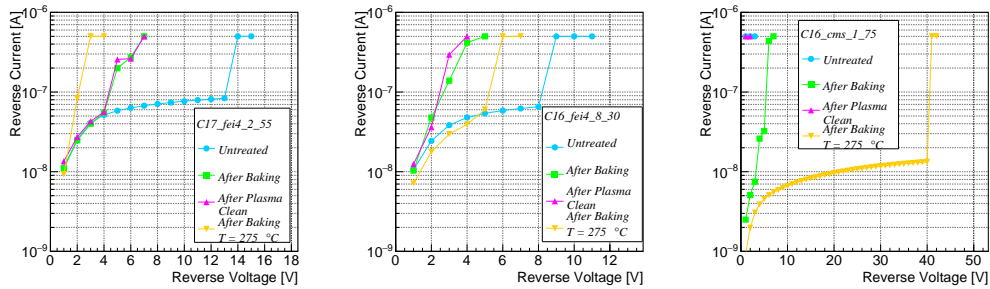
(a) IV curves of one strip (No. 55 from FEI4 sensor No. 2 of wafer C17).

(b) IV curves of one strip (No. 30 from the FEI4 sensor No. 8 of wafer C16).

(c) IV curves of one strip (No. 75 from the CMS sensor No. 1 of wafer C16).

Figure 6.2: IV curves measured at SINTEF, before any treatment (light blue circles), after the first baking (green squares), after the plasma cleaning (magenta up-triangles) and after the second baking (dark yellow down-triangles).

6.2.2 Dicing effects

When taking the measurements at SINTEF, the wafers were still undiced. According to literature [134, 162], a lower leakage current is expected with respect to diced sensors: the dicing procedure causes mechanical stress on the silicon lattice, breaking the atomic bonds at the sensor's edges, and favours the introduction of impurities on the silicon surface and on the edges. This effect is indeed observed in the results shown in Figure 6.3, where IV measurements of a BABY sensor before and after dicing are reported. Data were collected at a stable temperature of $t = +20\,°C$. The leakage current in the plateau region increases after the dicing by a factor ~ 4 at $U = 60$ V and the breakdown voltage is reduced by ~ 20 V.

6.2.3 Temperature dependence of the leakage current

The leakage current changes with the temperature according to Equation 3.11. Figure 6.4 shows its variation as a function of the voltage for different temperatures, for a proton-irradiated BABY sensor. As the temperature ranges from $t = -20\,°C$ to $t = +20\,°C$, the leakage current proportionally increases.

Figure 6.5 shows the Arrhenius plot for the leakage current as a function of the temperature for the same proton-irradiated BABY sensor as in Figure 6.4. The leakage current coordinate for each point is obtained by fitting with a line
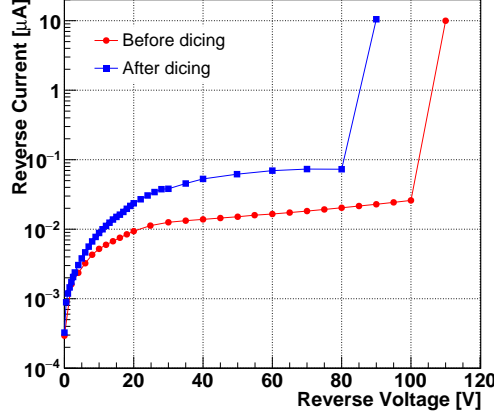
Figure 6.3: IV curves of one BABY sensor (No. 267 from wafer C25) before it was diced out from the wafer (red circles) and after the dicing (blue squares). Temperature was kept at $t = +20\,°\mathrm{C}$ during both measurements.

the plateau region of each curve of Figure 6.4, extracting its parameters p_0 and p_1 and applying the equation $I_{leak} = p_0 + p_1 \cdot U$ for $U = 70$ V, the mid-point of the plateau region.

The fit to the points, drawn in Figure 6.5, is described by the equation:

$$
\begin{aligned}
\ln\left(I_{Leak}\,[\mu\mathrm{A}]\right) &= p_0 + p_1 \frac{1}{T} \\
&= (27.55 \pm 0.1) + (-7331. \pm 20.)\frac{1}{T\,[K]}.
\end{aligned}
\tag{6.1}
$$

Considering that $\ln(I_{Leak}) \propto -\frac{E_g^{eff}}{2K_B T}$,

$$
E_g^{eff} = -2k_B \cdot p_1 \simeq (1.264 \pm 0.003)\ \mathrm{eV}.
\tag{6.2}
$$

This value is compatible with the literature value of $E_g^{eff} \simeq 1.21 \pm 0.06$ eV, which holds for both unirradiated and irradiated sensors [163, 164].

6.2.4 Frequency effects on capacitance measurements

Measurements of the capacitance-voltage characteristics performed setting different frequencies of the LCR meter, reported in Figure 6.6, show that if a too-low frequency is set on the LCR meter, the capacitance gets to non-physical

161
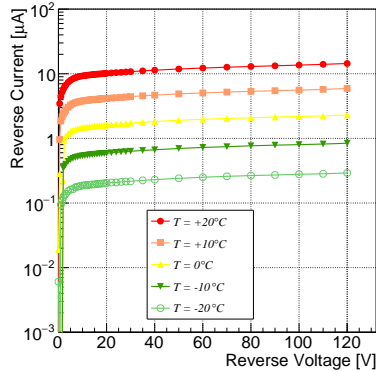
Figure 6.4: IV curves of one irradiated BABY sensor (No. 247 from wafer C23, irradiated to a fluence of $\phi \sim 2.5 \cdot 10^{14}$ n_{eq}/cm^2) at different temperatures, from $t = -20\,°C$ to $t = +20\,°C$.
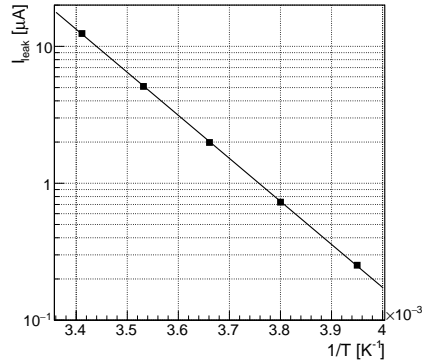
Figure 6.5: Arrhenius plot for the leakage current as a function of the temperature for the same sensor measured in Figure 6.4. The experimental errors are smaller than the marker size. The line corresponds to a fit.

negative values. The same observation can be made on both strip and BABY sensors produced by SINTEF.

The same behaviour is not observed when 3D sensors produced by other institutes or standard planar architectures are under test. Figure 6.7a shows the curves at different frequencies of a 3D sensor produced by CNM (described in Section 6.1). This device, whose end capacitance has a high value because of the small inter-electrode distance, does not show significant variations of the capacitance in the full range of the measured frequencies. Figure 6.7b shows the same type of comparison for a $n-$bulk planar sensor. The capacitance gets slightly smaller as the frequency increases, but the values are positive.

The phenomenon observed in the SINTEF 3D sensors can be explained in terms of a phase shift of the AC current with respect to the AC voltage used to perform the capacitance measurement: while in normal conditions the current leads the voltage in a capacitor, in the case of a negative capacitance the current lags behind the voltage. The process was studied in [165]: this paper concludes that for high frequencies the carrier transport process is "frozen" due to the finite
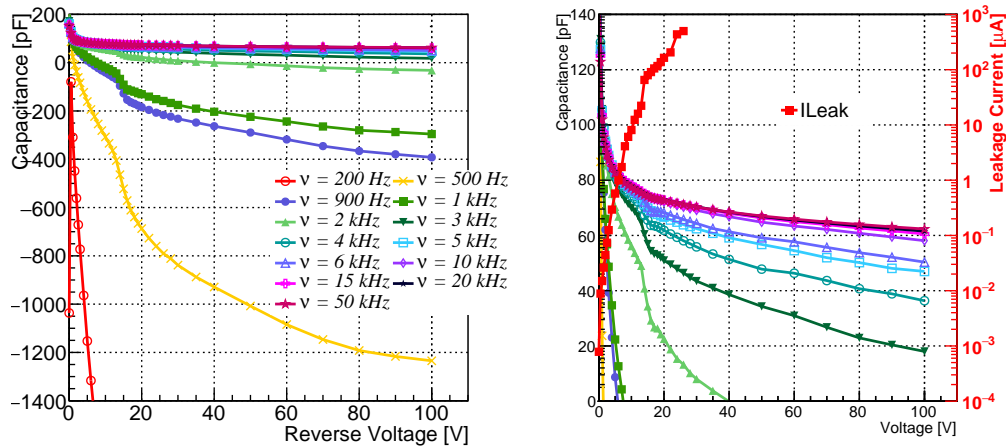
Figure 6.6: CV curves of an unirradiated single strip (strip No. 5 from the FEI4 sensor No. 8 of wafer C26) at different frequencies of the LCR meter at $t = +20\,°C$. Left: Full scale; Right: zoom in the positive capacitance range. The leakage current of the strip (red squares) overlays the CV curves for reference. Too low frequency gives non-physical values of the capacitance. A threshold effect is visible for frequencies $\nu \geq 10$ kHz.
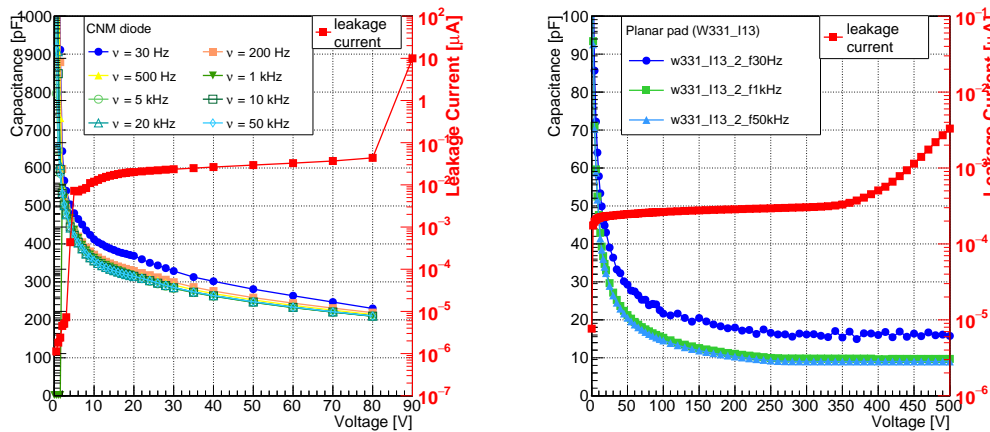
(a) CV curves of a 3D sensor produced by CNM (Barcelona - Spain).

(b) CV curves of a planar sensor.

Figure 6.7: CV curves of 3D CNM and planar sensors at different frequency settings on the LCR meter. For reference, the respective IV curves (solid red squares) are superimposed. Contrary to the SINTEF 3D sensors, these devices do not show negative capacitance at low frequencies.

inertia, while for low frequencies the contribution of the conduction current[1] exceeds the displacement current[2], causing the capacitance to become negative.

Figure 6.6 shows a threshold effect: for frequencies $\nu \geq 10$ kHz, the capacitance values does not change any longer with the operating frequency. The frequency of the LCR meter, when measuring SINTEF sensors, was set to $\nu = 20$ kHz.

6.2.5 Repetition effects on leakage current measurements

During the IVCV measurement campaign, some measurements were repeated, because the first measurement showed an irregular and unexpected shape (e.g. too low leakage current, symptom of bad connection between the sensor and the needles, or "bumps", temporary significant variations of the leakage current or the capacitance from the standard curve). It was observed that, most of the times, the repetition of the same IV measurement multiple times on sensors from wafers C21, C23 and C26 caused the new measurement to have a higher leakage current. The setup configuration was kept constant, in particular the temperature was set to $t = +20\,°\text{C}$. The phenomenon took place in both unirradiated and irradiated sensors of all geometries.

Figure 6.8a reports multiple IV measurements performed on the unirradiated BABY sensor No. 82 from wafer C23: the leakage current in the second measurement gets orders of magnitude higher and the typical shape of the reversed biasing IV curve cannot be observed because the compliance current is hit. The CV measurement, whose curve is shown for reference, was performed after all IV curves were taken. The CV curve shows a normal behaviour, indicating that the sensor did not break because of the high current applied along the IV measurements.

This variation of the IV curve when a measurement is repeated is rarely present in IV measurements on sensors from wafer C25 (as shown in Figure 6.8b for sensor No. 245). It is worth noting that, as described in Section 6.1, wafer C25 is one of the two wafers from SINTEF Run-C whose FEI4 sensors showed good electrical properties.

The origin of this reproducibility problem could be lying either in the instability of the setup or in some technology- or sensor-related problems.

---

[1]Conduction current: current that passes through the capacitor and does not create charge accumulation.

[2]Displacement current: effective current generated by the accumulation of charges on the geometrical capacitance.
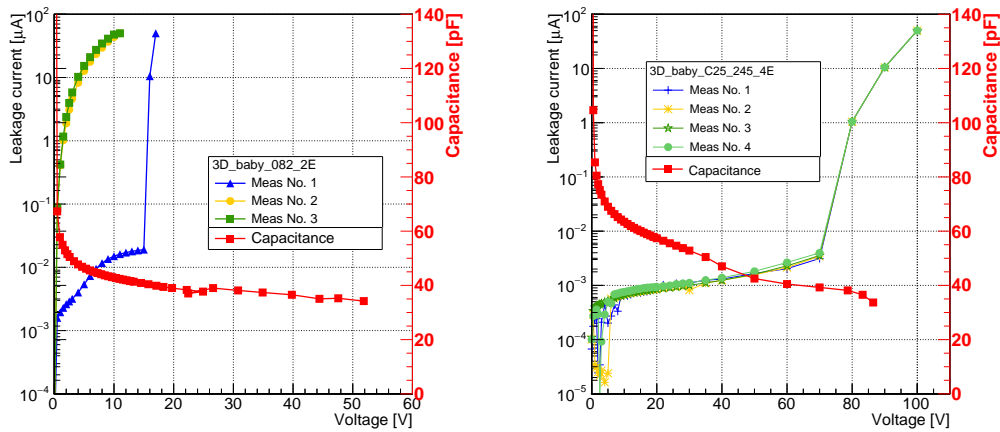
(a) Repeated IV curves of an unirradiated BABY sensor (No. 82 of wafer C23) show a variation of the electrical characteristics. The CV measurement was taken after the IV tests.

(b) Repeated IV curves of an unirradiated BABY sensor (No. 245 of wafer C25) do not show a variation of the electrical characteristics. C25 is one of the two "good" wafers from SINTEF Run-C.

Figure 6.8: Repetition of IV measurements on unirradiated sensors keeping the same settings of the setup. The CV curves are overlapped for reference.

To disentangle these two possible reasons, current-voltage measurements were repeated on a CNM 3D sensor and a planar sensor, devices already described in Section 6.1. The same phenomenon could not be observed in either of these devices, as shown in Figure 6.9: this indicates that the origin of the problem is not setup-related.

The cause of the inconsistency among repeated measurements could have been investigated by repeating the same measurements after a few months, to check if the effect is permanent or temporary. A longer-term measurement was not performed because sensors were meanwhile sent to the irradiation facilities.

6.2.6 Pixel configuration effects

Figure 6.10 shows the electrical properties, illustrated as CV and IV curves, for unirradiated BABY sensors, diced from wafer C23, with pixel configuration from 1E to 5E. Pixels from all BABY sensors have the same dimensions, but, as they contain a different number of electrodes per pixel cell, the inter-electrode distance is reduced with the increase in electrode density (see Table 5.1).

165
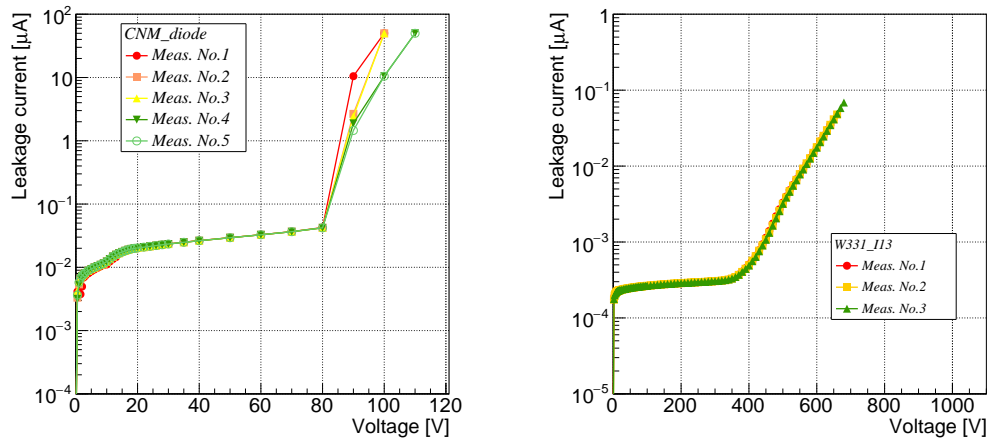
(a) IV measurements repeated on a 3D sensor produced by CNM.

(b) IV measurements repeated on a planar detector.

Figure 6.9: IV curves of a 3D CNM and a planar sensors, repeated multiple times with the same measurement settings.

When comparing the curves of the different pixel configurations, several features can be identified: first, a small increase in the leakage current in the plateau region can be appreciated as the number of electrodes per pixel cell increases. The closeness of the electrodes facilitates the current between the two electrodes to flow. This outcome was already observed during the first run of SINTEF prototyping [134].

Second, the breakdown voltage does not seem to be dependent on the pixel configuration, but it is peculiar of the single sensor and varies from a few volts to more than 120 V.

Third, there is an increase in the end capacitance when passing from 1E to 5E configuration. This effect is expected because the smaller inter-electrode distance leads to a higher capacitance after depletion.

Fourth, the CV curves show, generally, two trends: they either present a double or a single knee. The case of a double knee is expected for a 3D detector: as anticipated in Section 5.3, the first knee is formed when the depletion region connects neighbouring pixels along the long side of the pixel cell; the second knee is consequence of the complete depletion of the pixel.

Figure 6.11a divides, using a different colour code, the curves of Figure 6.10a according to their shape: curves that present a double knee are drawn in green,
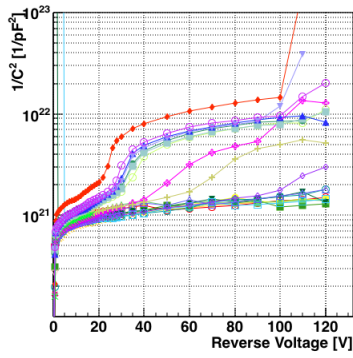
(a) CV curves for 1E BABY sensors.
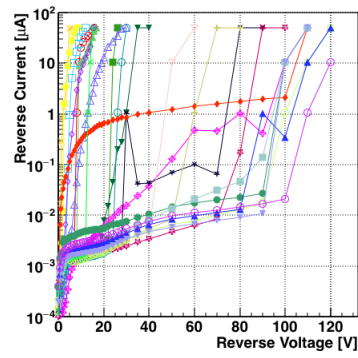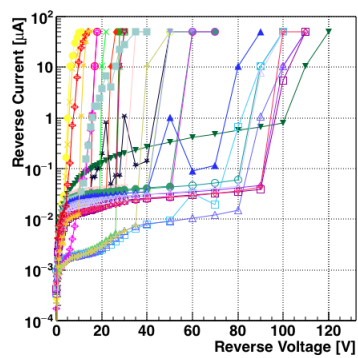

(b) IV curves for 1E BABY sensors.
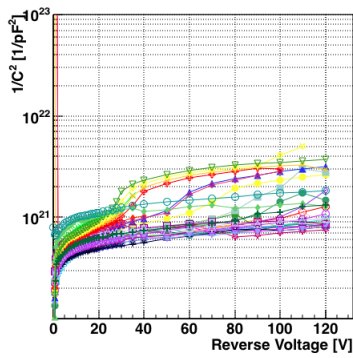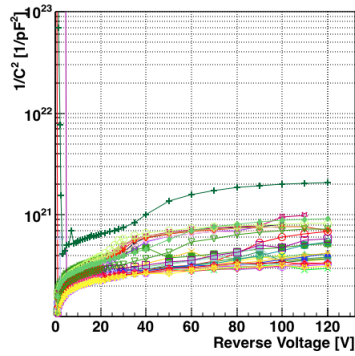

(c) CV curves for 2E BABY sensors.
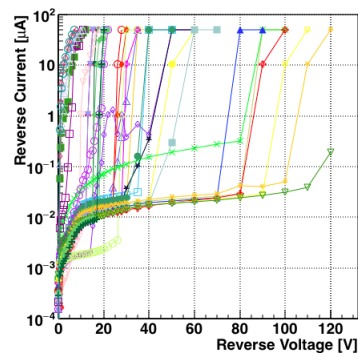
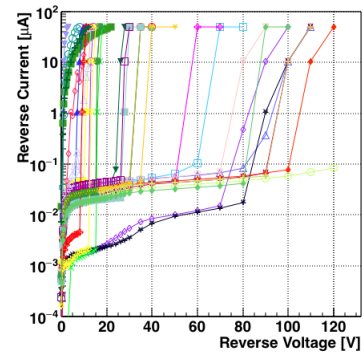(d) IV curves for 2E BABY sensors.
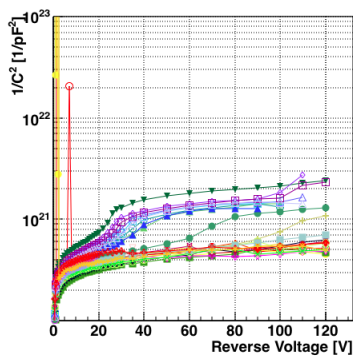
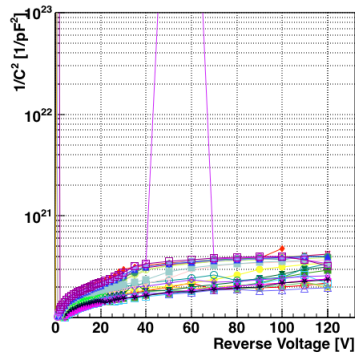(e) CV curves for 3E BABY sensors.
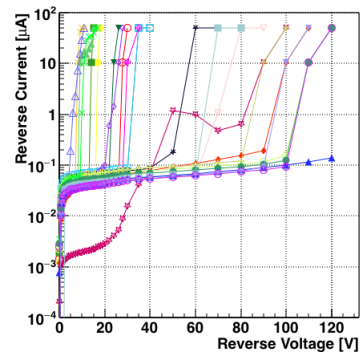

(f) IV curves for 3E BABY sensors.

167

(g) CV curves for 4E BABY sensors.

(h) IV curves for 4E BABY sensors.

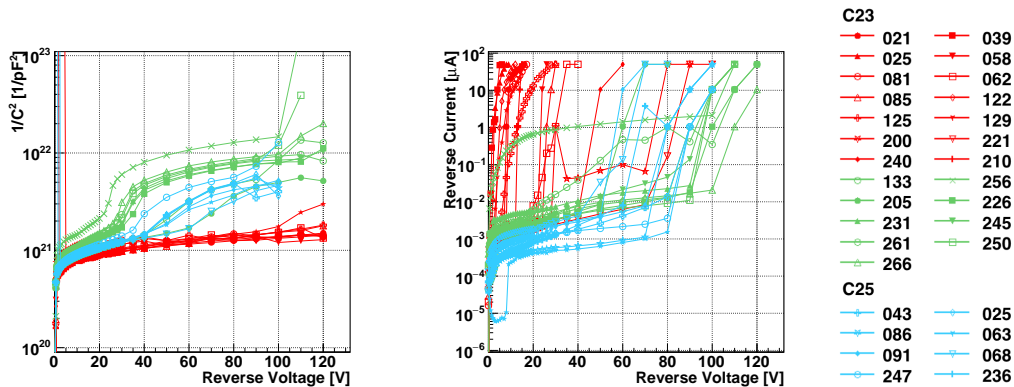

(i) CV curves for 5E BABY sensors.

(j) IV curves for 5E BABY sensors.

Figure 6.10: CV (left) and IV (right) characteristics for unirradiated BABY sensors, with configuration from 1E to 5E. Same marker/colour pair refers to the same sensor in the CV and IV curves.

while in red are drawn those with a single knee. For comparison, also the characteristics of the good wafer (C25) are added (light-blue curves). Figure 6.11b shows the corresponding IV curves (same marker/color pair identifies the same sensor as in Figure 6.11a). Comparing Figures 6.11a and 6.11b it can be observed that, in the majority of the cases, sensors presenting two knees have a better IV curve in terms of a lower leakage current on the plateau and a higher breakdown voltage. This is the case of the green and light-blue curves. Instead, red curves generally show larger capacitances (lower $1/C^2$) and the leakage current does not present a well-defined plateau and reaches compliance at very low voltages. Sensors from wafer C25 show an intermediate behaviour: the capacitance values

stay in an intermediate range between the two trends, the leakage currents in the plateau region are almost one order of magnitude lower and their breakdown happens slightly earlier than the green group of curves.

(a) CV curves for 1E BABY sensors.

(b) IV curves for 1E BABY sensors.

Figure 6.11: CV (left) and IV (right) characteristics for unirradiated BABY sensors, with 1E configuration. Light blue curves are from sensors of wafer C25; red and green curves are from sensors of wafer C23. C23 curves are the same as Figures 6.10a and 6.10b; they are split into two groups after two different trends were identified for CV curves: some CV curves have a double knee (curves in green), other sensors present a single knee (curves in red). Same marker/colour correspond to the same sensor.

A "geographical" distribution of behaviours can be observed across the wafer: as illustrated in Figure 6.12, the majority of sensors of wafer C23 having only one knee were diced out from the upper part of the wafer, while sensors with a double knee were mostly cut out from the lower part of the wafer.

The effect can be attributed to gradual inhomogeneities created during the wafer production. The same trend, however, is not visible when comparing the IV curves from the strips of FEI3 sensors from the same wafer: the dissimilarity of the different strips' response within a single FEI3 sensor is more pronounced than possible variations among different sensors. Pin-holes, randomly distributed across the wafer, determine a variation of the performance of electrical measurements. The larger the sensor is, the higher the probability of the presence of these production flaws.
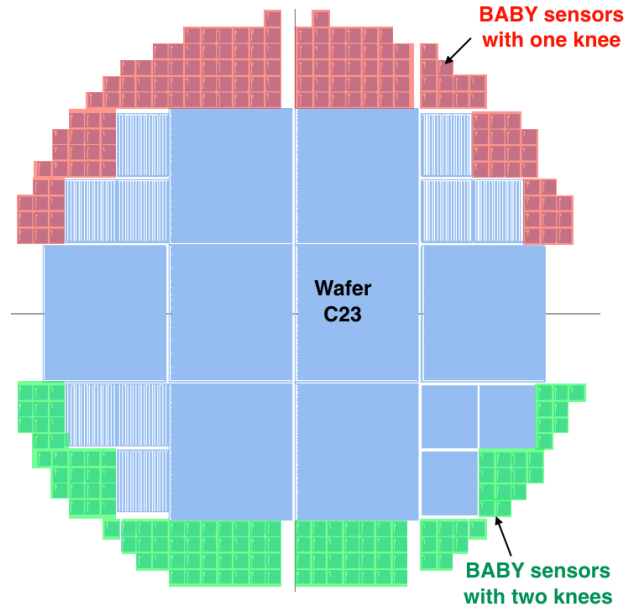
Figure 6.12: Double-knee CV curves (in green in Figure 6.11) are typical of sensors cut out from the lower part of the C23 wafer, while single-knee CV (in red in Figure 6.11) are from sensors diced out from the upper part.

6.2.7 Pixel cell dimensions influence on the capacitance

On the left-hand side of Figure 6.13, the CV curves for some strips of an unirradiated FEI4 sensor (No. 5, from wafer C26) are shown. On the right-hand side of the same figure the corresponding IV curves are reported for reference. Whilst all "internal" strips (from No. 5 to No. 75) show an end capacitance $C_{int} \sim 42$ pF at 100 V, the two outermost strips (No. 1 and 80) show a higher capacitance ($C_{ext} \sim 71$ pF at 100 V). The leakage current shows no significant difference among "internal" and outermost strips. The effect on the capacitance is determined by the larger dimensions of the pixels connected to the outermost strips, as shown in a sketch in Figure 6.14: the electrode distance is kept constant, but the pixel is longer to accommodate one more junction electrode and its surrounding ohmic columns. In fact, the FEI4 pixel size in the outermost pixels is $3/2$ that of the "internal" pixels: (375×50) μm^2.

Roughly speaking, there are 2 "cells" (each one formed by 4 p^+ columns with a n^+ column in the centre) in an "internal" FEI4 pixel, whilst the number of cells is 3 in an outermost pixel. The proportion between number of cells and
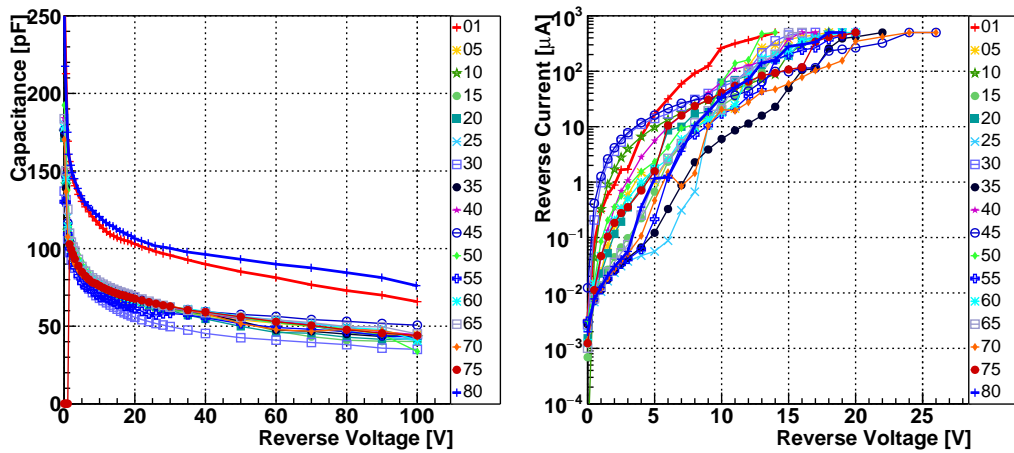
Figure 6.13: CV (left) and IV (right) curves of strips of an unirradiated FEI4 sensor. The outermost strips (No. 1 and No. 80) show a higher end capacitance with respect to the "internal" strips. Their IV curves do not show any significant trend variation with respect to the "internal" strips.
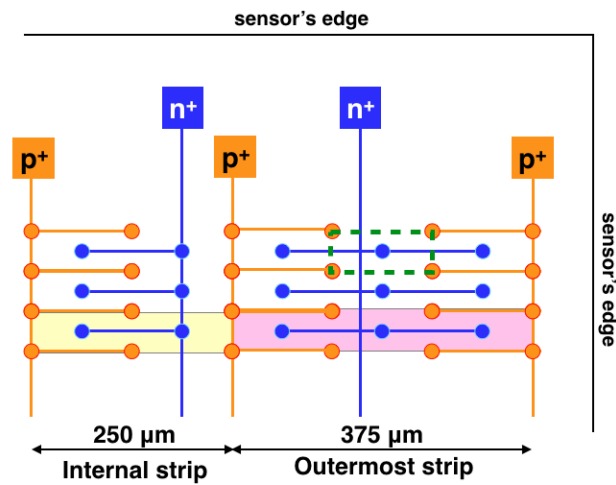

Figure 6.14: Sketch of the pixel configuration and metal connections in the outermost and "internal" strips of a FEI4 sensor. The filled circles represent the electrode columns, the solid lines are the metal connections between columns and the probing pads, which are drawn as solid-coloured squares. The dashed green line defines a "cell", described in the text. In the FEI4 case, outermost strips are connected to 3 cells (pink-shaded area), whilst "internal" strips are connected to 2 cells (yellow-shaded area).

171

end capacitance is

$$C_{int} : C_{ext} = 2 : x$$
$$\Rightarrow x = \frac{C_{ext} \cdot 2}{C_{int}} \simeq \frac{71 \cdot 2}{42} \sim 3,$$

corresponding to the electrode configuration of the outermost pixels.

Similar results were found comparing the curves of FEI3 sensors: in these devices the end capacitance measured in the outermost strips is $\sim 4/3$ the value measured in an internal strip: the "internal" strips have a 3E pixel configuration and (400×50) μm^2 pixel size, whilst the outermost ones are $(\sim 533 \times 50)$ μm^2 pixels with 4E configuration.

Using Equation 3.17, the end capacitance of 3D sensors can be calculated for a single n^+ column of a FEI4 sensor, given the inter-electrode distance of 67.3 μm and the column radius of 7 μm:

$$C_{\text{3D FEI4, 1 col}} = 2\pi\varepsilon_0\varepsilon_{Si} \cdot \frac{W}{\ln \frac{d}{r_{col}}}$$
$$= 2\pi \cdot 11.9 \cdot 8.85 \cdot 10^{-12} \cdot \frac{230 \cdot 10^{-6}}{\ln \frac{67.3}{7}}$$
$$\simeq 6.72 \cdot 10^{-2} \text{ pF}.$$

As one FEI4 strip is connected to several n^+ electrodes, the total capacitance is:

$$C_{\text{FEI4 strip}} = C_{\text{3D FEI4 1 col}} \cdot N_{n^+\text{electrodes/strip}}$$
$$= \begin{cases} C_{int} & = 6.72 \cdot 10^{-2} \cdot (336 \cdot 2) \simeq 45.2 \text{ pF} \\ C_{ext} & = 6.72 \cdot 10^{-2} \cdot (336 \cdot 3) \simeq 67.8 \text{ pF}. \end{cases}$$

The measured capacitances agree with the computed values within less than 10%.

Table 6.2 compares, for different SINTEF 3D sensors' geometries, the calculated capacitances to the measured values (at $U = 100$ V). The expected capacitance values agree, to a good approximation, with the measured values.

6.2.8 Radiation effects

This section focuses on the radiation damage effects on SINTEF 3D sensors irradiated at different fluences. In particular, it describes the fluence dependency

Sensor type	No. electrodes per strip/BABY	Interel. distance [μm]	Computed capacitance [pF]	Measured capacitance [pF]
FEI4 internal	336×2	67	$\simeq 45$	$\simeq 42$
FEI4 outermost	336×3	67	$\simeq 68$	$\simeq 71$
FEI3 internal	160×3	71	$\simeq 32$	$\sim 35 - 40$
FEI3 outermost	160×4	71	$\simeq 42$	$\sim 50 - 60$
BABY 1E	120×1	202	$\simeq 6.9$	$10 - 27$
BABY 2E	120×2	103	$\simeq 18.6$	$16 - 37$
BABY 3E	120×3	71	$\simeq 34.7$	$20 - 47$
BABY 4E	120×4	56	$\simeq 54.5$	$50 - 60$
BABY 5E	120×5	47	$\simeq 78.2$	$50 - 70$

Table 6.2: Comparison between calculated and measured end capacitance for unirradiated SINTEF 3D silicon sensors. For larger sensors, "internal" refers to internal strips, whilst "outermost" indicates the two outmost strips (see text). In the case of FEI4 sensors, the reported value is the mean value of the capacitance of the sensor's strips shown in Figure 6.13. In the case of FEI3 sensors, an average value is evaluated from all curves of all strips. For BABY sensors, the measured capacitance is expressed as a range of values because of the large spread of the capacitance values for the different BABY sensors, shown in Figures 6.10a, 6.10c, 6.10e, 6.10g and 6.10i.

of macroscopic parameters, such as the leakage current, the depletion and breakdown voltages and the capacitance. It is important to note that the sensors were irradiated only once, so different fluence steps are evaluated using different sensors. The presented results have been obtained exploiting the data analysis described in Section 5.3.3.

The fluence values expressed in the figures' legend are the nominal values. The effective irradiation fluences and their conversion into $1 \, \mathrm{MeV} \, n_{eq}/\mathrm{cm}^2$ are reported in Tables 5.3 and 5.4 for protons and neutrons, respectively.

The SINTEF 3D sensors irradiated in the two facilities and measured in the IVCV setup are listed in Table 6.3.

Fluence $[\mathrm{n_{eq}/cm^2}]$	Large sensors		BABY sensors - Pixel configuration				
	FEI3	FEI4	1E	2E	3E	4E	5E
				Proton irradiated			
0	C21-FEI3-1	C26-FEI4-1	200, 221	201, 222, <u>237</u>, <u>248</u>	202, 223, <u>238</u>, <u>249</u>	203, 219, 224	199, 220, 249
$3.3 \cdot 10^{13}$	C21-FEI3-2	C21-FEI4-1	240, 256	241, 257	207	208, 229	<u>2</u>, <u>10</u>
$1.0 \cdot 10^{14}$	C21-FEI3-3	C21-FEI4-2	<u>25</u>, <u>43</u>	<u>26</u>	242, 258	<u>23</u>	<u>24</u>
$2.5 \cdot 10^{14}$	C26-FEI3-1	C21-FEI4-3	<u>63</u>, 250, 266	<u>64</u>	247	<u>28</u>, 248, 264, <u>61</u>	<u>62</u>, <u>85</u>
$4.5 \cdot 10^{14}$	C26-FEI3-2	C21-FEI4-4	<u>68</u>	<u>69</u>, 211, 232	233	<u>28</u>	260
$2.2 \cdot 10^{15}$	C26-FEI3-3	C21-FEI4-5	205, 226	251, 267	252, 268, <u>233</u>, <u>244</u>	<u>234</u>, <u>245</u>	204, 225
$5.0 \cdot 10^{15}$	C23-FEI3-1	C21-FEI4-7	<u>236</u>, <u>247</u>	<u>258</u>, <u>267</u>	<u>254</u>, <u>259</u>, <u>263</u>, <u>268</u>	<u>255</u>, <u>264</u>	<u>235</u>, <u>246</u>
				Neutron irradiated			
0	C21-FEI3-1	C26-FEI4-1	200, 221	201, 222, <u>237</u>, <u>248</u>	202, 223, <u>238</u>, <u>249</u>	203, 224, 219	199, 220, 249
$4.50 \cdot 10^{13}$	C23-FEI3-4	C26-FEI4-2		59, 82, 196	197, 218		
$9.00 \cdot 10^{13}$	C23-FEI3-5	C26-FEI4-4	231	206			230
$4.50 \cdot 10^{14}$	C23-FEI3-6	C26-FEI4-5			18		
$9.00 \cdot 10^{14}$	C23-FEI3-7	C26-FEI4-6			131, 135		
$4.50 \cdot 10^{15}$	C23-FEI3-8	C26-FEI4-7					
$9.00 \cdot 10^{15}$	C23-FEI3-9	C26-FEI4-8					

Table 6.3: List of the proton/neutron-irradiated SINTEF sensors measured with the IVCV setup. For the large sensors, the wafer number is specified. For BABY sensors, underlined numbers are sensors from wafer C25, others are from wafer C23.

6.2.8.1 Radiation effects on the leakage current

The effect of the radiation on the leakage current was studied on BABY sensors with 3E pixel configuration, measured unirradiated and after proton irradiation at different fluences, from $3.3 \cdot 10^{13}$ n_{eq}/cm^2 to $5 \cdot 10^{15}$ n_{eq}/cm^2. The list of the used BABY sensors is shown in Table 6.4.

Figure 6.15a shows, on the left-hand side, the IV curves before irradiation, measured at $t = +20\,°C$. The central and right plots report IV curves after proton irradiation measured, respectively, at $t = +20\,°C$ and $t = -20\,°C$: irradiated sensors were firstly measured at $t = -20\,°C$ and then, after conserving them at low temperature for several months, they were measured at $t = +20\,°C$. The latter measurement was taken in order to more directly compare the devices before and after irradiation.

Although the BABY sensors did not show uniform behaviours in terms of the leakage current values in the plateau region before irradiation, some observations can be nevertheless made. As expected, there is a significant increase in the leakage current in the plateau with radiation fluence. This effect is observed both when comparing the same sensor before and after irradiation, and when comparing different fluences. There is a shift of the breakdown voltage toward higher voltages after the sensors were irradiated: the breakdown exceeds $U = 100$ V after irradiation. The effect of the radiation damage on the breakdown voltage will be discussed in Section 6.2.8.3. As already described in Section 6.2.3, the temperature plays a fundamental role in determining the magnitude of the leakage current: in fact, the dark current decreases by roughly two orders of magnitude when passing from $t = +20\,°C$ to $t = -20\,°C$.

Fluence $[n_{eq}/cm^2]$	Wafer No.	BABY No.
$3.3 \cdot 10^{13}$	C23	207
$1.0 \cdot 10^{14}$	C23	258
$2.5 \cdot 10^{14}$	C23	247
$4.5 \cdot 10^{14}$	C23	233
$2.2 \cdot 10^{15}$	C25	233
$5.0 \cdot 10^{15}$	C25	254

Table 6.4: BABY sensors used to evaluate the effects of radiation on the leakage current.

In Figure 6.15b, the corresponding CV curves are reported for reference. After irradiation, at $t = +20°$C, the curves for the two highest fluences (sensors No. 233 and 254) have a capacitance of about $C \sim 5$ pF. This low value is a symptom of bad performance of these sensors at high temperature. The corresponding IV curves present a leakage current lower than the foreseen increase caused by radiation damage: these two sensors were diced out from wafer C25, the "good" wafer, whose sensors usually show lower leakage current values. At low temperature, instead, both the IV and CV curves for these two sensors follow the expected trends.

The increase in the leakage current normalised by the volume, $\Delta I / Vol$, is proportional to the fluence according to Equation 3.23. The α factor, the damage constant, is [77]

$$\alpha = 3.99 \cdot 10^{-17} \text{ A/cm} \qquad \text{for } t = +20 \text{ °C.} \tag{6.3}$$

Figure 6.16a shows the dependence of $\Delta I / Vol$ on the fluence. The values of the leakage current are taken at $U = 40$ V, which is in the plateau region. The considered volume includes not only the pixel matrix, but extends to the physical dimensions of the sensor: although the volume outside the boundaries of the pixel matrix is not biased, free e^- and h diffuse in the material and contribute to the bulk leakage current. After irradiation, the leakage current increases because of the generation of new energy levels in the band gap, leading to an increase in the number of free charge carriers.

Curves for both temperatures are shown: with the exception of the two highest points of the $t = +20$ °C curve, the data points follow the expected trend. The two highest points of the $t = +20$ °C curve are not aligned to the first three points, as consequence of their lower IV curve with respect to the foreseen characteristic. The low-temperature data points show a much better agreement with the theoretical curve.

Performing a linear fit (not shown in the plot) on the two temperature data sets, fixing the constant term $p_0 = 0$ A/cm^3 and considering only the first three points for the $t = +20$ °C curve, the α values are

$$\begin{aligned} \alpha_{+20} &= (4.48 \pm 0.17) \cdot 10^{-17} \text{A/cm} \\ \alpha_{-20} &= (9.1 \pm 1.3) \cdot 10^{-19} \text{A/cm.} \end{aligned} \tag{6.4}$$

Scaling the leakage currents used to compute α_{-20} (for $t = -20$ °C) to the value they would have at $t = +20$ °C (using Equation 3.11), the damage constant
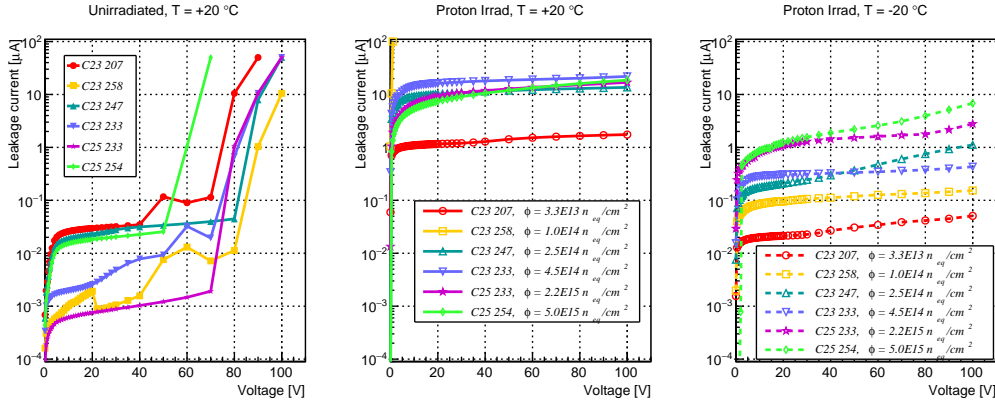
(a) IV curves.
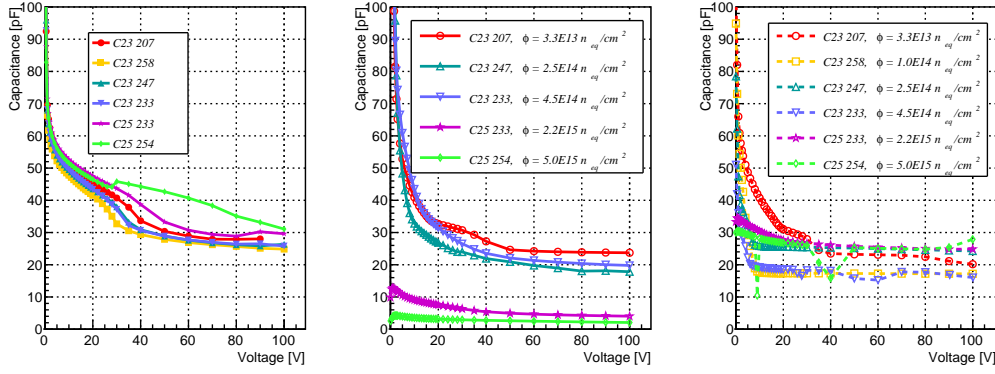
(b) CV curves.

Figure 6.15: IV and CV curves of 3E BABY sensors. Left: unirradiated sensors; centre and right: after exposure to proton irradiation at different fluences, respectively at $t = +20\,°\mathrm{C}$ and $t = -20\,°\mathrm{C}$. Same colour and same marker shape are used for the same sensor, filled markers indicate unirradiated BABY sensors and empty markers are used for irradiated samples; solid lines are for $t = +20\,°\mathrm{C}$, dashed lines for $t = -20\,°\mathrm{C}$.

becomes

$$\alpha_{-20\to+20} = (4.1 \pm 0.6) \cdot 10^{-17}\mathrm{A/cm}, \tag{6.5}$$

a value compatible to the theoretical one of Equation 6.3 within the errors.

In Figure 6.16b, the same exercise of evaluating the $\Delta I/Vol$ as a function of the fluence for $U = 40$ V is shown for all measured proton- and neutron-irradiated

177

sensors that satisfy two conditions: (i) the value of the breakdown voltage is larger than $U = 40$ V, because the value of the increase in the leakage current is taken at this specific voltage; (ii) the leakage currents before and after irradiation could be extracted from the IV curves. These conditions were never met by FEI4 sensors. Data points tend to lie above the theoretical line, especially at lower fluences.
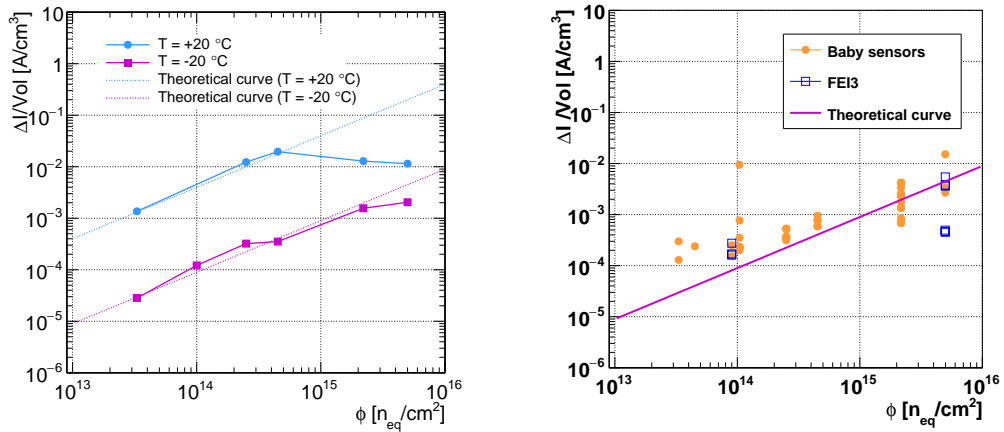
(a) For irradiated BABY sensors with 3E configuration. I_{leak} is extracted from IV curves of Figure 6.15a for $U = 40$ V, at temperature $t = +20\,°$C (circles) and $t = -20\,°$C (squares).

(b) For irradiated BABY (with different configurations) and FEI3 sensors, measured at $t = -20$°C. Orange-filled circles are BABY sensors, FEI3 strips are indicated with empty blue squares.

Figure 6.16: Fluence dependence of the leakage current of some of the measured sensors, compared to the "theoretical" curve, drawn in solid lines, from literature [77], corrected for $t = \pm 20\,°$C, with slope coefficient $\alpha = 3.99 \cdot 10^{-17}$ A/cm at $t = +20\,°$C.

Figure 6.17 shows the leakage current before and after irradiation as a function of the fluence, for 2E BABY and FEI3 sensors. The leakage current value is computed following Equation 5.10. In each figure, the left pad contains data from samples before irradiation, whilst the right pad shows data coming from samples after irradiation at various fluences. The same marker/colour pair in the $\phi = 0$ and $\phi \neq 0$ pads indicates the same sensor/strip measured before and after irradiation. In the case more sensors (or strips) were exposed to the same fluence, they have the same colour code, but different markers. The fluence reported in the legend is the nominal fluence; for the conversion to the effective fluences see Tables 5.3 and 5.4 (data points are set to the measured fluences, expressed

in $1\,\mathrm{MeV}\,\mathrm{n_{eq}/cm^2}$). The leakage current for non-irradiated measurements is temperature-corrected, following Equation 3.11, reporting on the plot values at $t = -20\,°C$. Error bars are the error computed on the single parameter. In some cases, they are too small to be visualised and fall within the dimension of the marker. These considerations are valid for all plots of this type, even when they show a different electrical parameter of the sensors.

Figure 6.17a shows the fluence-dependent leakage current for 2E BABY sensors. There is a significant variation of the leakage current after irradiation: the current increases by 2 to 4 orders of magnitude after irradiation. The points corresponding to irradiated sensors show an increase in the current as a function of the irradiation.

The FEI3 and FEI4 sensors (Figures 6.17b and 6.17c) show a broad range of values of the leakage current. Whilst an increase in the current is observed after irradiation, no significant trend is identified at different fluences, because the variation of the different strips of a single sensor is larger than the variations among different sensors exposed at different fluences.

Comparing the leakage current for proton- and neutron-irradiated 3E BABY sensors, shown respectively in Figures 6.18a and 6.18b, a larger radiation damage is observed in neutron-irradiated samples. However, the low statistics does not allow for a significative comparison.

Overall, results presented in this subsection show that the leakage current increases with the radiation damage. This results in a higher noise, leading to a lower signal-to-noise ratio, and higher power requirements to cool down the sensor to avoid thermal runaway (see Section 3.3.1).

SINTEF 3D sensors from the third prototype run do not usually comply with the specifications required of sensors for the HL-LHC phase, because they show too-high leakage currents at fluences that are lower than the HL-LHC ones ($\phi \sim 10^{16}\,\mathrm{n_{eq}/cm^2}$). As a comparison, the IBL-generation of 3D pixel sensors has demonstrated to have a power dissipation of $15\,\mathrm{mW/cm^2}$ at $U = 170\,\mathrm{V}$ after irradiation at $1 \cdot 10^{16}\,\mathrm{n_{eq}/cm^2}$ [166]. Converting it into current, this power corresponds to $I_{leak} \sim 350\,\mu\mathrm{A}$ across the entire sensor's volume and $I_{leak} \sim 4.4\,\mu\mathrm{A/strip}$. The leakage current measured in SINTEF 3D sensors is compatible with this value only when measured at much lower voltages ($U \sim 10\,\mathrm{V}$).
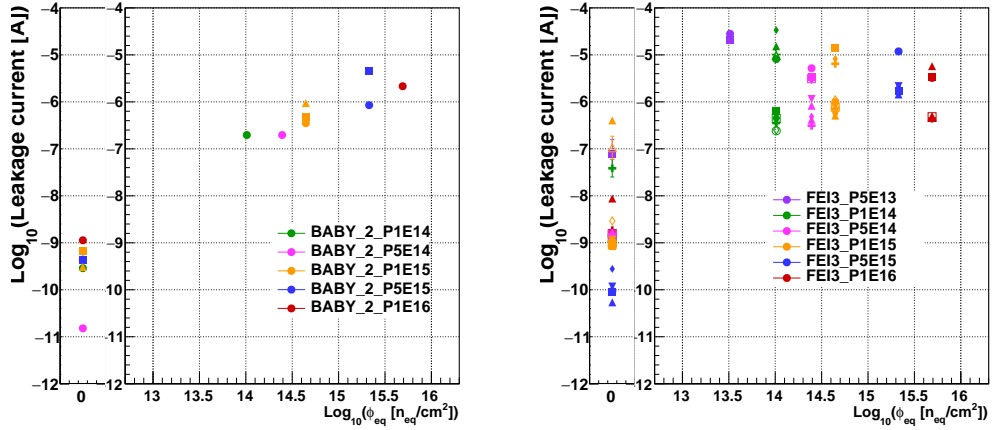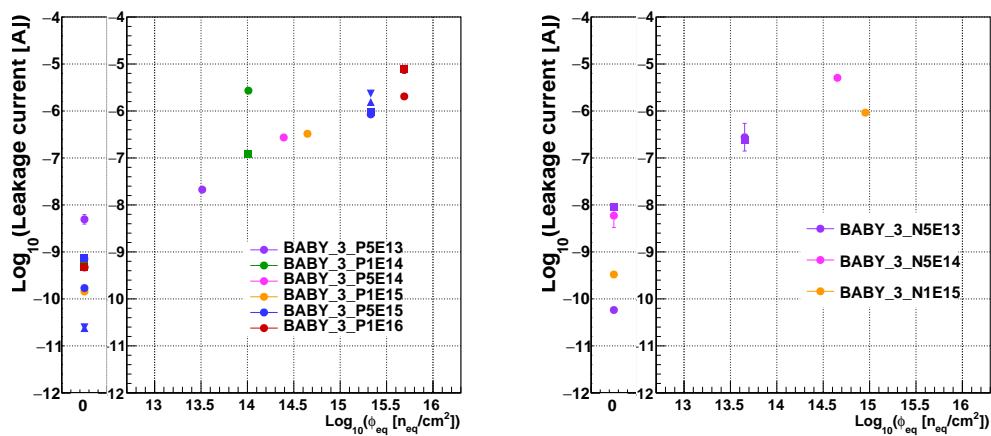
(a) For 2E BABY sensors.

(b) For FEI3 sensors.
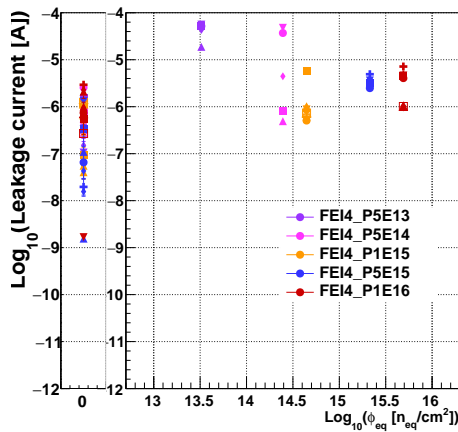
(c) For FEI4 sensors.

Figure 6.17: Leakage current as a function of the fluence for proton-irradiated sensors. In all canvases, the left pad contains the temperature-corrected values of the leakage current measured before irradiation; the right pad contains the values of the same strips or sensors after irradiation (same strip or sensor has the same marker/colour code). All measurements are reported for a temperature $t = -20\,°\mathrm{C}$. The fluences in the legend are the nominal values (whilst $x-$coordinates of the data points are the measured fluences, normalised to 1 MeV $\mathrm{n_{eq}/cm^2}$).

(a) For proton-irradiated 3E BABY sensors.

(b) For neutron-irradiated 3E BABY sensors.

Figure 6.18: Leakage current as a function of the fluence for (left) proton- and (right) neutron-irradiated 3E BABY sensors. In both canvases, the left pad contains the temperature-corrected values of the leakage current before irradiation; the right pad contains the values of the same sensors after irradiation (same sensor has the same marker/colour code). All measurements are reported for a temperature $t = -20\,^{\circ}\mathrm{C}$. The fluences in the legend are the nominal values, whilst $x-$coordinates of the data points are the measured fluences (normalised to $1\,\mathrm{MeV}\,\mathrm{n_{eq}/cm^2}$).

6.2.8.2 Radiation effects on the depletion voltage

The value of the depletion voltage can be extracted from both the current-voltage and the capacitance-voltage curves.

Literature [77, 167] and Figure 3.18 indicate that the depletion voltage should significantly increase with the fluence. A higher depletion voltage corresponds to a loss in the charge collection efficiency when the sensor is operated in an underdepleted condition, and to an increase in risk of breakdown if the sensor is operated at high biases. The collected data does not follow expectations. In Figure 6.15a, the depletion voltage seems to be stable after sensors have been exposed to radiation.

Figure 6.19 gives an overview of the relations, for various sensor geometries, between the depletion voltage, extracted both from IV and CV curves, and the fluence, both from proton and neutron irradiation. Plots are built in the same way as for the leakage current vs. fluence described above. Error bars are usually smaller than the marker size. In some cases, however, the error bars are significantly larger because of the lack of data points available over which fits are performed.

No significant variation of the depletion voltage can be observed, within the errors, as the fluence grows, regardless the geometry of the sensor or the nature of the irradiating particle. The comparison between Figures 6.19a and 6.19b shows that the depletion voltage extracted from the IV curve is usually smaller with respect to the one extracted from the CV measurement. This observation is common to all the sensor geometries and can be explained by a misjudgment of the range over which the fit describing the initial capacitance decrease is applied. A small variation of the fitting range greatly modifies the fitting parameters. The more complex nature of the CV curve, caused by the presence of the double knee and the strong dependence of the capacitance on the frequency (see Section 6.2.4), causes the fitting procedure to fail more often on CV curves with respect to the fit on IV curves. This issue is the origin of the lack of data points for some fluences on the CV-extracted depletion voltage plots.

Figures 6.19e and 6.19f, reporting U_{depl} for, respectively, FEI3 and FEI4 sensors, confirm a spread of the depletion voltage over the strips of a single sensor of the order of 10 V: the variation of the depletion voltage within a single sensor is more pronounced than the variation across different fluences.
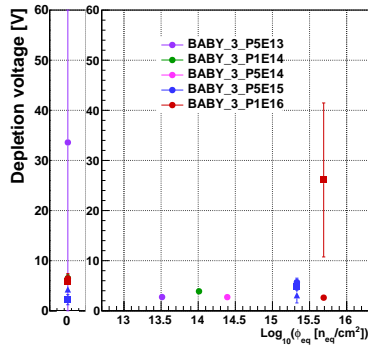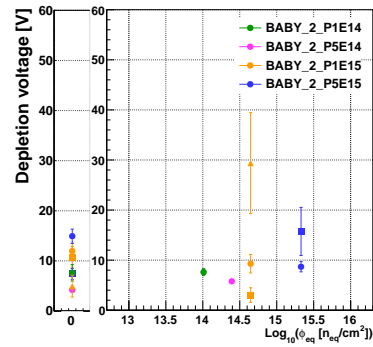
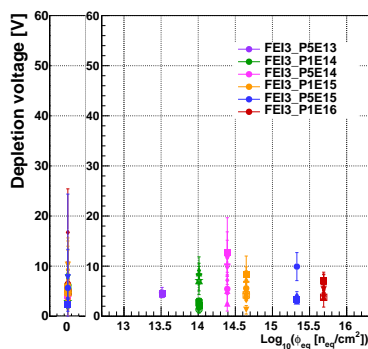(a) Proton-irradiated 3E BABY sensors, extracted from the IV curves.
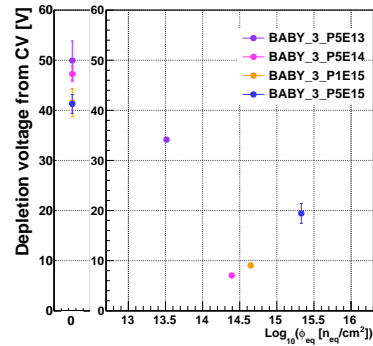
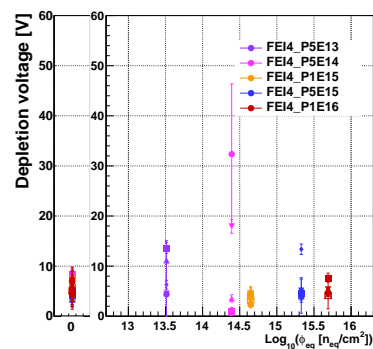(b) Proton-irradiated 3E BABY sensors, extracted from the CV curves.
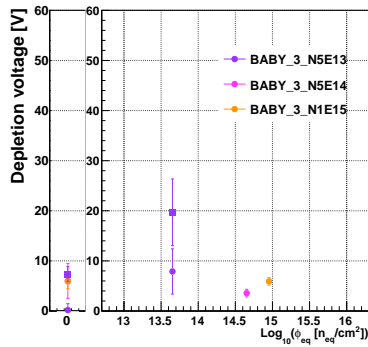
(c) Neutron-irradiated 3E BABY sensors, extracted from the IV curves.

(d) Proton-irradiated 2E BABY sensors, extracted from the IV curves.

(e) Proton-irradiated FEI3 sensors, extracted from the IV curves.

(f) Proton-irradiated FEI4 sensors, extracted from the IV curves.

Figure 6.19: Depletion voltage as a function of the fluence for various sensor geometries and fluence types.

6.2.8.3 Radiation effects on the breakdown voltage

Figure 6.20 presents, for FEI4 and 2E BABY sensors, the dependence of the breakdown voltage on the fluence. The errors associated with the data points are large because, as mentioned in Section 5.3.3, the $fitBD$ fit, which defines the breakdown increase in the current at high voltages, relies only on a few data points (usually 2 to 4).

Plots from all sensor geometries show that the breakdown voltage increases with the fluence. In particular, this is observed for the fluence-dependent breakdown voltage of FEI4 sensors, presented in Figure 6.20c. The value of the breakdown voltage is larger for irradiated samples with respect to non-irradiated ones and increases with the logarithm of the fluence. The conditions of temperature during the measurements play a role: unirradiated sensors were measured at $t = +20\,^{\circ}\mathrm{C}$, whilst irradiated ones were always kept at $t = -20\,^{\circ}\mathrm{C}$. The influence of the temperature on the breakdown voltage is less pronounced than that on the leakage current; still, measurements report an increase in the breakdown voltage for lower temperatures. This is in agreement with literature [168]. The most common behaviour, however, is represented in Figure 6.20a: although an increasing trend of the breakdown voltage after sensors were irradiated, the $\phi \neq 0$ values agree with the values measured before irradiation. A similar trend is observed also for neutron-irradiated samples. The typicality of each sensor or each strip seems to have more impact on the spread of the curves than the radiation damage itself.

6.2.8.4 Radiation effects on the capacitance

Figure 6.21 shows some examples of fluence-dependent capacitance for, respectively, proton-irradiated FEI3 and 3E sensors, and neutron-irradiated 3E sensors. A common aspect of the three plots is that the end capacitance of the sensors is reduced after irradiation. This trend is not found in the literature [168], which states that the capacitance should converge to the same value for voltages above depletion. A possible explanation is that the fluence varies the resistivity of the sensor and it effectively changes the probed volume.
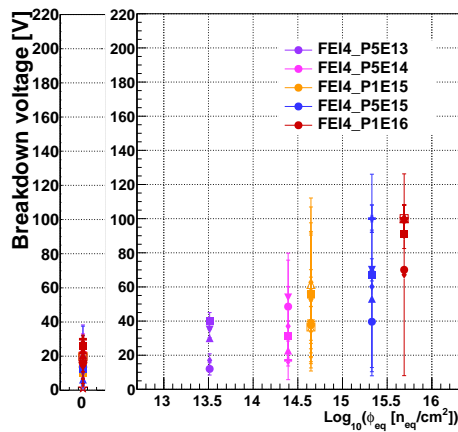
A common trend across many sensors is the fact that for the highest fluence, $\phi = 1 \cdot 10^{16}\ \mathrm{n_{eq}/cm^2}$, the capacitance most of the times gets to very low values ($C \sim 2 - 3$ pF). The corresponding IV curves rarely show the typical diode-like curve. The majority of the times, the IV curve does not show a good plateau.
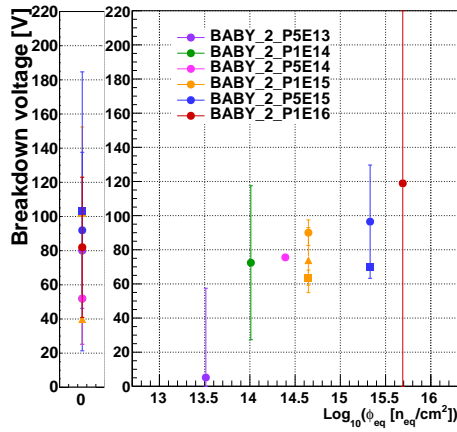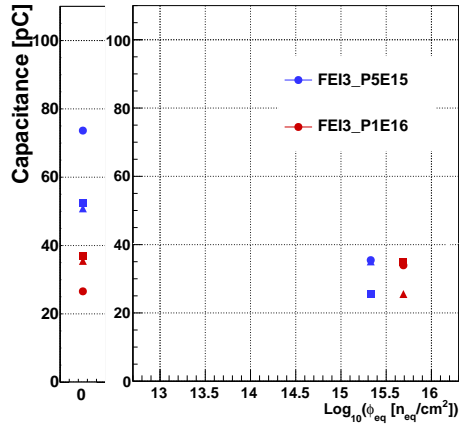
(a) For 2E BABY sensors.
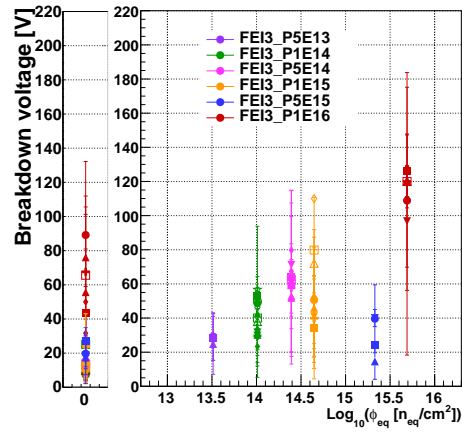

(b) For FEI3 sensors.

(c) For FEI4 sensors.

Figure 6.20: Breakdown voltage as a function of the fluence for proton-irradiated sensors.

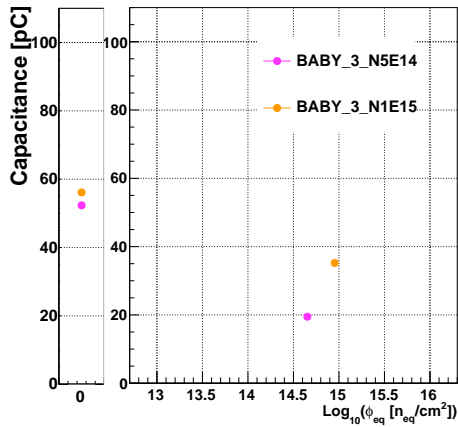## 6.2.9 Recurring unexpected behaviours observed during the IVCV measurement campaign

The IVCV measurement campaign gave, on various occasions, unexpected results. They are measurements performed on sensors or strips that do not work

(a) For proton-irradiated FEI3 sensors.
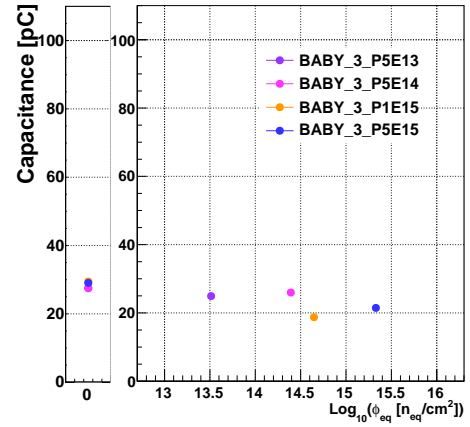
(b) For proton-irradiated 3E BABY sensors.

(c) For neutron-irradiated 3E BABY sensors.

Figure 6.21: End capacitance as a function of the fluence for proton- and neutron-irradiated sensors.

properly. The sensor exhibiting such behaviours were not further tested. In the following, some of these unforeseen outcomes are presented.

- Many CV curves showed, at low voltages, very small capacitances (with values in the sub-picoFarad range) or alternating large and small values. For higher voltages, the CV curves returned to a more expected behaviour. Examples are collected in Figure 6.22a. For the same sensors, the IV curves showed a regular behaviour. A misplacement of the needles, hence a bad contact between the needles and the sensor, is excluded from the possible causes of such misbehaviour at low voltages, because of the recovery at higher voltages. A bad positioning of the sensor on the chuck, causing the vacuum to not be fully working, should not have a big impact on the quality of the measurement either, because SINTEF sensors are not biased from the back side.

  The direct consequence of these types of issues is the impossibility to extract the depletion voltage from the CV curves.

- On some occasions, the leakage current shows two knees, the first one at very low voltages, the second at $U \sim 30 - 40$ V, followed by a very "slow" leakage current increase. An example is shown in Figure 6.22b. It is not fully clear whether this "slow" rise is the plateau region, or it is a "slow breakdown". For this reason it is difficult to determine the depletion and breakdown parameters. The same effect is observed for all geometries of SINTEF sensors.

- The leakage current in some strips and BABY sensors has a very high value and no proper plateau could be identified before the compliance current is reached (see Figure 6.22c). Increasing the compliance current was not an option, because it is dangerous for the sensor: a too-high current could permanently damage the sensor and burn the probing pads (as shown in Figure 6.22d). The absence of a plateau was observed both for unirradiated and irradiated sensors and it is common across the different sensor geometries. As a consequence, it is not possible to extract, from the curves, parameters of interest such as the depletion voltage and the breakdown voltage.

- As already mentioned in Section 6.2.5, some measurements presented "bumps", positive or negative peaks in the curve. Examples of IV
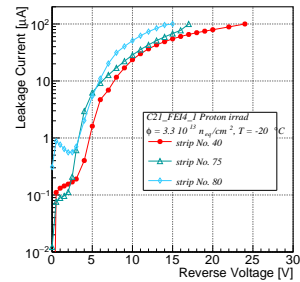
curves of various unirradiated sensors (all measured at $t = +20\,^\circ\mathrm{C}$) are presented in Figure 6.22e. These bumps make the identification of the important parameters (depletion and breakdown voltages, leakage current at plateau) difficult and certainly add complexity to the analysis devoted to the extraction of depletion and breakdown voltage and leakage current parameters.
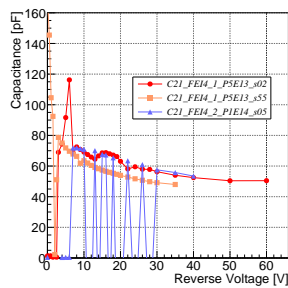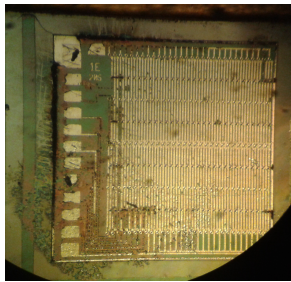

(a) CV curves showing unexpected behaviours at low voltages.
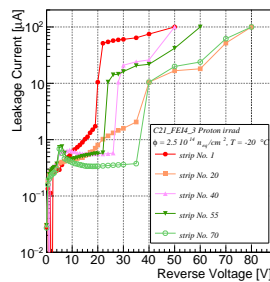
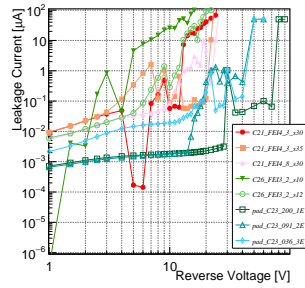(b) IV curves showing a slow rise at high voltages, not fully definable as breakdown or plateau.

(c) Examples of IV curves reaching compliance before defining a plateau.

(d) Photo of burnt probing pads. An excessive current flowed through the sensor and burned the metal deposition.

(e) IV curves from various unirradiated sensors showing bumps.

Figure 6.22: Examples of IVCV measurements that showed unexpected behaviours.

6.3 Laser characterisation results

Laser measurements were performed, using the TCT+ setup, on a selection of SINTEF BABY sensors of different pixel cell configurations, irradiated at increasing fluence steps. Table 6.5 lists the names of the BABY sensors measured during this campaign. Underlined numbers are sensors from wafer C25, the others are diced from wafer C23. Some combinations of "sensor type + fluence", as, for example, a 5E BABY sensor irradiated to $\phi = 1 \cdot 10^{14}$ p/cm^2, were not measured. The few neutron-irradiated measured sensors are used for comparison.

Nominal fluence [particles/cm^2]	BABY sensors - Pixel cell configuration					
	Proton irradiated					Neutron irradiated
	1E	2E	3E	4E	5E	3E
0	221	222	249	203	–	249
$5 \cdot 10^{13}$	–	257	207	208	–	218
$1 \cdot 10^{14}$	43	26	258	23	–	–
$5 \cdot 10^{14}$	250	–	247	248	85	–
$1 \cdot 10^{15}$	–	211	233	28	–	135
$5 \cdot 10^{15}$	–	251	233	245	–	–
$1 \cdot 10^{16}$	236	267	259	264	–	–

Table 6.5: List of the names of BABY sensors measured using the TCT+ setup, against nominal fluence and pixel cell configuration. Underlined numbers are sensors from wafer C25, others are from wafer C23. The nominal fluence is the set fluence during the irradiation campaigns. The measured fluences are listed in Tables 5.3 and 5.4, respectively for proton and neutron irradiations.

Measurements with the TCT+ setup were performed using the red top and IR top and bottom illuminations. The red bottom laser could not be used because of the presence of the support wafer that completely absorbs the short-penetrating photons. Instead, the penetration depth of the IR laser makes this wavelength suitable for both top and bottom illumination.

Both unirradiated and irradiated sensors were measured at $t = -20\,°$C. During all measurements, the attenuators of the laser heads (see Section 5.4.1) were kept with an aperture of 3.1 mm, therefore the flux of photons is small enough to not modify the electric field. A higher rate of photons could generate a "plasma effect", namely a local variation of the electric field structure induced by the presence of a very high concentration of electron-hole pairs produced by

the laser light-silicon interaction. Setting the aperture of both laser wavelengths to 3.1 mm determines, according to Figure 5.16, that there are about 10 MIPs injected inside the sensor for each measurement.

6.3.1   Signal as a function of the bias

Figures 6.23 and 6.24 provide an example of results of TCT+ measurements performed by varying the bias voltage on the BABY sensor No. 23 (4E) from wafer C25. This sensor, proton-irradiated to a fluence $\phi = 1 \cdot 10^{14} \, \mathrm{n_{eq}/cm^2}$, is characterised by a depletion voltage of $U_{depl} \sim 20$V, a breakdown voltage of $U_{bd} \sim 70$ V and a leakage current on the plateau of about $I_{leak} \sim 100$ nA.

Figure 6.23 reports the shapes of the signals collected during voltage scans using the three laser types. A single point on the sensor surface (the sensor-optic distance is constrained by the laser focus) was selected within a region giving a large signal.

The three scans give similar signal shapes, corresponding to the typical edge-TCT signal: in 3D sensors, in fact, performing a "normal TCT", top or bottom, is equivalent to an eTCT for a planar sensor, because the light crosses the sensor parallel to the electrodes and scans the active volume between the electrodes. The signal height for the red top measurements is larger than IR signals because the red light is entirely absorbed by the sensor. Vice versa, some of the IR light traverses the entire thickness and the beam does not release all its energy inside the sensor.

Signals get to their maximum within $t \sim 2$ ns and have a duration of about $(5 - 10)$ ns. A shift of the peak of the signal towards longer times can be appreciated for lower voltages: the electric field is less strong and charge carriers' velocity is reduced, according to Equations 3.6 and 3.7. The height of the signal amplitude generally increases with the increasing voltage, whilst the rise time gets smaller and the overall length of the signal shortens.

The collected charge as a function of the voltage for the three lights is presented in Figure 6.24. The charge is obtained by converting the signal into a current signal (dividing by the resistance $R = 50 \, \Omega$) and integrating it over $t = 25$ ns. All three plots show that, after a short linear increase with the applied voltage, the collected charge reaches a plateau. The value of the knee voltage depends, for 3D sensors, on the width of the laser beam and on the distance between the sampled point and the electrodes. Contrary to planar devices, it is not an indication of the depletion voltage.
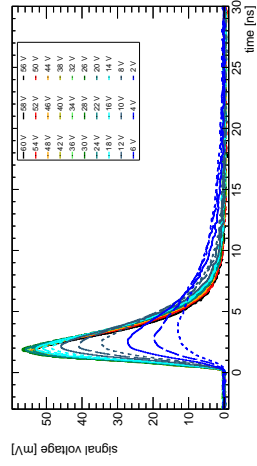
(a) Signal shapes U scan, red top.
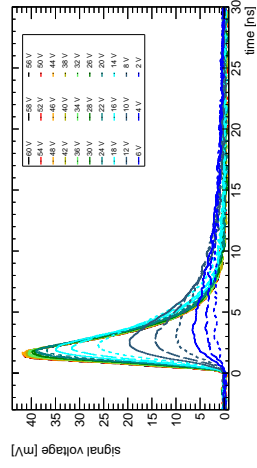
(b) Signal shapes U scan, IR top.
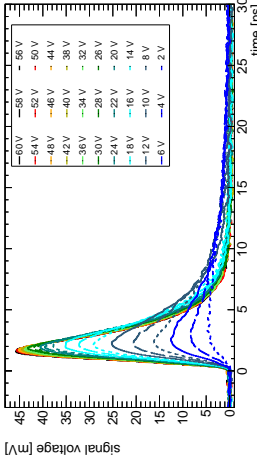
(c) Signal shapes U scan, IR bottom.

Figure 6.23: Signal shapes collected during voltage scans on sensor No. 23 (4E) from wafer C25, proton-irradiated to $\phi = 1 \cdot 10^{14}\ n_{eq}/cm^2$.
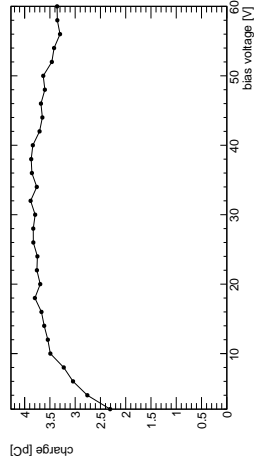
(a) Collected charge U scan, red top.
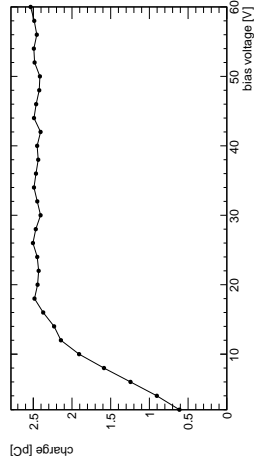
(b) Collected charge U scan, IR top.

(c) Collected charge U scan, IR bottom.

Figure 6.24: Collected charge as a function of the bias voltage, measured during voltage scans on sensor No. 23 (4E) from wafer C25, proton-irradiated to $\phi = 1 \cdot 10^{14}\ n_{eq}/cm^2$.

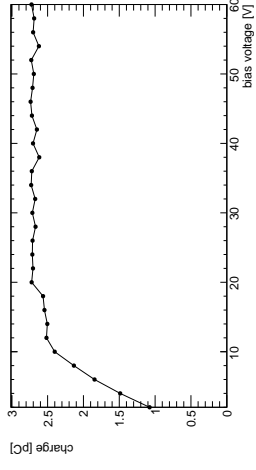It can be noticed that, for the red top laser measurement (see Figure 6.24a), the charge slightly reduces at voltages $U > 40$ V: the signal pulses (Figure 6.23a) are shorter in time and smaller in amplitude. While the first characteristics is foreseen, as a higher voltage determines a larger electric field and, therefore, a faster charge drift, the second behaviour is unexpected and no sensible explanation has been found. The stability of the laser cannot have influenced the charge collection, as the reference diode shows constant values of laser power during the data taking. This charge decrease at higher voltages was observed in many red top measurements. Some other sensors showed a steadily increase in the charge with the voltage, showing no plateau before the measurement reached the maximum voltage. No correlation was found between the wafer of origin (C23 or C25) and the shape of the voltage-dependent charge curves.

## 6.3.2 Signal as a function of the position

Surface scans performed on SINTEF 3D sensors provide information about the geometry of the sensors. The charge maps extracted from these scans show structures that are related to the depletion inside the bulk (IR-laser scans) and on the surface (red-laser scans). In this work, they are also used to evaluate the uniformity of the sensor in terms of charge collection. From these scans, the value of the mean collected charge is extracted (as explained in Section 5.4.2) and studied as a function of the fluence.

6.3.2.1 Full surface scan of an unirradiated sensor

Figure 6.25a shows the charge map obtained scanning with red light the entire surface of an unirradiated SINTEF 3D BABY sensor with 1E configuration. The sensor was part of a large silicon piece containing many sensors, so it can be considered as undiced.

This map is a laser-induced picture of the sensor, obtained by integrating the waveforms collected during the scan over the sensor surface. It reflects the geometry of the sensor, which is drawn in Figure 6.25b using Glade [169]. The electrodes and the metal lines are clearly visible as regions where the charge collection is lower. The regions with higher charge collection correspond to the depleted areas of the sensor that are not covered by metal. The depletion region is substantially confined within the pixel matrix of the sensor and only expands outside the borders along the long side of the pixel cells (yellow half-circle regions

of Figure 6.25a). A more in-depth analysis of the geometry within the pixel matrix area is given in Section 6.3.2.2.
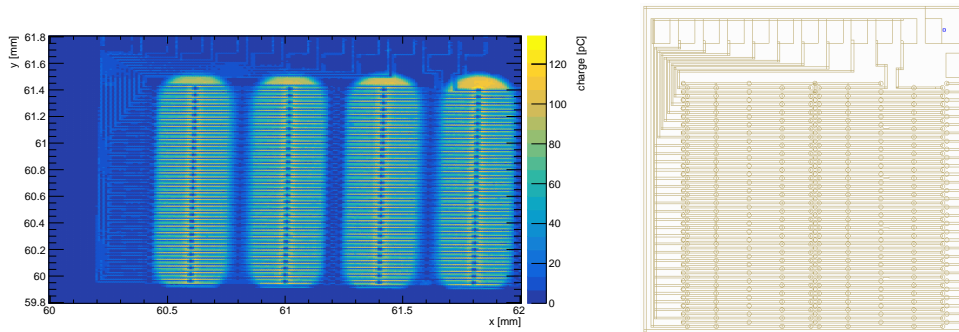
(a) Charge map of an entire BABY sensor, measured before irradiation using a red laser from top. Axes not to scale.

(b) Metal structure of a 1E BABY sensor, drawn using Glade [169].

Figure 6.25: Red TCT charge map scan over the entire surface of an unirradiated BABY sensor (2×2 mm^2). The metal structure, sketched on the right-hand side, is clearly visible in the laser measurement.

This image features a high charge collection, much larger than the measurements reported later in this work. This is justified by two factors: first, the measurement was performed at a temperature of $t = +20\,°\mathrm{C}$, rather than the set temperature for all other measurements ($t = -20\,°\mathrm{C}$). Second, the sensor was unirradiated and overdepleted.

This long scan is the only measurement carried out over the entire surface of the sensor, while all others are confined to smaller areas: the duration of the scan would become a limiting factor when it is required to measure many sensors. The full surface scan, consisting of more than 40000 data points, was executed with a not-yet optimised data acquisition system and took around 2.5 days. Given the regular geometry of the sensor, it is more interesting to scan with higher resolution (corresponding to a smaller step size) over a smaller area. Scanning a larger area would present the advantage of verifying the uniformity of charge collection across the entire sensor; at the same time, however, this homogeneity is very difficult to evaluate in the case of sensors whose surface contains many metal lines, like the sensors under test.

6.3.2.2 Signal versus position over small areas

Surface scans were performed on all BABY sensors listed in Table 6.5, using red top and IR top and bottom lasers. The same sensor was measured at three voltages, to evaluate the variation of the depleted region with the voltage.

Figure 6.26 shows the charge collected when scanning over a small area of sensor No. 23 (4E), already described in Section 6.3.1. The layout of the sensor is drawn on top of the charge map to guide the eye.

The measured sensor was biased at three voltages, $U = 2, 31, 60$ V. The scans spanned an area of (600×100) μm^2, with (10×5) μm^2 step resolution in the x and y directions while keeping z constant in the focusing plane. The intermediate voltage scan (at $U = 31$ V) is not shown in Figure 6.26 because at this voltage the sensor is already fully depleted and there is very little difference with respect to the $U = 60$ V maps. For each laser type and direction, the scans at the three voltages were performed sensing the same area, looping along the x and y coordinates. Therefore, the same coordinate on the maps at the two voltages correspond to the same point on the sensor. This fact does not hold when comparing different laser types: as the sensor was moved from one laser optic focus to another, it would be quite complex to position the laser in the exact same region of the sensor. This effort in scanning the same area is not strictly necessary for the scope of these measurements: thanks to the recursive geometry of the sensors, comparisons can be nevertheless made.

The structure of the sensors can be easily observed in the maps where the sensor was fully biased (Figures 6.26a, 6.26b and 6.26c). The electrodes are clearly visible as regions with the lowest charge collection ($Q \leq 0.5$ pC) in top-laser measurements or with the highest charge ($Q > 2.5$ pC) in the IR bottom scans. In top-laser measurements, a non-zero charge may still be collected where the columns are etched because of two reasons: first, the laser, even if focused, has a width of ~ 10 μm, therefore it may illuminate an overlapping region between the column and the nearby uncovered silicon; second, if the sensor's surface is slightly tilted with respect to the laser direction (this may happen as the sensor is manually glued onto the PCB), the IR top laser can partially cross the active volume, where it creates charges.

The metallic strips on top of the sensor are identified by the lower-charge line-shaped horizontal regions in the top-laser maps (Figures 6.26a and 6.26b), and, correspondingly, the higher-charge region in the bottom-laser map (Figure 6.26c). The strips are not parallel to the $x-$axis because the sensor was not aligned
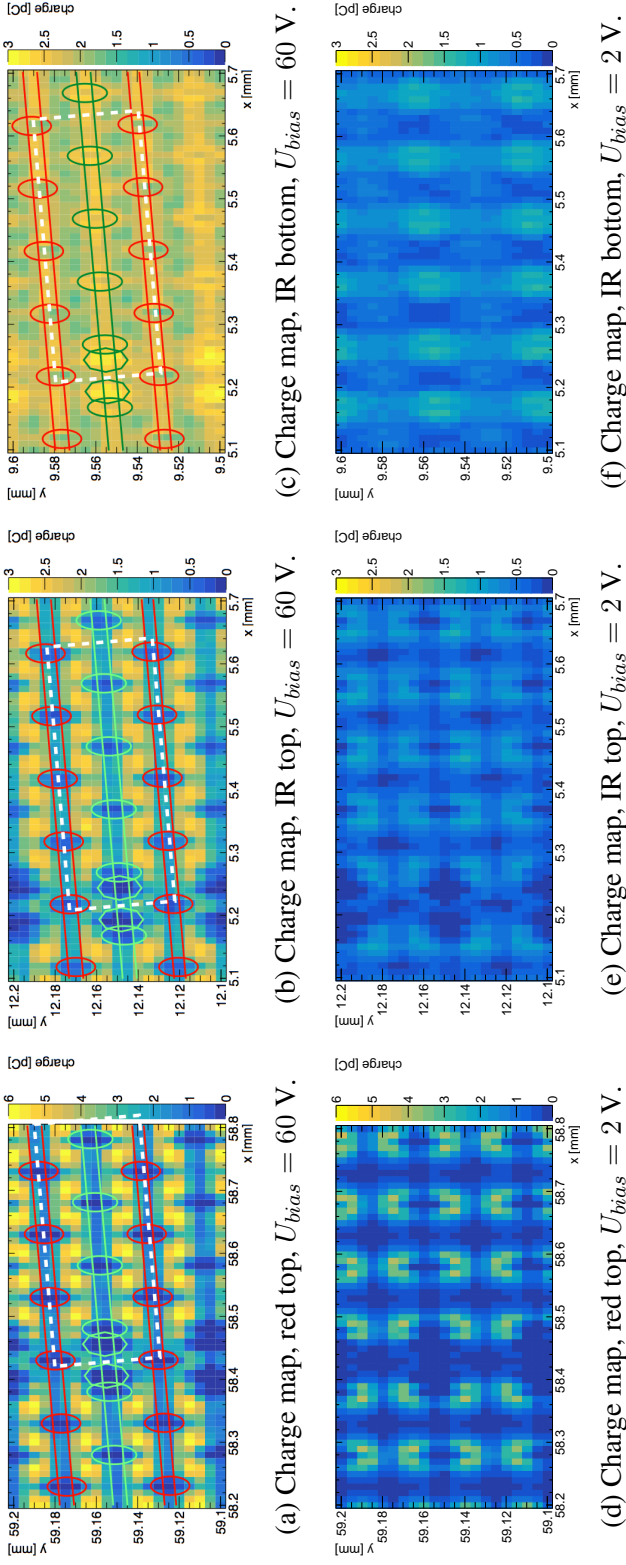
(a) Charge map, red top, $U_{bias} = 60$ V.

(b) Charge map, IR top, $U_{bias} = 60$ V.

(c) Charge map, IR bottom, $U_{bias} = 60$ V.

(d) Charge map, red top, $U_{bias} = 2$ V.

(e) Charge map, IR top, $U_{bias} = 2$ V.

(f) Charge map, IR bottom, $U_{bias} = 2$ V.

Figure 6.26: Charge maps of the BABY sensor No. 23 from wafer C25, with pixel configuration 4E, proton-irradiated at $\phi = 1 \cdot 10^{14}$ n_{eq}/cm^2. The scan was performed over an area of (600×100) μm^2, for different voltages and TCT laser wavelengths. x and y axes not to scale. Red ellipses indicate the p^+ electrodes, the green ones indicate the n^+ columns, strips are identified by pairs of same-colour lines. The octagonal shapes locate the position of the bump pads. The pixel area is identified by the white dashed rectangle. For the maps at $U = 2$ V, the position of these structures is the same as for the $U = 60$ V maps.

195

when glued. For top-illuminated maps, the low charge is caused by the external reflection of the light from the metal. When illuminating the sensor's backside, the IR laser gets reflected by the strips too, but in this case the reflection is internal to the active volume and the light effectively crosses twice the active volume. In Figure 6.26c, in fact, the charge is larger than in Figure 6.26b in regions covered by metal strips, while it is slightly lower in the metal-free regions. This small discrepancy can be attributed to a two-fold effect of the support wafer: first, it is not completely transparent to the IR laser and partially absorbs the light; second, given that its bottom surface is not polished, the photons get scattered and the flux that reaches the active silicon is reduced.

Together with the electrodes, also the bump-pads are visible as low-charge dots in top-laser scans (e.g. in the map of Figure 6.26a, the larger low-charge circles at coordinates $x = 58.4$ and 58.45 mm). In the IR bottom map (Figure 6.26c), the bump-pad dots are identifiable as the high-charge circles.

When the applied voltage completely depletes the sensor, the collected charge is maximum in the metal-free region between the n^+ and the p^+ electrodes and decreases when the laser spot overlaps any of the metal parts present on the surface of the sensors. As shown in the sketch of Figure 6.27, the area uncovered by metal is quite narrow with respect to the laser spot dimensions and this determines that only a small fraction of xy scan coordinates have a complete clearance. This effect is evident in Figure 6.28, which shows the charge collected during a red top TCT scan along the $y-$axis. The scan crosses the electrode columns and is perpendicular to the strips connecting all the same-type electrodes. Its minima ($Q_{norm} \sim 0.05$ a.u.) correspond to the presence of electrodes, where most of the laser light is reflected by the metal on top of the electrode. The local minima with a higher charge ($Q_{norm} \sim 0.4$ a.u.) are the strips: because of the width of the laser, a fraction of the beam reaches the silicon and generates some charge. The maxima, instead, are collected when the entire laser circle illuminates the active material. This scan confirms the small clearance on the surface of the sensor.

At $U = 2$ V (Figures 6.26d, 6.26e and 6.26f), the sensor is underdepleted, therefore not all generated charges are collected. The created charges undergo two processes: either they recombine, because the electric field is not strong enough to separate electrons and holes, or they diffuse in the bulk, possibly entering the residual electric field region in which they drift towards the junction electrodes. Charge maps at low voltages show a higher charge only in proximity of the n^+ electrodes, while in between these electrodes, in the metal-free areas, the charge collection is low.
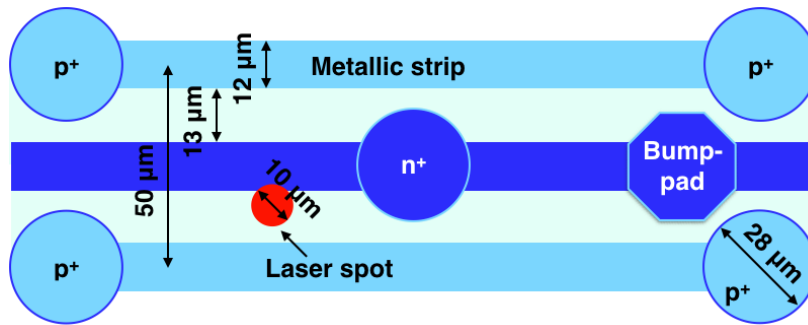
Figure 6.27: Sketch of the top structure of the SINTEF 3D sensors with the widths of the metallic strips, electrodes and bump-pad and the width of the focused laser. The areas of uncovered silicon are very narrow.
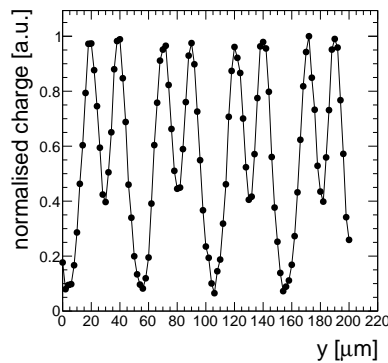

Figure 6.28: Charge, relative to the maximum, collected during a TCT scan across the Y axis, perpendicular to the strip direction and crossing a series of electrodes. Minima ($Q_{norm} \sim 0.05$ a.u.) correspond to the electrodes, local minima at a higher charge ($Q_{norm} \sim 0.4$ a.u.) are the strips, the maxima are where the laser is not reflected and releases energy in the sensor.

A direct comparison of the maximum collected charge for red and IR measurements of Figure 6.26 cannot be made because of different factors: first, the experimental setup settings affect on the intensity of the different lasers. The red optical system, in fact, delivers more light than the IR top/bottom system because of the lower number of splitting steps (see Figure 5.17). This effect is partially counterbalanced by the different power settings of the lasers, 40% for red and 60% for IR lights, as described in Section 5.4.1. Second, the dissimilar absorption length of the two laser types results in a different fraction of the

197

intensity effectively absorbed by the silicon.

The comparison between the maps at $U = 60$ V and those at $U = 2$ V proves that the collected charge decreases as the voltage decreases. In particular, in underdepleted sensors the low-charge (underdepleted) regions spread from the p^+ towards the n^+ columns. The presence of vertical higher-charge "stripes" in correspondence of the n^+ electrodes (interrupted by the horizontal metal strips) indicates the presence of a small electric field generated around the collecting electrodes. The vertical stripes with very low charge are underdepleted regions where the charge carriers generated by the laser-silicon interaction are not likely to reach the junction electrodes and recombine instead. The geometry of the sensor can still be distinguished at $U = 2$ V.

6.3.2.3   Comparison among surface scans using IR top lasers

Some surface scans, performed using the IR top laser, are shown as examples and compared among each other. The use of the IR top laser, because of its high penetration length, emulates the behaviour of a MIP-like particle inside the sensors and it is therefore preferred to the red illumination, which produces charge only in the first few microns of thickness.

6.3.2.3.1   Comparison between different voltages

Figure 6.29 shows the charge map for an unirradiated sensor with configuration 1E (sensor No. 221 from wafer C23), biased at $U = 2$ V and $U = 15$ V. The sensor, measured bare in the IVCV setup, was characterised by a long plateau and a breakdown voltage $U_{bd} > 70$ V (see Figure 6.30). Yet, when coupled to the TCT+ PCB and measured in the TCT+ setup, it could not be biased at voltages higher than $U = 15$ V, because the compliance current was otherwise reached. This limitation in the measurements is observed in many sensors and could be due to a large leakage current generated by an imperfect coupling with the PCB.

Comparing the maps at two voltages (Figures 6.29a and 6.29b), a substantial widening of the depleted region of this unirradiated sensor is observed. The maximum collected charge in proximity of the n^+ electrodes increases at the larger voltage. When biasing the sensor at $U = 15$ V, the volume is not completely depleted: a width of about 100 μm, in the central region between two n^+ electrodes around the p^+ columns, remains underdepleted and the generated charges only diffuse. The maximum charge collected slightly increases at the highest applied voltage.
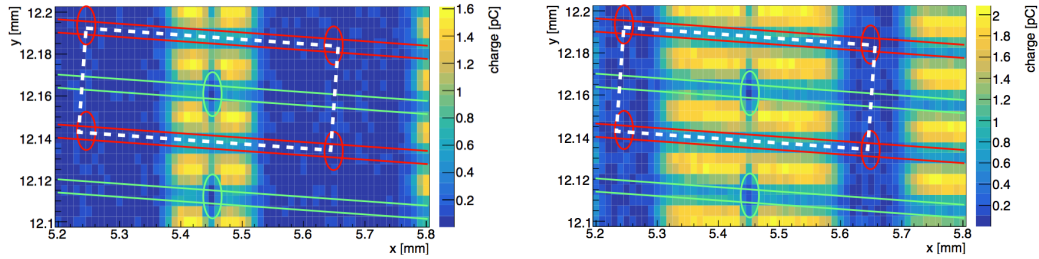
(a) Bias voltage $U = 2$ V.

(b) Bias voltage $U = 15$ V.

Figure 6.29: Comparison between the IR top charge maps of an unirradiated sensor (No. 221 (1E) from wafer C23) under bias $U = 2$ V (left) and $U = 15$ V (right). The map covers, on the $x-$axis, 1.5 pixels. The red ellipses locate the p^+ electrodes, the green ones identify the n^+ columns, the sensor strips are identified by pairs of same-colour lines. The white dashed rectangle defines the pixel.
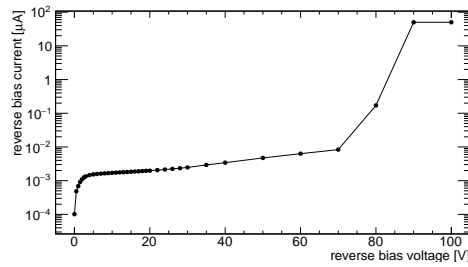

Figure 6.30: IV curve of the sensor No. 221 (1E) from wafer C23, unirradiated, measured in the IVCV setup, before being mounted on the TCT PCB.

6.3.2.3.2   Comparison between different configurations

Figure 6.31 compares two sensors irradiated to the same fluence, both diced out from wafer C23. Sensor No. 250 (Figure 6.31a) has configuration 1E and was biased at $U = 70$ V, while sensor No. 85 (Figure 6.31b) has configuration 5E and was biased at $U = 40$ V. The different biasing is dictated by the respective IV curves: sensor No. 85 presents a low breakdown voltage ($U_{bd} \sim 45$ V). The closeness of the electrodes in the 5E configuration certainly plays a role in decreasing the breakdown voltage, as it gives a higher electric field when the same bias voltage is applied.

Increasing the number of electrodes per pixel has the advantage of increasing the charge collection even at low voltage: the electric field is stronger given the
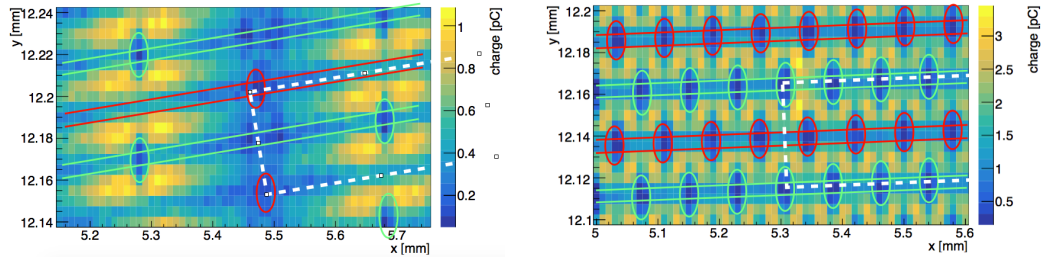
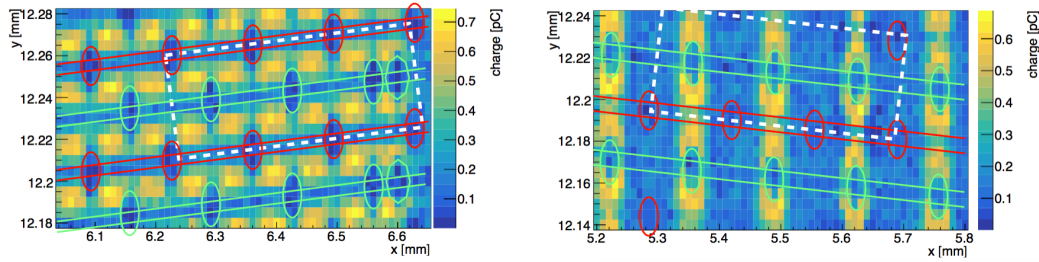(a) Proton-irradiated sensor No. 250 (1E) from wafer C23 under reverse biasing U = 70 V.

(b) Proton-irradiated sensor No. 85 (5E) from wafer C23 under reverse biasing U = 40 V.

Figure 6.31: Comparison between IR top charge maps of two sensors irradiated up to the same fluence ($\phi = 2.5 \cdot 10^{14}$ n_{eq}/cm^2) that have a different configuration: 1E (left) and 5E (right). Note the different colour scale. Red ellipses indicate the p^+ electrodes, the green ones indicate the n^+ columns, strips are identified by pairs of same-colour lines. A pixel is identified by the white dashed rectangle (the scan was not centred on a pixel, therefore the pixel cells are partially cut).

closeness of the electrodes. On the other hand, a large number of electrodes leads to inefficiencies caused by the inactive volumes occupied by the columns. In TCT scans, the metal covering the electrodes is another source of inefficiency.

6.3.2.3.3 Comparison between different fluences

Figure 6.32 shows two IR top charge maps obtained measuring two sensors with configuration 3E biased to the same voltage ($U = 70$ V) and proton-irradiated to different fluences: sensor No. 247 (Figure 6.32a) was irradiated to $\phi = 2.5 \cdot 10^{14}$ n_{eq}/cm^2, while sensor No. 259 (Figure 6.32b) was irradiated to $\phi = 5 \cdot 10^{15}$ n_{eq}/cm^2. The sensor irradiated at a higher fluence shows, with respect to sensor No. 247, larger areas with reduced charge collection in the mid region between n^+ electrodes. This effect can originate either from an insufficient biasing or because of the radiation damage, which created new energy levels that become trapping centres for the moving charges. Sensor No. 259 has a breakdown voltage of $U = 80$ V, therefore a measurement at higher voltage could not be performed.

(a) Sensor No. 247 (3E) from wafer C23, proton-irradiated at $\phi = 2.5 \cdot 10^{14}$ n_{eq}/cm^2.

(b) Sensor No. 259 (3E) from wafer C25, proton-irradiated at $\phi = 5 \cdot 10^{15}$ n_{eq}/cm^2.

Figure 6.32: Comparison between the IR top charge maps of two sensors with configuration 3E, both biased at $U = 70$ V, and irradiated at $\phi = 2.5 \cdot 10^{14}$ n_{eq}/cm^2 (left) and $\phi = 5 \cdot 10^{15}$ n_{eq}/cm^2 (right). Red ellipses indicate the p^+ electrodes, the green ones indicate the n^+ columns, strips are identified by pairs of same-colour lines. The octagonal shapes locate the position of the bump pads. The pixel area is identified by the white dashed rectangle.

6.3.3 Charge collection as a function of the fluence for different pixel configurations

A further analysis of the TCT+ results that summarises different sensors' measurements was implemented to identify possible variations of the charge collection as a function of fluence. The method is described in Section 5.4.2 and results are reported here for electrode configurations from 1E to 4E.

Extracting a sensible mean value of the charge from the 2D charge maps is not straightforward: the presence of the metal strips alters the distribution of the collected charge and makes the problem less intuitive with respect to the approach that could be used for a planar pad sensor (which has a large aperture on the metalization on the frontside of the sensor). For this reason, the analysis takes advantage of the use of a threshold to the minimum charge used to compute the mean value. The choice of such threshold will be discussed shortly (in Section 6.3.3.1).

The complexity of the estimation of the charge mean significantly increases when dealing with IR bottom charge maps: in the case of top-laser scans, in fact, the maximum charge is collected where the electric field has its maximum and no metal covers the sensor's surface, while in IR bottom charge maps the correspondence high-charge/high-field does not hold because of the internal

reflections leading to localised charge hotspots. Keeping the algorithm simple, it is more difficult to discriminate whether the charge, at a given location, is high because the sensor has a high electric field and high collection efficiency or because it is in the region covered by metal. Since the IR laser penetrates through the entire thickness of the sensor, the charge collected in the metal-free areas should ideally be the same for IR top and bottom measurements. It is observed that, in metal-free areas, the charge in IR top maps is about 12% higher than in IR bottom maps. This discrepancy, as already pointed out in Section 6.3.2.2, can be attributed to a small diffusion and absorption of the IR bottom laser caused by the presence of the support wafer. Nevertheless, the considerations towards the charge measured in IR top scans can be reasonably extended to the IR bottom scans. The results on the dependence of the charge on the fluence are therefore reported only for red top and IR top illuminations.

6.3.3.1 Choice of the charge threshold used to compute the mean charge of charge maps

The analysis used to evaluate the variation of the charge with fluence, described in Section 5.4.2, requires the definition of a threshold to avoid underestimating the charge because of the presence of the metal structure. Applying a threshold effectively means excluding some bins of the charge map from the calculation of the mean value. Figure 6.33 shows, as an example, the charge maps of the unirradiated 2E sensor No. 222, shone with IR-top laser, when different threshold cuts (applying Equation 5.21 for $f = 0, 0.35, 0.5, 0.65$) are used. The case $f = -1$, not shown in the figure, applies no cuts. The electrodes are removed when $f \geq 0$. When $f = 0.35$ is used, parts of the strips are removed, but it requires a higher threshold to completely cut the charge collected when the laser hit the metallic surfaces. Overall, choosing $f = 0.5$ is a good compromise between excluding laser-inaccessible metal regions and including a large fraction of the metal-free areas.

Figure 6.34 shows the effects of different threshold choices (the description of the curves' shape will be discussed in Section 6.3.3.2). It compares, on the left, the mean collected charge for 4E sensors, all biased at $U = 70$ V, as a function of the fluence when different thresholds are applied. On the right, the ratio between the curve with $f = 0.5$ and the other curves is presented.

Applying a threshold to the minimum charge used to compute the mean value has the obvious consequence of moving the mean collected charge to higher
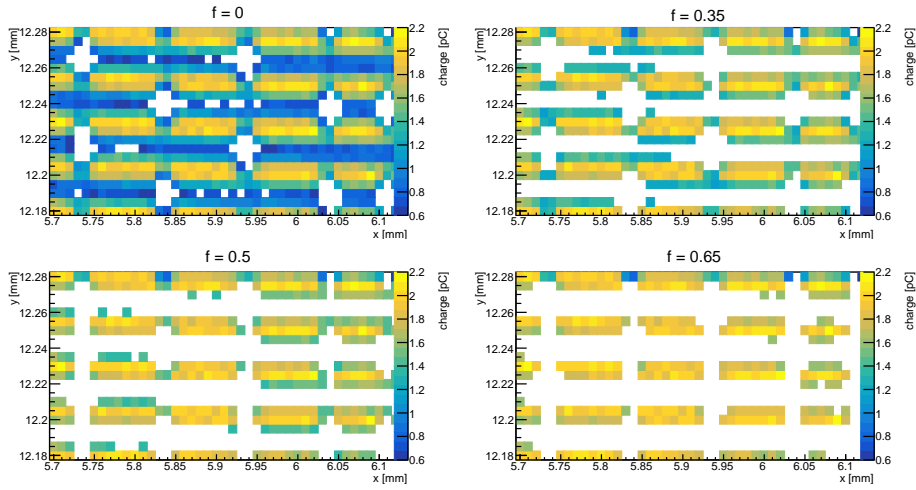
Figure 6.33: Charge maps of the unirradiated sensor No. 222 (2E) from wafer C23, biased at $U = 70$ V, after the application of 4 different threshold factor values ($f = 0, 0.35, 0.5, 0.65$) used in Equation 5.21.
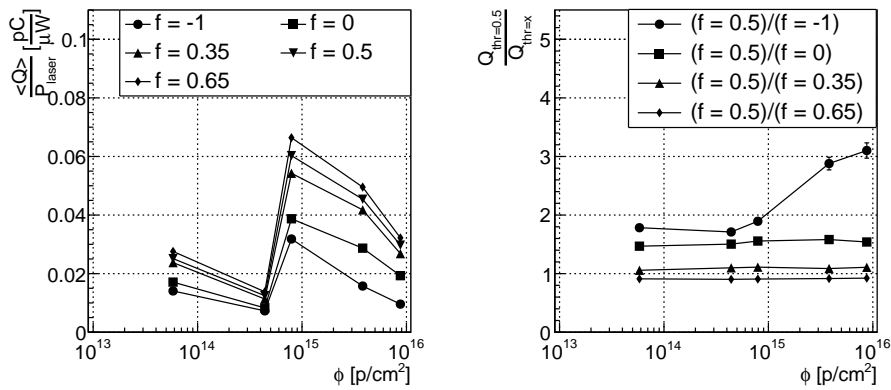
Figure 6.34: Left: mean charge values of 4E sensors, proton-irradiated and biased at $U = 70$ V, as a function of the fluence. Different curves related to different threshold factors f. Right: ratio between the curve with $f = 0.5$ and the other curves.

values. The shape of the curves, however, does not significantly change. The ratios between curves are rather constant as soon as a minimum threshold ($f = 0$) is applied. In particular, a variation of the charge of about 10% is observed when setting the threshold $\pm15\%$ with respect to the $f = 0.5$ curve.

The solid-circle graph of the right-hand side of Figure 6.34, showing the ratio between the curves for $f = 0.5$ and $f = -1$, has an increasing trend at high fluences. This growth is caused by the low-charge regions present in the high-fluence charge maps. If $f = -1$, all the points are considered for computing the mean, making the mean value small. Vice versa, if a threshold is applied, the low-charge regions are ignored: the mean charge is pushed to higher values. Hence, the ratio gets larger. The associated error bars at high fluences are larger than in the other curves because of the smaller sample size.

6.3.3.2 Mean charge variation with the fluence

Figures 6.35, 6.36 and 6.37 show the dependence of the mean charge on the fluence, normalised by the laser intensity, that is collected during position scans performed at different voltages (xyU scans), for BABY sensors with configuration from 1E to 4E for red top (left) and IR top (right) laser measurements. The measured sensors are listed in Table 6.5. Figures 6.35 and 6.36 report proton-irradiated data while Figure 6.37 combines neutron-irradiated sensor results. Although their IV curves showed a plateau extending up to $U \sim 80 - 100$ V, many sensors measured in the TCT+ setup could not be biased at voltages as high as $U = 70$ V because they reached the compliance current (set to $I_{compl} = 100 \ \mu$A) at lower voltages. The maximum bias voltages in the TCT setup, with respect to the maximum voltage measured in IV measurements, is reported in Table A2. As a consequence, the measurements could only be taken setting the bias voltage at (sometimes significantly) lower values and comparisons between sensors need to take into account the variety of applied voltages.

The data points are the value of the mean charge, computed using a factor $f = 0.5$ to cut the contribution from the metal strips and the electrodes and normalised by the laser intensity. In order to keep the plot clear, only the maximum voltage at which the sensors could be measured is drawn. The error bars of the points are the RMS of the charge distribution for each voltage and each fluence. Most of them are smaller than the marker size. The sensor names and their wafer of origin for each fluence point are indicated.

The charge decreases after irradiation and the higher the fluence, the more important the reduction of the mean charge. This observation holds when unirradiated sensors, even if biased to a lower voltage, are compared with irradiated ones.

The unirradiated values are comparable within each other, taking into
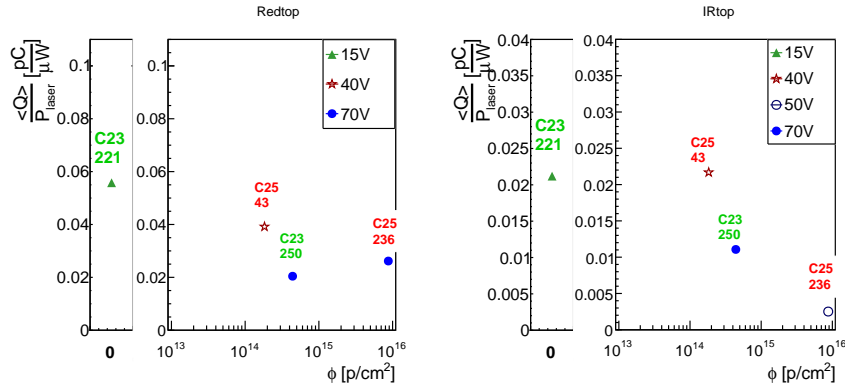
(a) Mean collected charge as a function of fluence for proton-irradiated 1E BABY sensors.
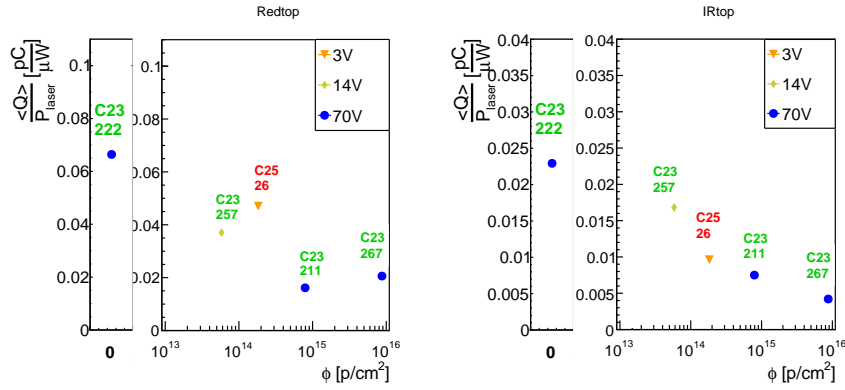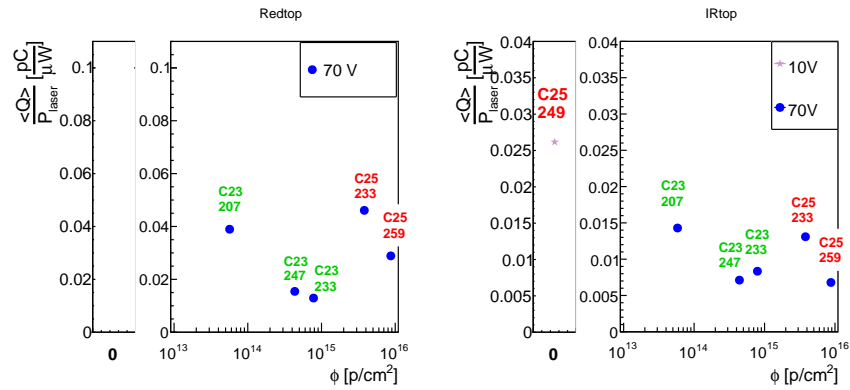

(b) Mean collected charge as a function of fluence for proton-irradiated 2E BABY sensors.

Figure 6.35: Mean collected charge, normalised to the laser power, as a function of the fluence, for proton-irradiated BABY sensors with configuration 1E and 2E illuminated with red top (left) and IR top (right) light.

account the bias voltage: as an example, for red measurements, the value is $Q/P \sim 0.065$ pC/μW for $U = 70$ V, and decreases as the voltage decreases.

The most interesting plot is Figure 6.36b, which reports data for sensors with 4E configuration. At the voltage of $U = 70$ V, the data points do not monotonically decrease with the increase in the fluence. Sensors No. 23 and 28, irradiated respectively at fluence $\phi = 1.8 \cdot 10^{14}$ n_{eq}/cm^2 and $\phi = 7.9 \cdot 10^{14}$ n_{eq}/cm^2, show a mean charge larger than sensor irradiated at lower fluences and are of the same order of magnitude (considering the bias voltage

(a) Mean collected charge as a function of fluence for proton-irradiated 3E BABY sensors.

(b) Mean collected charge as a function of fluence for proton-irradiated 4E BABY sensors.
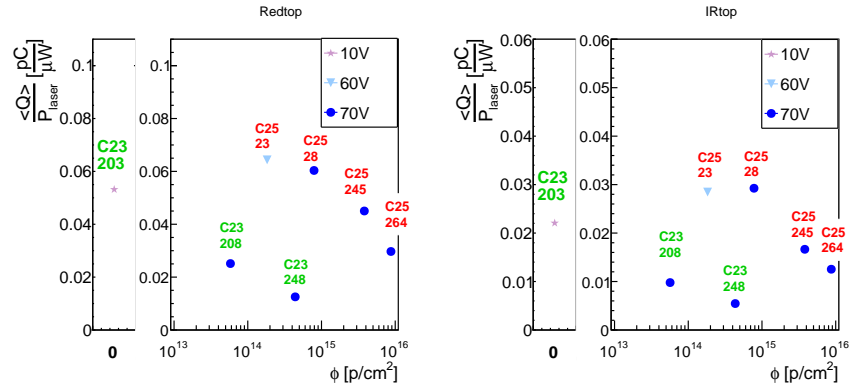
Figure 6.36: Mean collected charge, normalised to the laser power, as a function of the fluence, for proton-irradiated BABY sensors with configuration 3E and 4E, illuminated with red top (left) and IR top (right) light.

difference) as the unirradiated measurement. This can be explained taking into account the origin of the measured sensors: sensors coming from wafer C25, the "good" wafer, are characterised by a significantly larger mean charge with respect to sensors from wafer C23. This consideration can be extended to all other pixel configurations: sensors from wafer C25 show a larger mean charge even when they were exposed to higher fluences.

Considering only the C25 sensors, they present a monotonic mean charge reduction as a function of the increasing fluence. The trends of their data points

206

approximately have the same steepness for both IR and red plots.

Only two neutron-irradiated BABY sensors were measured in the TCT+ setup. Their mean charge, normalised to the laser power, is drawn as a function of the fluence in Figure 6.37. The comparison with the corresponding proton-irradiated sensors (Figure 6.36a), taking also into account the large variation within a single wafer and between the two wafers, does not lead to conclusive observations. Sensor No. 218 (from wafer C23), irradiated with neutrons at $\phi = 5 \cdot 10^{13}$ n_{eq}/cm^2, collects about the same charge as its corresponding proton-irradiated sensor No. 207 (wafer C23). The case of sensor No. 135, irradiated with neutrons to a fluence of $\phi = 1 \cdot 10^{15}$ n_{eq}/cm^2 is different: it shows a collected charge larger than the sensor irradiated with protons to the same fluence. This discrepancy is more likely to be caused by variations of behaviour within the same wafer, rather than being consequence of the radiation damage given by the two interacting particles.
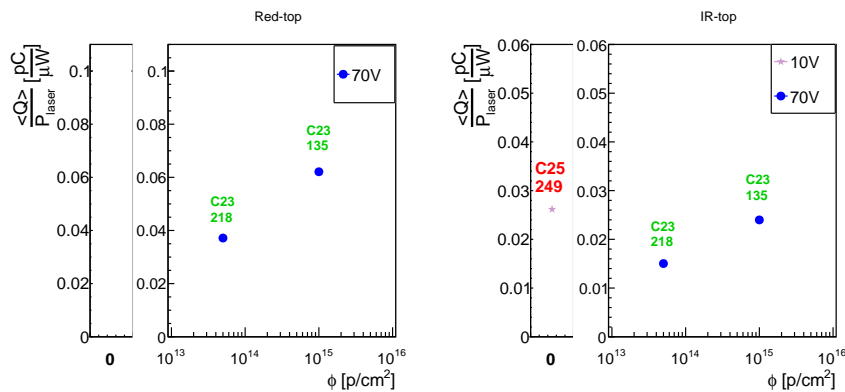
Figure 6.37: Mean collected charge, normalised to the laser power, as a function of fluence for neutron-irradiated 3E BABY sensors for red top (left) and IR top (right).

6.3.4 Charge collection as a function of the bias voltage

Figure 6.38 presents the mean charge, normalised by the laser power, for proton-irradiated sensors with configuration 4E, illuminated with red and IR top lights. Each sensor was biased to different voltages, with the maximum voltage limited by the compliance current, as explained in Section 6.3.3.2.

Figure 6.38: Mean charge, normalised to the laser power, collected by sensors with 4E configuration irradiated with protons at different fluences and biased at various voltages.

In the majority of the cases, the mean charge value increases with the voltage. For voltages above depletion, the increase is less significant: as an example, the charge collected by sensor No. 28, irradiated with protons at $\phi = 7.9 \cdot 10^{14}$ n_{eq}/cm^2, is similar for $U = 36$ V and $U = 70$ V and notably larger than for $U = 2$ V.
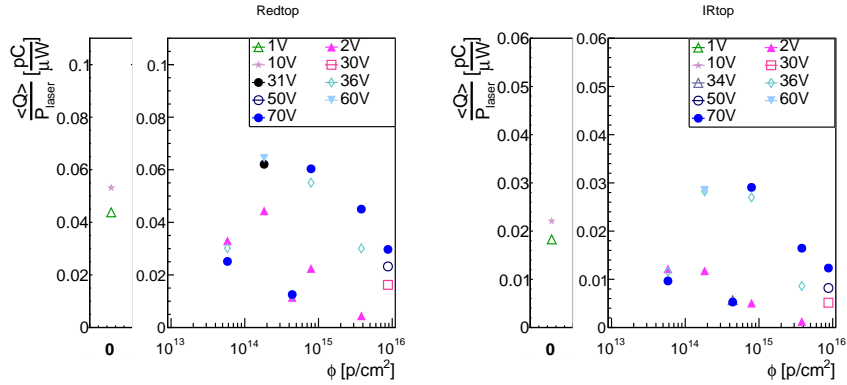
6.4 Radioactive source results

The performance of sensors can be measured in the most realistic conditions either using radioactive measurements or test beams. The first have, over the latter, the crucial advantage of being readily available in a laboratory. In this work, they were performed using the ALiBaVa read-out system available in the SSD laboratory (see Section 5.5).

Prerequisites
In order to get a good measurement with the ALiBaVa setup, some prerequisites have to be satisfied:

- The source, sensor and scintillators must be aligned. The positions of the radioactive source and the scintillator are fixed in the SSD setup and their alignment is guaranteed. The sensor is aligned by means of an $x - y$ stage.

- The trigger latency must be correctly set. The ALiBaVa GUI, implemented in the data acquisition system, includes an online monitoring of the signal as a function of the time (in a 100 ns-window acquisition time). This tool is used to determine the latency (see Section 5.5.2). The latency is correctly set when the rise time of the signal falls within the first 25 ns. It was found that the right latency for the SSD setup is 128 (in units of 25 ns).

- The trigger level must be correctly set. The trigger level is the threshold voltage to be applied on the photomultiplier to discriminate between random electronics noise and the trigger signal from a particle. A threshold of 40mV was used for all measurements. Further increasing the threshold level would lead to a reduction of the data acquisition rate.

- A good sensor, suited for taking measurements with the ALiBaVa setup, must be available. This last prerequisite, as it will be explained shortly, was found to be partially unmet when measuring SINTEF sensors.

Measured sensors

The ALiBaVa setup was used to perform radioactive source measurements on an unirradiated planar strip sensor and on a few unirradiated and irradiated SINTEF FEI3 and FEI4 sensors. Table 6.6 summarises some properties of the sensors measured in these tests.

The planar strip sensor, described in Section 6.1, was used as a reference sensor for debugging the acquisition system and the analysis.

As mentioned in Section 5.5.2, only half of the strips of FEI4 sensors could be wire bonded because of the larger dimension of the sensor with respect to the read-out fan-in. The wire bonds connected the half sensor that, overall, showed better IV and CV curves.

Sensors were biased, whenever possible, to a voltage above depletion. For many SINTEF sensors, the depletion voltage could not be uniquely identified because the IV and CV curves of their strips do not show well-defined plateaux and the depletion voltage knees, for the same strip, differ by about 10 V for the two types of measurements. The bias voltages, during ALiBaVa measurements, were limited by the compliance current, set to $I_c = 1$ mA.

The only exception is the FEI4 sensor irradiated at $4.5 \cdot 10^{14}$ n_{eq}/cm^2: it was the only SINTEF sensor, measured with the ALiBaVa setup, that could be biased at $U = 40$ V (well on the plateau region of both the IV and CV curves), while keeping a modest value of the leakage current. This sensor differs also for the strip

Sensor	Strip pitch [μm]	Nominal ϕ [n_{eq}/cm^2]	t [°C]	Chip No.[a]	U_{bias} [V]	I_{leak}[b] [μA]	C_{str}[c] [pF]
Planar Fz2328_11-7	80	0	-20	1	-300	38	0.3
3D FEI3-C21-1	400	0	$+20$	1	-11	875	~ 55
3D FEI4-C26-1	250	0	-20	2	-12	770	~ 75
3D FEI4-C21-2	250	proton, $1 \cdot 10^{14}$	-20	1	-10	795	~ 60
3D FEI4-C21-4	250	proton, $4.5 \cdot 10^{14}$	-20	2	-40	105	~ 45

Table 6.6: List of sensors measured using the ALiBaVa setup, some of their specifications (pitch size and irradiation fluence), and the measurement conditions. [a] The chip number indicates to which of the two Beetle chips on the ALiBaVa DB the sensor was wire bonded. [b] The leakage current is read from the power supply of the ALiBaVa setup, for $U = U_{bias}$. [c] The capacitance of a single strip, extracted from CV curves, is reported at the operating bias voltage $U = U_{bias}$.

capacitance, lower than the capacitance values for the other FEI4 sensors. The lower capacitance is not only consequence of the complete depletion, but it is a characteristic of this sensor: other FEI4 SINTEF devices present end capacitances, on single strips, of the order of $C \sim 55 - 60$ pF.

The measurements on SINTEF sensors needed various precautions because of their peculiar layout: first of all, they have no built-in AC coupling and therefore require the use of AC-coupled fan-ins to couple the sensor to the daughter board. Secondly, their strip pitch (respectively 400 μm for FEI3 and 250 μm for FEI4 sensors) does not allow for 1:1 wire bonding connections between the fan-in strips and the Beetle chip channels. This property of the SINTEF 3D required the masking, in the analysis, of all disconnected channels.

6.4.1 Pedestals, common mode noise and noise

Pedestal, common mode noise and noise need to be computed in order to measure the correct charge collection of a sensor.

6.4.1.1 Pedestal

Figure 6.39 shows the pedestal values for each channel of the Beetle chip to which, respectively, the planar sensor (Figure 6.39a), the unirradiated FEI3 sensor (Figure 6.39b) and the unirradiated FEI4 sensor (Figure 6.39c) are wire bonded. In the case of the SINTEF sensors, only the active channels are shown (this is true for all presented plots).
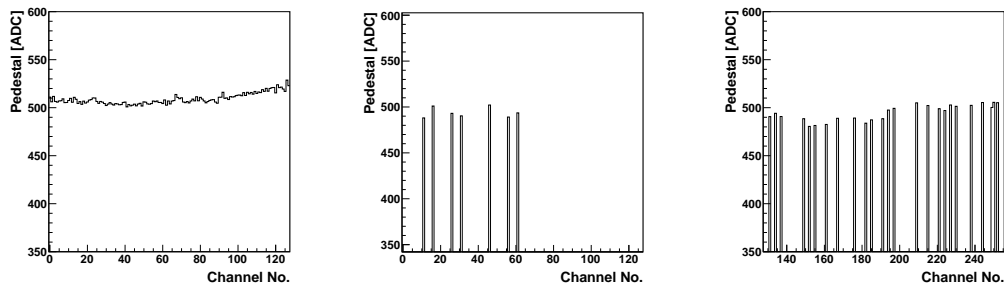
(a) Planar strip sensor, unirradiated.

(b) SINTEF FEI3 sensor, unirradiated.

(c) SINTEF FEI4 sensor, unirradiated.

Figure 6.39: Pedestal value for each read-out channel of the Beetle chip wire bonded to the sensor. Measurements for the planar sensor (left) and for the unirradiated SINTEF 3D FEI3 (centre) and FEI4 (right) sensors. Only the channels connected to the sensor are shown.

The pedestal values of the active strips are about 500 ADC, for all three sensors. Only 7 channels of the FEI3 sensor are shown because the other strips have a too-high noise value.

6.4.1.2 Common mode noise

The common mode noise distributions, for the four ports of each Beetle chip, are shown in Figure 6.40 for the three unirradiated sensors. The distributions are normalised by the number of entries.

There is a good agreement among the distributions characterising the 4 ports of each read-out chip. All distributions are peaked at ~ 0 ADC. The only exception is represented by Port2 and Port3 of the FEI3 sensor: their common mode is 0 because of the absence of active channels in the second half of the Beetle chip.

The distributions measured with the planar sensor are broader than those measured with the SINTEF 3D sensor. Being the common mode noise a coherent
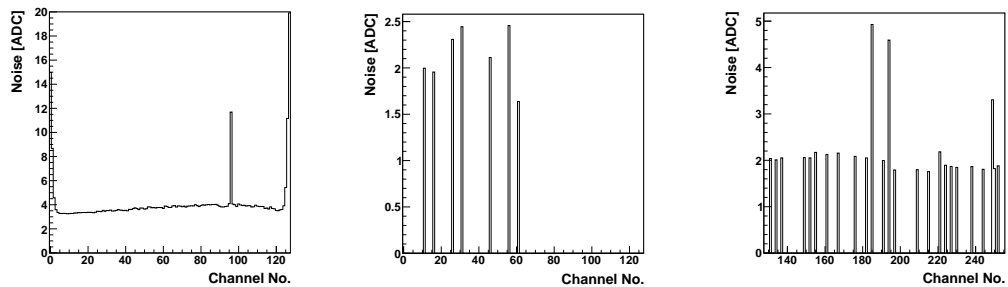
211

(a) Planar strip sensor, unirradiated.
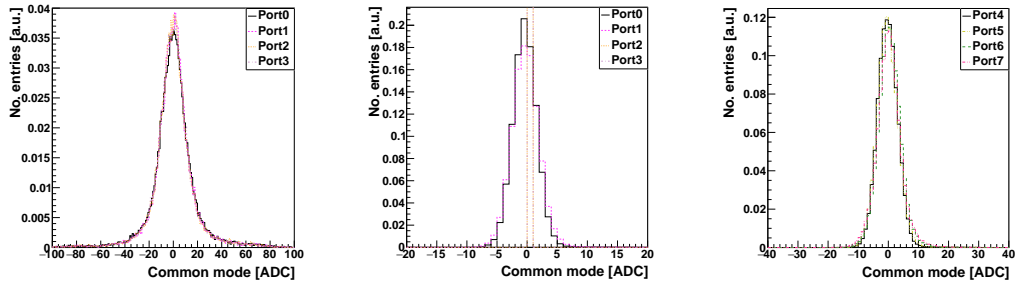
(b) SINTEF FEI3 sensor, unirradiated.

(c) SINTEF FEI4 sensor, unirradiated.

Figure 6.40: Common mode distributions for the planar sensor (left), the unirradiated SINTEF 3D FEI3 sensor (centre) and the SINTEF 3D FEI4 sensor (right). All curves are normalised by their number of entries.

shift of the baseline caused by environmental factors, the higher level in the planar sensor could be due to the fact that this sensor was connected to an old DB, which could have worse performance (e.g. because of the accumulation of dust).

6.4.1.3 Noise

The noise is defined in Section 5.5.3. The noise values are computed for each active read-out channel and are presented in Figure 6.41 for the three sensors.

(a) Planar strip sensor, unirradiated.

(b) SINTEF FEI3 sensor, unirradiated.

(c) SINTEF FEI4 sensor, unirradiated.

Figure 6.41: Noise value for each read-out channel of the connected Beetle chip. Measurements for the planar sensor (left), the unirradiated SINTEF 3D FEI3 (centre) and the unirradiated FEI4 (right) sensors.

212

The distribution related to the planar device shows a low noise level across the entire sensor, with the exception of a peak for channel No. 96 and for the external channels. The external channels are known to have a higher level of noise and are masked by default in the analysis. Channel No. 96 is also excluded from the analysis.

The noise distributions for the unirradiated SINTEF sensors are displayed only for the active channels. The noise levels, expressed in ADC counts, are lower than those in the planar sensor. This difference can be explained by the different age of the DBs.
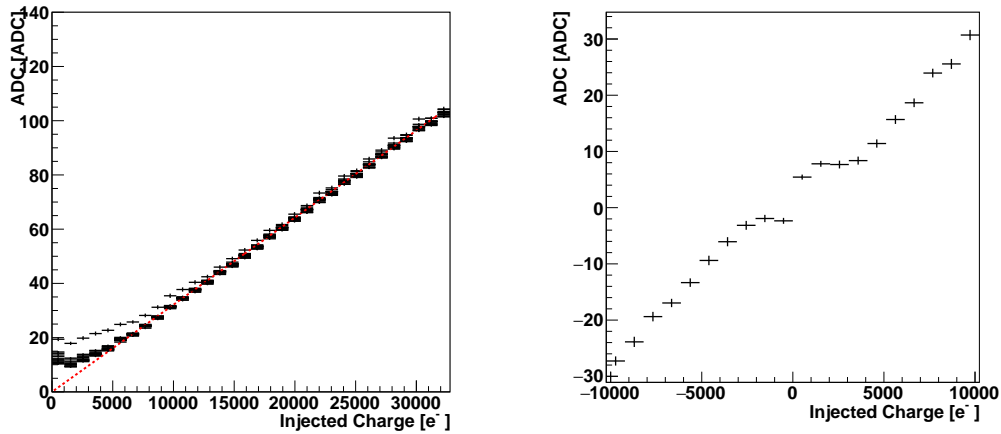
6.4.2 Calibrations

Obtained through calibration scans, the calibration curves visualise the measured ADC counts as a function of the absolute values of the injected charge, which is scanned in both polarities.

Figure 6.42a shows the calibration curves for every tenth channel in the planar sensor. With the exclusion of a single curve, there is an excellent agreement among all calibration curves. The only curve that does not follow the same trend at low charge corresponds to channel No. 0: this channel, as mentioned above, is masked by default. Overall, the calibration is uniform across the entire sensor.

The data points do not pass by the origin of the axes: this effect, already observed by other research groups[3], is attributed to the fact that the calibration circuit is less sensitive in the low-charge region and does not correctly read out the ADC counts corresponding to the injected charge. The calibration curve of a single strip (No. 40), extended to both the positive and negative ranges, is shown in Figure 6.42b for the zoomed-in range around 0. Excluding the region around 0, the steepness of the curve in the positive and negative ranges is very similar.

Figures 6.43a and 6.43b show, respectively, the calibration curves for all active strips of the unirradiated FEI3 sensor and the calibration curves for every fifth active strip of the unirradiated FEI4 sensor. Unlike the planar sensor, these calibration curves present a variety of trends, which can be ascribed to the different capacitances of these sensor' strips. Literature [156] confirms a dependence of the calibration factor on the detector capacitance seen by the Beetle chip: large capacitances lead to smaller calibration factors.

---

[3]This information was obtained by a private communication with the CMS members of the IFCA group, Santander, Spain.
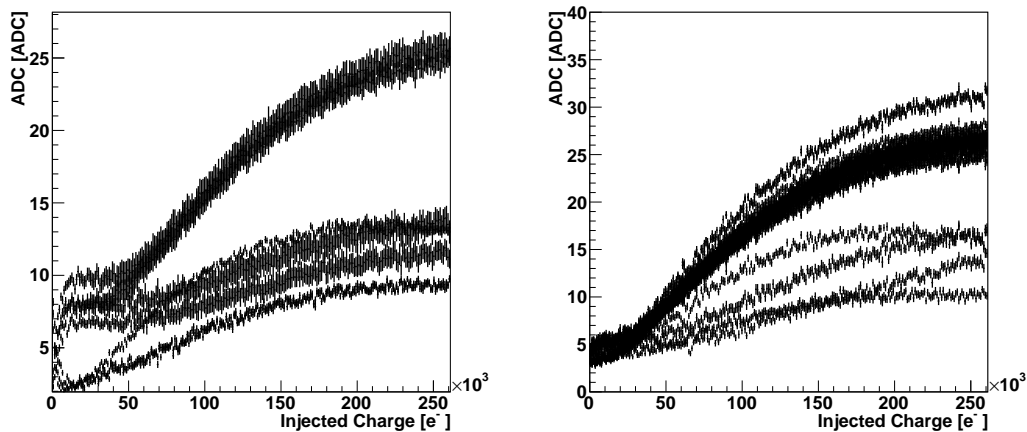
(a) Calibration curve shown for every tenth active channel of the connected Beetle chip. The dashed line is the fit to one of the curves.

(b) Calibration curve of strip No. 40, with range extending from negative to positive injected charge, zoomed-in in the range around 0. The calibration circuit does not correctly identify the injected charge for charges close to 0.

Figure 6.42: Calibration curves for the unirradiated planar strip sensor.

In addition, calibration curves of these SINTEF sensors show very low slopes when compared with the planar ones. Such behaviour may be caused by the very high leakage current drawn by the sensors: according to the literature [156], a high leakage current, besides increasing the total power consumption and leading to a higher noise, may also lead to a large growth of the DC signal current that bypasses the AC coupling. Another effect, consequence of the high capacitance, could sum up to the leakage current impact: the high capacitance, in fact, could limit the "efficiency" of the mechanism of measurement of the ADC output during calibration scans. As mentioned in Section 5.5.1, both injected charge's polarities are scanned during calibration. This ALiBaVa run is performed as follows: for a single charge injection, half of the channels is injected a positive charge, the other half a negative one. The sign of the injected charge is alternated with the channel number. In the successive event, 25 ns later, the polarity is inverted [156]. The RC time constant is longer in the case of a large capacitance: this may lead to an incomplete discharge of the sensor between two pulse injections.

From the calibration curves, the calibration factors are computed for each channel, fitting them with a linear function, over the range $[5, 32]$ ke$^-$ for the

(a) SINTEF FEI3 sensor, unirradiated. Calibration curve shown for all active channels.

(b) SINTEF FEI4 sensor, unirradiated. Calibration curve shown for every fifth active channel of the connected Beetle chip.

Figure 6.43: Calibration curves for some active channels. Measurements for the SINTEF 3D FEI3 sensor (left) and for the SINTEF 3D FEI4 sensor (right).

planar sensor and over the range $[5, 100]$ ke$^-$ for SINTEF sensors, and fixing the intercept of the fitting function to 0. The calibration factors for the three sensors are reported in Figure 6.44. For the planar sensor, the calibration factors are uniform across its strips. In SINTEF sensors, instead, some strips have a noticeably smaller calibration factor with respect to the majority of the channels.

The planar sensor's calibration factors are $\sim 3 \cdot 10^{-3}$ ADC/e$^-$. The unirradiated FEI4 sensor have much lower calibration factors, about $1 \cdot 10^{-4}$ ADC/e$^-$, and the factors are even lower in the case of the FEI3 strips. These low values can be consequence of two above-mentioned concurrent factors: the high capacitance and the high leakage current of the sensors. If these low calibration factors were used to convert the charge from ADC to electrons, the result would be a too high value with respect to the charge expected to be created by β-particles.

6.4.3 Cluster size, cluster charge and equivalent charge noise

The passage of a particle through a silicon sensor, such as the β-particles emitted by the radioactive source used for ALiBaVa measurements, creates electron/hole

215

(a) Planar strip sensor, unirradiated.
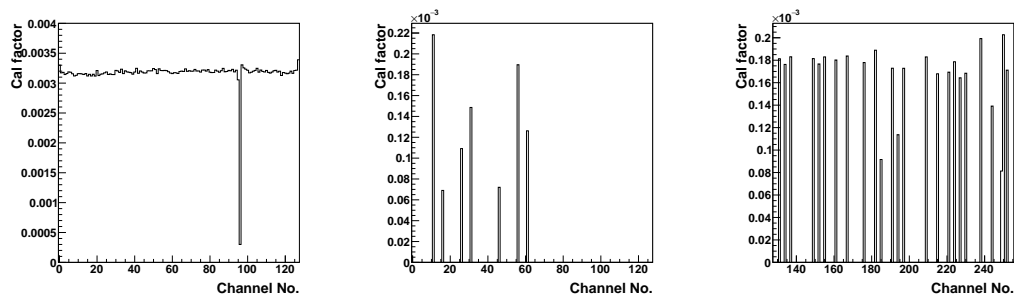
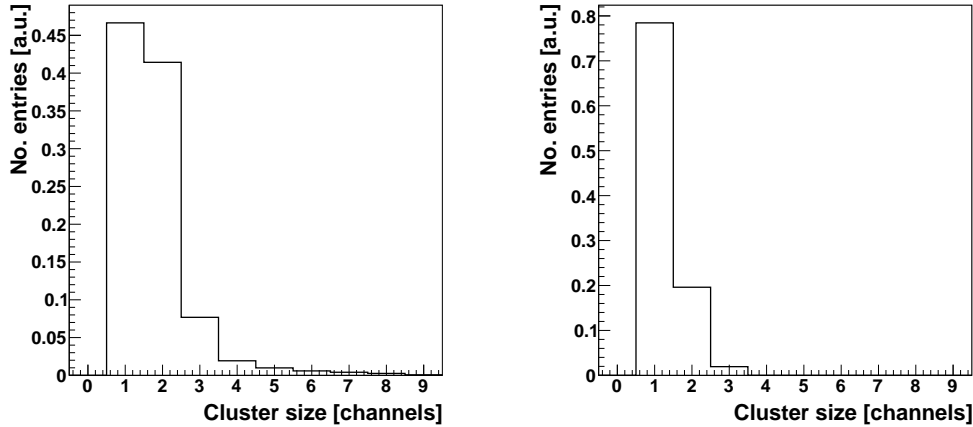(b) SINTEF FEI3 sensor, unirradiated.

(c) SINTEF FEI4 sensor, unirradiated.

Figure 6.44: Calibration factors extracted from the calibration curve for each readout channel. Measurements for planar sensor (left), for SINTEF 3D FEI3 (centre) and for SINTEF 3D FEI4 (right).

pairs along its path (see Section 3.2.1). These charges drift, following the electric field lines, towards the electrodes and induce a signal on the electrodes. Segmented sensors usually share the collected charge among several strips: for this reason the correct identification of the cluster is essential to measure the total deposited charge.

The FEI3 sensor collected a small number of clusters ($\sim$ 30) and no meaningful cluster charge distribution could be reconstructed. Results are hence shown only for the planar and the FEI4 devices.

6.4.3.1 Cluster size

In the planar sensor, it is observed (as shown in Figure 6.45a) that the cluster size distribution has a peak for values of cluster size 1 and 2, and the tail of the distribution does not exceed cluster size $\sim$ 10. Considering a strip pitch of 80 μm, a cluster size of 10 corresponds to a spread of the signal across 800 μm in the planar structure. In SINTEF sensors 800 μm correspond to 2 strips for FEI3 and $\sim$ 3 strips for FEI4 sensors. Thus, it is expected that the majority of the clusters in SINTEF sensors have size 1. The expectation is confirmed by the measured cluster size presented in Figure 6.45b for the unirradiated FEI4. The distribution has mean 1.2 ± 0.5 and is peaked for cluster size 1: in most cases, the charge is entirely collected by a single strip. The case of cluster size 2 happens when the incident electron crosses the sensor in a narrow region between two strips and the generated charge drifts in opposite directions towards the two junction electrodes.

(a) Planar strip sensor, unirradiated.   (b) SINTEF FEI4 sensor, unirradiated.

Figure 6.45: Cluster size distributions, namely the number of strips whose charge contributes to the total cluster charge, are shown for planar sensor (left) and for SINTEF 3D FEI4 (right). Values extracted from the radioactive source run. Distributions are normalised by the number of entries.
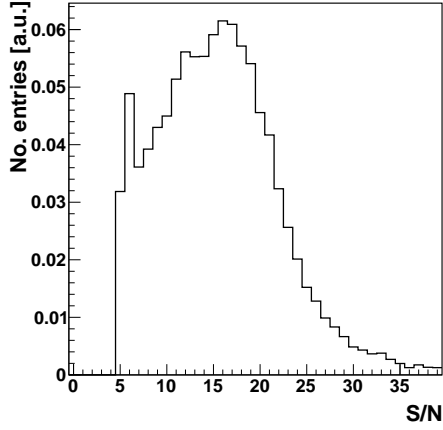
6.4.3.2 Signal-to-noise ratio

The strength of the signal is expressed in terms of signal-to-noise ratio (SNR). Figure 6.46 presents the distributions of the SNR of the cluster seed, for the planar and the unirradiated SINTEF FEI4 sensors. Both distributions have a hard low cut in the SNR at 5, given by the analysis (Equation 5.26).

The planar sensor shows an excellent discrimination between signal and noise. Its distribution peaks at 16. The unirradiated 3D FEI4 has a SNR mean of 5.95 ± 1.04, not far from the threshold imposed by the analysis. Trials were performed to evaluate if relaxing the cut for the selection would improve the charge collection spectrum, but, as they gave negative outcomes, are not reported here.

6.4.3.3 Charge distribution

The cluster charge distributions, in units of ADC counts, are shown in Figure 6.47a for the unirradiated planar sensor and in Figure 6.47b for the unirradiated FEI4 sensor.

Both cluster charge distributions are fitted with a Landau-Gaussian
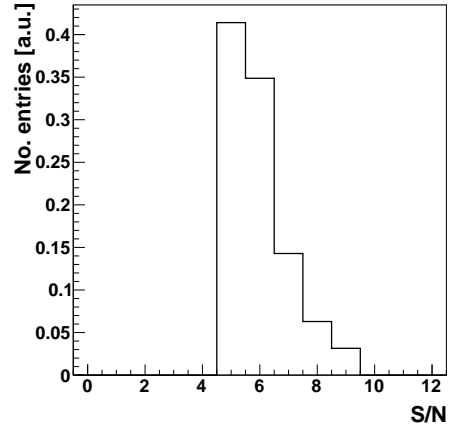
(a) Planar strip sensor, unirradiated.   (b) SINTEF FEI4 sensor, unirradiated.

Figure 6.46: Seed-strip signal-to-noise ratio distributions for the planar (left) and the unirradiated SINTEF 3D FEI4 (right) sensors. Distributions are normalised by the number of entries.
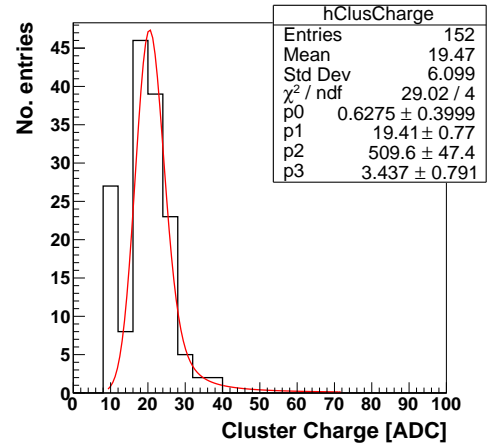
(a) Planar strip sensor, unirradiated.   (b) SINTEF FEI4 sensor, unirradiated.

Figure 6.47: Cluster charge distributions for the planar (left) and the SINTEF 3D FEI4 (right) sensors.

convolution. The MPVs of the convolutions are:

$$MPV_{Planar} \simeq 74.5 \pm 0.2 \text{ ADC} \tag{6.6}$$

$$MPV_{FEI4} \simeq 19.4 \pm 0.8 \text{ ADC} \tag{6.7}$$

Assuming a charge deposition of 80 (e/h) pairs/μm for a MIP, the number of electron-hole pairs generated is
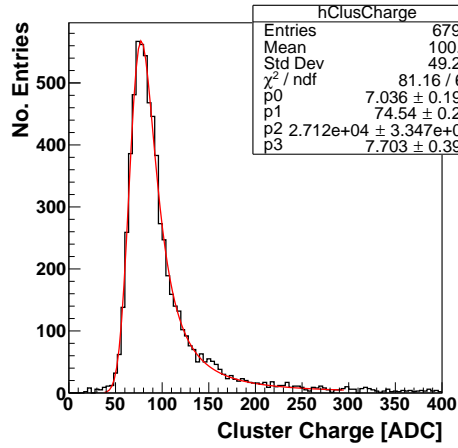
$$Q_{Planar} = 80 \times 300 = 24000 \text{ e}^- \tag{6.8}$$

$$Q_{3D} = 80 \times 230 = 18400 \text{ e}^-. \tag{6.9}$$

To obtain the foreseen charge values (in electrons), the calibration factor should be, for the planar and the FEI4 sensors respectively,

$$cal = MPV_{ADC}/Q_{expected} \tag{6.10}$$

$$cal_{Pl} = 75/24000 \simeq 3.13 \cdot 10^{-3} \text{ ADC/e}^- \tag{6.11}$$

$$cal_{3D} = 19/18400 \simeq 1.03 \cdot 10^{-3} \text{ ADC/e}^-. \tag{6.12}$$

The computed calibration factor for the planar sensor is very similar to the measured one, therefore it is expected that the planar sensor would present a good cluster charge distribution when expressed in units of electrons. In the case of the FEI4 sensor, instead, if the measured calibration factor was applied, the output charge would be a factor 10 higher than expected and would thus be meaningless from the physics point of view.

6.4.3.4 Charge distribution after calibration

Figure 6.48 reports the cluster charge distribution after the conversion into electrons of the planar sensor. This distribution is peaked at a charge $Q \sim (23350 \pm 80)$ e$^-$, close to the expected value indicated in Equation 6.8.

6.4.3.5 Equivalent noise charge

As the planar sensor could be successfully calibrated, the ENC can be calculated. Figure 6.49 shows, for the active channels, the noise as measured in electrons. For the planar sensor, the ENC is ~ 1100 e$^-$ (excluding the channels that get masked): it is of the expected order of magnitude to have the measured value of $SNR = 16$.

6.4.4 Irradiated sensors

The SINTEF 3D FEI4 sensors No. 2 and 4 from wafer C21, proton-irradiated at a fluence of respectively $\phi = 1 \cdot 10^{14}$ n$_{eq}$/cm^2 and $\phi = 4.5 \cdot 10^{14}$ n$_{eq}$/cm^2 were measured using the ALiBaVa setup.
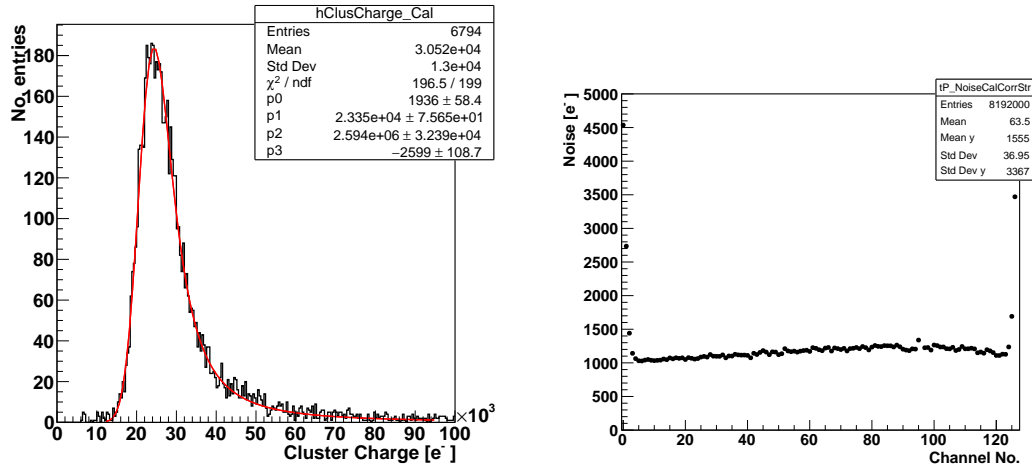
Figure 6.48: Cluster charge distribution after calibration, for the planar sensor.

Figure 6.49: ENC for the active channels of the planar sensor.

6.4.4.1 SINTEF sensor proton-irradiated at $1 \cdot 10^{14}$ n$_{eq}$/cm^2

Figure 6.50 shows the results of measurements on sensor FEI4-C21-2, irradiated at $\phi = 1 \cdot 10^{14}$ n$_{eq}$/cm^2.

The pedestal values (Figure 6.50a) are rather uniform across the entire sensor. A small positive trend is observed going towards the higher strip number.

The common mode distributions for the 4 ports are shown in Figure 6.50b. The distributions are not centered in 0 and, passing from the first to the last port, a shift in the mean value towards negative values is observed.

The ADC noise level measured in this irradiated FEI4 (shown in Figure 6.50c) is similar to the noise of the unirradiated FEI4 sensor.

Figures 6.50d and 6.50e show, respectively, the calibration curves for every fifth active channel and the extracted calibration factors for each active channel. The calibration curves are similar, but, as in the case the unirradiated FEI4 sensor (Figure 6.43b), they have very low values of ADC for high injected charges. The calibration factors are of the order of $2 \cdot 10^{-4}$ and there is an increasing trend with the increasing channel number. The variation of the electrical properties (leakage current and capacitance) across the sensor causes a variation in the response of the sensor in terms of pedestal values, common mode and calibration factor.

After irradiation, the cluster size distribution (presented in Figure 6.50f) has

a shape very similar to the unirradiated sensor. The generated charge is mostly collected by a single strip: the mean value is 1.2 ± 0.4.

The SNR distribution (see Figure 6.50g) features a maximum at 6 and has mean 6.6 ± 1.4. The value is slightly better than the maximum SNR of the unirradiated FEI4 sensor. This improvement, however, cannot be attributed to a "beneficial" effect of the irradiation, but are most probably given by the variety of responses typical of SINTEF sensors from Run-C.

Figure 6.50h presents the cluster charge distribution reconstructed using data from the low-irradiated FEI4 sensor. The MPV value is 14.09 ± 0.14 ADC. If an attempt of conversion between charge and ADC was performed, the distribution of the charge expressed in electrons would have an unphysically high value. On the other hand, a direct comparison between the charge collected by the irradiated and the unirradiated sensors expressed in ADCs (hence without applying the calibration factor) is meaningless because two different DBs were connected to the sensors.

6.4.4.2 SINTEF sensor proton-irradiated at $4.5 \cdot 10^{14}$ n_{eq}/cm^2

Results from measurements on the FEI4 sensor No. 4 from wafer C21, irradiated at $\phi = 4.5 \cdot 10^{14}$ n_{eq}/cm^2 are presented in Figure 6.52. Overall, this sensor showed good features, which can be traced back to its lower capacitance and modest leakage current (with respect to the other FEI4 sensors), which are presented for all measured strips in Figure 6.51. These curves are characterised by long and flat plateaux, extending for tens of volts.

When measured using the ALiBaVa setup, the sensor showed only 13 active strips: the other ones registered a too-high raw noise and were masked in the analysis. The pedestals for the active strips have a value of about 470 ADC (see Figure 6.52a).

In Figure 6.52b, the common mode noise of the three ports in which there are active channels are presented. These quasi-Gaussian distributions are not peaked at 0 ADC: this is an indication of some external pick-ups give a small interference with the data acquisition system. The source of this shift was not found, but it did not compromise the measurements during the radioactive source run.

The noise of the sensor (see Figure 6.52c) features a value around 2.5 ADC for most of the active strips and few strips with higher noise.

Figure 6.52d presents the calibration curves for the active channels. They can be separated in two different behaviours: some channels have a steeper curve,

while in the majority of the cases the slope is lower. Contrary to the previously-reported FEI4 sensors, however, the curves have a general good agreement and, most importantly, they reach significantly high values of the ADC counts for large injected charge. This trend is confirmed when the calibration factors are computed: they are in the range of $\sim 1 - 2.5 \cdot 10^{-3}$ ADC/e$^-$ (see Figure 6.52e). The calibration was therefore successful and results can be expressed also in electron units.

The cluster size of this sensor (see Figure 6.52f) has a higher mean value (equal to 1.6 ± 0.6) with respect to the ones shown in Figures 6.45 and 6.50f: the 3-strip cluster percentage is not negligible, even though the majority of the clusters, as expected, has size 1 or 2. The signal-to-noise distribution is presented in Figure 6.52g. Its MPV is reduced with respect to the one measured on the low-dose irradiated FEI4 sensor and is equal to 6.1 ± 1.2.

The cluster charge distributions are shown in Figures 6.52h and 6.52i, respectively in ADC and electrons units. The MPV of the charge collection is 22.16 ± 1.07 ADC, corresponding to a charge Q of

$$Q = 15600 \pm 1200 \text{ e}^-. \tag{6.13}$$

Assuming that the charge collection of an unirradiated sensor with a thickness of $230 \ \mu$m should be $Q \sim 18400$ e$^-$, the charge collection efficiency, CCE, of the measured sensor, irradiated at $4.5 \cdot 10^{14}$ n$_{\text{eq}}$/cm^2, is

$$CCE = Q_{irr}/Q_{unirr} = 15600/18400 \sim 0.85. \tag{6.14}$$

The high charge collection efficiency indicates the good performance of this sensor after irradiation, which is certainly linked to the good electrical properties.

6.5   Conclusions

SINTEF 3D sensors produced during Run-C showed, in preliminary tests, suboptimal properties such as high leakage current, low breakdown voltage and short carrier lifetime. The origin of such issues was unknown when the measurement campaign presented in this work was performed. It was discovered during the processing of Run-D, the ongoing new prototyping run: issues in the production process cause the formation of randomly-located and highly-doped pin-holes that alter the configuration of the electric field of the sensor. The

randomness of these defects makes the sensor responses very diverse and often significantly different from the expected outcomes.

Electrical measurements (IVCV) show a large variety of behaviours among sensors and among strips of a single sensor. However, common trends are observed: unirradiated SINTEF sensors respond following expectations to the variation of temperature; they show an increase in the capacitance and in the leakage current with the increase in closeness between electrodes; the spread of the electrical properties across sensors diced out from the same wafer follows a trend that depends on the original position of the sensor on the wafer; the capacitance depends on the pixel cell dimensions. In irradiated devices, the leakage current follows, for BABY sensors, the expected dependence on the fluence and the extracted damage constant is compatible with the value found in literature. In large sensors, the spread of the leakage current of strips of the same sensor is usually larger than the variation of this parameter with fluence. The depletion voltage does not significantly change with fluence and remains, for all sensors, below $U_{depl} = 20$ V. On the contrary, an increase in the breakdown voltage as a function of the fluence is observed. Finally, the end capacitance has a decreasing trend for higher fluences.

TCT measurements were performed only on 3D BABY sensors. The amount of charge collected depends on two parameters: where the laser hits the sensor and the bias voltage. The reflection of the metal structures on the sensor's surface determines a lower (higher) collected charge in top (bottom) illuminations. In the metal-free areas, the charge is higher in regions closer to the n^+ electrodes and diminishes towards the p^+ electrodes if the sensor is not fully depleted. Sensors with a higher number of electrodes per pixel show a higher collected charge (because the electric field is more intense), but have the disadvantage of presenting a reduced active volume. It is observed that a higher fluence shrinks the depleted region, causing a lower charge collection in regions far from the junction electrodes. The analysis developed to evaluate the variation of the charge with fluence highlights two main characteristics: first, the mean charge decreases with fluence; second, BABY sensors diced from wafer C25 (the wafer showing good IV curves in preliminary measurements) always collect more charge than sensors from wafer C23, even if irradiated to higher fluences. This suggests that electrical measurements are an excellent indicator of the quality of the sensor and of its performance under laser beams.

This statement is true also for charged particle exposure: the ALiBaVa measurements generally follow the behaviour anticipated by the IV and CV

223

curves. In fact, the sensors that present flat plateaux of both curves and are characterised by a low leakage current and a low capacitance when measured in the IVCV setup show good results, namely a Landau-Gaussian distributed charge collection and a sensible calibration factor, when measured with the ALiBaVa read-out system. A too-high leakage current compromises the measurement of the charge collection because of the high noise it generates, and is potentially dangerous for the setup itself, because the large current could mistakenly be injected into the read-out chip.
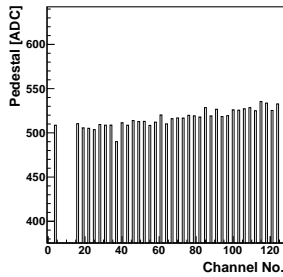
(a) Pedestal values for each active channel.
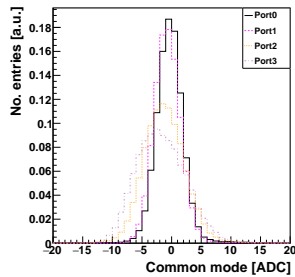
(b) Common mode distributions, normalised by the number of entries, for the 4 Beetle chip ports.
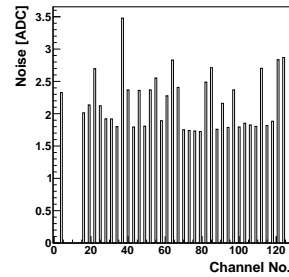
(c) Noise values for each active channel.
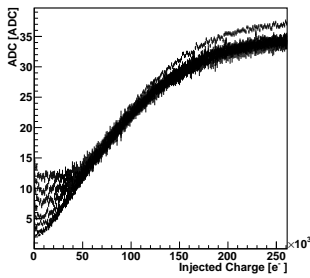
(d) Calibration curves, for every fifth active channel.
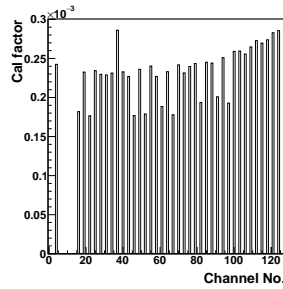
(e) Calibration factor for each active channel.
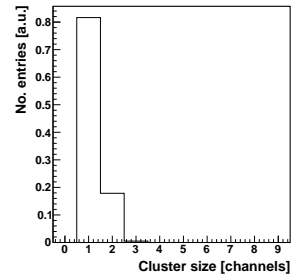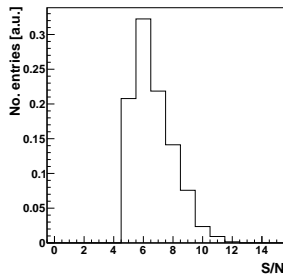
(f) Cluster size distribution, normalised by the number of entries.

(g) Signal-to-noise ratio, normalised by the number of entries.
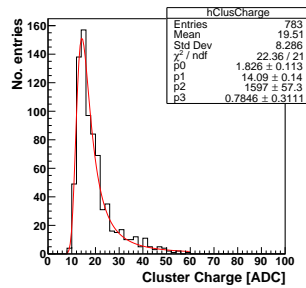
(h) Cluster charge distribution, in units of ADC counts, fitted with a Laudau-Gaussian convolution.

Figure 6.50: Characterisation with radioactive source measurements of FEI4-C21-2 sensor, proton-irradiated at $\phi = 1 \cdot 10^{14}$ n$_{eq}$/cm^2.

225
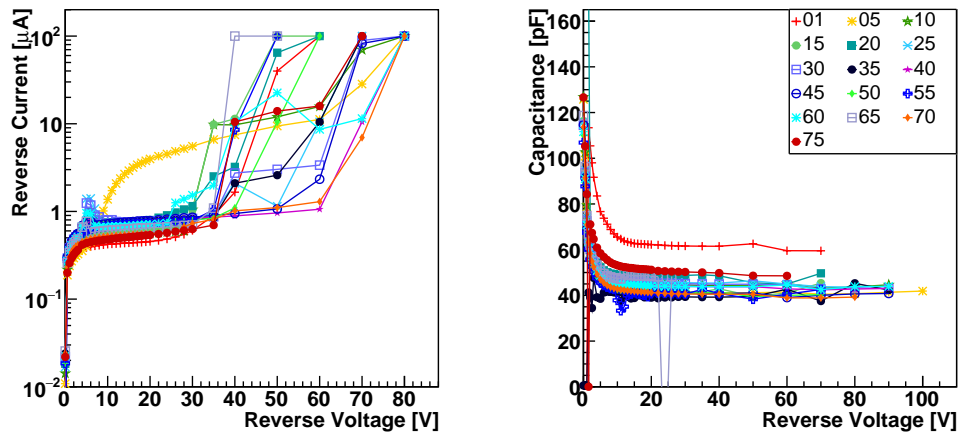
Figure 6.51: IV (left) and CV (right) curves of FEI4 sensor No. 4 from wafer C21 after proton irradiation at $4.5 \cdot 10^{14}$ n_{eq}/cm^2. The temperature was set to $t = -20\,°C$. The legend shows the strip numbers and refers to both plots.
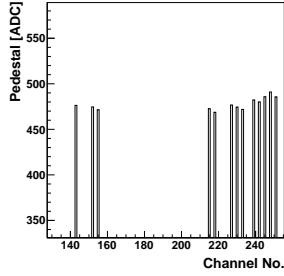
(a) Pedestal values for each active channel.
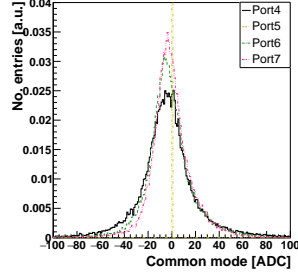
(b) Normalised common mode distributions for the 4 Beetle chip ports wire bonded to the sensor.
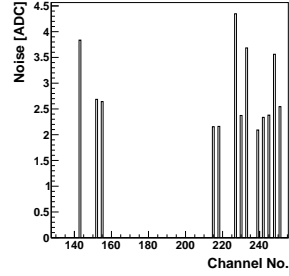

(c) Noise values for each active channel.
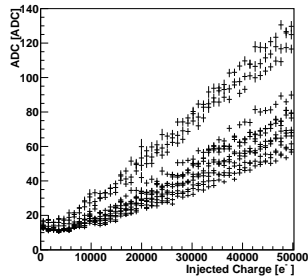
(d) Calibration curves for each active channel.
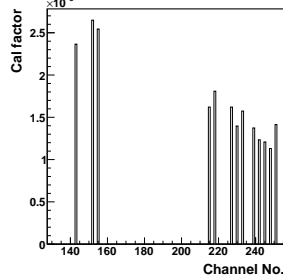
(e) Calibration factors for each active channel.
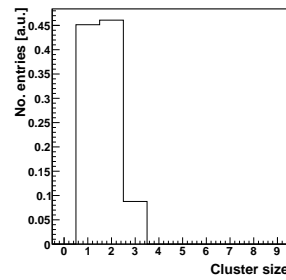
(f) Cluster size distribution, normalised by the number of entries.

(g) Signal-to-noise ratio, normalised by the number of entries.

(h) Cluster charge distribution, in units of ADC counts, fitted with a Laudau-Gaussian convolution.

227
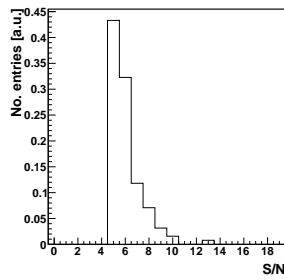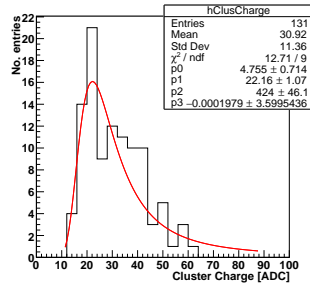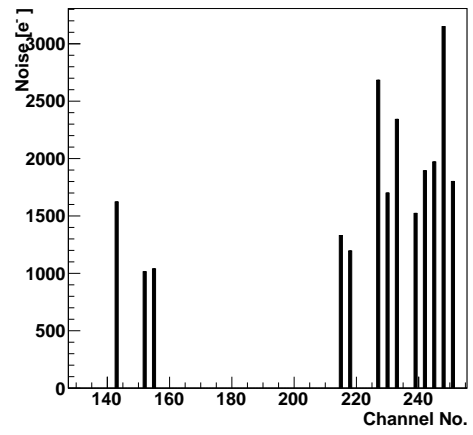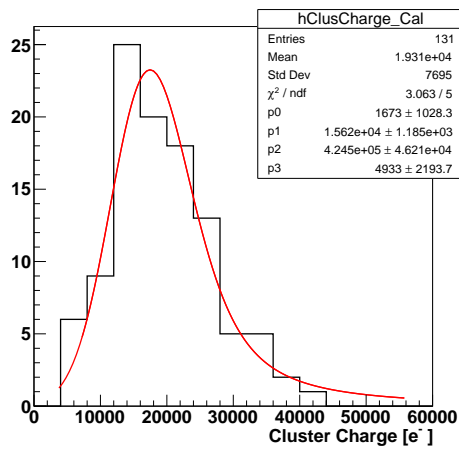
(i) Cluster charge distribution, converted into electrons, fitted with a Laudau-Gaussian convolution.

(j) ENC for the active channels.

Figure 6.52: Characterisation with radioactive source measurements of FEI4-C21-4 sensor, proton-irradiated at $\phi = 4.5 \cdot 10^{14}$ n$_{eq}$/cm^2.

Chapter 7

Conclusions and outlook

The LHC is a unique and powerful tool to investigate the building blocks of nature and how they mutually interact. The experimental discovery of all particles predicted by the Standard Model (SM) was concluded in 2012 with the announcement of the discovery of the Higgs boson. Yet, the LHC journey is not over: its physics programme includes more precise measurements of the properties of the Higgs boson as well as continued searches for physics beyond the SM. To achieve these goals, the LHC schedule foresees an increase in the machine luminosity, which will be reached during the High Luminosity (HL-LHC) phase.

During the first Long Shutdown (2013-2014), the ATLAS Pixel detector was refurbished and equipped with a new innermost layer, the Insertable B-Layer (IBL). The novel detector offers excellent performance in terms of impact parameter resolution, $b-$tagging performance and occupancy. It was instrumented with state-of-the-art technologies in all its aspects, from the sensors to the read-out electronics, mechanics and cooling.

The IBL byte stream converter
The first part of this thesis work was performed in the framework of the offline software activities for the integration of the IBL detector inside the ATLAS experiment. The aim of the task was the implementation of the IBL byte stream converter, a tool developed inside Athena, the ATLAS offline software architecture. This software decodes the data coming from the IBL: it transforms the binary stream, composed of 32-bit words, into information (such as hit position and Time over Threshold, a parameter proportional to the collected charge) whose format is readable by the offline reconstruction algorithms. It

also encodes the information produced by simulations into a simulated IBL byte stream.

The IBL data format has new features with respect to that of the Run I Pixel detector, to take into account the differences between the two read-out electronics. The most striking novelty of the IBL data format is the use of condensed hits: four 32-bit words contain information related to up to 10 pixel hits, while the same number of Run I Pixel detector hit words would only transmit 4 pixel hits.

The preliminary validation of the IBL byte stream converter is reported in this work. This offline tool has demonstrated to be fully operative in the ATLAS data taking chain since the beginning of Run II.

The R&D work on SINTEF 3D silicon sensors

Parallel to the offline software-related activities, an intensive R&D campaign was carried out to characterise the performance of 3D silicon pixel sensors. This technology, firstly proposed by S. I. Parker in 1997, features electrodes etched through the thickness of the device. The geometry offers advantages over the standard planar technology in terms of charge collection time and radiation hardness. However, 3D sensors have higher capacitances (and therefore higher noise levels) and their complex production process generally leads to lower yields.

The sensors measured for this work belong to the third prototyping run (Run-C) of SINTEF. The institute aims at participating in the instrumentation of the next ATLAS tracking detector that will be used during the HL-LHC phase. Three categories of $p-$bulk 3D sensors from Run-C were tested:

FEI3 sensors: they have the same dimensions and pixel matrix as the ATLAS Run I pixel sensors; the junction columns are joined together in strips by means of a metal layer.

FEI4 sensors: they have the same dimensions and pixel matrix as the IBL sensors; their read-out is segmented in strips, obtained with the application of a metal layer on the surface.

BABY sensors: they are test structures, with pixel cell configuration from 1E to 5E; all same-type electrodes are connected together to form a pad-like layout.

Sensors from several Run-C wafers were tested. The large majority showed, in preliminary measurements, high leakage currents, low breakdown voltages and short charge carrier lifetimes. The only exception is represented by sensors

from wafer C25, which showed good electrical characteristics. During the fourth (currently-ongoing) prototype run (Run-D), a failing step during the production process was discovered: it was observed that the mask layer preceding the etching step was too thin to be effective. This flaw caused the formation of pin-holes on the surface of the sensor that modify the electric field configuration.

The experimental measurements carried out on Run-C devices consisted of electrical tests (current-voltage as well as capacitance-voltage characterisations), and measurements of the charge collection using both a laser setup (which exploits the TCT technique) and a radioactive source setup (an ALiBaVa read-out system was used). A set of sensors was irradiated with protons or neutrons to different fluences in the range $[3.3 \cdot 10^{13}, 9 \cdot 10^{15}]$ $\text{n}_{\text{eq}}/\text{cm}^2$.

Measurements indicate two main outcomes: first, the different experimental methods lead to consistent results. Sensors presenting good electrical characteristics (large breakdown voltage, low leakage current) show higher charge collection under laser exposure compared to sensors with worse IV and CV curves; a low capacitance and a low leakage current are essential requirements to be able to perform radioactive source measurements with the ALiBaVa setup. Second, measurements are in agreement with the SINTEF Run-D findings: obtained independently, the experimental results can be explained taking into consideration the random presence of pin-holes.

Experimental results are summarised in Section 6.5. Here, only the most relevant are reported.

Electrical characterisation

Electrical measurements highlight that there is a significant spread of the electrical parameters among sensors and among strips of a single sensor. These inhomogeneous responses are consistent with the SINTEF Run-D findings. Sensors presenting a double-knee CV curve, expected for the 3D silicon technology, have a higher breakdown voltage and a lower leakage current with respect to SINTEF 3D sensors featuring a single-knee CV curve. Evaluated according to these characteristics, the sensor quality presents a gradient across the wafer. This is symptomatic of an improvable production process. The IV curves for SINTEF 3D sensors from Run-C are generally not reproducible if the measurement is repeated multiple times. This phenomenon is attributed to an effect of built-up of charge inside the sensor.

After irradiation, sensors experience an increase in the leakage current

proportional to the fluence. The proportionality factor, the so-called damage constant, is $\alpha = (4.1 \pm 0.6) \cdot 10^{-17}$ A/cm, in agreement with literature. The depletion voltage does not significantly change with radiation: it remains below $U_{depl} \leq 20$ V regardless of the fluence level. Irradiating the samples has a positive effect on their breakdown voltage, which increases with fluence. The capacitance decreases after irradiation.

Laser characterisation

A study of the laser-induced charge collection as a function of bias voltage and fluence was carried out. BABY sensors with different pixel cell configurations were measured. TCT measurements show an increase in the depleted region when a higher bias voltage is applied. An increase in charge collection is observed when electrodes get closer (e.g. for sensors featuring a higher density of electrodes in the pixel). After irradiation, charge collection decreases with fluence. The amount of collected charge is larger for sensors from wafer C25 compared to sensors from the other wafer.

Radioactive source characterisation

Radioactive source measurements were performed on a few FEI3 and FEI4 sensors, both unirradiated and proton-irradiated. Priority was given to the charged-hadron irradiation because it gives a larger contribution to the radiation damage in the tracking region of the experiments compared to the neutral hadrons.

The sensors were measured using the ALiBaVa read-out system. The characterisation was completely successful for a FEI4 sensor, proton-irradiated to a fluence $\phi = 4.5 \cdot 10^{14}$ n_{eq}/cm^2. This sensor had a lower capacitance and a lower leakage current compared to other SINTEF devices. Its cluster charge collection efficiency after irradiation is 85% at $U_{bias} = -40$ V. Technical difficulties in the measurements, given by the underperforming sensors and a nonideal compatibility between the sensors and the read-out system, prevented the radioactive source characterisation of other sensors from being carried out.

Outlook

The understanding of the origin of the problems encountered during Run-C was an important advance. Looking forward towards the currently-ongoing prototyping run, the opportunity to limit the issues observed during the Run-C campaign and manufacture a larger sample of optimally-performing sensors is crucial to

establish the Norwegian research institute as a strong candidate for the new sensor production. A complete characterisation, such as the one presented in this thesis, should be performed on sensors from the new Run-D batch to evaluate their performance.

The best approach to study the evolution of the performance of these device with radiation would be to iteratively perform measurements (which include electrical as well as laser and radioactive source characterisations) and expose the sensors to increasing irradiation levels. Sensors failing the performance criteria at any fluence level would be discarded and would not be further measured or irradiated. Laboratory measurements should be corroborated by simulations, which are especially important given the complexity of the 3D layout. Test beams would be essential to prove the performance of the sensors in real conditions. If meant to be measured with the ALiBaVa setup, future sensors would require a precautious design of the read-out geometry, to reduce the capacitance. A customised fan-in would be advantageous.

Appendix A

This appendix collects two tables: the first one contains the geometrical parameters of BABY sensors. It highlights, as a function of the pixel cell configuration, the volume occupied by the electrode columns and the surface covered by the temporary metal layer.

The second table second compares, for the BABY sensors selected to be measured in the TCT setup, the breakdown voltages measured using the IV setup and the maximum voltage that could be applied to the same sensors during TCT+ measurements (see Sections 5.3 and 5.4 for details on the experimental setups and Section 6.3 for laser characterisation results).

Geometrical properties of BABY sensors

Table A1 contains geometrical parameters of the BABY sensors. For each electrode configuration, the table reports the number of electrodes in the single pixel cell, the volume of the pixel columns, the fraction of filled volume (occupied by the columns) and the fraction of active volume. The total metallised surface (strip + electrode cover + bump pad metallisation) and the fraction of covered and free surfaces are also indicated.

Breakdown voltages in IV and TCT measurements

Table A2 reports, for each proton-irradiated BABY sensor measured in the TCT+ setup, the values of the maximum voltage at which the BABY sensors were biased during TCT scans (V_{max}^{TCT}) and the maximum operating voltage observed in IV scans (V_{BD}^{IV}). Comparing these two voltages, some sensors do not show the same capability to withstand an equal potential during TCT measurements as they do during IV scans. This represented a limiting factor for what concerns the direct comparison between TCT results, because it forced measurements to be taken at different voltages.

Cfg.	No. Electrodes	Column Volume $(10^3 \mu\mathrm{m}^3)$	Fraction Filled Vol %	Fraction Sensitive Volume %
1	2	71	1.54	98.46
2	4	142	3.08	96.92
3	6	212	4.62	95.38
4	8	283	6.16	93.84
5	10	354	7.70	92.30

Cfg.	No. Electrodes	Metallised surface $(10^3 \mu\mathrm{m}^2)$	Fraction Covered surface %	Fraction Free surface %
1	2	10.3	51.3	48.7
2	4	10.7	53.7	46.3
3	6	11.2	56.0	44.0
4	8	11.7	58.4	41.6
5	10	12.2	60.8	39.2

Table A1: Geometrical parameters of a single pixel of 3D BABY sensors. The columns report the pixel cell configuration, the total number of columns within the area of a single pixel (400 μm $\times$ 50 μm), the volume occupied by the columns in a pixel, the fraction of the pixel's volume occupied by the columns and the fraction of sensitive pixel volume; the total metallised area (strips + electrode + bump pads), and the fraction of covered and metal-free surfaces.

Nominal fluence ϕ [p/cm^2]	Pixel cell configuration					
	1E			2E		
	No.	V_{max}^{TCT}	V_{BD}^{IV}	No.	V_{max}^{TCT}	V_{BD}^{IV}
	No.	[V]	[V]	No.	[V]	[V]
0	**221**	15	80	**222**	30	80
5×10^{13}	–	–	–	**257**	14	$^{(*)}$
1×10^{14}	**43**	40	50	**26**	3	80
5×10^{14}	**250**	70	$> 100^{(b)}$	–	–	–
1×10^{15}	–	–	–	**211**	70	$> 100^{(b)}$
5×10^{15}	**205**	$^{(**)}$	–	**251**	70	$> 120^{(c)}$
1×10^{16}	**236**	70	$> 120^{(a)}$	**267**	7	70-80$^{(*)}$

ϕ [p/cm^2]	3E			4E		
	No.	V_{max}^{TCT}	V_{BD}^{IV}	No.	V_{max}^{TCT}	V_{BD}^{IV}
	No.	[V]	[V]	No.	[V]	[V]
0	**249**	10	60	**203**	20	60
5×10^{13}	**207**	70	70-80$^{(***)}$	**208**	70	70-80$^{(***)}$
1×10^{14}	**258**	0	$> 100^{(b)}$	**23**	60	80
5×10^{14}	**247**	70	$> 100^{(c)}$	**248**	70	$> 120^{(c)}$
1×10^{15}	**233**	70	70-80	**28**	70	50
5×10^{15}	**233**	70	80-90	**245**	70	80$^{(***)}$
1×10^{16}	**259**	70	$> 100^{(c)}$	**264**	30	70

Table A2: Comparison between V_{max}^{TCT} and V_{BD}^{IV} for the BABY sensors measured, respectively, in the TCT and IVCV setups (with configuration up to 4E). The V_{max}^{TCT} is the maximum voltage applied during TCT measurements. The use of a voltage $V_{max}^{TCT} < 70$ V was dictated by the compliance current. The V_{BD}^{IV} is the maximum operating voltage according to IV scans. For many sensors, V_{BD}^{IV} is not reachable during TCT measurements.

Maximum leakage currents of the IV curves:

$^{(a)}$ $I_{leak}^{max} < 10^{-3}$ μA;

$^{(b)}$ 0.1 μA $\leq I_{leak}^{max} \leq 0.5$ μA;

$^{(c)}$ 1 μA $\leq I_{leak}^{max} \leq 5$ μA.

Particular shapes of the IV curves or other notes:

$^{(*)}$ the IV curve has two very neat knees, the first at $V = 15$ V;

$^{(**)}$ the sensor got burnt because a too-high voltage, leading to a too-high leakage current, was applied;

$^{(***)}$ very slow breakdown.

Bibliography

[1] S. Glashow, *Partial Symmetries of Weak Interactions*, Nuclear Physics 22 (1961) 579, 1961.

[2] S. Weinberg, *A Model of Leptons*, Phys. Rev. Lett. 19 (1967) 1264, 1967.

[3] A. Salam and J. C. Ward. *Electromagnetic and weak interactions*, Phys. Lett. 13, 168, 1964.

[4] O. S. Bruning et al., *The LHC design report, Volume I: The LHC Main Ring*, CERN-2004-003, 2004.

[5] L. Evans, P. Bryant, *LHC Machine* 2008 JINST 3 S08001.

[6] L. Rossi, O. Brüning, *High Luminosity Large Hadron Collider: A description for the European Strategy Preparatory Group*, CERN-ATS-2012-236, 2012.

[7] The ATLAS Collaboration, *ATLAS Detector and Physics Performance - Technical Design Report, Volume I*, 1999.

[8] The ATLAS Collaboration, *ATLAS Insertable B-Layer Technical Design Report*, CERN-LHCC-2010-013 / ATLAS-TDR-019, 2010.

[9] S. I. Parker et al., *3D - A Proposed New Architecture for solid state radiation detectors*, Nuclear Instruments and Methods in Physics Research A 395 328-343, 1997.

[10] The ATLAS Collaboration, *ATLAS Phase-II Upgrade, Scoping Document*, CERN-LHCC-2015-020, 2015.

[11] SINTEF website, `http://www.sintef.no/`.

[12] Image of the CERN's accelator complex `https://cds.cern.ch/record/2225847?ln=en`.

[13] The ALICE Collaboration, *ALICE physics performance: Technical Design Report*, CERN-LHCC-2005-030, ALICE-TDR-13, 2005.

[14] The CMS Collaboration, *CMS Physics Technical Design Report Volume I: Detector Performance and Software*, CERN/LHCC 2006-001, CMS TDR 8.1, 2006.

[15] The LHCb Collaboration, *LHCb: Technical Proposal*, CERN-LHCC-98-004, LHCC-P-4, 1998.

[16] F. Gianotti for the ATLAS Collaboration, *Status of Standard Model Higgs searches in ATLAS* [slides] CERN, July 4, 2012.

[17] J. Incandela for the CMS Collaboration, *The Status of the Higgs Search* [slides] CERN, July 4, 2012.

[18] The ATLAS and CMS Collaborations, *Combined Measurement of the Higgs Boson Mass in pp Collisions at $\sqrt{s} = 7$ and 8 TeV with the ATLAS and CMS Experiments*, Phys. Rev. Lett. 114, 191803, 2015.

[19] Image of the Standard Model interactions, `https://en.wikipedia.org/wiki/File:Interactions.png`.

[20] P. W. Higgs, *Broken Symmetries and the Masses of Gauge Bosons*, Phys. Rev. Lett. 13 508, 1964.

[21] F. Englert and R. Brout, *Broken Symmetry and the Mass of Gauge Vector Mesons*, Phys. Rev. Lett. 13 321, 1964.

[22] The LHCb Collaboration, *Observation of $J/\psi p$ resonances consistent with pentaquark states in $\Lambda_0^b \to J\psi K^- p$ decays*, arXiv:1507.03414v2 [hep-ex], 2015.

[23] I. J. R. Aitchison, A. J. G. Hey, *Gauge Theories in Particle Physics - a Practical Introduction - Non-Abelian Gauge Theories: QCD and the Electroweak Theory*, Institute of Physics Publishing Ltd, 2004.

[24] F. Mandl, G. Shaw, *Quantum Field Theory*, John Wiley & Sons, 1984.

[25] D. Griffiths, *Introduction to Elementary Particles*, Wiley & Sons, 1987.

[26] N.J. Evans, *An Introduction to QED & QCD*, Lectures presented at the School for High Energy Physics, September 2008.

[27] J. B. Hansen, *Physics at run 2 - The ultimate search engine: LHC*, WLCG Collaboration workshop 2013, November 2013.

[28] P. Wells, *Physics Program of the LHC Upgrades*, [slides] presented at the Lepton Photon Conference, San Francisco, 2013

[29] W. Greiner, B. Müller, *Gauge Theory of Weak Interactions*, Springer, 1986.

[30] K. S. Krane, *Introductory Nuclear Physics*, Miley & Sons, 1988.

[31] The LHCb Collaboration, *First Observation of CP Violation in the Decays of B_s^0 Mesons* Physical Review Letters 110, 221601, 2013.

[32] A. Canepa, *Selected Highlights from the LHC and HL-LHC Physics Program*, [slides] Winter Aspen Meeting, 2015.

[33] M. Lamont, *Status of the LHC*, Journal of Physics: Conference Series 455 (2013) 012001 doi:10.1088/1742-6596/455/1/012001, 2013.

[34] ATLAS Luminosity public results, `https://twiki.cern.ch/twiki/bin/view/AtlasPublic/`.

[35] M. Nessi, *Detector plans for LS1*, proceedings of Chamonix 2012 workshop on LHC Performance, Chamonix, 2012.

[36] G. Volpi, *ATLAS Physics Prospects at the Upgraded LHC*, slides presented at the Lake Louise Winter Institute Conference, ATL-PHYS-SLIDE-2015-035, 2015.

[37] S. Welch, J. Dopke, *The ATLAS pixel nSQP readout chain*, ATL-INDET-PROC-2012-018, 2012.

[38] M. Shochet et al., *Fast TracKer (FTK) Technical Design Report*, CERN-LHCC-2013-007, ATLAS-TDR-021, 2013.

[39] L. Adamczyk et al., *Technical Design Report for the ATLAS Forward Proton Detector*, CERN-LHCC-2015-009, ATLAS-TDR-024, 2015.

[40] A. Clark, M. Elsing, P. Wells, *Performance Specifications of the Tracker Phase II Upgrade*, ATL-UPGRADE-PUB-2012-003, 2012

[41] M. Bianco, *Micromegas detectors for the muon spectrometer upgrade of the ATLAS experiment*, Nuclear Instruments and Methods in Physics Research A 824 (2016) 496-500, 2016.

[42] B. T. Huffman, *Plans for the Phase II upgrade to the ATLAS detector*, JINST 9 C02033, 2014.

[43] Image CERN-GE-0803012-01, `http://cds.cern.ch/record/1095924/`.

[44] The ATLAS Collaboration fact sheet, `http://www.atlas.ch/pdf/ATLAS_fact_sheets.pdf`.

[45] The ATLAS Collaboration, *The ATLAS Inner Detector commissioning and calibration*, The European Physical Journal C, Volume 70, Issue 3, pp 787-821, 2010.

[46] W. R. Leo, *Techniques for Nuclear and Particle physics Experiments*, Springer Verlang, 1987.

[47] Particle Data Group `http://pdg.lbl.gov/2013/reviews/rpp2013-rev-passage-particles-matter.pdf`, revised by H. Bichsel et al., 2013.

[48] Image CERN-EX-1301009-01, `https://cds.cern.ch/record/1505342`.

[49] C. Grupen, B. Shwartz, *Particle Detectors*, Cambridge University Press, 2008.

[50] Image CERN-GE-0803014-03, `http://cds.cern.ch/record/1095926`.

[51] ATLAS Collaboratio, *Inner Detector, Technical Design Report - Volume I*, CERN/LHCC 97-16, 1997.

[52] A. Heinson, T.R. Junk, *Observation of Single Top Quark Production*, Annual Review of Nuclear and Particle Science, Volume 61, 171-196, 2011.

[53] The ATLAS Collaboration, *Expected performance of the ATLAS experiment: detector, trigger and physics*, arXiv:0901.0512, CERN-OPEN-2008-020, 2008.

[54] A. La Rosa for the ATLAS Collaboration, *ATLAS Pixel Detector: Operational Experience and Run-1 to Run-2 Transition*, PoS Vertex2014 001 arXiv:1410.6347 [physics.ins-det] ATL-INDET-PROC-2014-007, 2015.

[55] The ATLAS Pixel Collaboration, Approved Plot Pixels webpage `https://twiki.cern.ch/twiki/bin/view/AtlasPublic/ApprovedPlotsPixel`.

[56] The ATLAS Collaboration, *ATLAS pixel detector electronics and sensors*, 2008 JINST 3 P07007, 2008.

[57] The ATLAS Collaboration, *The ATLAS Experiment at the CERN Large Hadron Collider*, 2008 JINST 3 S08003, 2008.

[58] R. Versaci et al, *Exploiting the Undesired: Beam-Gas Interactions at the LHC*, Proceedings of IPAC2012, New Orleans, Louisiana, USA, 2012.

[59] A. Gorišek, *ATLAS Diamond Beam Monitor*, 7th Trento Workshop on Advanced Silicon Radiation Detectors, 2012.

[60] W. E. Selph, *Neutron and Gamma-Ray Albedos*, reprint of Chapter 4 of *Weapons Radiation Shielding Handbook*, 1968.

[61] Y. Arai, M. Asai, E. Barberio, T. Emura, J. Goldberg, K. Homma, M. Ikeno, M. Imori, K. Ishii, H. Ishiwaki, et al., *Timing optimization of thin gap chambers for the use in the ATLAS muon endcap trigger*, Nuclear Instruments and Methods in Physics Research Section A, 367, 398-401, 1995.

[62] W. Buttinger, *The ATLAS Level-1 Trigger System*, Journal of Physics: Conference Series 396 (2012) 012010, 2012.

[63] H. P. Beck et al., *The ATLAS Event Filter*, CHEP 1998.

[64] The ATLAS Collaboration, *Public results, Event Displays from Upgrade Physics Simulated Data*, `https://twiki.cern.ch/twiki/bin/view/AtlasPublic/UpgradeEventDisplays`.

[65] The ATLAS Collaboration, *Technical Design Report for the ATLAS Inner Tracker Strip Detector*, CERN-LHCC-2017-005, ATLAS-TDR-025, 2017.

[66] The ATLAS Collaboration, *Letter of Intent for the Phase-II Upgrade of the ATLAS Experiment* https://cds.cern.ch/record/1502664/files/LHCC-I-023.pdf.

[67] FLUKA website, http://www.fluka.org/fluka.php

[68] H. Hayward, *ATLAS ITK Requirements and Layout*, slides from ACES 2014 - Fourth Common ATLAS CMS Electronics Workshop for LHC Upgrades, CERN, 2014.

[69] G. Lutz, *Semiconductor Radiation Detectors*, Springer, 1999.

[70] Image of the energy levels in silicon, `http://www.optique-ingenieur.org/en/courses/OPI_ang_M05_C02/co/Contenu.html`.

[71] Image of energy levels for insulator, semiconductors and metals, `http://chemed.chem.purdue.edu/genchem/topicreview/bp/materials/defects3.html`.

[72] Image of direct and indirect band gaps, `https://en.wikipedia.org/w/index.php?curid=14519297` and By Profjohn - Own work, CC BY-SA 3.0, `https://commons.wikimedia.org/w/index.php?curid=3994494`.

[73] C. Gallrapp, *Studies on irradiated pixel detectors for the ATLAS IBL and HL-LHC upgrade*, Ph.D. Thesis, Technical University of Berlin, 2015.

[74] L. Rossi, P. Fischer, T. Rohe, N. Wermes, *Pixel Detectors - From Fundamentals to Applications*, Springer-Verlag Berlin Heidelberg, 2006.

[75] N. Pacifico, *Radiation Damage Study on Innovative Silicon Sensors for the CMS Tracker Upgrade*, Ph.D. Thesis, University of Bari, 2012.

[76] J. P. Balbuena Valenzuela, *Development of innovative silicon radiation detectors*, Ph.D. Thesis, University of Barcelona, 2012.

[77] M. Moll, *Radiation Damage in Silicon Particle Detectors - microscopic defects and macroscopic properties*, Ph.D. Thesis, Hamburg University, 1999.

[78] Esteban Currás Rivera, *Advanced silicon sensors for future collider experiments*. Ph.D. Thesis, Santander, 2017.

[79] M. Červ, *The ATLAS Diamond Beam Monitor*, Topical Workshop on Electronics for Particle Physics 2013, 23-27 September 2013, Perugia, Italy, 2014 JINST 9 C02026.

[80] J. W. Tsung et al., *Signal and noise of diamond pixel detectors at high radiation fluences*, 2012 JINST 7 P09009.

[81] The BaBar Collaboration, *Technical Design Report*, 1995.

[82] The CDF Collaboration, *The CDF-II detector: Technical design report*, FERMILAB-DESIGN-1996-01, 1996.

[83] V. Chmill, *Radiation Tests of Semiconductor Detectors*, Thesis, Royal Institute of Technology, Stockholm, 2006.

[84] M. Rogalla, *Systematic Investigation of Gallium Arsenide Radiation Detectors*, Ph.D. Thesis, University of Freiburg, 1997.

[85] Z. He, *Review of the Shockley-Ramo theorem and its application in semiconductor gamma-ray detectors*, Nuclear Instruments and Methods in Physics Research A 463 250-267, 2001.

[86] CERN Bonding Lab website, `http://bondlab-qa.web.cern.ch/bondlab-qa/Basic_Info.html`.

[87] M. Krammer et al., *Silicon Detectors*, slides from EDIT 2011 School, CERN, 2011.

[88] CMS webpage on silicon sensors, `http://cms.web.cern.ch/news/silicon-pixels`.

[89] E. Cabruja et al., *Special bump bonding technique for silicon pixel detectors*, Nuclear Instruments and Methods in Physics Research A 576 150-153, 2007.

[90] G. Traversi et al., *2D and 3D CMOS MAPS with high performance pixel-level signal processing*, 2010.

[91] W. Snoeys, *CMOS monolithic active pixel sensors for high energy physics*, Nuclear Instruments and Methods in Physics Research A 765, 167-171, 2014.

[92] T. Hemperek, T. Kishishita, H. Krüger, N. Wermes, *A Monolithic active pixel sensor for ionizing radiation using a 180nm HV-SOI process*, Nuclear Instruments and Methods in Physics Research A 796, 8-12, 2015.

[93] P. Riedler, *Overview of Monolithic Silicon Pixel Detectors*, slides from public CERN CLIC seminar, 2015, `http://indico.cern.ch/event/ 374145/contribution/0/attachments/745477/1022655/CLIC_ seminar_032015_priedler.pdf`.

[94] C. Da Vià, *Radiation hardness properties of full-3D active edge silicon sensors*, Nuclear Instruments and Methods in Physics Research A 587 243-249, 2008.

[95] C. Da Vià, *Silicon sensors go 3D*, CERN Courier, May 31, 2012.

[96] D. Pennicard, *3D detectors for synchrotron applications*, Ph.D. Thesis, University of Glasgow, 2009.

[97] R. Bosch GmbH, Patents No. 4855017 and 4784720 (USA) and No. 4241045C1 (Germany), 1994.

[98] C. Da Vià, *3D silicon sensors: Design, large area production and quality assurance for the ATLAS IBL pixel detector upgrade*, Nuclear Instruments and Methods in Physics Research A 694 321-330, 2012.

[99] C. Da Vià, *3D sensors and micro-fabricated detector systems*, Nuclear Instruments and Methods in Physics Research A 765 151-154, 2014.

[100] R. Engel, *PHOJET manual* Program version 1.05c.

[101] G. Beck et al., *Analytic model of thermal runaway in silicon detectors*, Nuclear Instruments and Methods in Physics Research A, 618 131-138, 2010.

[102] G. Lindström et al., *Radiation hardness of silicon detectors - a challenge from high-energy physics*, Nuclear Instruments and Methods in Physics Research A 426 (1999) 1-15, 1999.

[103] G. Casse, *The effect of hadron irradiation on the electrical properties of particle detectors made from various silicon materials*, Ph.D. Thesis, University of Grenoble, 1998.

246

[104] The ROSE Collaboration, `http://rd48.web.cern.ch/RD48`.

[105] A. Vasilescu, *Notes on the fluence normalisation based on the NIEL scaling hypothesis*, ROSE/TN/2000-02.

[106] M. Huhtinen, *Simulation of non-ionising energy loss and defect formation in silicon*, Nucl. Instr. and Meth. in Phys. Res. A, 491:194-215, 2002.

[107] A. Vasilescu, *The NIEL scaling hypothesis applied to neutron spectra of irradiation facilities in the ATLAS and CMS SCT*, ROSE/TN/1997-2.

[108] A. Chiochia et al., *Simulation of Heavily Irradiated Silicon Pixel Sensors and Comparison with Test Beam Measurements*, IEEE Transactions on Nuclear Science, Vol. 52, 1067-1075, 2005.

[109] M. C. Moroni, *Evaluation of Silicon sensors for the ATLAS Silicon Tracker, and TPC reconstruction in the HARP Experiment*, Ph.D. Thesis, University of Geneva, 2003.

[110] I. Gorelov, *A measurement of Lorentz angle and spatial resolution of radiation hard silicon pixel sensors*, Nuclear Instruments and Methods in Physics Research A, 481 204-221, 2002.

[111] P. Hansson, J. Balbuena, C. Barrera, E. Bolle, M. Borri et a;, *3D silicon pixel sensors: Recent test beam results*, Nuclear Instruments and Methods in Physics Research A 628, 216-220, 2011.

[112] D. Giugni, *The ATLAS Insertable B-Layer Detector (IBL)*, slides from the 11th ICATPP Conference on Astroparticle, Particle, Space Physics, Detectors and Medical Physics Applications, Como, Italy, 5-9 Oct 2009.

[113] ATLAS News website, `http://atlasexperiment.org/news/2014/a-new-sub-detector-for-ATLAS.html`.

[114] F. H*ü*gging for the ATLAS Collaboration, *The ATLAS Pixel Insertable B-Layer (IBL)*, Nucl.Instrum.Meth. A 650 45-49 arXiv:1012.2742 [physics.ins-det] 2011.

[115] L. Zwalinski, *CO_2 cooling system for Insertable B-Layer detector into the ATLAS Experiment*, TIPP Conference Proceedings, 2014.

[116] The FE-I4 Collaboration, *The FE-I4B Integrated Circuit Guide*, Version 2.3, 2012.

[117] C. Gallrapp, *Overview of the ATLAS Insertable B-Layer (IBL) Project*, slides from the 7th Trento Workshop on Advanced Radiation Detectors (3D and p-type), Jožef Stefan Institute, Slovenia, 2012.

[118] G. Mullier, *The upgraded Pixel Detector of the ATLAS Experiment for Run-2 at the Large Hadron Collider*, ATL-INDET-PROC-2015-013, 2015.

[119] O. M. Røhne, *Overview of the ATLAS Insertable B-Layer (IBL) Project*, Nuclear Instruments and Methods in Physics Research A 731 18-24, 2013.

[120] The ATLAS Collaboration, *Expected performance of the ATLAS b-tagging algorithms in Run-2*, ATL-PHYS-PUB-2015-022, 2015.

[121] C. Gemme, *The ATLAS insertable B-Layer (IBL) project*, ATL-INDET-PROC-2011-018, 2011.

[122] A. Polini, G. Bruni, M. Bruschi, I. D'Antone, J. Dopke, D. Falchieri, T. Flick, A. Gabrielli, J. Grosse-Knetter, J. Joseph et al., *Design of the ATLAS IBL Readout System*, Physics Procedia 37 (2012) 1948-1955, 2012.

[123] The ATLAS Collaboration, *Athena - The ATLAS Common Framework*, Version 8, 2006.

[124] D. A. Dobos, *Commissioning Perspectives for the ATLAS Pixel Detector*, Ph.D. Thesis, University of Dortmund, 2007.

[125] The ATLAS Collaboration, *ATLAS High-Level Trigger, Data Acquisition and Controls; Technical Design Report*, 2003.

[126] M. Dobson, F. Wickens, *ATLAS TDAQ Glossary webpage*, `http://mdobson.web.cern.ch/mdobson/tdaq/glossary.html`.

[127] I. Bird et al., *Update of the Computing Models of the WLCG and the LHC Experiments*, CERN-LHCC-2014-014 / LCG-TDR-002, 2014.

[128] ATLAS Event Display from Non-Collision data, `https://twiki.cern.ch/twiki/bin/view/AtlasPublic/EventDisplayRun2Start`.

[129] ATLAS Event Display from Collision data, `https://twiki.cern.ch/twiki/bin/view/AtlasPublic/EventDisplayRun2Collisions`.

[130] S. I. Parker, C. J. Kenney, *Performance of 3-D Architecture Silicon Sensors After Intense Proton Irradiation*, IEEE Transactions on Nuclear Science, Vol. 48, No. 5, 2001.

[131] A. Kok, T-E. Hansen, T. A. Hansen, N. Lietaer, A. Summanwar et al., *Fabrication of 3D silicon sensors*, 19th International Workshop on Vertex Detectors, Loch Lomond, UK, 2010.

[132] A. Kok, T. E. Hansen, T. A. Hansen, N. Lietaer, M. M. Mielnik et al., *3D Detector Activities at SINTEF MiNaLab - Wafer Bonding and Deep Reactive Ion Etching*, International Wafer Level Packaging Conference, San Jose, 2008.

[133] A. Kok, *Fabrication of full 3D active edge sensors*, 6th Trento Workshop on Advanced Radiation Detectors, Trento, 2011.

[134] T. E. Hansen, *First fabrication of full 3D-detectors at SINTEF*, JINST 4 P03010, 2009.

[135] A. Kok, *Status of 3D sensors processing at SINTEF MiNaLab*, 5th Trento Workshop on Advanced Radiation Detectors, Manchester, 2010.

[136] A. Kok, *3D Processing Status*, [slides].

[137] A. L. Heggelund, *Analysis of 3D Pixel Detectors for the ATLAS Inner Tracker Upgrade*, Master Thesis, University of Bergen, 2017.

[138] CiS website, `http://www.cismst.org/`.

[139] Gianluigi Casse, A. Affolder, P.P. Allport, H. Brown, M. Wormald, *Enhanced efficiency of segmented silicon detectors of different thicknesses after proton irradiations up to 1×10^{16} $n_{eq}cm^2$*, Nuclear Instruments and Methods in Physics Research A 624, 401-404, 2010.

[140] F. Ravotti et al., *A New High-intensity Proton Irradiation Facility at the CERN PS East Area*, PoS (TIPP2014) 354, 2014.

[141] The JSI webpage of the AIDA project, `http://aida2020.web.cern.ch/content/jsi`.

[142] The AIDA project, `http://aida2020.web.cern.ch/`.

[143] I. Mateu, M. Moll, F. Ravotti, *Experimental determination of the NIEL hardness factor for the new CERN proton irradiation facility*, slides presented at the 28th RD50 Workshop, Torino, 2016.

[144] A. Curioni, R. Froeschl, M. Glaser, E. Iliopoulou, F. P. La Torre et al., *Single- and multi-foils $^{27}Al(p, 3pn)^{24}Na$ activation technique for monitoring the intensity of high-energy beams*, Nuclear Instruments and Methods in Physics Research A, 858, 101-105, 2017.

[145] M. Glaser, F. Ravotti, M. Moll, *Dosimetry Assessments in the Irradiation Facilities at che CERN-PS Accelerator*, IEEE Transactions on Nuclear Science, Vol. 53, No. 4, 2006.

[146] Keithley, *C-V Characterization of MOS Capacitors Using the Model 4200-SCS Semiconductor Characterization System*, Keithley Application Note Series, No. 2896.

[147] G. Amorese, *LCR / Impedance Measurement Basics*, Hewlett-Packard Company, 1997.

[148] CERN ROOT Analysis Framework website, `https://root.cern.ch/`.

[149] CERN ROOT Analysis Framework website, TProfile class, `https://root.cern.ch/doc/master/classTProfile.html`.

[150] I. Mandić, *TCT measurements of irradiated strip detectors with a focused laser beam*, JINST 8 P04016, 2013.

[151] C. Gallrapp et al., *Effects of Radiation on Solid State Particle Detector Performance & Workshop on the characterization of irradiated silicon sensors*, [slides] ESIPAP School - February 2015.

[152] Cividec website, `https://cividec.at/`.

[153] C. Gallrapp, E. Curras, M. Fernandez, J. Gonzalez, H.Neugebauer et al., *The TCT+ setup - a system for TCT, eTCT and timing measurements*, [slides], 1st TCT Workshop DESY, October 2015.

[154] J. Lange, E. Cavallaro, F. Förster, S. Grinstein, I. López Paz et al., *Studies of small-pitch CNM 3D detectors*, slides presented at the 29th RD50 Workshop, CERN, 2016.

[155] ALiBaVa System website, `http://www.alibavasystems.com/`.

[156] R. M. Hernández, *Design, development and implementation of a readout system for microstrip silicon sensors. Upgrade for test beam measurements*, Ph.D. Thesis, University of Valencia, 2012.

[157] S. Löchner, *Development, Optimisation and Characterisation of a Radiation Hard Mixed-Signal Readout Chip for LHCb*, Ph.D. Thesis, University of Heidelberg, 2006.

[158] S. Löchner, M. Schmelling, *The Beetle Reference Manual - chip version 1.3, 1.4 and 1.5 -*, LHCb-2005-105, ELECTRONICS, 2006.

[159] R. M. Hernández, *A Portable Readout System for Microstrip Silicon Sensors (ALIBAVA)*, IEEE Transactions on Nuclear Science, Vol. 56, No. 3, 2009.

[160] C. Lacasta, *Alibava GUI*, `https://www.alibavasystems.com/images/Catalogo/alibava-usermanual.pdf`.

[161] M. Adams, R. Lipton, *Analysis of Pedestal Data of the Silicon Muon Scanner*, Summer student report, Fermilab, 2016.

[162] M. R. Coluccia, J. A. Appel, G. Chiodini, D. C. Christian and S. Kwan, *Characterization of Prototype BTeV Silicon Pixel Sensors Before and After Irradiation*, IEEE Transactions on Nuclear Science, Vol. 49, No. 4, 2002.

[163] H. Spieler, *Semiconductor detectors - Basic concepts II*, SLUO Lectures on Detector Techniques, 1998.

[164] A. Chilingarov, *Temperature dependence of the current generated in Si bulk*, JINST 8 P1003, 2013.

[165] M. Ershov, H. C. Liu, L. Li, M. Buchanan, Z. R. Wasilewski, A. K. Jonscher, *Negative capacitance effect in semiconductor devices*, IEEE Transactions on Electron Devices, arXiv:cond-mat/9806145v1 [cond-mat.mes-hall], 1998.

[166] C. Gemme, *The ATLAS tracker Pixel detector for HL-LHC*, Proceedings - The 25th International workshop on vertex detectors, La Biodola, Isola d'Elba, Italy, ATL-ITK-PROC-2017-001, 2017.

[167] Z. Li, *Radiation hardness tolerance of Si sensor detectors for nuclear and High Energy Physics experiments*, Proceedings - PIXEL International Workshop Carmel, CA, 2002.

[168] R.Mendicino, M. Povoli, G. F. Dalla Betta, M. Boscardin, G. Giacomini, N. Zorzi, *Investigation of the electrical Characteristics of double-sided silicon 3D sensors after irradiation with different particles*, [slides], 8th "Trento" Workshop on Advanced Silicon Radiation Detectors (3D and P-type Technologies), Trento, 2013.

[169] Glade webpage, `http://www.peardrop.co.uk/`.